

https://dspace.org/

Charecterisation of Geothermal Resources at Kwako Hills in Zambia using magnetic and natural source audio-magnetotelluric

Chinamora, Blessing

2019

https://hdl.handle.net/10539/28714

Downloaded from a DSpace repository. https://dspace.org/



CHARACTERISATION OF A GEOTHERMAL RESOURCE AT KWAKO HILLS IN ZAMBIA USING MAGNETIC AND NATURAL SOURCE AUDIO-MAGNETOTELLURIC METHODS

Blessing Chinamora

School of Geosciences, University of the Witwatersrand

A dissertation submitted to the Faculty Science, University of the Witwatersrand, Johannesburg, in fulfilment of the requirements for the degree of Master of Science in Geophysics.

Johannesburg, 2019

Supervised by: Dr. Mike Jones and Prof. Susan Webb

DECLARATION

I declare that this dissertation is my own, unaided work. It is being submitted for the Degree of Master of Science at the University of the Witwatersrand, Johannesburg. It has not been submitted before for any degree or examination at any other University.

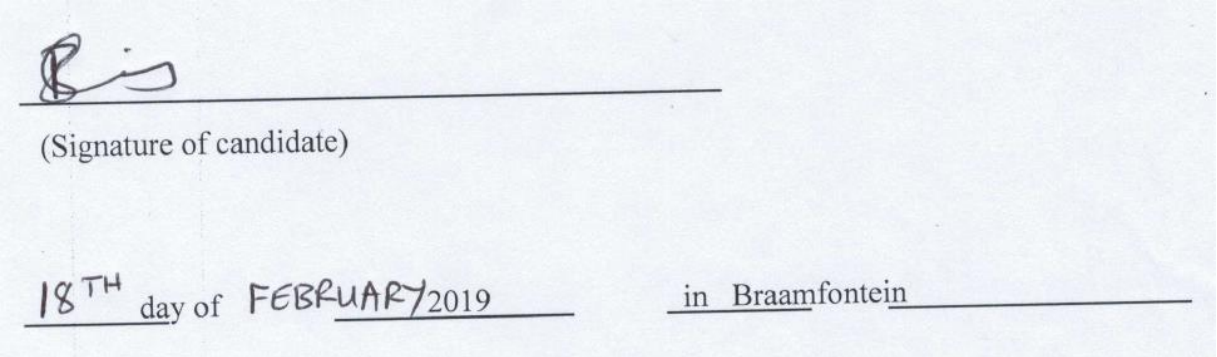

(Signature of candidate)

18TH day of FEBRUARY 2019 in Braamfontein

Abstract

The announcement by the Zambian government that geothermal energy will be recognized as an energy source in the 2013 national budget drew a lot of attention to investors and scientists. Since the 1950s reconnaissance geoscientific surveys have been carried out on geothermal targets in Zambia by the Geological Survey of Zambia (GSZ). The GSZ, together with an Italian company (DAL, SpA), studied various hot springs (Legg, 1974) and as a result, various prospects have been considered for development or exploration. In this research, the Kwako Hills prospect which is located near Mumbwa district, about 150 km northwest of Lusaka, hosts two hot springs which are good surface manifestations for geothermal energy potential was investigated for its geothermal energy reservoir potential using magnetic and natural source audio-magnetotelluric (NSAMT) geophysical methods. The focus of these surveys was on examining the structural controls that govern the occurrence of the hot springs and the outcropping Hook Batholith just to the north of the east-west trending alluvium filled valley. The northern branch of the alluvium valley has a northwest–southeast trend which is the same as the minor fault controlling the two hot springs. These structural controls increase the vertical permeability in the area causing the thermal waters to circulate to depths where they acquire their heat. Permeability is high at intersections of faults and fracture zones, intersection of major and minor faults or intersection of faults and sedimentary aquifers. Major ENE and NE trending faults were mapped along the Mwembeshi Shear Zone and the boundary between the Hook Batholith and the Katanga sediments respectively. The area is underlain by foliated basement granitic gneiss, Hook Batholith granites and Katanga metasediments that are broken into fractures along the foliation trends that control the occurrence and flow of rivers and streams. Overlying the basement rocks are the recent Karoo and Kundelungu sediments which are also permeable along the bedding or cleavage planes. The vegetation pattern, flow and occurrence of rivers or streams reflect trends of zones of weakness in the basement. Fractured zones developed along these foliations and were mapped at outcropping scale using Google Earth, aeromagnetic and ground magnetic data interpretation. Interpretation of aeromagnetic data confirmed the foliation trends that were suggested by Abell (1970) and Naydenov et al. (2014). One dimensional (1D) and two dimensional (2D) magnetotelluric (MT) resistivity models were created on the basis of a 120 MT sounding data set. A dimensionality and distortion analysis of the NSAMT data was carried out based on the approach of Groom and Bailey (1989) and it was concluded that the data were collected almost perpendicular to

strike, which is also supported by the geological mapping. MT smooth inversion models showed the lateral and vertical extent of the potential geothermal reservoir. Different 2D MT inversion approaches were applied to investigate the lateral continuity of the conductive sedimentary layer of the Kundelungu unit (slate, siltstone and shale). In order to map the subsurface structure of the area, a magnetic model was then produced using the acquired ground magnetic data and constrained using magnetic susceptibility measurements, MT data and geology mapped on the surface. Magnetic data interpretation confirmed an NW-SE fault controlling the hot springs, which was mapped using the NSAMT inversion results. The research shows that there is a lateral conductive, water saturated zone (reservoir) present between 150 m and 550 m depth and deeply seated faults in the basin. Along the deeply seated faults the conductive zones are vertical and continue with depth. The information shows that the thermal waters of the hot springs appear to circulate to depths more than 2.5 km along deep seated faults and foliation fractures penetrating the foliated rocks of the Hook Batholith and basement rocks. This water is heated by the regional geothermal gradient of 23ºC/km. Further exploration can be carried out on the study area to prove its potential for a geothermal resource.

Acknowledgements

The author would like to thank the following:

- The almighty God for the gift of life and all the blessings
- Dr. Mike Jones, Mr. Neville Brown and Prof. Susan Webb for constant supervision and moral support.
- Neville Brown, S.A.G.A and Peter Vivian Neal for the financial support
- Dr. Alan Jones and Dr. David Khoza for the technical assistance
- Peter Nyabeze, Emmanuel Chirenje, Desmond Mhlanga, Mhaka Ushendibaba, Brian Makone and Emmanuel Sakala for the technical and moral support
- University of the Witwatersrand, School of Geosciences
- Dr. Musa Manzi
- My mother, Ms M. Chinamora, Buhle Dlamini, Joseph Mangi, Taurai Chinamora, Stellah Chinamora, Tsitsi Chinamora, Willard Katsande, Jimmy Jambo, Ovidy Karuru, Tatenda Takawira, Cleo and Desmond Munemo, Tawanda Munyuki, Lorraine Chinamora, Takura Tendayi, Martin Chinamora, Linda Chinamora, Simon Chinamora, Moffat, family and friends for all their unlimited love and support

This dissertation is dedicated to my beautiful daughter Amayah Esther Luyanda Chinamora.

Table of Contents

Abstract iii
Acknowledgements v
1 Chapter 1 Introduction 1
1.1 Background 1
1.2 Previous work 5
1.3 Prospectus 8
2 Chapter 2 Geological and Geophysical Review 10
Background geology 10
2.1 Pan-African evolution 11
2.1.1 First mobile belt forming event 11
2.1.2 Second mobile belt forming event 11
2.2 Regional tectonic evolution 13
2.3 Geological setting of the Kwako Hills 16
2.4 Geophysical review 18
2.4.1 Aeromagnetic data 18
3 Chapter 3 Magnetic method 21
3.1 Earth's magnetic field 21
3.2 Temporal variations 22
3.2.1 Diurnal variations 22
3.2.2 Micropulsations 23
3.2.3 Magnetic storms 23
3.2.4 Secular variations 23
3.2.5 Geomagnetic reversals 23
3.2.6 Magnetic anomalies 23
3.3 Magnetic properties of rocks and minerals 24
3.3.1 Induced and remanent magnetisation 24
3.3.2 Magnetic susceptibility 24
3.4 Magnetic data collection 26
3.5 Magnetic data correction 26
3.5.1 Data checking and editing 26

3.5.2 Diurnal correction 26
3.5.3 Geomagnetic Reference Field removal 26
3.6 Gridding 27
3.7 Data processing and enhancement 27
3.7.1 Reduction to pole 27
3.7.2 Vertical derivatives 28
3.7.3 Upward and downward continuation 28
3.7.4 Analytic signal 28
3.7.5 Euler deconvolution 29
4 Chapter 4 Analysis and Interpretation of aeromagnetic, magnetic susceptibility and ground magnetic data 30
4.1 Aeromagnetic data analysis 30
4.2 Interpretation of aeromagnetic data 35
4.2.1 Anomaly type 1 41
4.2.2 Anomaly type II 41
4.2.3 Anomaly type III 42
4.2.4 Anomaly type IV 42
4.2.5 Anomaly type V 42
4.2.6 Summary 43
4.3 Magnetic positive and negative lineaments 43
4.4 Summary of Qualitative interpretation of Aeromagnetic data 48
4.5 Magnetic susceptibility 51
4.5.1 Data collection 51
4.5.2 Results and discussion 52
4.6 Ground Magnetic Survey 55
4.6.1 Application of Ground magnetic 55
4.6.2 Methodology- Data collection 55
4.6.3 Magnetic data processing 57
Magnetic data quality control 57
Diurnal variation correction 59
4.6.4 Data visulisation (qualitative interpretation) 60
2D Profiling 60
Gridding 60

Geomagnetic Reference Field removal 61
Reduction to the Pole (RTP) 63
Analytical Signal 64
Vertical derivative 65
4.6.5 Ground magnetic data interpretation 67
4.6.6 Summary 73
4.7 Magnetic modelling 73
4.7.1 Euler deconvolution 73
4.7.2 Construction of the forward models 74
4.7.3 2D magnetic forward models 75
4.7.4 Model interpretations 76
5 Chapter 5 Natural Source Audio-Magnetotelluric 78
5.1 Application of resistivity survey 78
5.2 Magnetotelluric sources 80
5.3 Assumptions of the MT Method 81
5.4 The fundamental equations of the Magnetotelluric technique 82
5.5 The Impedance Tensor 86
5.6 The Impedance tensor for 1D Earth 87
5.7 The Impedance tensor for 2D Earth 88
5.8 Distortion effects 91
5.9 Groom- Bailey decomposition 93
5.10 NSAMT Data Collection and Processing 93
5.10.1 Methodology 93
5.10.2 Data quality control 96
5.10.3 Static Corrections 96
5.10.4 Strike Analysis and Decomposition 100
5.11 NSAMT Bostick inversion and modelling 102
5.11.1 Forward Modelling 102
5.11.2 SCS2D Inversion Modelling workflow and parameters used 104
5.11.3 Data review after building models 106
5.11.4 1D Inversion Modelling 106
5.11.5 Results of the AMT 1D inversion cross sections 108

5.12 2D Inversion Modelling 113
5.12.1 Results of the 2D MT inversion cross-sections 114
5.12.2 Summary 122
6 Chapter 6 Data integration and discussion 124
6.1 Profile L3500 124
6.2 Profile L4500 127
6.3 Profile L5500 130
6.4 Summary 133
7 Chapter 7 Conclusions and future work 139
7.1 Conclusions 139
7.2 Proposed future work 140
Appendix A 141
Appendix B 143
Appendix C 145
Appendix D 147
Appendix E 148

List of Figures

Figure 2.1. Regional geological setting of south-central Africa. The study area (red box inside the black circle) is sandwiched between the Zambezi Belt and Lufilian Arc, lies on the Hook granites and along the Mwembeshi Shear Zone (MwZ). The surrounding tectonic blocks are also shown. Modified from Naydenov et al. (2014). . 10
Figure 2.2. Simplified tectonic model of the Pan-African evolution. a) emplacement of the first portion of the Hook Batholith shown in pink (HB) during event D1 (E–W collision); b) development of the sinistral Nalusanga Zone (NZ). Emplacement and deformation of the SE portion of the batholith; c) emplacement of the southern and central portion of the batholith and development of the pure-shear Itezhi-Tezhi Zone (ITZ); d) molasse type sedimentation was a consequence of regional N–S shortening of the granitoids and adjacent metasedimentary; e) N-S shortening during the stitching of the Lufilian and Zambezi Belts resulted in the formation of D2 structures in the granitoids and its host rocks along the Mwembeshi Shear Zone (MwZ). Direction of shortening is represented by the large arrows (Naydenov et al., 2014). 12
Figure 2.3. Simplified tectonic and stratigraphic evolution model of eastern Gondwana between the Congo and Kalahari cratons, with the Lufilian Arc marked as LA, the Zambezi Belt as ZB, the Mwembeshi Shear Zone as MwZ, the Late Katanga sediments as KS, the Hook Batholith as HB and the recent alluvium sediments as A. a) deformation of the basement granites of the cratons during the Kibaran orogenic event; b) opening up of basins due to the rifting between the Kalahari and Congo cratons c) deposition of the Katanga sediments into the basins; d) deformation of rocks due to compression between the Congo and Kalahari cratons during the Pan African Orogeny leading to formation of fold and thrust belts of the Lufilian Arc and Zambezi Belt. This was accompanied by intrusion and emplacement of post Katanga Hook Batholith; e) due to compression between the Congo and Kalahari cratons during the Pan African Orogeny stitching of the Lufilian Arc and Zambezi Belt along the Mwembeshi Shear Zone; f) deposition of the upper Katanga sediments (KS) that were later partly covered by recent Karoo sediments and alluvium (A) (Abell, 1970 and Naydenov et al., 2014). 15
Figure 2.4. Geological map around the Hook Batholith (D) intrusion area compiled from the published 1:100000 geological map of the Nansenga River Area, Zambia (Abell, 1970) showing the two hot springs and the study area outlined by a red circle and a red box respectively. 17
Figure 2.5. International Geomagnetic Reference Field (IGRF) corrected aeromagnetic Total Magnetic Intensity (TMI) map of Zambia gridded at 250 m. Digitised from paper copies by the Council for Geoscience, Pretoria. 19
Figure 2.6. Structural map around the Hook Batholith area with foliations presented as lines with the inclinations added where data is available. Also shown are the faults of the Mwembeshi Shear Zone passing through our study area outlined by the red box (Naydenov et al., 2014). 20
Figure 3.1. The vector total magnetic field defined either as the scalar magnitude of the total field, F, the inclination from the horizontal, I and the declination from true (geographic) north, D (Reeves, 2005). 22
Figure 4.1. International Geomagnetic Reference Field (IGRF) corrected aeromagnetic Total Magnetic Intensity (TMI) grid around the Hook Batholith area showing the study area (red box). Grid cell size 250 m. Digitised from paper copies by the Council for Geoscience, Pretoria. IGRF at the time of data acquisition has been removed. 31
Figure 4.2. Sunshaded (at inclination and declination of 45°) International Geomagnetic Reference Field (IGRF) corrected and Reduced To Pole (RTP) aeromagnetic Total Magnetic Intensity (TMI) grid around the Hook Batholith area showing the study area (red box). Grid cell size 250 m. Digitised from paper copies by the Council for Geoscience, Pretoria. IGRF at the time of data acquisition is removed. RTP corrected using inclination of −54.16° and declination of −5.07° 32
Figure 4.3. International Geomagnetic Reference Field (IGRF) corrected, Reduced To Pole (RTP) and first vertical derivative (1-VD) aeromagnetic Total Magnetic Intensity (TMI) gridded data around the Mwembeshi Shear Zone showing the study area red box. 33
Figure 4.4. Analytic Signal map of the International Geomagnetic Reference Field (IGRF) corrected and Reduced To Pole (RTP) aeromagnetic Total Magnetic Intensity (TMI) gridded data around the Mwembeshi Shear Zone showing the study area red box. 34

Figure 4.5. International Geomagnetic Reference Field (IGRF) corrected, Reduced To Pole (RTP) and first vertical derivative (1-VD) filtered aeromagnetic Total Magnetic Intensity (TMI) grid showing outlines of the enhanced anomaly types encountered in the area. The anomaly types were determined using their different wavelengths. 37
Figure 4.6. International Geomagnetic Reference Field (IGRF) corrected, Reduced To Pole (RTP) and analytic signal filtered aeromagnetic Total Magnetic Intensity (TMI) grid showing outlines of the enhanced anomaly types encountered in the area. 38
Figure 4.7. Geological map around the Hook Batholith intrusion area compiled from the published 1:100000 geological map of the Nansenga River Area, Zambia (Abell, 1970) showing the different anomaly types interpreted from aeromagnetic data, the two hot springs (red circle) and the study area (red box). 39
Figure 4.8. Google Earth image around the Hook Batholith intrusion area showing the different anomaly types from aeromagnetic data, the two hot springs (red circle) and the study area (red box). The blue lines represent rivers and streams. 40
Figure 4.9. Map of the negative magnetic lineaments mapped using phase symmetry algorithm that was developed by (Kovesi, 1997). A smallest filter wavelength of 500 m, and 4 filter scales were used to detect negative magnetic lineaments (black) orientated at all angles and positive magnetic lineaments (green) outlined in Type V anomaly. 44
Figure 4.10. Linear magnetic anomalies overlain on International Geomagnetic Reference Field (IGRF) corrected, Reduced To Pole (RTP) and first vertical derivative (1-VD) filtered aeromagnetic Total Magnetic Intensity (TMI) grid around the Mwembeshi Shear Zone showing the study area (red box) and hot springs (red circle) with outlines of the types of anomalies as interpreted from the aeromagnetic data. Only positive lineaments (green) in Type V anomaly are shown whilst negative lineaments (black) were mapped for the whole area. 45
Figure 4.11. Negative (black) and positive (white) linear magnetic anomalies overlain on Google Earth image of the study area with the outlines of the types of anomalies as interpreted from the aeromagnetic data. Only positive lineaments in type V anomaly are shown. 46
Figure 4.12. Negative magnetic lineaments (white lines) on the new geological map interpretation of aeromagnetic data, Google Earth image and geological map of the area published by Abell (1970). 47
Figure 4.13. a): the old geological map by Abell (1970) and b): the new geological map as interpreted from the aeromagnetic data, Google Earth image and geological map by Abell (1970) showing the non-magnetic fractured foliations or joints. 50
Figure 4.14. Location of magnetic susceptibility measurements overlaid on the colour shaded first vertical derivative image of the aeromagnetic data of the study area. 54
Figure 4.15. G-856 proton precession magnetometer used to take magnetic measurements. 56
Figure 4.16. Ground magnetic grid (red box) overlain on the geological map with linear negative magnetic lineaments (white lines) interpreted from aeromagnetic data, Google Earth and geological map of the area and showing the area covering the two hot springs (red circle) 57
Figure 4.17. Profiles of ground magnetic data obtained from the traversed lines L2500, L3000, L3500, L4000, L4500, L5000, L5500, L6000 and L6500 58
Figure 4.18. Base station data for different days. 59
Figure 4.19. a) Total Magnetic Intensity grid using Oasis Montaj's minimum curvature gridding algorithm at 150 m grid cell size and a desampling factor of 2 and b) sunshaded grid of the surveyed area showing the north-south traverse lines and east-west tie lines. 61
Figure 4.20a) IGRF and b) sunshaded corrected TMI data after removal of the regional field showing the north-south traverse lines and east-west tie lines. 45° inclination and declination angles were used for sunshading. ... 62
Figure 4.21. IGRF corrected ground magnetic data of the area of study. a) is the Total Magnetic Intensity (TMI) image and b) is the image after the data were Reduced To Pole. The anomalies labelled with 1 show the transformation from asymmetric anomalies to symmetric anomalies while the anomalies associated labelled with 2 shows a change from a narrow anomaly to a wide anomaly after application of RTP operator. 64
Figure 4.22. IGRF corrected ground magnetic data of the area of study. a) is the Reduced To Pole Total Magnetic Intensity (TMI) image and b) is the image after analytic signal filter was applied to the data. 65

Figure 4.23. Ground magnetic data of the study area. a) is Reduction To Pole (RTP) filtered data. b) First vertical derivative filtered data. First vertical derivative filter (1VD) enhances noise compared to RTP data..... 66
Figure 4.24. Reduce to pole (RTP) Total Magnetic Intensity (TMI) grid overlain on the new geological map of the study area that was interpreted from the aeromagnetic data, the geological map by Abell (1970) and the Google Earth image. The high amplitude anomaly corresponds well with the Hook Batholith rocks and is bounded by "quiet" low amplitude, low-frequency anomalies corresponding to the metasedimentary rocks of the Lufilian Arc and the Zambezi Belt in the north and south respectively. Refer to Figure 3.8 for legend to the geology and Figure 4.9a for legend to the RTP TMI image 67
Figure 4.25. Reduce to pole (RTP) first vertical derivative (1-VD) filtered total magnetic intensity (TMI) image of the study area overlain on the new geological map of the study area that was interpreted from the aeromagnetic data, the geological map by Abell (1970) and the Google Earth image. The high amplitude gradient corresponds well with the Hook Batholith rocks and is bounded by "quiet" low gradient, low-frequency anomalies corresponding to the metasedimentary rocks of the Lufilian Arc and the Zambezi Belt in the north and south respectively. Refer to Figure 3.9a for legend to the geology and Figure 4.9b for legend to the first vertical derivative image..... 68
Figure 4.26. Reduce to pole (RTP) first vertical derivative (1-VD) filtered total magnetic intensity (TMI) image of the study area overlain on the new geological map of the study area that was interpreted from the aeromagnetic data, the geological map by Abell (1970) and the Google Earth image. The small grid is the gridded 250 m line spaced data. The high amplitude anomaly corresponds well with the Hook Batholith rocks and is bounded by "quiet" low amplitude, low-frequency anomalies corresponding to the metasedimentary rocks of the Lufilian Arc and the Zambezi Belt in the north and south respectively. The black diamonds represent the hot springs. Refer to Figure 3.9a for legend to the geology and Figure 4.9b for legend to the first vertical derivative image. 70
Figure 4.27. Reduce to pole (RTP) first vertical derivative (1-VD) filtered total magnetic intensity (TMI) image of the study area overlain on the new geological map of the study area that was interpreted from the aeromagnetic data, the geological map by Abell (1970) and the Google Earth image. The small grid is the gridded 250 m line spaced data. The white lines represent the negative magnetic lineaments. Refer to previous Figure for legends. 71
Figure 4.28. Old and new negative magnetic lineaments (white lines) on the new geological map interpreted from aeromagnetic data, Google Earth image and geological map of the area published by Abell (1970). The new negative magnetic lineaments were enhanced by smaller line spacing. 72
Figure 4.29. 3D Euler's depth solutions (structural index 1) plotted on the colour shaded IGRF RTP total magnetic intensity map. 74
Figure 4.30. Location of the 2D magnetic profiles (black lines) overlain on the Reduced To Pole Total Magnetic Intensity map of the area showing the negative magnetic lineaments inferred using the ground magnetic data (white lines) and the two hot springs. Overlain on the map are the 3D Euler's depth solutions and the IGRF RTP total magnetic intensity image. 75
Figure 4.31. 2D magnetic model of profile L4500 with the interpretation of faults and lithological units. The upper panel is the profile's magnetic response with the green dots representing the observed magnetic response and the solid black line the calculated magnetic response from the geological model. The lower panel is a simplified geological interpretation of the 2D magnetic model showing lithologies and magnetic susceptibility values. The location of the profile is shown in Figure 4.16. The Hook Batholith has the highest magnetic susceptibility and the Katanga sediments have the lowest. 77
Figure 5.1. Zonge GDP- 3224 multi-receiver system for acquisition of controlled and natural source geoelectric and EM data..... 78
Figure 5.2. Variation of electrical resistivity or conductivity of common Earth materials (Miensopust, 2010)... 79
Figure 6.1. AMT section for profile L3500 overlain on the a) RTP TMI, b) first vertical derivative images and c) geological map with conductive layers, conductive bodies, resistive layers and discontinuities zones labelled as CL, CB, RL and D respectively. M, D and Q represent the psammitic schists, porphyroblastic biotite adamellite and argillaceous quartzite respectively as labelled on the geological map. The white lines represent the magnetic low lineaments mapped using the magnetic data..... 126

Figure 6.2. AMT section for profile L4500 overlain on the a) RTP TMI, b) first vertical derivative images and c) geological map with conductive layers, conductive bodies, resistive layers and discontinuities zones labelled as CL, CB, RL and D respectively. M, D and Q represent the psammitic schists, porphyroblastic biotite adamellite and argillaceous quartzite respectively as labelled on the geological map. The white lines represent the magnetic low, lineaments mapped using the magnetic data. 129
Figure 6.3. AMT section for profile L5500 overlain on the a) RTP TMI, b) first vertical derivative images and c) geological map with conductive layers, conductive bodies, resistive layers and discontinuities zones labelled as CL, CB, RL and D respectively. M, D and Q represent the psammitic schists, porphyroblastic biotite adamellite and argillaceous quartzite respectively as labelled on the geological map. The white lines represent the magnetic low, lineaments mapped using the magnetic data. 132
Figure 6.4. Correlation between the 2D MT invariant mode resistivity section (top) and the 2D magnetic model showing the contacts, faults and different rocks. 135
Figure 6.5. Correlation between the magnetic and resistivity contrasts of the crust at 1000 m depth with geologically mapped lithologies. On the geological map, the white lines represent the magnetic low, lineaments. The lateral conductive anomaly represents the aquifer at about 150 m depth. Vertical conductive anomalies represent steeply dipping fractures associated with either shearing or faulting. On surface their strike was mapped by either magnetic method or geological mapping and is represented by dashed or solid lines. 137

List of tables

Table 2.1. Stratigraphy and sequence of events of the Nansenga River area (modified from Abell, 1970). 18
Table 3.1. Susceptibilities of various rocks and minerals (Clark and Emerson, 1991). 25
Table 3.2. Structural indices used to estimate the depth and extent of simplistic magnetic sources beneath the aeromagnetic profiles (after Reid et al., 1990; FitzGerald et al., 2004). . 29
Table 4.1. Magnetic susceptibility measurements of the collected samples. 53
Table 4.2. IGRF results for Mumbwa. Based upon (12th Generation IGRF Results, 2014), with the permission of the British Geological Survey. Location (-14˚, 27˚). 62.

Chapter 1 Introduction

1.1 Background

High levels of electricity supplies are needed to sustain today's energy consumption rates. However, an increase in fossil fuel prices and the unfriendly nature of fossil fuels has increased the interest in geothermal energy by governments and the private sector. One percent of the thermal energy contained within the first 10 thousand meters of the Earth amounts to approximately 500 times that contained in all hydrocarbon resources of the world (Duffield and Sass, 2003).

Geothermal energy is energy generated and stored in the Earth. The heat is generated by accretion during the formation of the Earth, organisation of the Earth into layers and the decay of radioactive elements (Glassley, 2010). It is transferred to the surface by radiation, convection, or conduction. This results in geological processes of rifting and including those occurring at continental rift zones such as the East African Rift System and mid-oceanic ridges, hotspots such as Hawaii and Yellowstone and subduction zones surrounding the Pacific Ocean.

The East African Rift System (EARS) is thought to have been caused by asthenosphere upwelling followed by lithospheric extension and extents from Afar to Mozambique (Omenda, 2010). It is part of a larger tectonic system consisting of three main arms: the Red Sea Rift, the Gulf of Aden Rift, and the East African Rift which developed through Eritrea, Ethiopia, Kenya, Tanzania, Zambia, Malawi and Northern Mozambique (Omenda, 2010) (Figure 1.1). The EARS possesses geothermal potential worthy of attention as is spectacularly shown by its volcanoes, Earthquakes, hot springs and fumaroles (Teklemariam, 2008). This is a zone where the heat energy of the interior of the Earth escapes to the surface and is already being exploited in countries such as Kenya and Ethiopia.

Exploration and utilization of geothermal energy resources in the East African region (mainly Kenya) for the last thirty years has demonstrated that the region has a vast untapped, indigenous and reliable geothermal resource that is environmentally clean and economically viable (Teklemariam, 2008). The question is how to find and benefit from this vast amount of thermal energy.

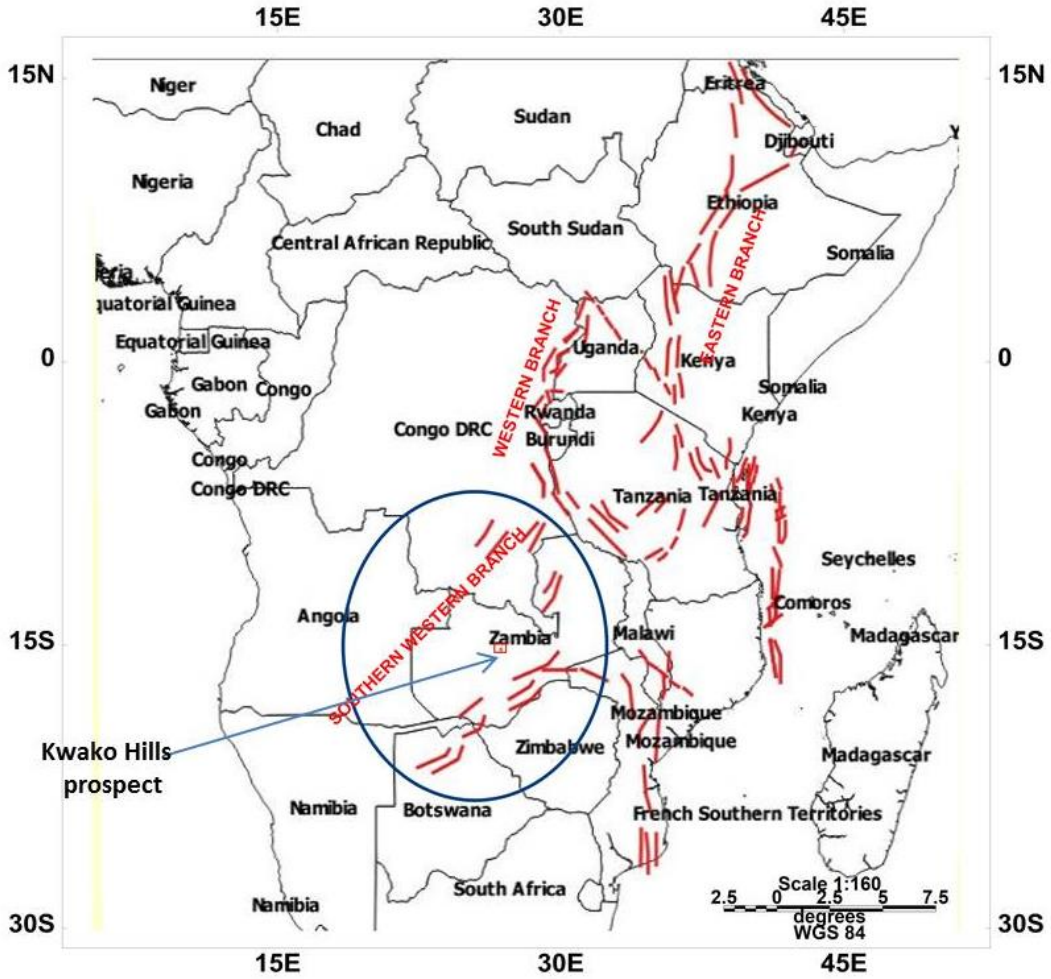

Figure 1.1. The East African Rift System showing the south-western branch which passes through Zambia in the blue circle and rift zones as red lines (modified from Atekwana et al., 2004). Also the small red polygon pointed by the blue arrow is the Kwako Hills prospect.

Zambia has a number of geothermal fields where hot springs have geothermometer temperatures (reservoir temperature calculated from geothermal fluid composition) up to 150-200 °C. These include Bwenga hot springs located in the Kafue trough southwest of Lusaka (Legg, 1974). The springs were described under seven groups according to their geographical locations namely: 1) Northern, 2) Mansa- Copperbelt, 3) Western, 4) Eastern, 5) South-eastern, 6) Choma and 7) Lochinvar groups (Legg, 1974) (Figure 1.2). However, very little has been done to explore most of them for potential geothermal resources. Only two hot springs, Chinyunyu and Kapisya springs, located on the Chinyunyu valley and in Nsumbu respectively, were investigated geoscientifically with published results (Kombe and Sinyiza, 2008). Reconnaissance geochemistry, geological and geophysical surveys were carried out

on geothermal targets in Zambia since the 1950s by the Geological Survey of Zambia (GSZ). The GSZ together with an Italian company studied various hot springs (Legg, 1974). As a result of the findings at Chinyunyu and Kapisya springs, development has been considered on various prospects such as the Bwenga River.

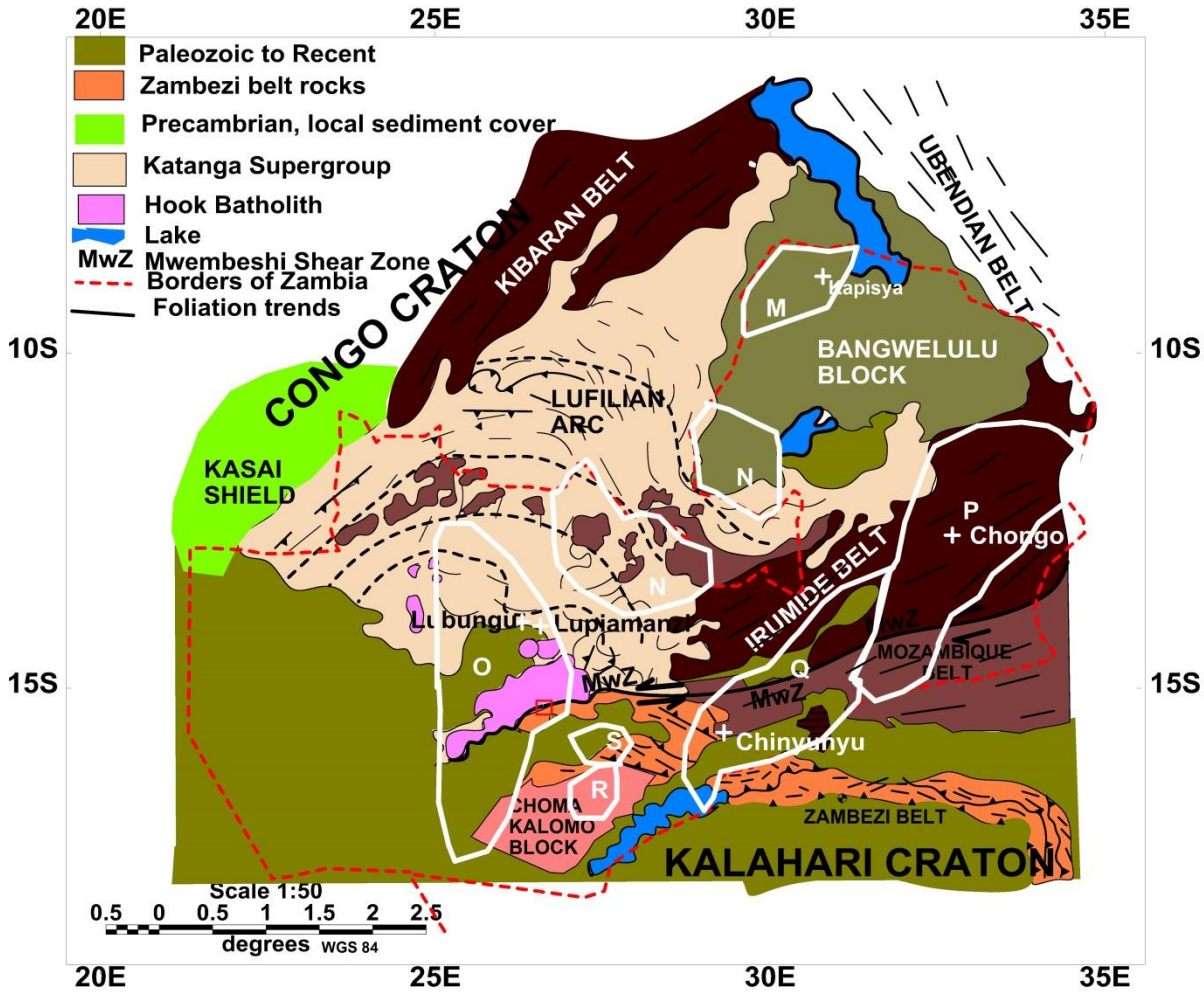

Figure 1.2. The outlines and locations of the seven groups of mineral springs (white borders) overlain on the geological map of Zambia with the study area outlined by the red polygon (modified after Legg, 1974 and Nyambe and Phiri, 2010). M: Northern group, N: Mansa-Copperbelt group, O: Western group, P: Eastern group, Q: South-eastern group, R: Choma group, S Lochinivar group. The dashed red line shows Zambia international boundary.

Lack of understanding of geothermal systems and the variability of the geological environment negatively affects geothermal exploration (MacNitt, 1970). Geophysics plays a very important role in the exploration of geothermal resources as shown by work done by

Barnwell (1973) and (Mantlik and Karous, 2013). Recent geoscientific data from targets around Zambia indicate a high potential for geothermal resources based on their geological setting and geothermometer temperatures. The conceptual model is of meteoric water circulating through very deep fault systems and being heated by the natural geothermal gradient. The rising hot water is held beneath an impermeable cap rock within sedimentary basins (Kalahari GeoEnergy, 2013).

A reliable geological model needs to be constructed from geophysical exploration data to determine whether suitable geothermal conditions exist for the construction of a geothermal electrical plant. A geophysical study was carried out at the Kwako Hills prospect (Figure 1.3) in order to come up with a preliminary geological model based on the integration of geophysical and geological data. This study was part of a research project setup between Kalahari GeoEnergy and the School of Geosciences at the University of the Witwatersrand to assess the geothermal energy potential of a sedimentary basin hosting a low enthalpy geothermal energy system at Kwako Hills in Zambia using geophysical methods (Figure 1.3). Natural source audio-magnetotelluric (NSAMT) and magnetic data have been modelled in conjunction with supporting geological mapping to image the subsurface. The investigation contributes to the understanding of the extent and continuity of the permeable sedimentary basin aquifer and will form the starting point for subsequent reservoir characterisation.

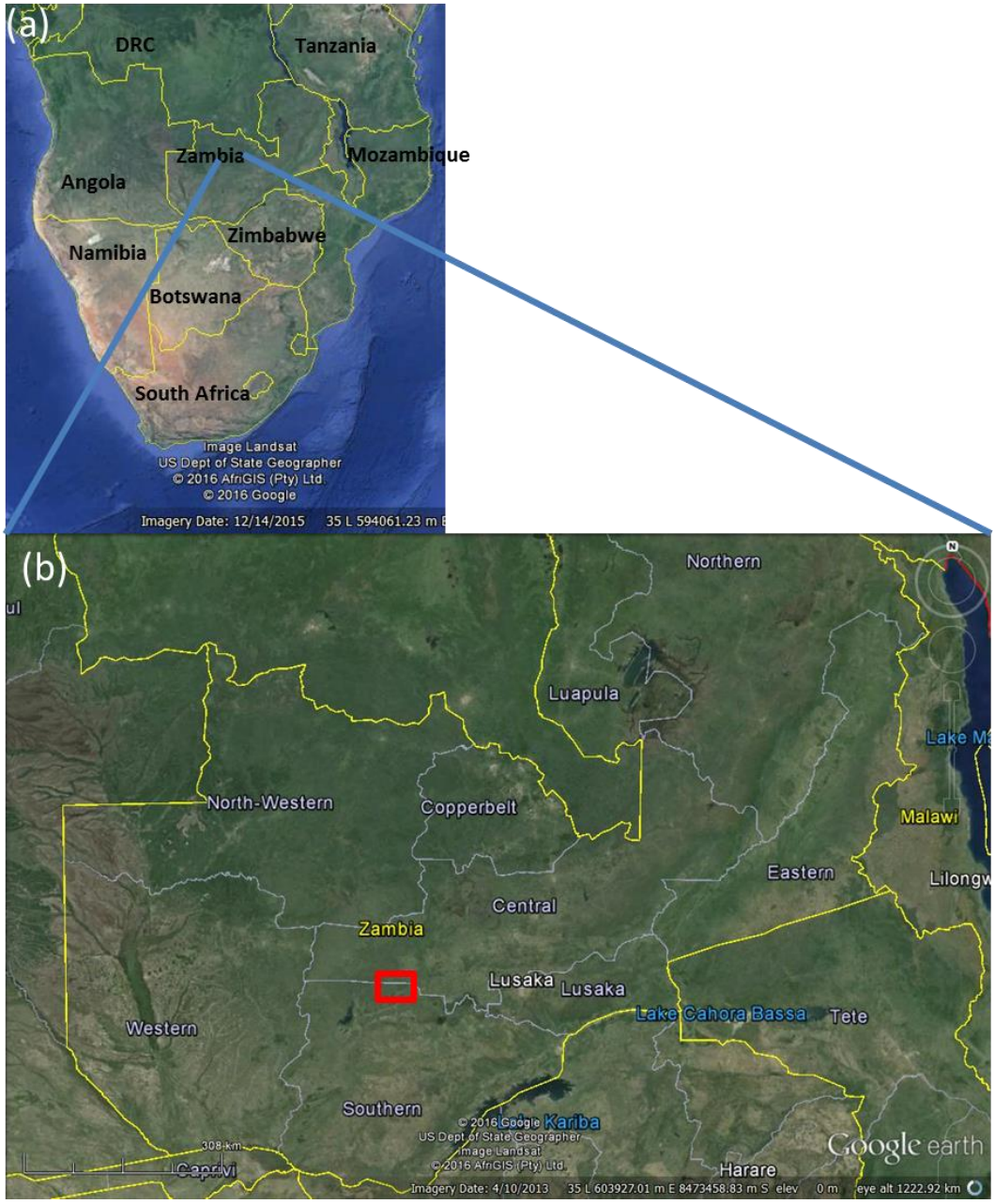

Figure 1.3. Locality map of the study area. (a) Map of southern and central Africa. (b) The enlarged map of Zambia showing the study area (red polygon).

1.2 Previous work

Geochemistry tools such as geothermometry and hydrochemistry were and are still being used to study and characterise geothermal reservoirs in the world in order to investigate the subsurface temperatures, water compositions and origin of the thermal waters (Ármannsson and Fridriksson, 2009).

Most of the hydrochemistry of the hot springs in Zambia was conducted by Legg (1974). A reconnaissance survey was carried out by the Geological Survey of Zambia between 1971 and 1974 to determine the potential for commercial production of salt particularly sodium chloride, to determine if there is enough thermal energy to generate power or for other uses and to analyse the properties of individual and groups of springs (temperatures, water compositions, mode of occurrence and the variations and similarities) (Legg, 1974). Legg (1974) described the springs under seven geographical groups namely the northern group, the Mansa-Copper Belt group**,** the western group**,** the eastern group**,** the south-eastern group**,** the Choma group and the Lochinvar group (Figure 1.3). Legg (1974) briefly studied the geological setting around each spring, took samples of water for analysis and took measurements of water temperature, discharge rate and radioactivity.

The results showed that the hot springs of Zambia occur mainly on extensive regional normal faults buried under thick sedimentary basins (~1.5 km) and often at the contacts of Karoo sediments with older rocks (Legg, 1974). In most cases, analyses of the water compositions and temperatures were compatible with the model of deep circulation by gravity, convection in fault zones, and leaching of the wall rocks adjacent to the faults (Legg, 1974). Due to the low concentrations of boron and lithium, the results also showed that none of the springs appear to be of volcanic origin and after a detailed study of springs, Legg (1974) concluded that the springs were not hot enough and hence potential for geothermal power generation is low.

After taking into consideration a number of factors such as economic and sociological considerations as well as accessibility of the sites, this list by Legg (1974) was further reduced to seven priority sites namely Kasho, Lubungu, Lupiamanzi, Chinyunyu, Chikowa, Kapisya and Chongo (Musonda and Sikazwe, 2005). The Lubungu, Lupiamanzi and Chikowa springs are from the western group whilst the Kapisya, Chongo and Chinyunyu springs are from the northern, eastern and south-eastern groups, respectively (Figure 1.2).

Although little work has been done relating to geothermal energy of Zambia, it resulted in the building of a pilot geothermal plant at Kapisya (Figure 1.4). Geothermal exploration at Kapisya started in early 1986 and included geology, geochemistry, photogeology, trace geochemistry, radon surveys, shallow drilling (<150 m), magnetic and natural source audio-magnetotelluric (NSAMT) geophysical methods. Kapisya was chosen as the most suitable

site because of its maximum surface temperature of 85 ˚C and its socio-economic impact. Fifteen exploration and production wells up to 150 m deep were drilled in 1987 and 1988. A pilot plant with four wells fitted with submersible pumps, was set up by December 1988 (Figure 1.4).



Figure 1.4. Pilot geothermal plant at Kapisya (courtesy of Kalahari GeoEnergy).

It is unfortunate that the plant never became operational because transmission lines were not constructed since the bilateral agreement between the Zambian and Italian government did not cover it and also the maximum surface temperature of 85°C was below the temperatures for which the turbo generators were designed (Musonda and Sikazwe, 2005). This was due to lack of knowledge about binary geothermal energy systems whereby the low temperature water can be used to heat up a liquid with a low boiling temperature which can easily be used for electricity generation.

In 2004, Kenya Electricity Generating Company Limited (KenGen) was hired by Zambia Electricity Supply Corporation Limited (ZESCO) to carry out an assessment of the Kapisya and Chinyunyu geothermal prospects (Figure 1.3). The aim of the project was to rehabilitate commission and investigate the possibility of expanding the Kapisya plant capacity (KenGen, 2014). A team of geothermal experts from KenGen carried out geophysical investigations (MT and magnetic surveys), radon and carbon dioxide gas measurements, and geological investigations between 15th October and 15th November 2006. The results included a geological model of the geothermal energy reservoir. A report submitted to ZESCO revealed that the geothermal system conceptual model of meteoric water circulating through very deep

fault systems and being heated by the natural geothermal gradient was operating at Kapisya (Omenda et al., 2010). Omenda et al. (2010) estimated that each of the prospects can generate up to 2 MW using binary technology (pumping warm water through a heat exchanger filled with a low boiling point fluid where it is turned into steam and used to turn turbines).

1.3 Prospectus

The main purpose of this study is to characterize a potential geothermal reservoir of the study area named the Kwako Hills prospect found in Mumbwa, Zambia (Figure 1.3) which hosts two thermal springs. The two springs are located on a NW-SE trending alluvium filled valley (refer to Chapter 2). This dissertation also investigates faults along the trend of the outcropping Hook granite to the north of the valley by the use of airborne magnetic, ground magnetic, natural source audio-magnetotelluric geophysical methods and geological mapping. Chapter 2 geological maps show that the area lies in a region of active extensional tectonics which provides a geological setting conducive to sedimentary-hosted geothermal systems (Figure 2.3). The Mwembeshi Shear Zone (MwZ) cuts through the area of study separating two branches of the Pan-African Orogen: the Lufilian Arc and the Zambezi Belt (Figure 1.2). The Mwembeshi Shear Zone is a regional transfer fault accompanied by smaller faults and joints. A review of existing aeromagnetic data was also carried out in Chapter 2. The principles and theory of the magnetic method, the processing and enhancement filters were all explained in Chapter 3. Magnetic susceptibility measurements of surface rocks samples were taken and used as constraints during magnetic forward modelling and are also reported in Chapter 3. Chapters 4 and 5 discuss the collection of ground magnetic and magnetotelluric data which were then processed to determine the overburden thickness and investigate the presence and location of faults. In Chapter 6, the natural source audio magnetotelluric, geological mapping, magnetic susceptibility and magnetic data are integrated. The resistivity sections from NSAMT data are overlain on the geological map. Reduced to pole TMI and first vertical derivative filtered data and geological maps of the study area, ground magnetic and aeromagnetic data are integrated for interpretation. In order to determine a preliminary geological model 2D magnetic forward modelling was performed in Chapter 6. Geological, AMT and magnetic susceptibility data were used as constraints for modelling. A 3D voxi resistivity model was also incorporated in establishing a new 3D geological model of the resource. Although no boreholes were available in the area to help

constrain depths to different lithologies, estimates based on resistivity sections from the AMT method were relied on. The new geological map will assist in the siting of exploratory and production wells through which hot fluids will flow. In Chapter 7, based on the results of the integrated 3D geological model, the author suggests various locations for exploratory boreholes and the expected depth of the geothermal reservoir. Further work is also recommended in Chapter 8 such as heat flow measurements and geothermal gradients and also closely spaced AMT profiles.

Chapter 2 Geological and Geophysical Review

Background geology

Zambia is underlain by ancient Paleozoic rocks of the Kalahari and Congo cratons. Multiple tectono-thermal events lead to the country's complex geology (Figure 2.1).

The Mwembeshi Shear Zone (MwZ) cuts through the study area separating two branches of the Pan-African Orogen: the Lufilian Arc and the Zambezi Belt to the south (Figure 2.1). To the north of the MwZ, the Hook granite intruded the Katangan metasedimentary rocks of the Neoproterozoic Lufilian Arc (Abell, 1970).

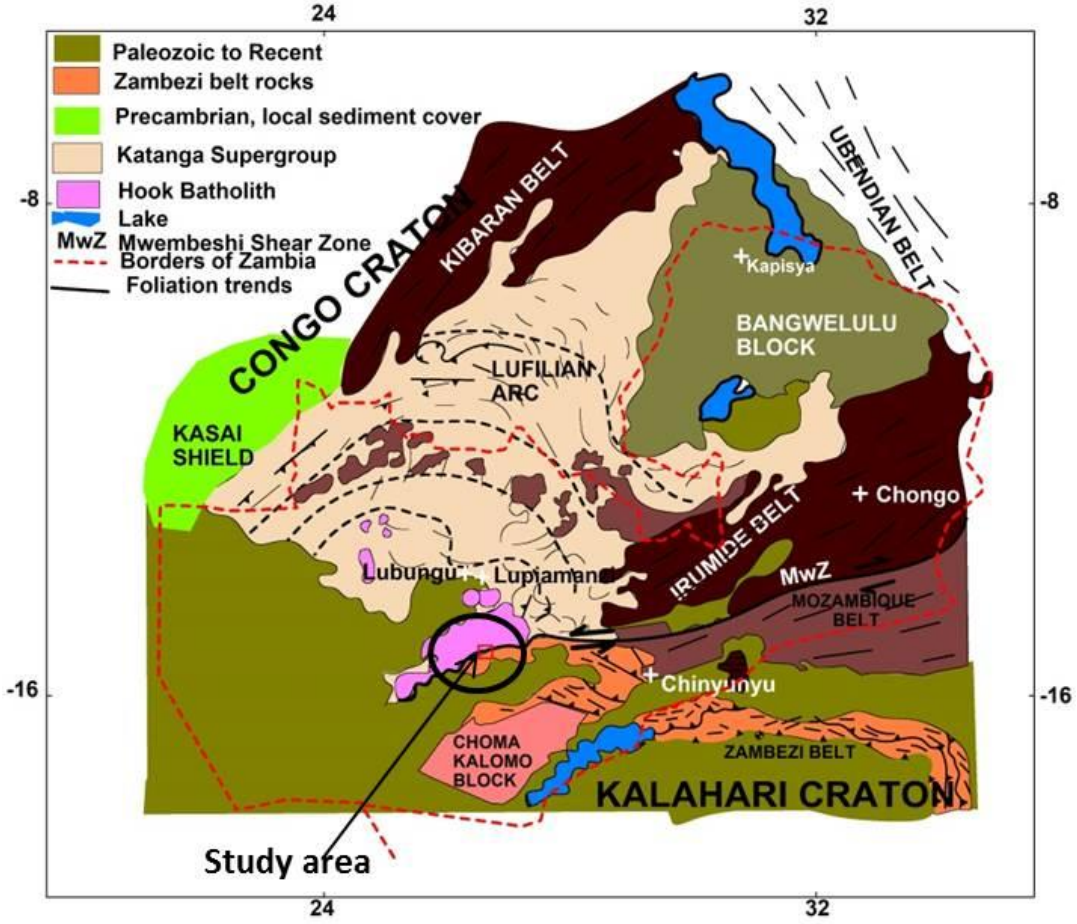

Figure 2.1. Regional geological setting of south-central Africa. The study area (red box inside the black circle) is sandwiched between the Zambezi Belt and Lufilian Arc, lies on the Hook granites and along the Mwembeshi Shear Zone (MwZ). The surrounding tectonic blocks are also shown. Modified from Naydenov et al. (2014).

2.1 Pan-African evolution

The collision of Archaean to Mesoproterozoic cratons during Gondwana amalgamation between about 870 and 550 Ma caused a Neoproterozoic (500 Ma) tectono-thermal event which resulted in the formation of the Kibaran mobile belt (Kroner and Stern, 2004). This tectono-thermal event comprised of two temporally separated mountain forming events and was accompanied by geothermal activity (Naydenov et al., 2014).

2.1.1 First mobile belt forming event

The Kalahari and Congo Cratons collided resulting in the suturing of the Pan-African (Neoproterozoic to earliest Palaezoic) Zambezi Belt and Lufilian Arc and formation of the Mwembeshi Shear Zone (Johnson and Oliver, 2004). The Lufilian Arc is a belt made up of metasedimentary rocks belonging to the Katanga Supergroup of Neoproterozoic age curving northwards (Figure 2.2). The Zambezi Belt is a fold-and-thrust complex that was rotated towards the SW to SSW. In southern Zambia it is composed of late Mesoproterozoic (1500 to 1000 Ma) basement gneisses and granites unconformably underlying or in tectonic contact with a thick metasedimentary succession (Katongo et al., 2004; Johnson et al., 2007; Mantlik and Karous, 2013). The section of the Zambezi Belt that is found in northern Zimbabwe is made up of southwest directed thrusting and duplex formation in which small portions from the Kalahari Craton basement gneisses are tectonically intercalated with the super-crustal sequence (Dirks et al., 1999). The intrusion of the Hook Batholith was syn-tectonic to this first event. Figure 2.2a, b and c explain the events that took place between ca 550 and 533 Ma as indicated by U–Pb zircon dating (Naydenov et al., 2014). The first event was characterised by regional low grade metamorphism due to the east–west collision of the surrounding Archaean to Mesoproterozoic cratons that resulted in different strain distribution between north–south pure shear and north-west sinistral simple-shear dominated domains (Figure 2.2).

2.1.2 Second mobile belt forming event

After ca. 530 Ma there was a second north–south shortening event (Figure 2.2d and e). This compressional event was dated using deformed molasse-type sedimentary rocks in the Hook Batholith that are probably syntectonic to the exhumation of the Hook Batholith. The second event also resulted in the development of an E to ENE trending pure shear zone in the Hook

Batholith to the south called the Mwembeshi Shear zone (Naydenov et al., 2014). The Mwembeshi Shear Zone (MwZ) marks the boundary between the Lufilian Arc and the Zambezi Belt (Figure 2.2). This shear zone juxtaposes the metasedimetary rocks of the Zambezi Belt with metamorphic rocks of the Lufilian Arc inner zones (de Swardt et al., 1965; John et al., 2003, 2004a, 2004b; Vrána et al., 1975).

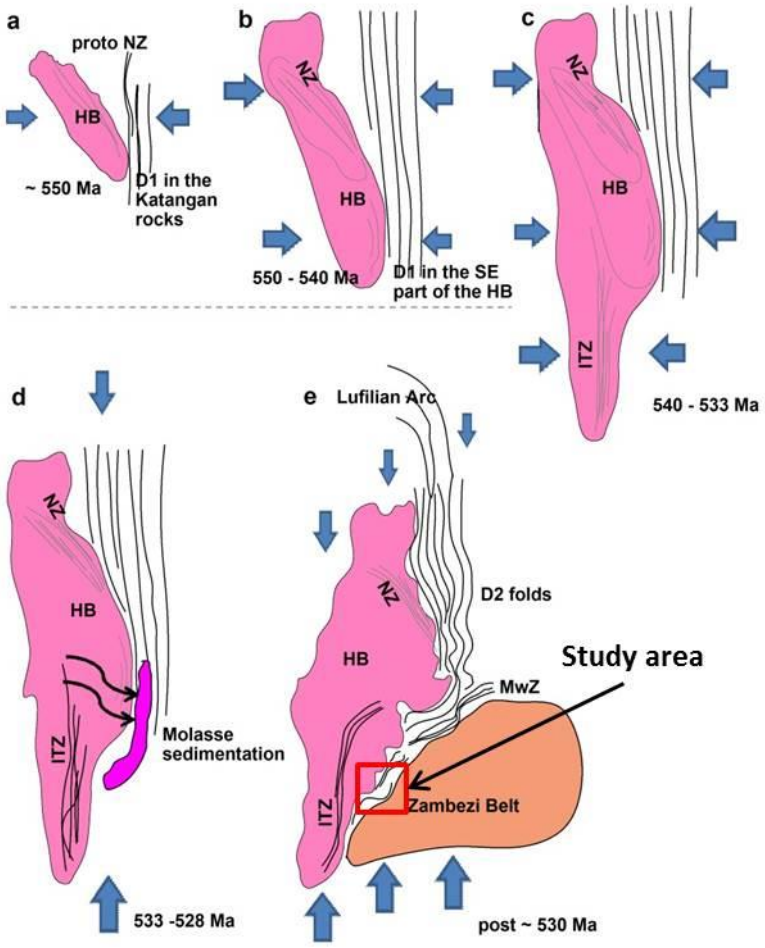

Figure 2.2. Simplified tectonic model of the Pan-African evolution. a) emplacement of the first portion of the Hook Batholith shown in pink (HB) during event D1 (E–W collision); b) development of the sinistral Nalusanga Zone (NZ). Emplacement and deformation of the SE portion of the batholith; c) emplacement of the southern and central portion of the batholith and development of the pure-shear Itezhi-Tezhi Zone (ITZ); d) molasse type sedimentation was a consequence of regional N–S shortening of the granitoids and adjacent metasedimentary; e) N-S shortening during the stitching of the Lufilian and Zambezi Belts resulted in the formation of D2 structures in the granitoids and its host rocks along the Mwembeshi Shear Zone (MwZ). Direction of shortening is represented by the large arrows (Naydenov et al., 2014).

Although many authors interpreted the MwZ as a major strike-slip shear zone (e.g. Coward and Daly, 1984; Daly, 1986; de Swardt et al., 1965), in the area south of the Hook Batholith Naydenov et al. (2014) suggested that the Mwembeshi Shear Zone in the Hook area is a syn-tectonic structure that developed to accommodate pure-shear deformation caused by regional N-S convergence of the Congo and Kalahari Cratons and marks the contact between the low grade metamorphic inner zones of the Lufilian Arc and the high-grade rocks of the Zambezi Belt.

Naydenov et al. (2014) dated the event that formed the MwZ using U–Pb isotope geochronology methods using detrital zircon population of a metaconglomerate sample that shows deposition after ca. 530 Ma.

2.2 Regional tectonic evolution

The basement of the Hook Batholith area is made up of Paleoproterozoic or Mesoproterozoic aged crystalline rocks consisting of granite, granite-gabbro and granite gneiss which were emplaced ~ 2100 – 2000 Ma ago (Abell, 1970). The Kibaran event which took place ~ 1350 – 1100 Ma ago (Figure 2.3) was accompanied by reconstitution and shearing of the basement rocks associated with construction of Rodinia (Kampunzu et al., 2003). Collision of the Congo Craton with the Kalahari Craton resulted in the formation of the medium grained porphyroblastic granite, granite gneiss, coarse grained gneiss and biotite gneiss rocks of the basement (Abell, 1970). Naydenov et al. (2014) suggested that the Hook Batholith was emplaced about 550 Ma ago as indicated by U–Pb zircon dating (Figure 2.3). On top of the basement rocks are sedimentary rocks of the Katanga Supergroup (Figure 2.3) that were deposited into two basins namely the Roan and Nguba rifts (Abell, 1970). These basins were opened as a result of rifting between the Congo and Kalahari cratons (Wendorff, 2011). The pan African orogeny of ~590 – 530 Ma ago resulted in the metamorphism of sedimentary rocks to high grade metasediments of the thrust and fold belts of the Lufilian Arc and Zambezi Belt. This orogenic event also led to the intrusion of porphyroblastic biotite adamellite and quartz monzonite with hornfels and xenoliths. The upper Katanga rocks made up of slates, siltstone and quartzite are partly covered by recent Karoo sediments that underlie alluvium deposits and are made up of conglomerate, slate, feldspathic grit and strongly

brecciated siltstones. These sediments were deformed due to the Mwembeshi Shear Zone that stitches the Lufilian Arc and the Zambezi Belt (Naydenov et al., 2014). Sedimentary rocks of the Karoo system overlie the Katanga system and act as a thermal cap to the geothermal aquifers. Most of the rocks around the Hook Batholith are foliated depending on their position in relation to major structures and their lithology. Elongated quartz grains and wisps of biotite define the foliation in the basement granites and granite-gneiss. Usually the foliation is along the strike of the structure or bedding.

The Section discusses why the study area has a structural setting that is conducive for geothermal energy resources. A lot of folding, faulting and foliation in the area was a result of shearing and mobile belts formed due to the Pan African evolution mountain forming events.

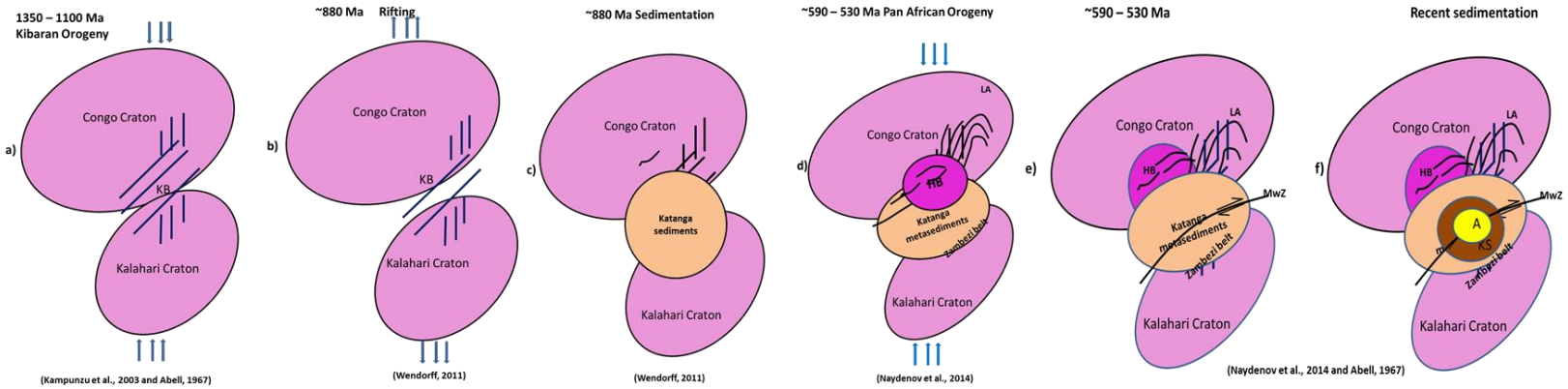

Figure 2.3. Simplified tectonic and stratigraphic evolution model of eastern Gondwana between the Congo and Kalahari cratons, with the Lufilian Arc marked as LA, the Zambezi Belt as ZB, the Mwembeshi Shear Zone as MwZ, the Late Katanga sediments as KS, the Hook Batholith as HB and the recent alluvium sediments as A. a) deformation of the basement granites of the cratons during the Kibaran orogenic event; b) opening up of basins due to the rifting between the Kalahari and Congo cratons c) deposition of the Katanga sediments into the basins; d) deformation of rocks due to compression between the Congo and Kalahari cratons during the Pan African Orogeny leading to formation of fold and thrust belts of the Lufilian Arc and Zambezi Belt. This was accompanied by intrusion and emplacement of post Katanga Hook Batholith; e) due to compression between the Congo and Kalahari cratons during the Pan African Orogeny stitching of the Lufilian Arc and Zambezi Belt along the Mwembeshi Shear Zone; f) deposition of the upper Katanga sediments (KS) that were later partly covered by recent Karoo sediments and alluvium (A) (Abell, 1970 and Naydenov et al., 2014).

2.3 Geological setting of the Kwako Hills

The Kwako Hills (Kalilwe) hot springs are located at the northern end of a northwest-southeast trending alluvium filled valley (Figure 2.4). The valley cuts across the contact between the Hook Batholith and the Katangan sequence as shown in (Figure 2.4) (Abell, 1970). Metasediments and crystalline rocks underlie the Nansenga river area. These consist of basement granites, granite gneiss to gabbro and syenite of post Katanga age and weakly metamorphosed rocks of the Kundelungu series (Abell, 1970). Coarse grained porphyroblastic biotite adamellite and quartz monzonite with hornfels xenoliths and well-formed potash-feldspar porphyroblasts intruded this assemblage of granitoids (Abell, 1970). The newly formed magma was contaminated whilst intruding the sediments and this resulted in satellite bodies of gabbro and syenite (Abell, 1970). Most of the rocks round the Hook Batholith are foliated depending on their position in relation to major structures and their lithology. The north-west trend of Lufilian age and north-south and north-east foliation trends of pre-Katanga age are the main structures observable in the area (Abell, 1970). To the south of the area lies the Mwembeshi Shear Zone which was discussed earlier. This zone was accompanied by small joints and faults which makes the area conducive for a geothermal energy resource due to increased rock permeability. The schists within the MwZ show steep to vertical E–W striking S2 crenulation cleavage (Naydenov et al., 2014). Table 2.1 shows the geological events and successions to which these rock types belong.

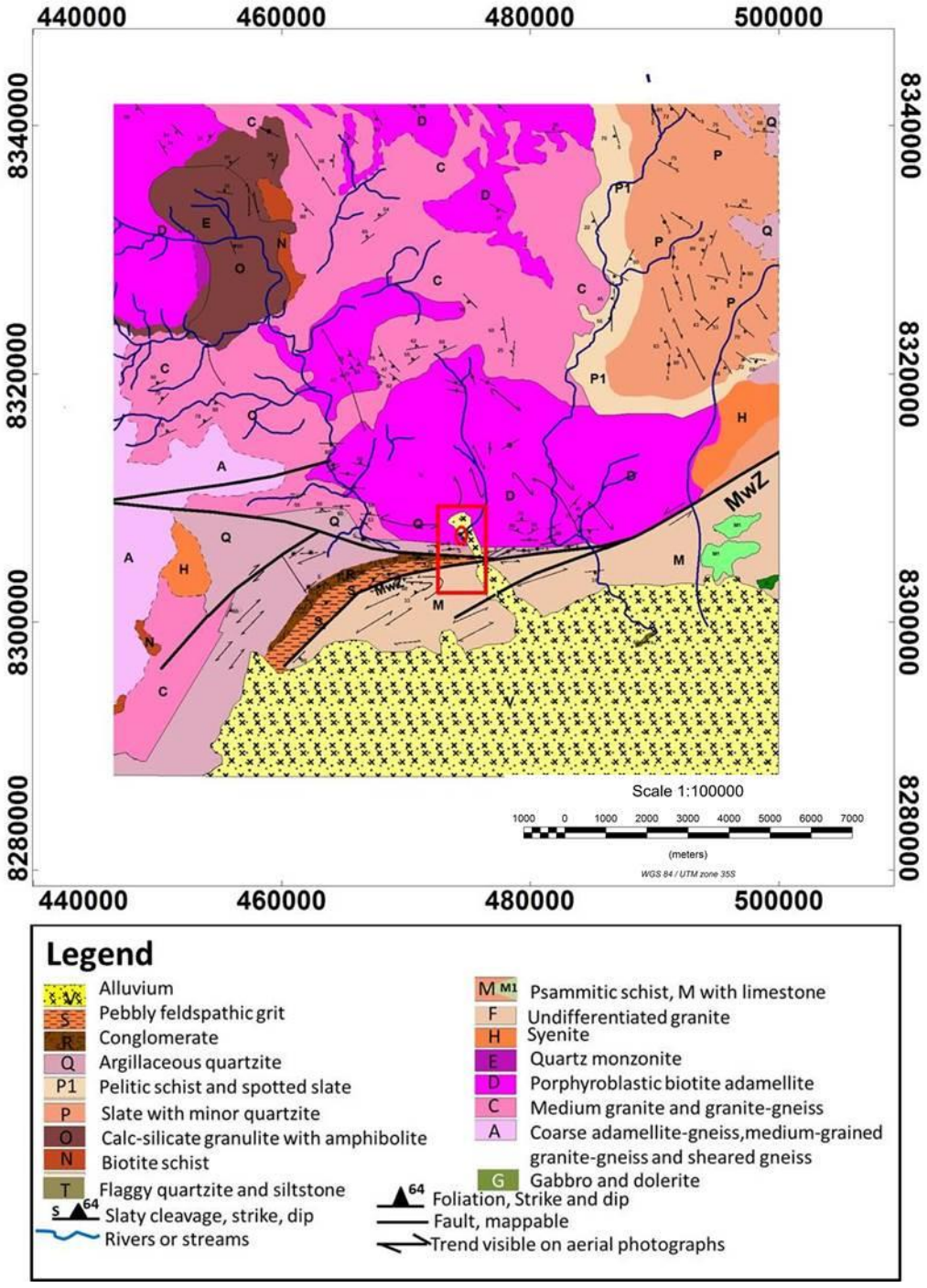

Figure 2.4. Geological map around the Hook Batholith (D) intrusion area compiled from the published 1:100000 geological map of the Nansenga River Area, Zambia (Abell, 1970) showing the two hot springs and the study area outlined by a red circle and a red box respectively.

Table 2.1**. Stratigraphy and sequence of events of the Nansenga River area (modified from Abell, 1970).**

Group	Formation	Process	Rock type
Karoo Supergroup		Sedimentation	Conglomerate, mudstones, siltstones and sandstone
Katanga System	Upper Kundelungu	Sedimentation	Quartzite and siltstone
		Igneous activity	Quartz tourmaline bodies and iron ore deposits Satellite bodies: syenite, gabbro, quartz feldspar porphyry Pegmatite, aplite and micro-granite dykes Coarse porphyroblastic biotite adamellite and quartz monzonite
	Lower Kundelungu	Sedimentation	Conglomerate, grit, quartzite, siltstone, slate, limestone, pelitic schist
	Mine series	Sedimentation, deformation & metarmophism	Mica-schist, skarn, amphibolite, thin limestone and calc-silicate rocks
Basement complex		Deformation & metamorphism	High grade schists and gneisses, biotite-gneiss, coarse-granite gneiss, fine to medium grained porphyroblastic granite and granite-gneiss

In the next section, a review of existing geophysical data mainly aeromagnetics data was done. Geophysical data are used to delineate the major faults, shear zones, fault zones and foliated zones which create a permeable environment favourable for geothermal waters. It were also used to understand if the two hot springs are structurally controlled.

2.4 Geophysical review

2.4.1 Aeromagnetic data

Aeromagnetic data were used to investigate geological features and deep tectonic/ faulting around Zambia e.g. the Mwembeshi Shear Zone. It measure variation in the Earth's magnetic field resulting from magnetic properties of the rocks. Magnetic anomalies result from changes in susceptibility and remanence which can be related to structural disturbances variations in lithology and structure such as dykes and faults or from mineralisation and alteration of rock composition. It also effectively discerns the underlying rocks covered by a non-magnetic sedimentary cover (Cordell and Grauch, 1985).

The digital aeromagnetic dataset used in this study is a compilation of various digitised contour maps of the aeromagnetic surveys carried out across Zambia compiled by the Geological Survey of Zambia from 1967 to 1982 (Katongo et al., 2002 and Saviaro, 1980). The data were acquired at a mean flight height of 150 m with a line spacing of between 800 m and 2000 m. Isaacs (1968) manually produced contoured magnetic intensity maps, at a scale of 1:50 000 from data obtained from these surveys. The Council of Geosciences of South Africa digitised and merged these maps and data collected from later surveys to produce the regional 250 m grid cell size digital map of Zambia (Figure 2.5).

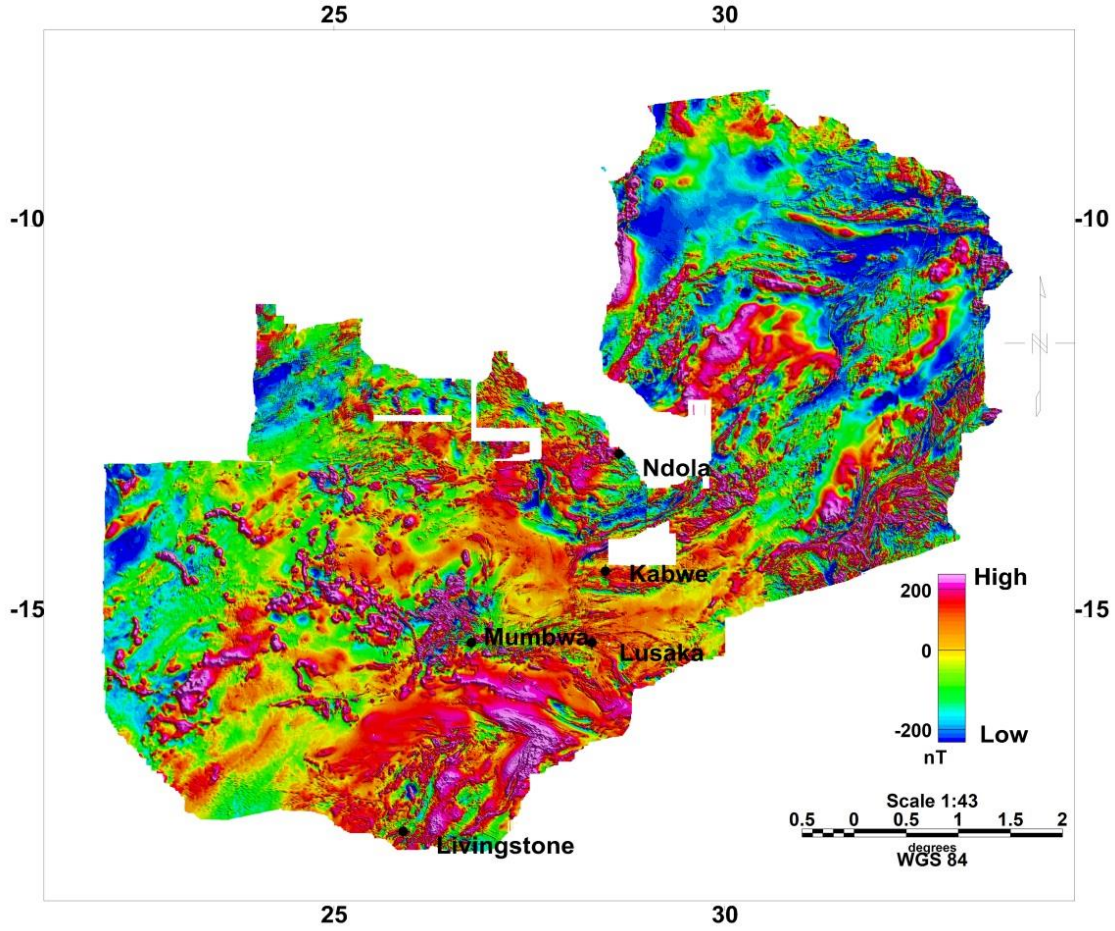

Figure 2.5. International Geomagnetic Reference Field (IGRF) corrected aeromagnetic Total Magnetic Intensity (TMI) map of Zambia gridded at 250 m. Digitised from paper copies by the Council for Geoscience, Pretoria.

Naydenov et al. (2014) used interpretation of the available aeromagnetic data, detailed structural field-studies and U–Pb dating of to show that the Pan-African evolution of the Hook area is

marked by the Nalusanga Zone (NZ) and the Itezhi-Tezhi Zone (ITZ) shear zones in the NE and SW part of the Hook Batholith respectively (Figure 2.6). Naydenov et al., (2014) showed that the Mwembeshi Shear Zone is a structure which marks the contact between the highly metamorphosed rocks of the Zambezi Belt and the less metamorphosed rocks of the inner Lufilian Arc (Figure 2.6).

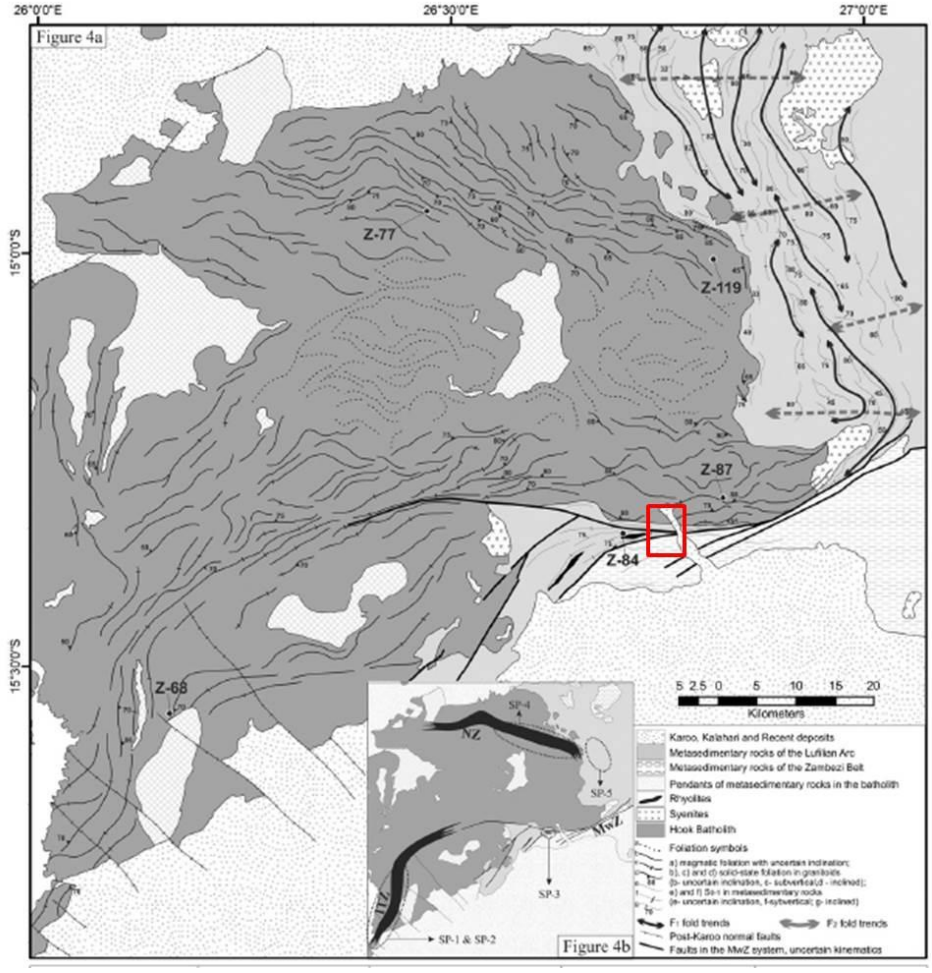

Figure 2.6. Structural map around the Hook Batholith area with foliations presented as lines with the inclinations added where data is available. Also shown are the faults of the Mwembeshi Shear Zone passing through our study area outlined by the red box (Naydenov et al., 2014).

The following chapter outlines the background and principles of the magnetic method followed by the author's own analysis and interpretation of the existing aeromagnetic data around the Mwembeshi Shear zone, magnetic susceptibility and ground magnetic data around the study area.

Chapter 3 Magnetic method

Magnetics is a geophysical method that makes use of the magnetic field properties of minerals to map the Earth's subsurface. The fact that the magnetic anomalies and lineaments are often associated with mineral structures (ore deposits) or regional structures, has led to the magnetic method being used in exploration as an aid in geological mapping and understanding economic mineral deposits (Grant, 1985).

3.1 Earth's magnetic field

The Earth's magnetic field whose amplitude is what we measure during magnetic surveys is composed of three components:

I. The main internal magnetic field due to the convection process occurring in the molten iron rich inner core. This process give rise to a magnetic field dipolar in nature resembling that of a bar magnet aligned along the Earth's axis of rotation. This field varies slowly (Merrill et al., 1996).
II. A small external magnetic field varying rapidly relative to the main field which is due to the charged solar particles orbiting around the Earth (Telford et al., 1990).
III. A secondary field caused by spatial variations in the main field due interactions between the present (induced magnetism) and past (remanent magnetism) magnetic field with magnetite rich rocks in Earth's crystalline basement and sedimentary section at T< 580 ˚C. These rocks interact with the core field giving rise to a secondary induced field. These are the magnetic anomalies recorded during magnetic surveys (Doell and Cox, 1967). The magnitudes of the fields causing these anomalies are directly related to the magnetic susceptibilities and spatial distribution of the crustal materials.

The dipolar geomagnetic field is oriented vertically downward at the north magnetic pole, horizontal (and pointing north) at the magnetic equator and points vertically upwards at the south magnetic pole (Figure 3.1a).

The geomagnetic field at any point on the earth's surface can be described by the scalar magnitude **F**, the angle it makes above or below the horizontal plane known as the magnetic inclination, I and the angle between the vertical plane containing **F** and true (geographic) north known as the magnetic declination, D (Figure 3.1b). The inclination, I is conventionally positive

north of the magnetic equator and negative to the south of it. The declination, D is reckoned positive to the east and negative to the west.

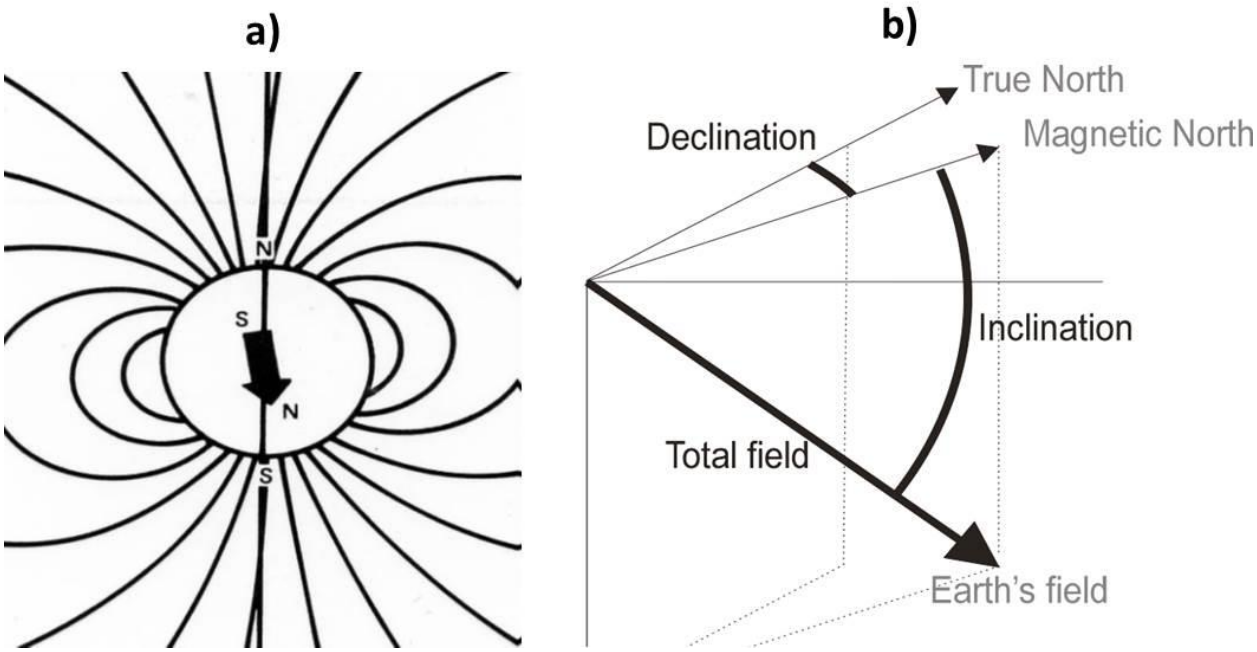

Figure 3.1. The vector total magnetic field defined either as the scalar magnitude of the total field, F, the inclination from the horizontal, I and the declination from true (geographic) north, D (Reeves, 2005).

3.2 Temporal variations

The solar activity results in temporal variations of the external magnetic field portion of the measured total magnetic field over time scales ranging from seconds to millions of years. Some of the effects of the variations are:

3.2.1 Diurnal variations

These diurnal variations of the Earth's magnetic field are short term variations of the interaction of the solar wind and the magnetosphere that follow a daily cycle. They are due to the Earth's rotation and its orbital movement around the Sun and the orbital motion of the Moon around the Earth (Telford et al., 1990).

3.2.2 Micropulsations

These are very rapid variations that occur on periods as short as a few minutes. They have amplitudes of a few nT but have a significant on measurements made at a base station on the ground or on measurements done during an aeromagnetic survey (Telford et al., 1990).

3.2.3 Magnetic storms

These are temporal interruptions of the magnetic field associated with sunspot activity and are characterised by variations of about 1000 nT at most latitudes and even larger ones around polar regions. Although eratic, magnetic storms can last for days

Although most of the above variations do not significantly affect magnetic surveys, except for magnetic storms, they should be carefully monitored and corrected for in order to have spatial, time-invariant magnetic anomalies (Telford et al., 1990).

3.2.4 Secular variations

These are slow variations of the main field that were monitored and documented accurately on magnetic observatory records for hundreds of years. The secular variations globally are clearly shown by changes in size and position of the main field from a simple dipolar field over years and decades. The declination has changed by about 35 ° from and the inclination has changed by 10 °. Careful observations have also shown that the main magnetic field monitored at the same location are varying (Telford et al., 1990).

3.2.5 Geomagnetic reversals

The Earth's magnetic field has also reversed direction over time evidenced in the remanent magnetisation of rocks collected on the lake floors and sea-floor spreading (Telford et al., 1990).

3.2.6 Magnetic anomalies

Variations in near surface rocks' magnetic minerals content results in local changes in the Earth's main magnetic field. These are observed on magnetic maps as anomalies. The

anomalies are associated with upper crustal features. Hence a magnetometer will record the sum of these local anomalies, internal and external magnetic fields (Telford et al., 1990).

3.3 Magnetic properties of rocks and minerals

3.3.1 Induced and remanent magnetisation

Magnetic minerals mostly magnetite and pyrrhotite contained in the rocks cause the magnetic anomalies. These magnetic minerals are not so many though. Materials can be differentiated according to how they behave when exposed to an external magnetic field. Induced magnetisation occurs when a material is placed in a magnetic field and becomes magnetised itself resulting in its own magnetic field which in turn reinforces the inducing external field. When the external field is removed some materials are left with a permanent magnetism oriented in the same direction of the removed external field. This residual magnetism is called remanent magnetisation and is exhibited by rocks of the crust together with induced magnetisation since they are situated in the geomagnetic field. These magnetic properties of rocks and minerals only exist at temperatures below 550 to 600 °C (Curie point) or between depths of 30 and 40 km (Telford et al., 1990).

3.3.2 Magnetic susceptibility

Magnetic susceptibility measures how a material is magnetised if placed in an external magnetic field (Telford, et al., 1990). The magnetic susceptibility of a rock unit is controlled by the magnetic minerals in that rock sample and their percentage. Lithologies can retain magnetization when they undergo metamorphism or cooling. Paramagnetic minerals such as mafic silicates can also control magnetic susceptibility. However, ferromagnetic minerals such as magnetite and pyrrhotite control magnetic susceptibility the most. The magnetic susceptibility can be affected by temperature or pressure changes either on shear and fault zones and/or lithological contacts. Therefore, the measured magnetic susceptibility depends on the geochemistry and mineralogy of the sample and on later alteration processes.

In a uniform magnetic material, it is defined as;

$$\mathbf{S} = M\mathbf{H} \tag{3.1}$$

where **S** is the intensity of magnetisation related to the strength of the magnetic field **H**, through the magnetic susceptibility M (dimensionless scalar). S can have either negative or positive values. A positive magnetic susceptibility is a consequence of the induced magnetisation being in the same direction as the inducing field, *H*, and negative values are due to the induced magnetisation in a different direction to the inducing field, H (Irving, 1964).

Clark and Emerson (1991) carried out a comprehensive and informed review of the magnetic susceptibilities of a variety of rocks (Table 3.1). Their results showed that even the same type of rock has a wide range of magnetic susceptibilities which results in an overlap between different rocks and that igneous rocks have the highest magnetic susceptibilities whilst sedimentary rocks have the lowest.

Table 3.1. Susceptibilities of various rocks and minerals (Clark and Emerson, 1991).

Material	Susceptibility x 10^3 (SI)
Air	~0
Quartz	-0.01
Rock salt	-0.01
Calcite	-0.001 – 0.01
Sphalerite	0.4
Pyrite	0.05 – 5
Hematite	0.5 – 35
Illmenite	300 – 3500
Magnetite	1200 – 19200
Limestones	0 – 3
Sandstones	0 – 20
Shales	0.01 – 15
Schist	0.3 – 3
Gneiss	0.1 – 25
Slate	0 – 35
Granite	0 – 50
Gabbro	1 – 90
Basalt	0.2 – 175
Peridotite	90 – 200

3.4 Magnetic data collection

Instruments that measure the total magnetic field are usually used to carry out magnetic field measurements. These include proton precession and caesium vapour magnetometers which are carried by a person or mounted onto a fixed wing aircraft or helicopter during acquisition of ground magnetic or aeromagnetic data respectively. Data is collected at discrete points along parallel lines that cover up your survey area in air (aeromagnetic), on ground (ground magnetic) or on water bodies. Aeromagnetic data is relatively cheap and quick to acquire compared to ground magnetic data although ground magnetic data has a higher resolution compared to aeromagnetic data.

3.5 Magnetic data correction

Since we measure the sum of the magnetic field due to regional and local fields and we are only interested in the magnetic field caused by the geology of the upper crust (local field), we need to remove the influence of the Earth's main field, external magnetic field and the field due to cultural features (Blakely et al., 2005). This is achieved by subtracting a model of the main field from the survey data.

3.5.1 Data checking and editing

This process involves systematic viewing of data as stacked profiles so as to notice and remove unwanted data (spikes) usual caused by man-made features (e.g. power lines) from the survey data.

3.5.2 Diurnal correction

Time synchronized diurnal variations of the Earth's magnetic field are recorded at a base station and then removed from the survey data using a common technique called diurnal correction. The base station magnetometer is also used to monitor any magnetic storms on a daily basis and usually the survey is suspended or data are recollected if the amplitude is more than 50 nT. This technique assumes that the temporal variation of the main field at the field station and at the base station is the same.

3.5.3 Geomagnetic Reference Field removal

We need to remove the influence of the Earth's main field and this is achieved by subtracting a model of the main field from the survey data. The International

Geomagnetic Reference Field (IGRF) model is calculated producing the field strength, inclination and declination from given longitude and latitude of the survey area and then subtracting the calculated main field from the survey data.

3.6 Gridding

The data are usually not acquired along straight lines and more readings are usually taken along lines than across lines so the data are then interpolated onto a regular grid to enable image processing and enhancement. This procedure is called gridding and several gridding algorithms are used e.g. (Briggs, 1974 and Fitzgerald et al., 1997).

3.7 Data processing and enhancement

3.7.1 Reduction to pole

The geomagnetic field is dipolar in nature and this causes magnetic anomalies located anywhere except at the Earth's magnetic poles to be generally asymmetric even when the source of the magnetic distribution is not symmetrical. This makes it difficult to interpret the TMI magnetic data. The reduction to pole (RTP) operator is applied to the TMI grid to transform the magnetic anomalies measured at any inclination to be those of an area whose inclination is vertical and anomalies are symmetrical i.e. the magnetic poles (Baranov, 1957).

Geosoft uses the frequency domain algorithm below developed by Baranov (1975):

$$(\theta) = \frac{[\sin(I) - i\cos(I)\cos(\varphi - \theta)]^2}{[\sin^2(I_\alpha) + \cos^2(I_\alpha)\cos^2(\varphi - \theta)] \cdot [\sin^2(I) + \cos^2(I)\cos^2(\varphi - \theta)]} \quad (3.1)$$

If $(|I_\alpha|) < (|I|)$, $I_\alpha = I$

where, I is the geomagnetic inclination, φ is the declination, θ is the wavenumber and I_α is the inclination for amplitude correction, which is never less than 1, $\sin(l)$ is the magnitude component and $i\cos(l)\cos(\varphi - \theta)$ is the phase component.

The RTP algorithm assumes that remanent magnetisation is absent, which might not be true for this study area. If the remanence parameters are known, remanent magnetisation can be corrected for (Cooper and Cowan, 2005).

3.7.2 Vertical derivatives

A vertical derivative is a high pass filter that is very effective in enhancing anomalies due to shallow sources (high frequencies) (Blakely, 1995). Vertical derivatives narrow the wavelength of the magnetic anomaly due to the source body hence locating the source bodies more accurately than the RTP and TMI images. They enhance shallower features at the expense of noise.

Geosoft calculates vertical derivative in the frequency domain using Laplace's equation. The formula is given by ;

$$\left(\frac{\partial^n}{\partial z^n} T\right) = k^n \cdot T(f) \qquad (3.2)$$

where the frequency, $k^n = \sqrt[n]{k_x + k_y}$, T is the Fourier representation of the field and n is the order of the vertical derivative (Cooper and Cowan, 2004). z is assumed to be positive downwards.

3.7.3 Upward and downward continuation

These filters calculate the magnetic field at a different height to that at which it was acquired thereby enabling ground magnetics to be compared with aeromagnetic data and used to merge data collected at different heights. Downward continuation is a high pass filter and therefore enhances detail at the cost of enhancing high frequency noise whilst upward continuation is a low pass filter which smooths the data.

3.7.4 Analytic signal

For map data the analytic signal (AS) is defined as the square root of the squared sum of the vertical and horizontal derivatives (x, y and z) of the magnetic field (Roest et al., 1992).

$$AS = \sqrt{\left(\frac{df}{dx}\right)^2 + \left(\frac{df}{dy}\right)^2 + \left(\frac{df}{dz}\right)^2} \quad (3.3)$$

3.7.5 Euler deconvolution

It is an inversion process for deriving the apparent depth and location to a magnetic anomaly source by using Euler's equation. It relates the magnetic field and its gradient components to the location of the anomaly source, with the degree of homogeneity expressed as a "structural index" (El Dawi et al., 2004). The structural index (SI) is a measure of how the field falls per unit time with distance from the source. Euler deconvolution is given by the following equation:

$$\frac{\delta F}{\delta x}(x - x_0) + \frac{\delta F}{\delta y}(y - y_0) + \frac{\delta F}{\delta z}(z - z_0) = N\,(B - F) \quad (3.4)$$

Where (x_0, y_0, z_0) is the location of the magnetic source whose total field (F) is measured at (x, y, z,) (Thomson, 1982).

N is the structural index (SI) whilst B is the regional magnetic field. N depends on the geometry of the source (El Dawi et al., 2004). Approximate structural index values for magnetic sources are provided in Table 3.2.

Table 3.2. Structural indices used to estimate the depth and extent of simplistic magnetic sources beneath the aeromagnetic profiles (after Reid et al., 1990; FitzGerald et al., 2004).

Structural index (N)	Model features
0	Contact
1	Fault
1	Dyke
2	Vertical pipe
3	Sphere

Chapter 4 Analysis and Interpretation of aeromagnetic, magnetic susceptibility and ground magnetic data

4.1 Aeromagnetic data analysis

For this study, only the aeromagnetic data that cover the geological map by Abell (1970) was extracted from the data of the whole country. The International Geomagnetic Reference Field (IGRF) corrected Total Magnetic Intensity (TMI) grid (Figure 4.1) shows high magnetic anomalies (purple) with magnetic amplitude ranging to values >300 nT that are usually bounded by zones of high magnetic intensities (red) with magnetic amplitude ranging from 100 to 300 nT. Low magnetic intensity (green to orange) that covers most of the grid can also be observed, associated with magnetic amplitudes ranging from -100 to 100 nT. A very low magnetic anomaly (blue) is also observed in the middle of the grid characterised by magnetic amplitudes ranging to lower than -100 nT (Figure 4.1).

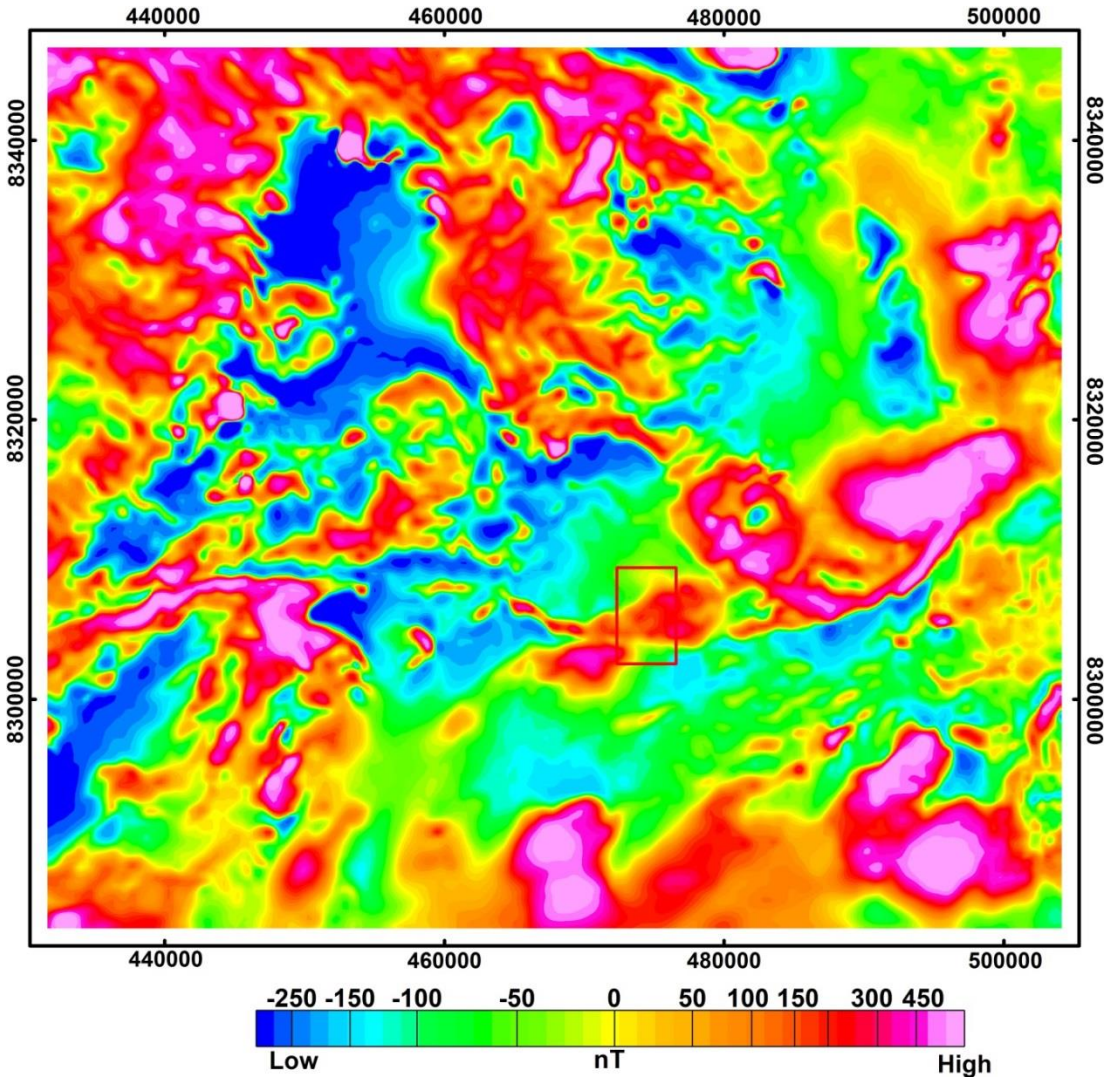

Figure 4.1. International Geomagnetic Reference Field (IGRF) corrected aeromagnetic Total Magnetic Intensity (TMI) grid around the Hook Batholith area showing the study area (red box). Grid cell size 250 m. Digitised from paper copies by the Council for Geoscience, Pretoria. IGRF at the time of data acquisition has been removed.

Since the geological mapping was done using outcropping rocks and a greater part of the study area is covered by soil, the confidence of the geological mapping in the study area is reduced because of interpolation. Aeromagnetic data were used to map the subsurface and enhancing the anomalies in order to reveal contacts of different lithologies below the soil cover. For better interpretations, the influence of the Earth's main field was then removed from the measured TMI data. The Earth's field strength, inclination and declination at a particular area are calculated using the International Geomagnetic Reference Field model

from given longitude and latitude values of the area. Since the data provided had the IGRF already removed, the data were then gridded and processed using Geosoft Oasis Montaj software (Geosoft) version 8.1. The gridded data were then Reduced To Pole (Figure 4.2) and a first vertical derivative filter (Figure 4.3) followed by analytic signal filter were then applied to them.

Reduction to pole (RTP) filter was applied to the Total Magnetic Intensity (TMI) grid using an inclination of −54.16° and a declination of −4.207°. The inclination and declination were determined using the dates when the data were collected.

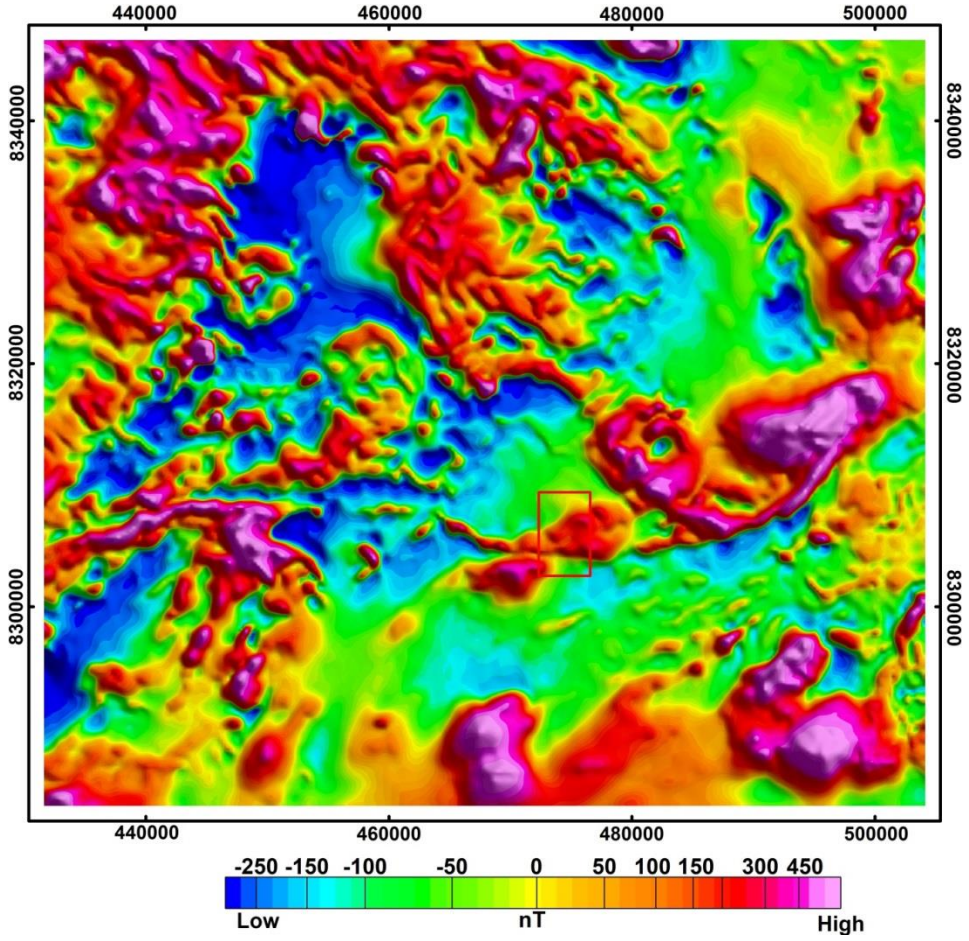

Figure 4.2. Sunshaded (at inclination and declination of 45°) International Geomagnetic Reference Field (IGRF) corrected and Reduced To Pole (RTP) aeromagnetic Total Magnetic Intensity (TMI) grid around the Hook Batholith area showing the study area (red box). Grid cell size 250 m. Digitised from paper copies by the Council for Geoscience, Pretoria. IGRF at the time of data acquisition is removed. RTP corrected using inclination of −54.16° and declination of −5.07°.

The aeromagnetic RTP map shows anomalies with varying amplitudes, frequencies and wavelengths which define basement lithologies or sources according to their compositions at different depths.

The first vertical derivative (Figure 4.3) and analytic signal (Figure 4.4) were computed to enhance the near surface, short wavelength magnetic fabrics of the granitoids and to detect faults and contacts of different lithologies which are covered by sediments.

A vertical derivative is a high pass filter that is very effective in enhancing anomalies due to shallow sources (high frequencies) (Blakely, 1995). Vertical derivatives narrow the wavelength of the magnetic anomaly due to the source body hence locating the source bodies more accurately than the RTP and TMI images. They enhance shallower features at the expense of noise.

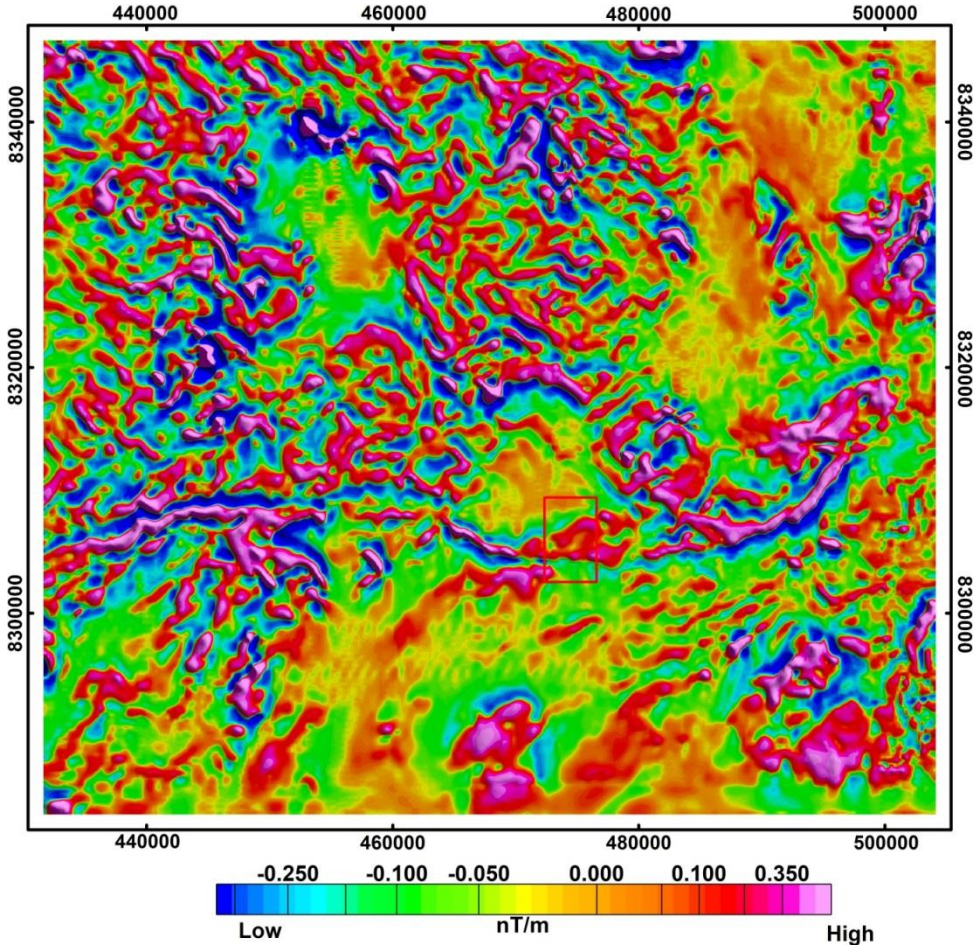

Figure 4.3. International Geomagnetic Reference Field (IGRF) corrected, Reduced To Pole (RTP) and first vertical derivative (1-VD) aeromagnetic Total Magnetic Intensity (TMI) gridded data around the Mwembeshi Shear Zone showing the study area red box.

Highest magnetic amplitude anomalies (>300 nT) were divided into linear alternating positive and negative anomalies after applying the 1VD filter (Figure 4.3). It can be easily noticed that there is a difference in the anomalies of Figure 4.2 and Figure 4.3.

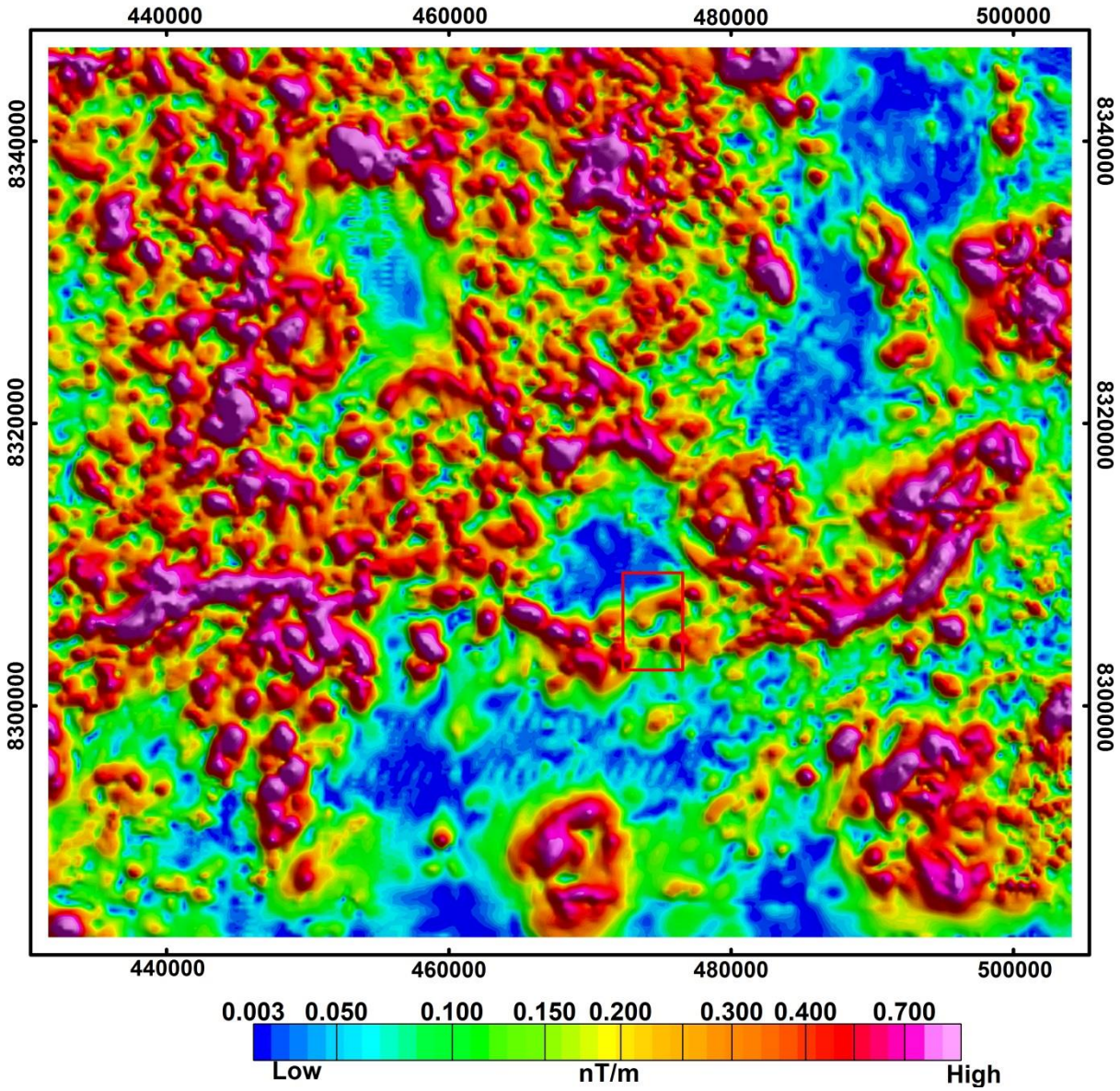

Figure 4.4. Analytic Signal map of the International Geomagnetic Reference Field (IGRF) corrected and Reduced To Pole (RTP) aeromagnetic Total Magnetic Intensity (TMI) gridded data around the Mwembeshi Shear Zone showing the study area red box.

The analytic signal filter uses the horizontal and vertical gradients to calculate the analytic signal amplitude which can be used to locate contacts and edges of bodies. Both the 1VD and analytic signal filters enhance edges and sharpen anomalies at the expense of noise.

Abell (1970) stated that the aeromagnetic data was too late to be in-cooperated in both the surface geological map and report which led to the poor correlation between the different lithological boundaries and the potential field anomalies at local scale. For example, there is a circular magnetic anomaly just northeast of the survey grid (red box) that was mapped as porphyroblastic adamellite on the geological map (D) based on outcrops whilst it actually has a lower magnetic gradient than the anomalies that are attributed to the porphyroblastic adamellite rocks in the study area. This could have been due to a high degree of interpolation since the area does not have outcropping rocks or a lower magnetic susceptibilty. Also the rocks south of the MwZ are overlain by sediments which made geological mapping difficult. There are a lot of joints in the Hook Batholith rocks that could have been due to foliation fracturing. Regions of foliation are susceptible to weathering which creates zones of weakness (pathways) where the streams found in the Hook Batholith rocks flow. Whilst in the study area, the author noticed that the two warm hot springs follow a NW-SE trend which could suggest a fault or joint with the same trend. The faulting and joints in the area suggest good rock permeability. The two hot springs, shallow aquifers and rivers around the area are an indication of sufficient water. There are two hot springs to the NE and SW (Mumbwa and Bilili hot springs) of our study area that have relatively high surface temperatures of 41.5 °C and 66.2 °C. These hot springs also have geothermometer temperatures of about 150 - 200 °C (Legg, 1974). The water, permeability and temperature in the area provide us with justification to explore whether the area hosts a geothermal energy resource. In the next section, the aeromagnetic data will be analysed in-order to map fractures, joints, faults and to complement the geological map by Abell (1970) and Naydenov et al. (2014).

4.2 Interpretation of aeromagnetic data

In order to unravel the sources of the different magnetic anomalies and to motivate the use of ground magnetic survey to implement geological mapping, four different processes where integrated: i) interpretation of aeromagnetic geophysical images, ii) analysis of geological and structural data in published papers, iii) use of Google Earth Pro (GEP) for geological and structural mapping at outcrop scale and iv) measurement and application of magnetic susceptibility of the rocks. Discontinuities (joints, fractures, bedding planes, rock cleavage, foliation, shear zones, faults and other contacts) and lithologies were mapped on GEP images.

Certain parts of the area with rocks that are exposed and that were mapped by Abell (1970) were correlated with the GEP image and the aeromagnetic maps.

The Reduced To Pole TMI data image shows the area is mostly covered by a very high magnetic anomaly (purple), a low magnetic anomaly (blue) in the middle of the area striking NE and another moderate magnetic anomaly (orange to green) in the eastern and southern parts (south of the MwZ) of the map (Figure 4.2).

Different anomaly types or magnetic signatures were determined using the first vertical derivative image (Figure 4.5), the analytic signal image (Figure 4.6), the surface geological map (Figure 4.7) and the Google Earth image (Figure 4.8). The criteria used are explained in the next section. The area is mostly covered by outcropping basement Hook granites and granite gneiss which show NE and NW foliation trends (Abell, 1970). Small rivers and streams are also observed in the area with NE and NW trends. There is a very close coincidence between the high (red) and low (blue) magnetic anomalies with outcropping granites and foliation trends, rivers or streams respectively. Now the geological boundaries on the map by Abell (1970) can be revised using aeromagnetic data and interpretation of analytical signal and first vertical derivative images as well as the Google Earth image.

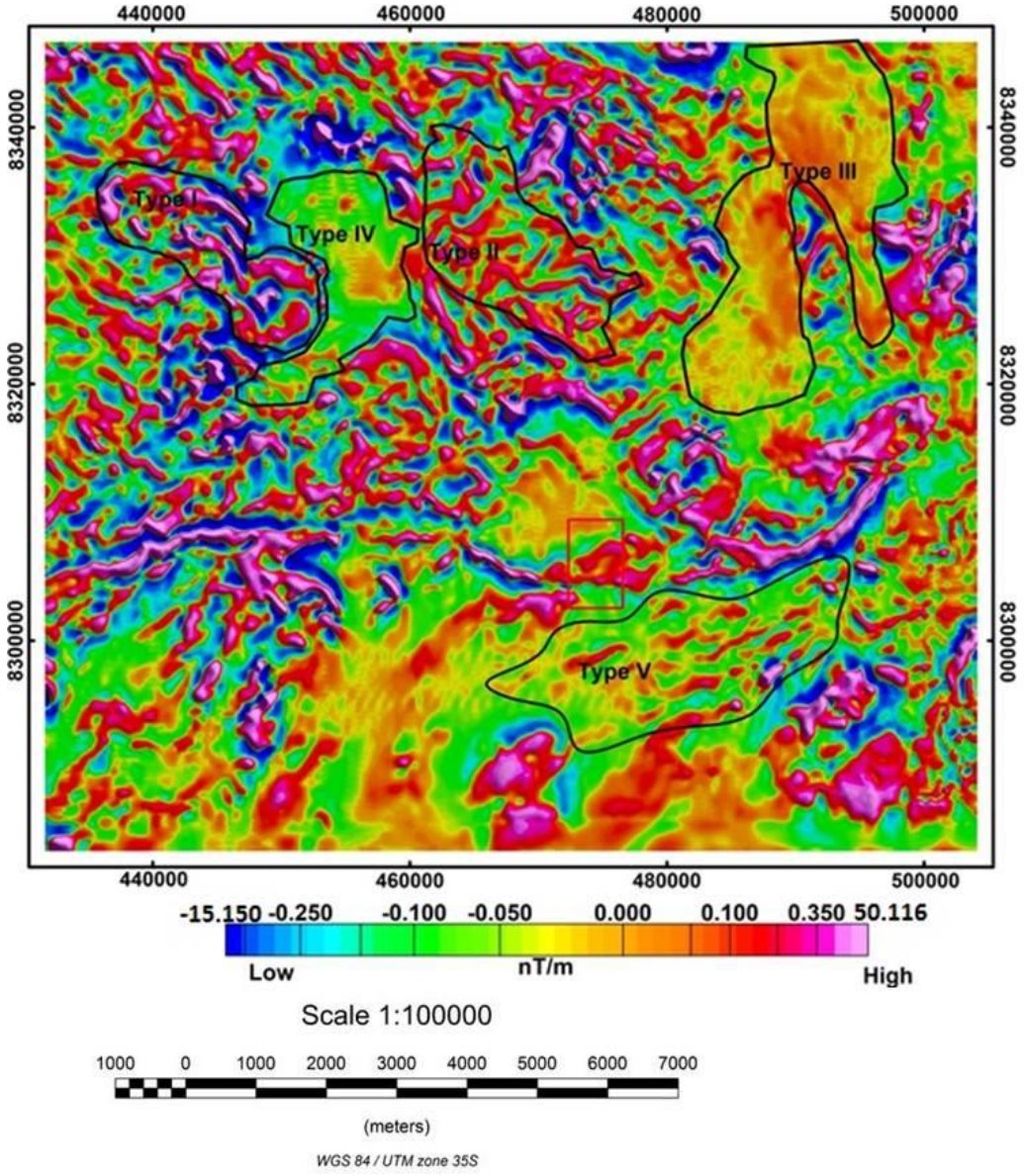

Figure 4.5. International Geomagnetic Reference Field (IGRF) corrected, Reduced To Pole (RTP) and first vertical derivative (1-VD) filtered aeromagnetic Total Magnetic Intensity (TMI) grid showing outlines of the enhanced anomaly types encountered in the area. The anomaly types were determined using their different wavelengths.

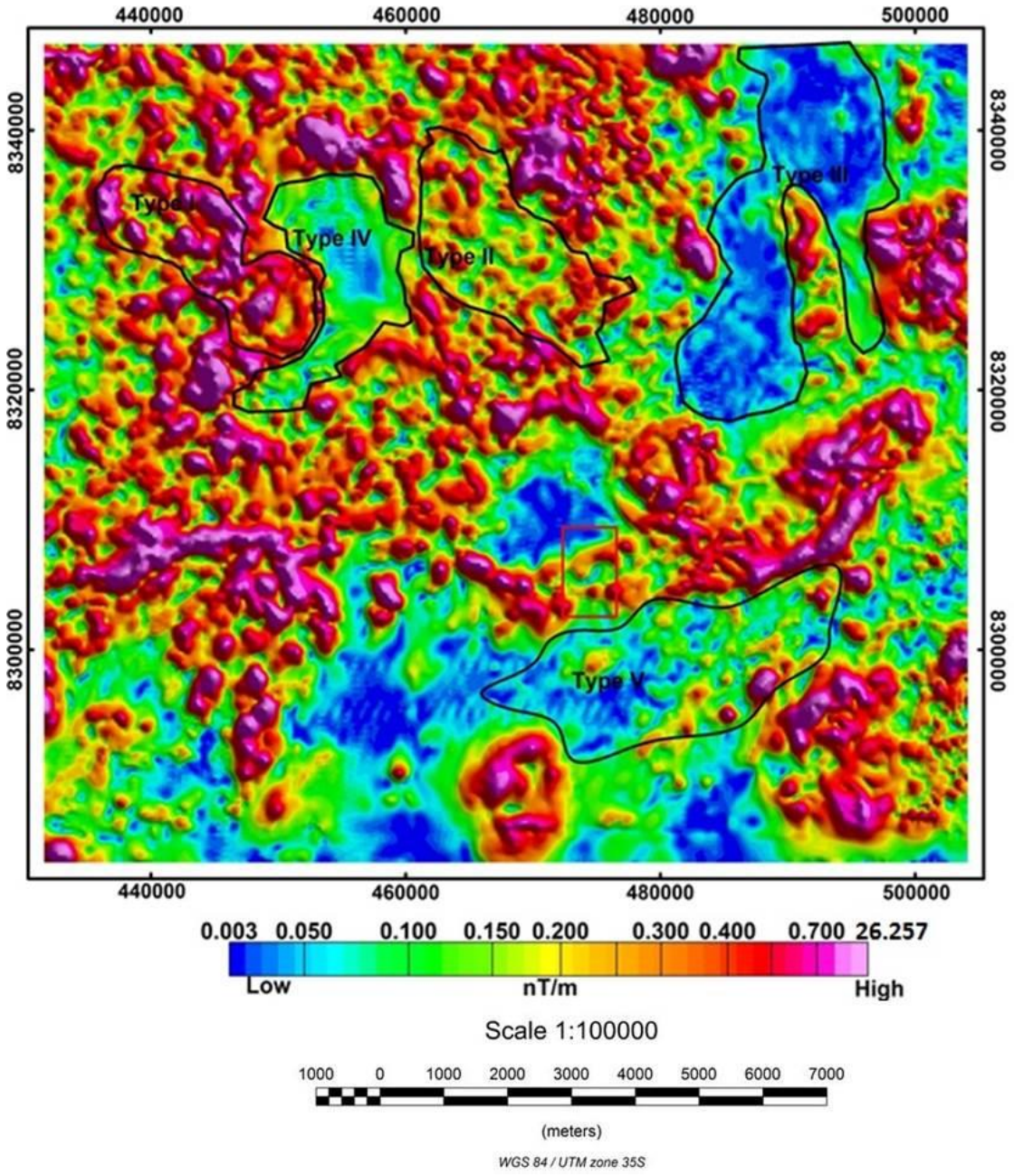

Figure 4.6. International Geomagnetic Reference Field (IGRF) corrected, Reduced To Pole (RTP) and analytic signal filtered aeromagnetic Total Magnetic Intensity (TMI) grid showing outlines of the enhanced anomaly types encountered in the area.

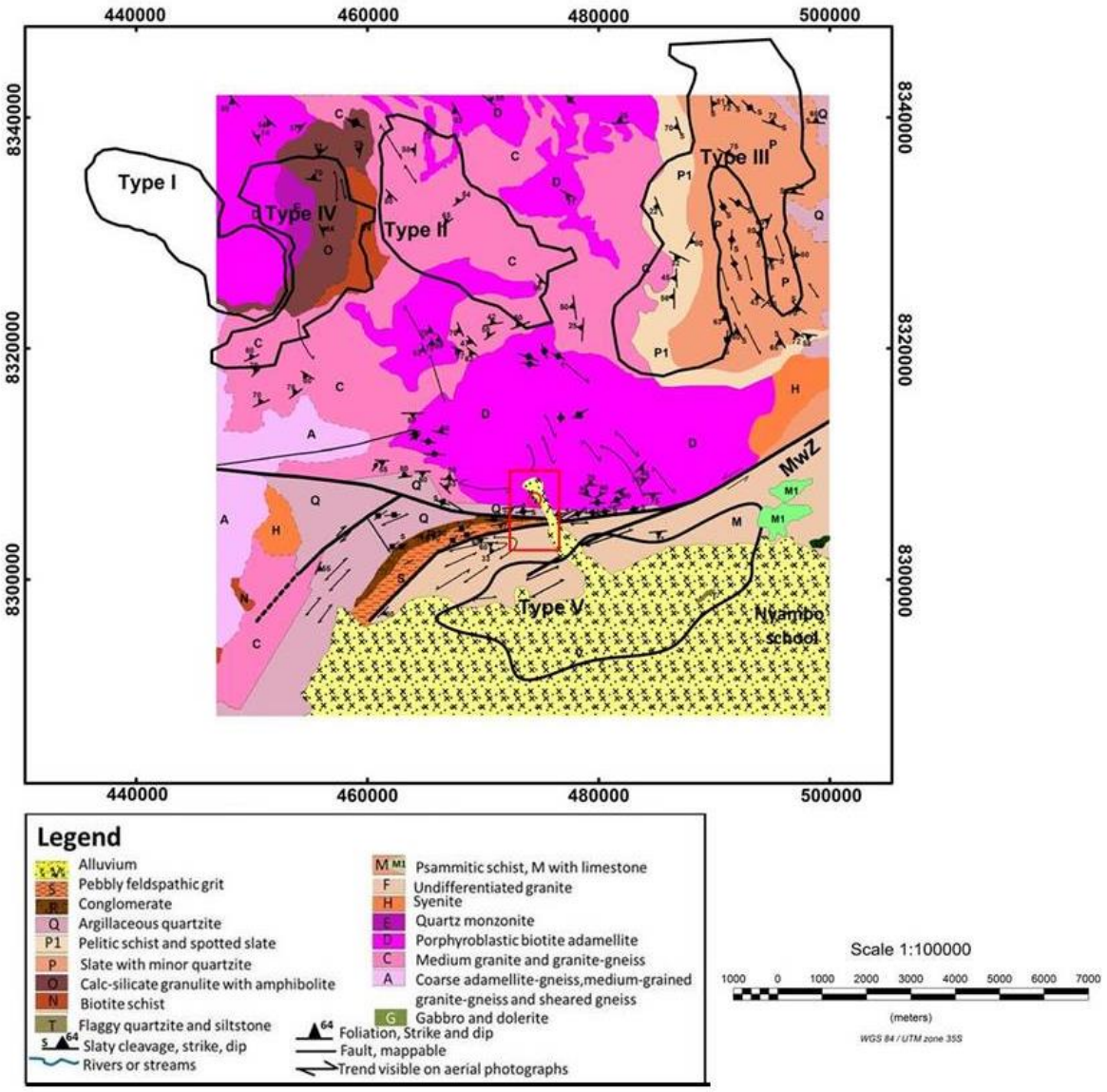

Figure 4.7. Geological map around the Hook Batholith intrusion area compiled from the published 1:100000 geological map of the Nansenga River Area, Zambia (Abell, 1970) showing the different anomaly types interpreted from aeromagnetic data, the two hot springs (red circle) and the study area (red box).

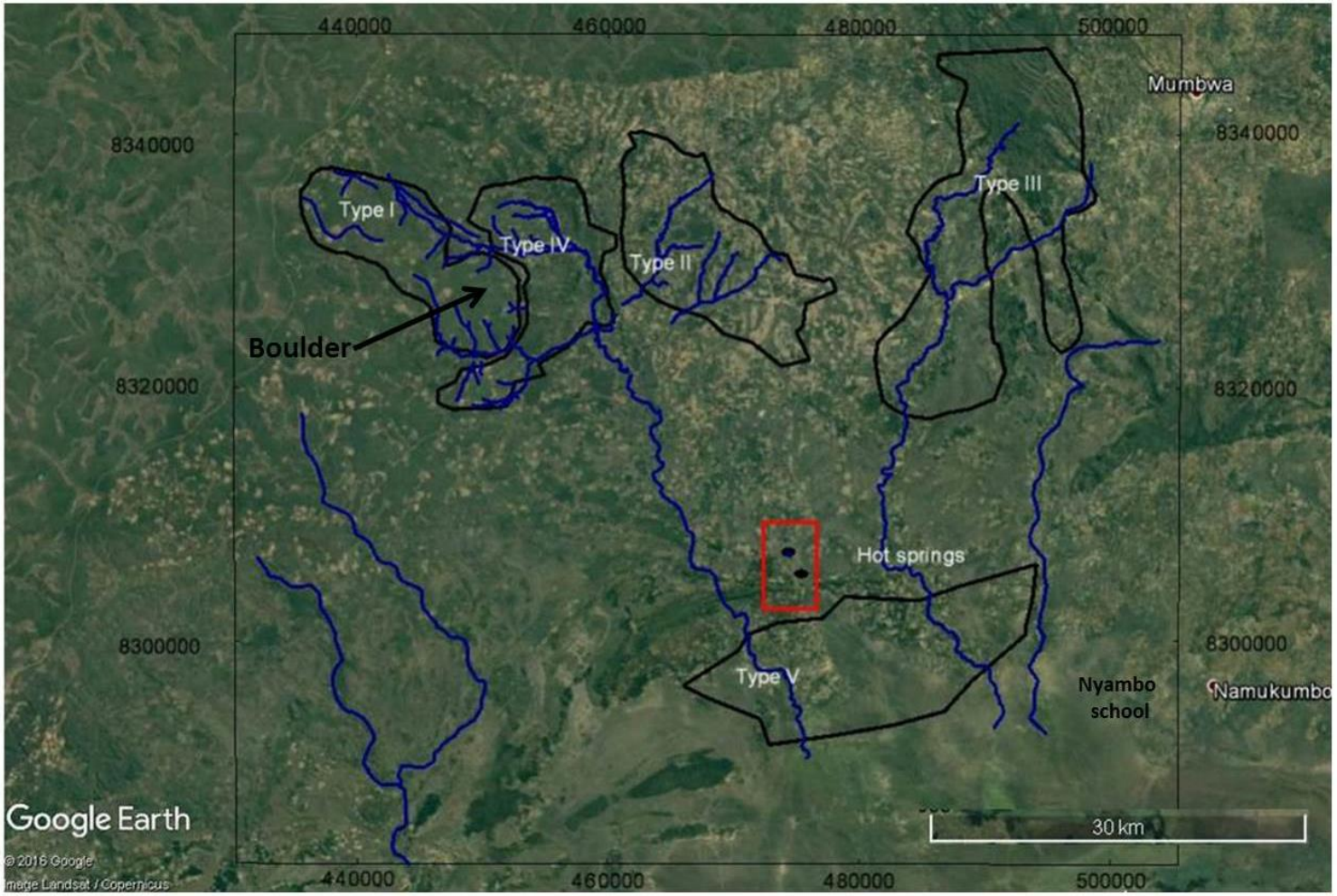

Figure 4.8. Google Earth image around the Hook Batholith intrusion area showing the different anomaly types from aeromagnetic data, the two hot springs (red circle) and the study area (red box). The blue lines represent rivers and streams.

4.2.1 Anomaly type 1

These anomalies (magenta colour) are characterised by the highest magnetic amplitude values and the highest (steepest) vertical magnetic gradient with values greater than 300 nT (Figure 4.2) and 0.35 nT/m (Figure 4.5) respectively. On the analytic signal map, they are characterised by the magenta colour shade which represents the highest analytic signal amplitude (Figure 4.6). Type I anomalies correspond well with the outcropping porphyroblastic biotite adamellite rocks of the Hook Batholith (D) overlying deep magnetic basement rocks (Figure 4.7). The high magnetism of the rocks can be attributed to the high content of ferromagnetic minerals like magnetite in the rocks (Naydenov et al., 2014). The outcropping rocks can also be viewed on Google Earth images as large boulders surrounded by streams (Figure 4.8). The streams and outcrops are more pronounced on the first vertical derivative image as magnetic lows (blue) around the edge of the boulders or lineaments trending parallel to magnetic high lineaments respectively (Figure 4.5). Naydenov et al. (2014) suggested that the biotite minerals in the rocks form well-developed elongated domains that are aligned in the foliation planes and in the shear bands which resulted in the formation of these magnetic low, lineaments.

4.2.2 Anomaly type II

Type II anomalies are characterised by red colour representing high magnetic amplitude and high magnetic gradient values (red colour) ranging from 100- 300 nT (Figure 4.2) and 0.1 - 0.35 nT/m (Figure 4.5) respectively. On the analytic signal map, they are characterised by the red to orange colour shade which represents high analytic signal amplitude (Figure 4.6). On the geological map, they correspond well with the outcropping basement rocks (medium grained granite and granite gneiss, sheared gneiss, coarse adamellite gneiss of the basement rock labeled C or A (Figure 4.7). The high magnetism of the rocks can be attributed to the high content of ferromagnetic minerals like magnetite in the rocks (Naydenov et al., 2014). The outcropping rocks can also be viewed on Google Earth images as large boulders (Figure 4.8). The magnetic low, lineaments are not so pronounced in this anomaly type because the basement rocks do not have much biotite like the Hook granites.

4.2.3 Anomaly type III

Type III anomalies are low amplitude magnetic signatures (green) characterised by low magnetic amplitude and low amplitude magnetic gradients (orange) of -100 - 100 nT (Figure 4.2) and -0.05 - 0.1 nT/m (Figure 4.5) respectively. On the analytic signal map, they are characterised by the blue colour which represents the low analytic signal amplitude of < 0.05 nT/m (Figure 4.6). The causative bodies are very deep seated as shown by the broad wavelength and low frequency. They coincide with mapped outcropping metasediments of the Katangan sequence overlying the highly magnetic Hook Batholith (Figure 4.7). This low magnetic signature is due to the deeply buried highly magnetic basement granites and granite gneiss and outcropping argillaceous quartzite and siltstone.

4.2.4 Anomaly type IV

Type IV is the anomaly characterised by the lowest negative magnetic amplitude and very low magnetic gradient values, less than -100 nT coloured in blue (Figure 4.2) and less than -0.05 nT/m coloured in green (Figure 4.5). The low magnetic vertical gradient and long wavelength shows that the causative magnetic source is deeply buried in these areas. On the analytic signal map, they are characterised by the blue colour which represents the low analytic signal amplitude of 0.05 - 0.15 nT/m (Figure 4.6). The analytic signal clearly distinguishes the anomaly from its surrounding anomalies. The type IV anomalies can be attributed to outcropping biotite schist and granulite with amphibolite metasediments of the Katanga sequence (Figure 4.7).

4.2.5 Anomaly type V

This anomaly type is found south of the Mwembeshi Shear Zone and southeast of the study area. It is characterised by alternating NE striking magnetic lineaments with magnetic amplitude ranging 0 -50 nT (Figure 4.2) and gradient of about and 0.1 nT/m flanked by a low magnetic amplitude and gradient signature (Figure 4.5). The anomalies' short wavelength and high magnetic gradient shows that they are due to shallow bodies. A small portion of the anomaly as well as its strike corresponds well with a small outcrop northwest of Nyambo School. The outcrop forms two hillocks flanked by alluvium and was mapped as recent flaggy quartzite belonging to the Luiri formation of the Katanga system striking almost NE

and having an average dip of 70˚ to almost vertical (Figure 4.7). The signature of the anomalies can be attributed to the folded flaggy quartzite rocks forming the hillocks.

4.2.6 Summary

There are five types of magnetic anomalies associated with the rocks around the Hook Batholith area that correlate well with some of the mapped lithologies and structures as well as rivers or streams observed on Google Earth images. There are smooth, broad positive and negative anomalies due to deeper-seated granitoids of the basement or Hook Batholith and metasediments of the Katanga sequence respectively. High frequency alternating positive and negative magnetic lineaments can be attributed to the alignment in a common direction of magnetic minerals and micaceous (biotite) minerals respectively. The negative lineaments seem to follow foliation and fault trends which correspond with jointed or fractured regions where the rivers flow. In the next section the negative lineaments were analysed in order to come up with a structural map of the study area.

4.3 Magnetic positive and negative lineaments

Geosoft Oasis Montaj CET Grid Analysis extension was used to automatically detect, vectorise and effectively map the alternating shallow magnetic positive and negative lineaments that were enhanced by the first vertical derivative filter and are attributed to the alignment of the magnetite and micaceous minerals in the gneissic rocks. The negative lineaments correspond to the foliation trends, which also map the foliation fractures and joints that could have been zones of weakness where rivers and streams follow. The extension uses the phase symmetry algorithm that was developed by (Kovesi, 1997). The algorithm detects continuous linear regions of lateral discontinuity because linear features produce highly symmetrical response when not sampled parallel to them. These points of symmetry give rise to a distinguishable pattern of local phase (Kovesi, 1997). A smallest filter wavelength of 500 m, and 4 filter scales were used to detect negative magnetic lineaments orientated in all directions (Figure 4.9).



Figure 4.9. Map of the negative magnetic lineaments mapped using phase symmetry algorithm that was developed by (Kovesi, 1997). A smallest filter wavelength of 500 m, and 4 filter scales were used to detect negative magnetic lineaments (black) orientated at all angles and positive magnetic lineaments (green) outlined in Type V anomaly.

The geological boundaries, the foliation, cleavage, strike and dip of different rocks, trends, folds and faults mapped by Abell (1970) and Naydenov et al. (2014) were overlaid on the Reduced To Pole First Vertical Derivative TMI data image (Figure 4.10). Also, the locations of the two hot springs were plotted on the same map and their NW-SE alignment might suggest an unmapped fault along them which is not visible on the Google Earth image (Figure 4.11).

The good correlations between the lithological boundaries, magnetic data, foliation trends, rivers, streams and rock outcrops that were observed above were then extended to the whole study area where there are fewer outcrops due to sedimentary cover. A number of criteria that were suggested by Singhal and Gupta (2010) were used to decipher the presence of faults,

joints or fractures such as alignment of springs or ponds, vegetation alignment, rectilinearity of streams and indication of sudden anomalous changes along a river course.

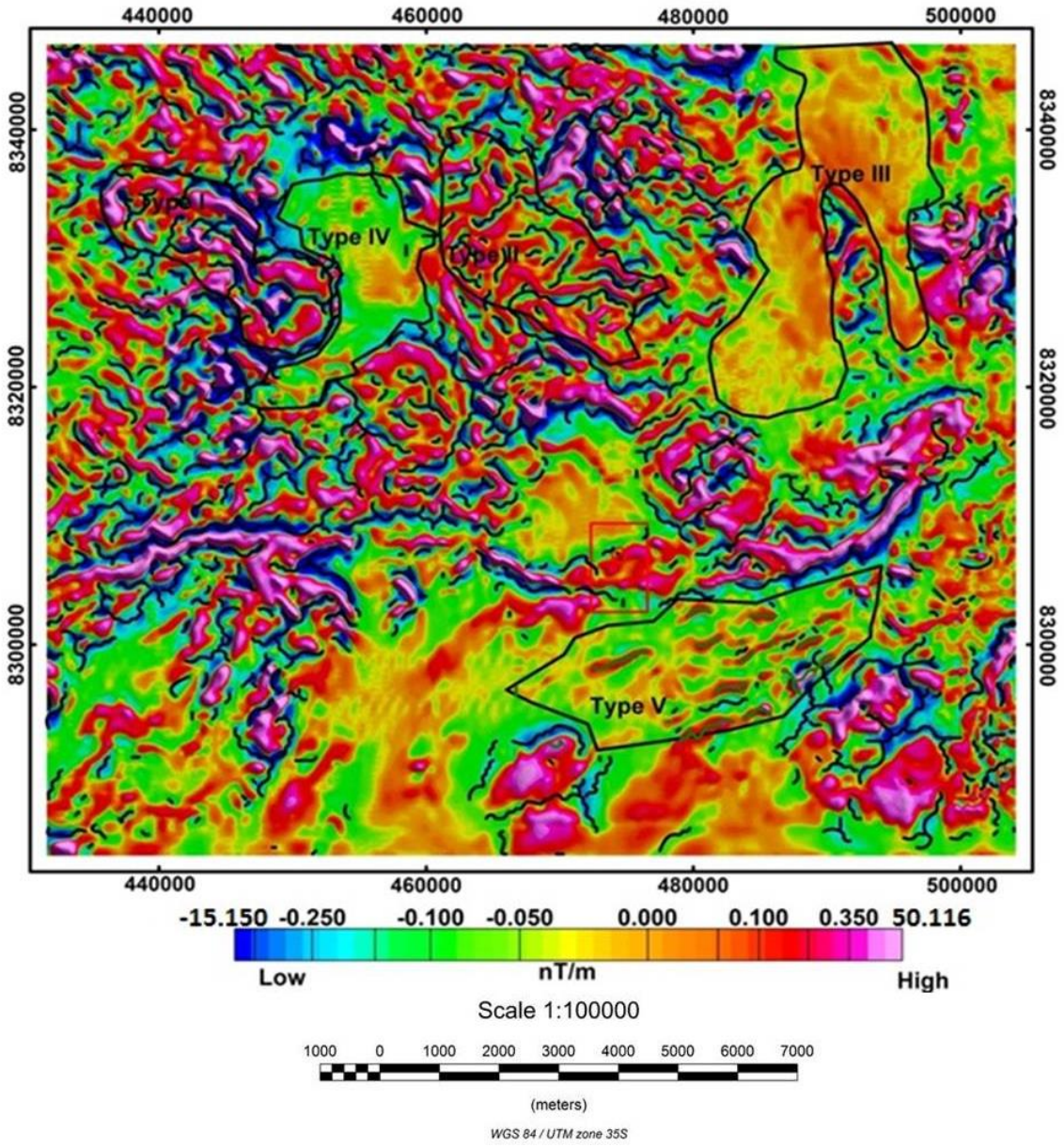

Figure 4.10. Linear magnetic anomalies overlain on International Geomagnetic Reference Field (IGRF) corrected, Reduced To Pole (RTP) and first vertical derivative (1-VD) filtered aeromagnetic Total Magnetic Intensity (TMI) grid around the Mwembeshi Shear Zone showing the study area (red box) and hot springs (red circle) with outlines of the types of anomalies as interpreted from the aeromagnetic data. Only positive lineaments (green) in Type V anomaly are shown whilst negative lineaments (black) were mapped for the whole area.

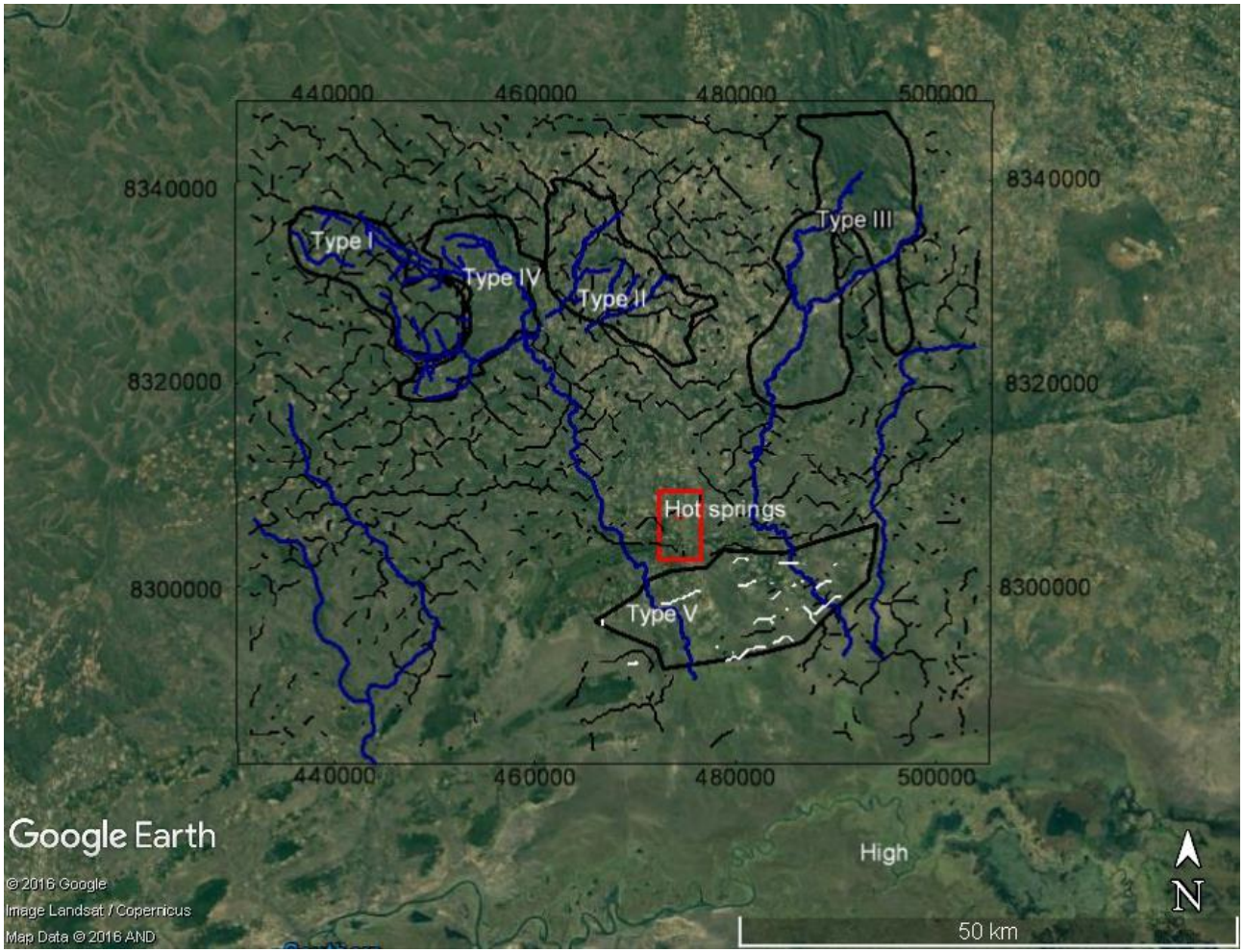

Figure 4.11. Negative (black) and positive (white) linear magnetic anomalies overlain on Google Earth image of the study area with the outlines of the types of anomalies as interpreted from the aeromagnetic data. Only positive lineaments in type V anomaly are shown.

Magnetic lineaments that were mapped using aeromagnetic data analysis; outcropping rocks and hot springs that were mapped using geological mapping; magnetic susceptibility measurements that were taken on rock samples and rivers that were mapped using Google Earth Pro and published geological maps were used to compliment or revise the geological map using the aeromagnetic data of the study area (Figure 4.12).

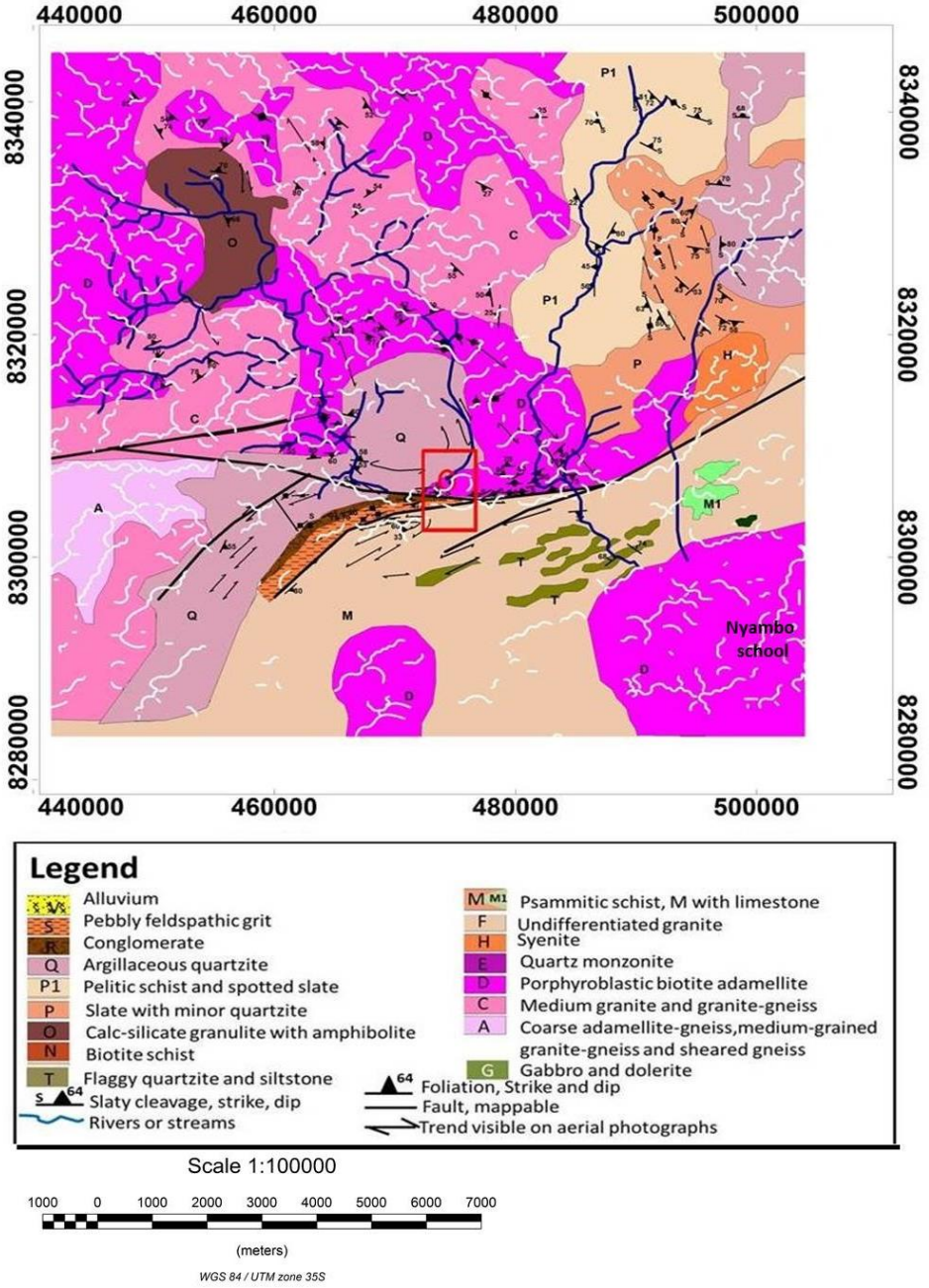

Figure 4.12. Negative magnetic lineaments (white lines) on the new geological map interpretation of aeromagnetic data, Google Earth image and geological map of the area published by Abell (1970).

4.4 Summary of Qualitative interpretation of Aeromagnetic data

Some of the inferred geological boundaries on the lithologies mapped by Abell (1970) were readjusted using the aeromagnetic data and Google Earth Pro image. Observations made in the previous section and foliation fractures were also added on the new geological map (Figure 4.13). Four main structural trends can be observed in the area as suggested by Abell (1970) and Naydenov et al. (2014). A NW-SE trend observed in the metasediments of the lower Katanga Supergroup could be associated with the Pan African orogeny. The primary structures were due to the folding of the beds during Lufilian orogeny developing slates with a NW axial plane cleavage that are steeply dipping or vertical (Abell, 1970). These rocks also show secondary E-W to ENE folds which were due to the shearing along the Mwembeshi Shear Zone and have bedding parallel to steeply dipping or vertical cleavage which follow the foliation trend in the MwZ (Naydenov et al., 2014). Abell (1970) suggested that the east-northeast trend is younger than the primary NW trend. The aeromagnetic method was able to depict two bodies (A and B) of the Hook Batholith granites (Figure 4.13b) that are overlain by recent sediments (Figure 4.13b). The two bodies also have NE and NW foliation trends with the NE foliations being longer than the NW ones. About five flaggy quartzite bodies (C) with a NE strike the same as that of the only outcrop in the area were also mapped by the aeromagnetic survey south of the Mwembeshi Shear Zone (Figure 4.13b). These could also be shallow. Another NW fault is suggested from the observed alignment of the two hot springs close to the MwZ although this could not be revealed by the aeromagnetic data. During this research a ground magnetic follow-up was carried out so as to reveal the existence of the inferred fault. The Hook granites and the basement rocks have magnetic low, lineaments that run parallel to the high magnetic anomalies and correlate well with the mapped NE, NS and NW foliation trends. An alternating positive and negative magnetic lineament running E to ENE which branches into two towards the west correlates with the mapped Mwembeshi Shear Zone (MwZ) and the cleavage trends mapped along it by Abell (1970). This anomaly separates the two metasediments of the Lufilian Arc (LA) and Zambezi Belt (ZB) to the north and to the south, respectively. The non-magnetic (green-orange) metasediments of the Lufilian Arc and the Zambezi Belt mapped by the aeromagnetic data seem to correlate quite well with those mapped on surface. Although the greater part of the Zambezi Belt is largely covered by sediments, the aeromagnetic data shows that metasediments still underlie these Katanga sediments further to the south (Figure 4.13b). The

outcropping metasedimetary rocks show less or no foliation structures which is also confirmed by few negative magnetic lineaments (Figure 4.13b).

The structures in the basement rocks and lower Katangan metasediments have N–S and NE-SW trending folds associated with sub-vertical axial-planar cleavage or dipping northeast at 30 - 40˚ respectively (Abell, 1970). The foliation on the eastern side of the massif (high magnetic anomalies) which is associated with negative magnetic lineaments shows a strong NW-SE strike. Key et al. (2001) suggested that the N-S trending folds can be associated to the Kibaran orogeny whilst Abell (1970) suggested that the NW-SE trends were due to refoliation of the basement caused during Lufilian orogeny.

The high magnetic amplitudes characterizing the granitoids can be attributed to high magnetic susceptibilities due to the high content of ferromagnetic minerals, like magnetite and pyrrhotite in the granitoids. Naydenov et al. (2014) revealed that the deformed granitoids' minerals are aligned in the shear bands and foliation planes. At the outcrop scale, it is along the strike of these foliation planes, consisting mostly of amphibolite and biotite gneiss were productive foliation fractures appear to form. The feldspar-dominant biotite gneiss is very susceptible to surface and deep weathering leading to fracture and joint systems that can transmit water into the bedrock. The fracture openings are recharged laterally from the outcrop or through vertical conduits or joint sets, further breaking up the rock.

A conjugate of weathered foliation and cleavage fractures on granitoids or metamorphic rocks and a well-developed network of steeply dipping joints can form a fracture system which can transmit water into the bedrock. This creates a deep seated permeable environment which is conducive for a geothermal reservoir. Since the study area is mostly covered by sediments the aeromagnetic method was successful in mapping these deeply buried fractures at the expense of shallow ones that could have been aliased. The metasedimetary rocks are quartz rich, making these rock types less prone to differential weathering hence less or no foliation structures.

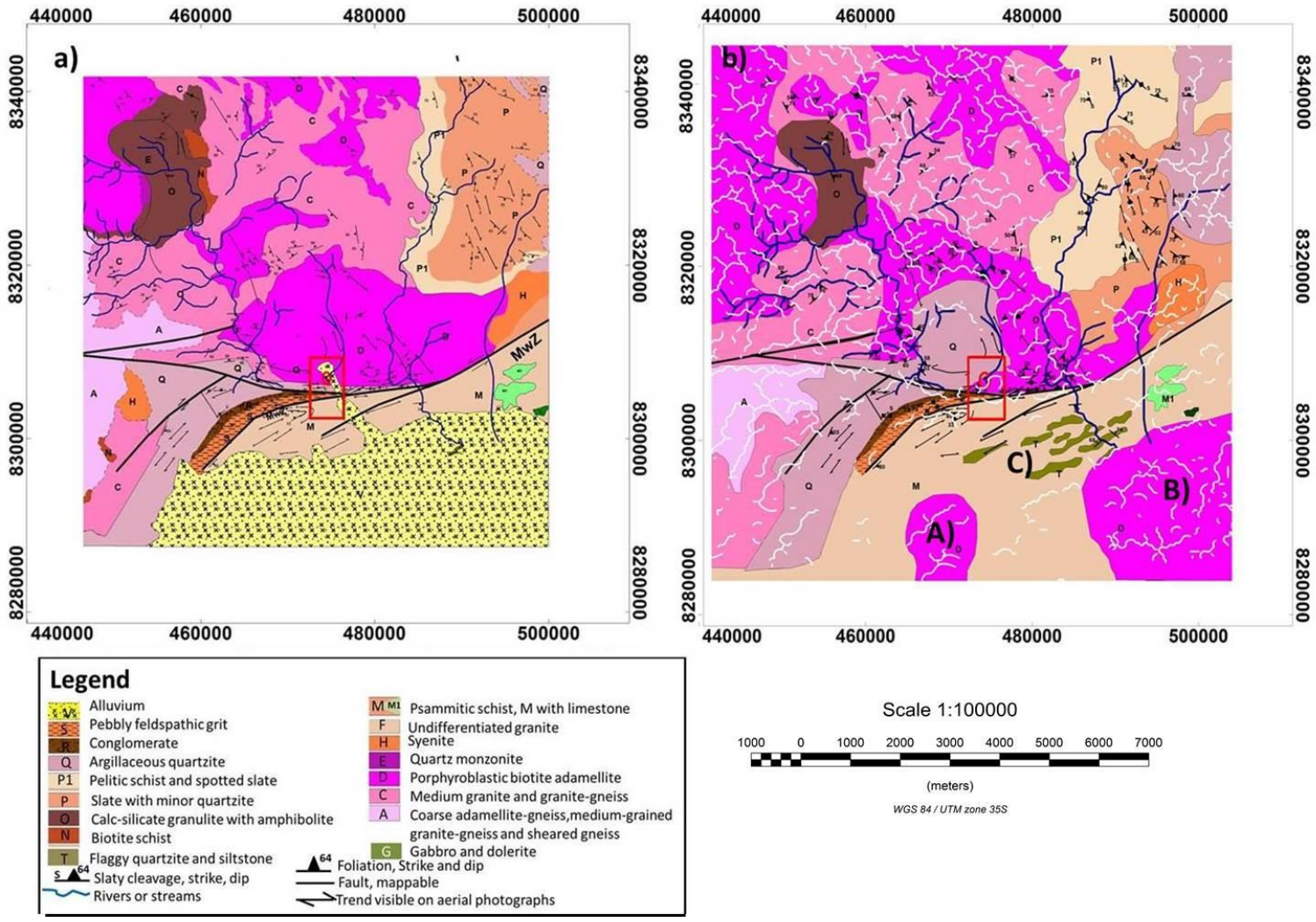

Figure 4.13. a): the old geological map by Abell (1970) and b): the new geological map as interpreted from the aeromagnetic data, Google Earth image and geological map by Abell (1970) showing the non-magnetic fractured foliations or joints.

Aeromagnetic data analysis clearly delineates the extent of the Hook Batholith granite and the Katangan metasediments due to the abundance of ferromagnetic minerals like magnetite in the basement rocks. In addition to that they also aid in mapping foliated fractures and joints due to the alignment of biotite minerals along the foliation trend. The revised geological map from aeromagnetic data does not include recent sediments like the alluvium filling the valley since they are not magnetic.

In order to efficiently interpret magnetic data for lithological and structural mapping, we need to solve the effect of source ambiguity, aliasing of small anomalies and anomaly superposition. To limit this problem, it is important to understand the regional stratigraphic evolution (Figure 2.2), understand the magnetic properties of the surrounding rocks, carry out a ground magnetic survey and analyse the data and investigate the correlation of aeromagnetic anomalies with other geophysical methods anomalies. For this study, natural source audio magnetotelluric method was used to map the subsurface and ground magnetic data to limit the problem of aliasing. The following section correlates the aeromagnetic data and the magnetic susceptibilities measured on outcropping rocks.

4.5 Magnetic susceptibility

4.5.1 Data collection

In this study, magnetic susceptibility of rock samples was measured to characterise the rock units and associated intrusions in the study area that may be responsible for the observed magnetic anomalies. Since most of the study area is covered by alluvium deposits only a few outcrops could be accessed in the Kwako and Chalobeti Hills which lie south of the grid.

Magnetic susceptibility measurements were recorded on 36 samples (12 rock types with 3 samples per rock) using a SM 30 handheld magnetic susceptibility meter, accurate to $1X10^{-7}$SI units (Table 4.1). Three measurements were taken on each sample to check for repeatability and the average was recorded. Measurements were carried out on, flat, broad and fresh surfaces of the sample and in a magnetic noise free environment.

A Garmin Etrex 10 handheld Global Positioning System (GPS) was used for recording station co-ordinates, The Universal Transverse Mercator projection (UTM) grid system zone 35S for Zambia and WGS 1984 datum were used. The description of the lithologies encountered at each outcrop and their associated magnetic susceptibility were recorded in a

notebook. To aid understanding the causes of the magnetic intensity anomalies and outstanding magnetic susceptibility values, the magnetic susceptibility data was integrated with the aeromagnetic and geological mapping data (Figure 3.14).

4.5.2 Results and discussion

The lithologies measured have a range of magnetic susceptibilities, which is a common trend (Telford et al., 1990). The medium grained granitic gneiss of the basement complex has the highest mean magnetic susceptibility value of (4.330 ± 0.183) x 10^{-3} SI units (Table 4.1). Schist rock samples from the Kwako Hills also have outstanding high magnetic susceptibility values with an average of (2.490 ± 0.092) x 10^{-3} SI units (Table 4.1). Granitic gneiss with quartzite inclusions has mean magnetic susceptibility value of (0.5131 ± 0.007) x 10^{-3} SI units. The sample was picked up from an outcrop that lies close to the contact of the granitic gneiss and quartzite lithologies. Thus the inclusion of quartzite which has low magnetic susceptibility values will consequently reduce the resultant measured magnetic susceptibility values on the sample. The felsic-rich porphyroblastic biotite adamellite of late or post Katanga age has an average magnetic susceptibility value of (0.465 ± 0.067) x 10^{-3} SI units. The low magnetic susceptibility values can be associated with the absence of magnetite in rock samples.

Table 4.1. Magnetic susceptibility measurements of the collected samples.

Lithology		**Magnetic susceptibility x 10^{-3} SI**				
Sample number		**1**	**2**	**3**	**Average**	**Std Dev**
Quartzite	OC2	-0.060	-0.070	-0.051	-0.060	0.010
Feldspathic metarinite	OC3	0.540	0.589	0.592	0.574	0.029
Granitic gneiss with quartzite inclusions	OC4	0.54	0.43	0.57	0.513	0.007
Granitic gneiss	OC5	4.530	4.170	4.290	4.330	0.183
Porphyroblastic biotite adamellite	OC6	0.392	0.524	0.479	0.465	0.067
Syenite	OC7	-0.060	-0.06	-0.012	-0.044	0.028
Granite	OC8	0.101	0.108	0.109	0.106	0.004
Feldspathic grit	OC9	0.057	0.063	0.051	0.057	0.006
Schist	OC10	2.470	2.470	2.310	2.490	0.092
Quartzite	OC11	-0.030	-0.013	-0.010	-0.0176	0.011
Quartzite	OC12	-0.008	-0.007	-0.009	-0.008	0.001
Feldspathic grit	OC13	0.050	0.038	0.042	0.0433	0.006

Quartzite and felspathic grit samples have mean magnetic susceptibility values of -0.060 ± 0.010) x 10^{-3} SI units and (0.057 ± 0.060) x 10^{-3} SI units respectively. These are metasediments of the Lower Kundelungu series of Katanga age and the low magnetic susceptibilities could have arisen from regional high grade metarmophism of rocks of sedimentary origin due to shearing and faulting along the Mwembeshi Shear Zone. Lowest magnetic susceptibilities are also observed to occur around the granite intrusions as contact aureoles.

Rock units with highest magnetic susceptibilities belong to the Hook Batholith (granites, gneiss and biotite adamellite). These can be attributed to the presence of ferromagnetic minerals, strong alignment of biotite grains and low silica content (Naydenov et al., 2014). Higher grade metamorphism of an igneous origin (gneiss and schist) around the Hook Batholith intrusion can be the cause of higher magnetic susceptibility values while the lower values can be associated with low-grade metamorphism of sedimentary origin (quartzite).

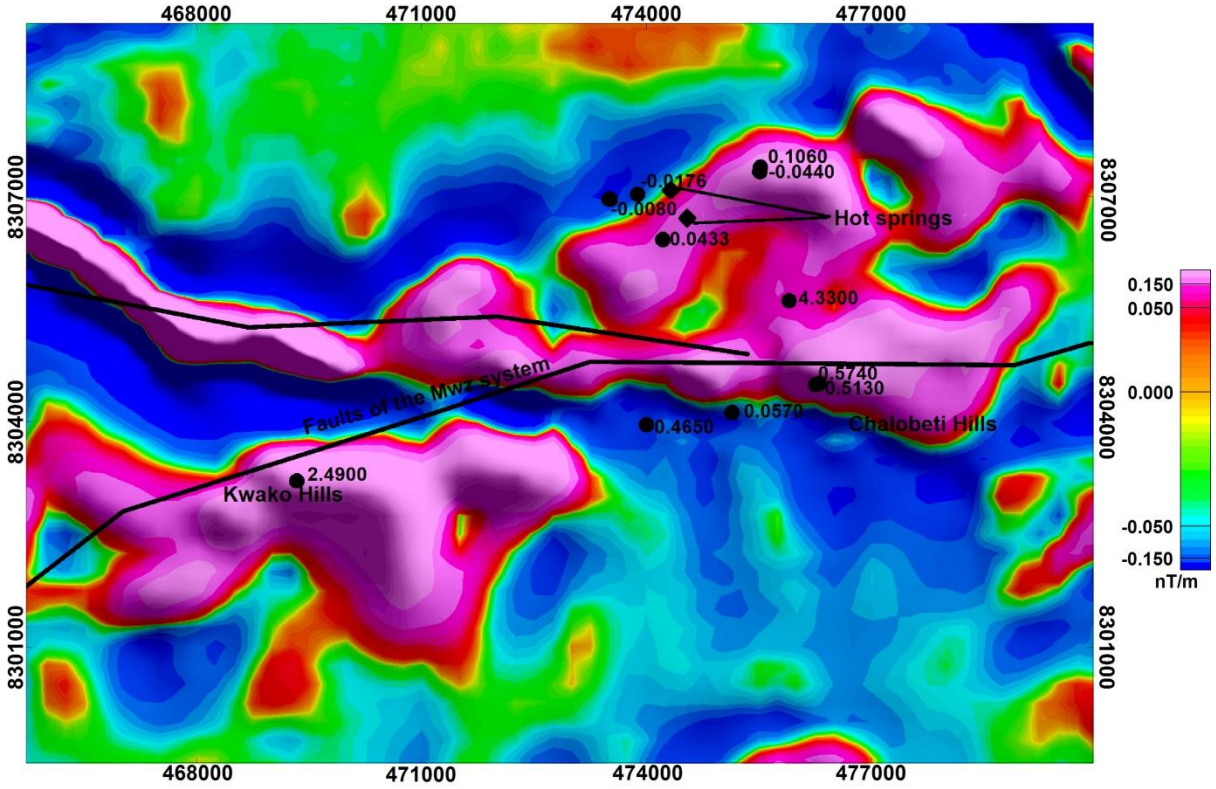

Figure 4.14. Location of magnetic susceptibility measurements overlaid on the colour shaded first vertical derivative image of the aeromagnetic data of the study area.

In general, the metasedimentary units have the lowest magnetic susceptibility values due to felsic minerals and high grade metamorphism of rocks of sedimentary origin along the Mwembeshi Shear Zone. The igneous and metamorphic lithologies have the highest magnetic susceptibilities due to ferromagnetic minerals and high grade metarmophism of rocks of igneous origin along the Mwembeshi Shear Zone. The measured magnetic susceptibility measurements correlate with the anomalies on the first vertical derivative map (Figure 4.14). The granitic gneiss of the Hook Batholith and schist lithologies are responsible for the high (red) magnetic field anomalies whilst the quartzite and felspathic grit are responsible for the lowest (blue) magnetic anomalies which stand out on Figure 4.14.

4.6 Ground Magnetic Survey

4.6.1 Application of Ground magnetic

In geothermal energy exploration, magnetic methods are widely used for mapping geological structures. The most important applications are for mapping faults, dykes, intrusives and locating hydrothermally-altered areas. It has many field applications including but not limited to mining, geological and faults mapping and detection of buried magnetic materials.

4.6.2 Methodology- Data collection

A Geometrics 856 Proton precession magnetometer (Figure 4.15) was used to collect ground magnetic data. It measures the Earth's total magnetic field intensity to an accuracy of 0.1 nT. Geometrics 856 proton precession magnetometer is made up of a console or receiver that is connected to magnetic coils mounted on the pole for measurement.

Ground magnetic data were collected perpendicular to the strike of the faults associated with the Mwembeshi Shear Zone (Figures 4.16). Nine 6 km lines with a spacing of 500 m were surveyed in a north-south direction across the two hot springs which are located along a a suspected fault (Figure 4.17). Two lines 2.8 km long were also traversed as in fills around the hot springs. Three tie lines were traversed perpendicular to the survey lines' direction. Magnetic readings were taken at 20 m station spacing along north-south traverses, whilst the base station readings were taken at every thirty seconds for diurnal correction (see section 4.3.2).



Figure 4.15. G-856 proton precession magnetometer used to take magnetic measurements.

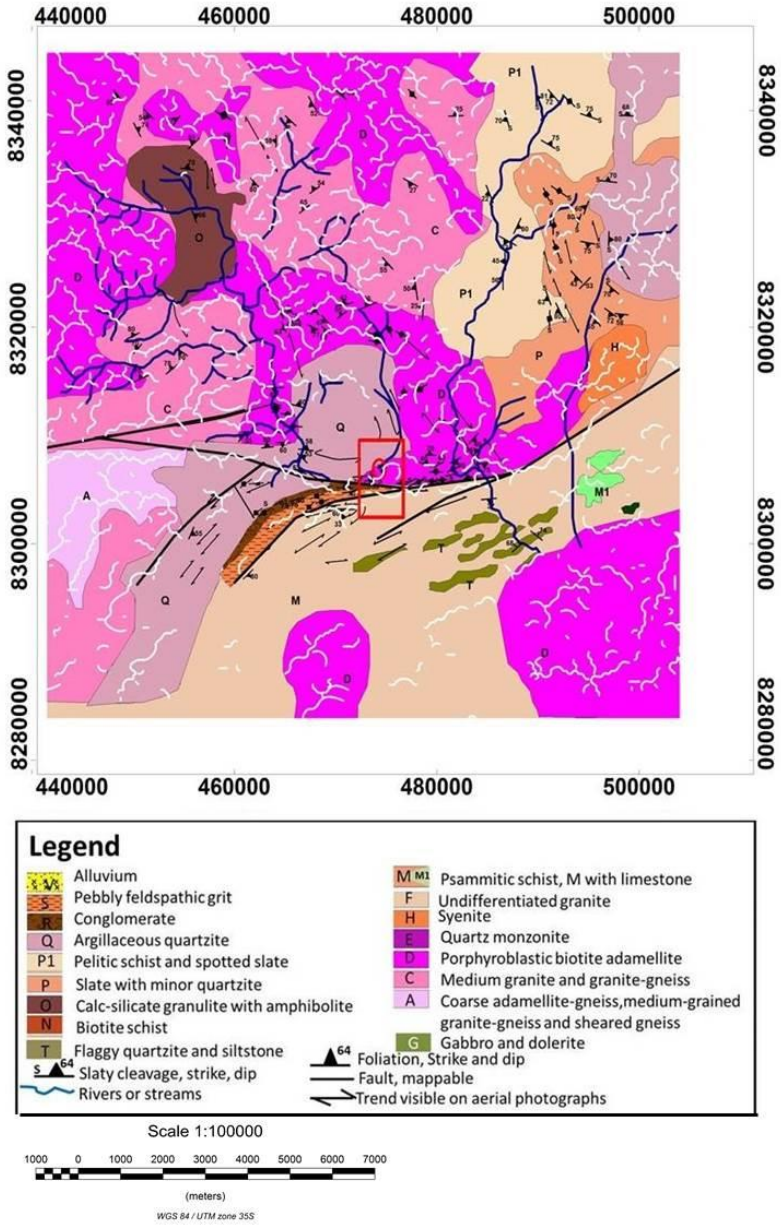

Figure 4.16. Ground magnetic grid (red box) overlain on the geological map with linear negative magnetic lineaments (white lines) interpreted from aeromagnetic data, Google Earth and geological map of the area and showing the area covering the two hot springs (red circle) .

4.6.3 Magnetic data processing

Magnetic data quality control

Data were viewed systematically in graphical profile form to eliminate spurious noise and spikes (Figure 4.17). This was carried out in Microsoft excel by adding 1000 nT to each line and then draw all the data from each line on top of each other so as to examine them.

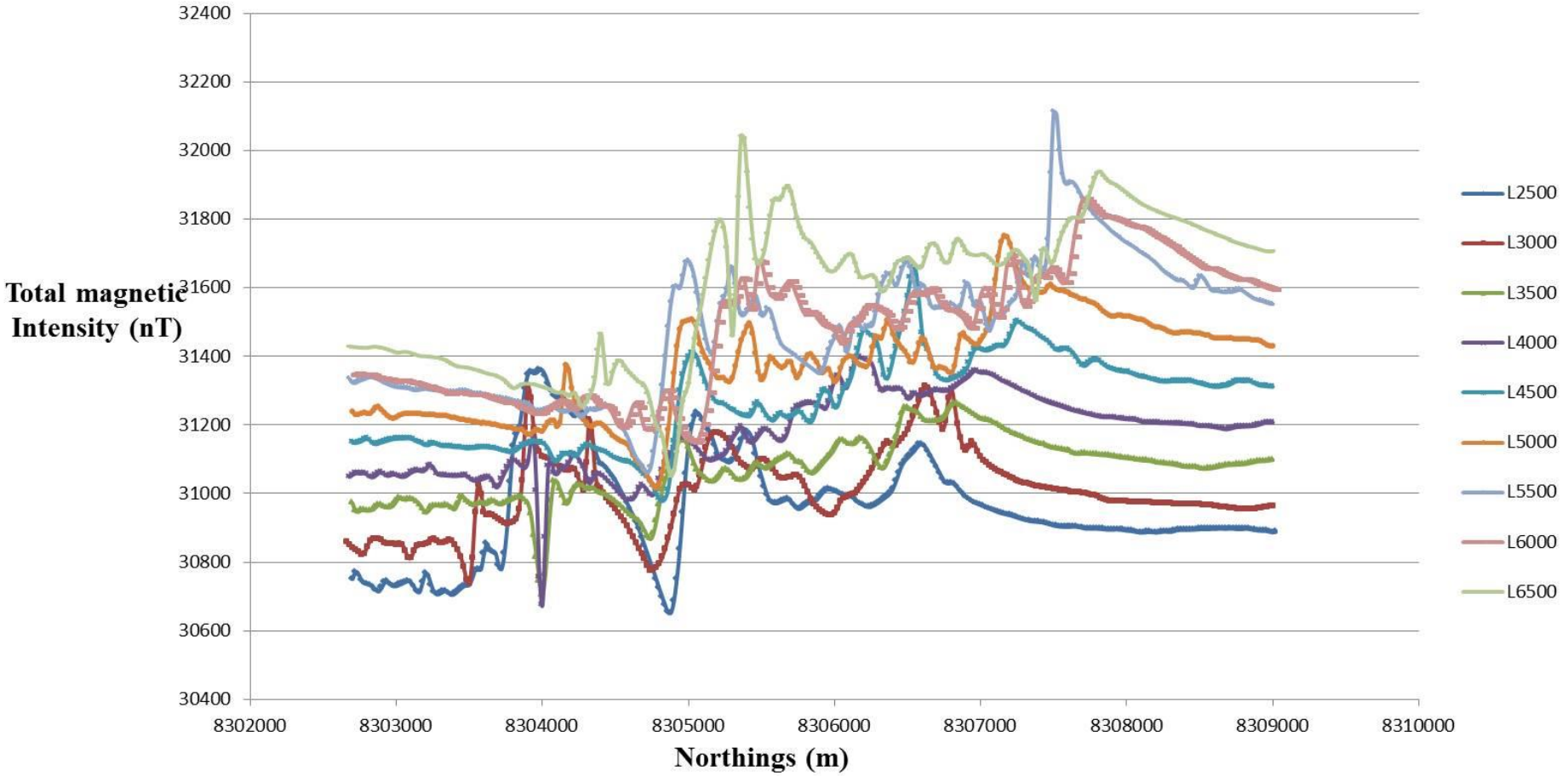

Figure 4.17. Profiles of ground magnetic data obtained from the traversed lines L2500, L3000, L3500, L4000, L4500, L5000, L5500, L6000 and L6500

Diurnal variation correction

Diurnal variations of the Earth's magnetic field due to the rotation of the Earth with respect to the solar wind causing time varying field that is recorded at a base station and then removed using a common technique called diurnal correction. These diurnal variations of the Earth's magnetic field are short term variations of the interaction of the solar wind and the magnetosphere that follow a daily cycle. These are due to the Earth's rotation and its orbital movement around the Sun and the orbital motion of the Moon around the Earth.

Base station magnetic measurements were taken at 30 s intervals at a fixed location in the survey area for the duration of the survey (Figure 4.18). The diurnal variations were computed by determining the difference between the time-synchronised measured base station readings and survey data. This technique assumes that the temporal variation of the main field at the field station and at the base station is the same. The procedure was carried out using Geometrics MagMap 2000 version 4.90 software.

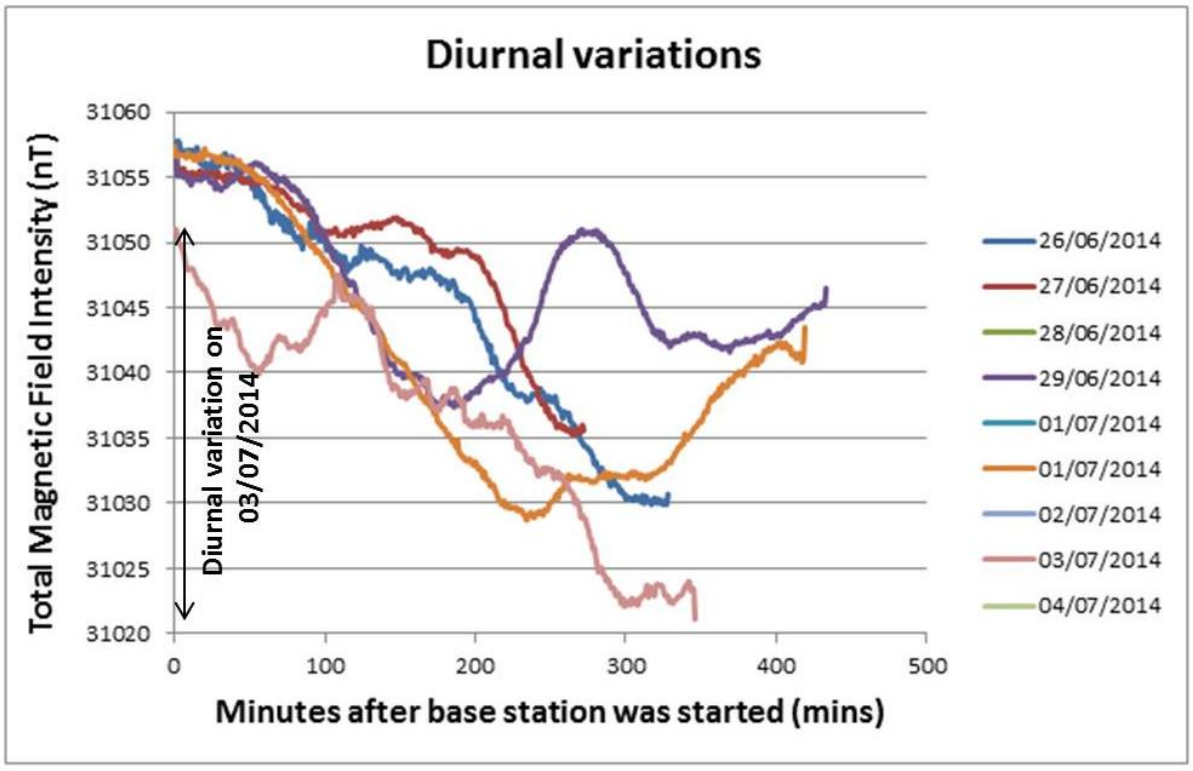

Figure 4.18. Base station data for different days.

If the maximum diurnal variation is greater than 100 nT, it could be due to a magnetic storm and that survey must be repeated. During the course of this survey, the maximum diurnal variation was about 35 nT.

4.6.4 Data visulisation (qualitative interpretation)

2D Profiling

For visualisation and further processing the corrected data were viewed as 2D profile stacks called fence plots. The TMI data for the nine profiles were plotted against the station spacing as shown in the 2D profiles in section 4.63 (Figure 4.17).

Further enhancements were carried out on the obtained magnetic data, using various filtering techniques (discussed below) so as to aid with interpretation.

The magnetic data images were all colour shaded to create a 3-dimensional effect or view using 2-dimensional rendering.

Gridding

The total magnetic field data were gridded using Geosoft Oasis Montaj's minimum curvature gridding algorithm using 150 m grid cell size based on Reid's criteria and a desampling factor of 2 (Figure 4.19). Desampling is a filtering technique that removes errors caused by taking too many readings along a line as compared to the line spacing. This method uses the algorithm of Swain (1976) to fit the smoothest (minimum) possible 2D surface (curvature) to a given set of xyz data points.

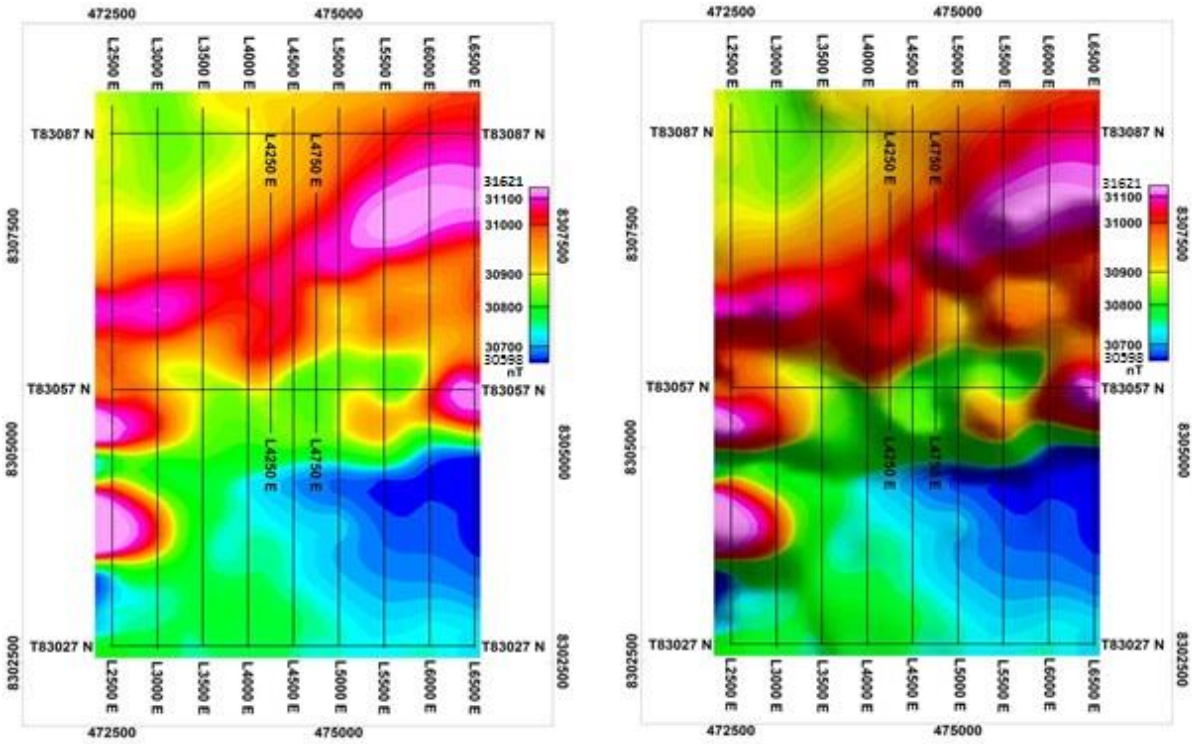

Figure 4.19. a) Total Magnetic Intensity grid using Oasis Montaj's minimum curvature gridding algorithm at 150 m grid cell size and a desampling factor of 2 and b) sunshaded grid of the surveyed area showing the north-south traverse lines and east-west tie lines.

Geomagnetic Reference Field removal

Since we measure the sum of the magnetic field due to regional and local fields and we are only interested in the magnetic field caused by the geology of the upper crust (local field), we need to remove the influence of the Earth's main field (Blakely et al., 2005). This was achieved by subtracting a model of the main field from the survey data. The International Geomagnetic Reference Field (IGRF) was calculated producing the field strength, inclination and declination from given longitude and latitude values of the area (Table 4.2). The IGRF corrected data were gridded in Geosoft using the same gridding algorithm and parameters discussed above (Figure 4.20)

Table 4.2. IGRF results for Mumbwa. Based upon (12th Generation IGRF Results, 2014), with the permission of the British Geological Survey. Location (-14°, 27°).

Component	Field Value	Secular Variation
Declination	-4.207 degrees	3.4 arcmin/year
Inclination	-52.162 degrees	3.0 arcmin/year
Horizontal Intensity	19129 nT	5.8 nT/year
North Component	19077 nT	7.2 nT/year
East Component	-1403 nT	18.4 nT/year
Vertical Intensity	-24627 nT	36.4 nT/year
Total Intensity	31184 nT	-25.1 nT/year

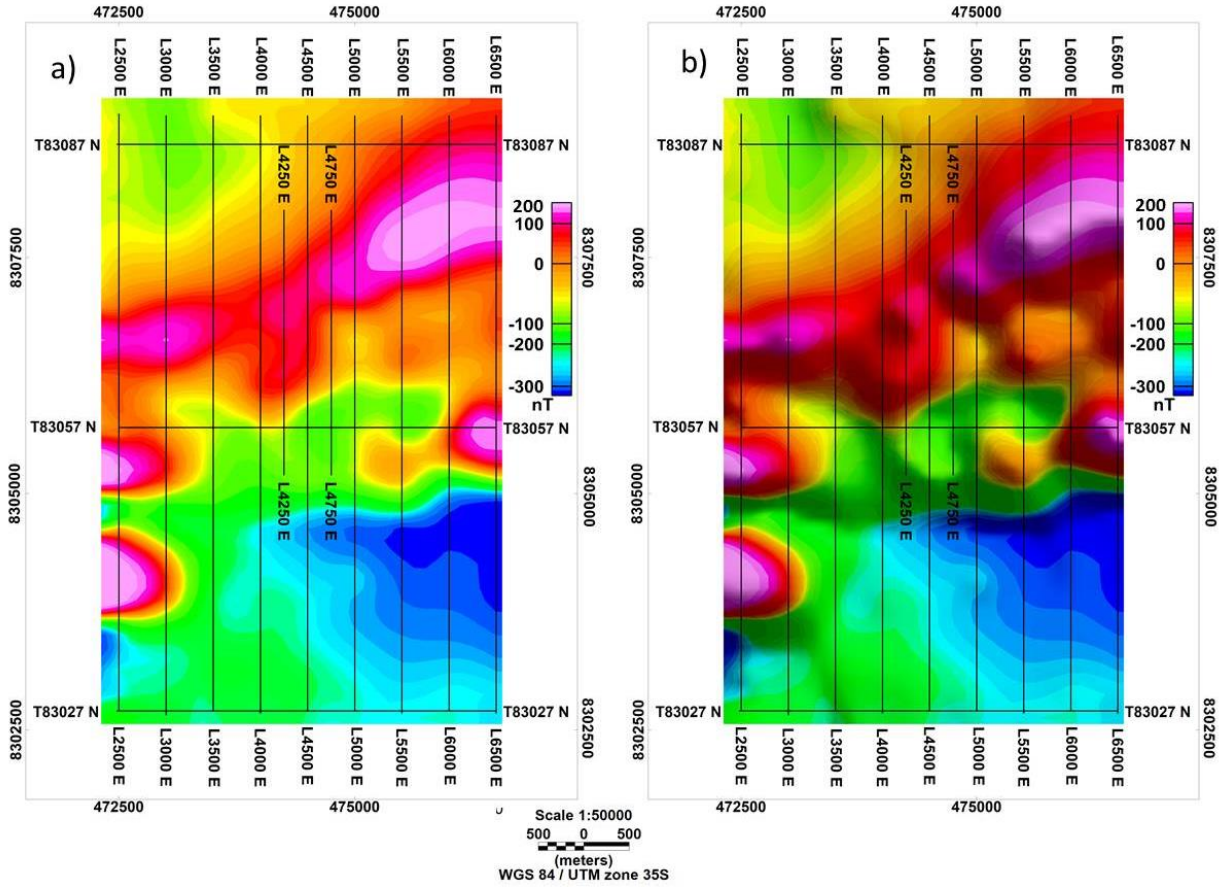

Figure 4.20a) IGRF and b) sunshaded corrected TMI data after removal of the regional field showing the north-south traverse lines and east-west tie lines. 45° inclination and declination angles were used for sunshading.

Moving from south to north, it can be observed that the lines cut across three magnetic anomalies which reveal three different magnetic sources. A very low magnetic anomaly (blue colour) characterised by magnetic amplitude less than -200 nT. This anomaly seems to be striking EW and covers the eastern half of the southern part of the grid. It has a very broad wavelength which depicts deep causative body. Another NE striking magnetic anomaly is observed in the middle of the grid coloured red to magenta. It is characterised by the highest magnetic amplitudes that are greater than 50 nT. It has narrow wavelength which can be attributed to a shallow source. This NE striking anomaly is bounded to its north and south by another magnetic anomaly characterized by magnetic amplitudes ranging from -200 to 0 nT.

Reduction to the Pole (RTP)

This filter was defined and discussed in Chapter 3. It was then applied to the TMI data and the resultant responses of the grid processed with and without RTP were then compared (Figure 4.21a). Parameters used to compute the RTP were taken from Table 4.2.

The Total Magnetic Intensity map shows anomalies that are asymmetric (1) (Figure 4.21a), while in the RTP map the anomalies have a more symmetric nature (Figure 4.21b). A change in the wavelength of the anomalies can be observed from the difference in the anomalies labelled as 2 in both diagrams.

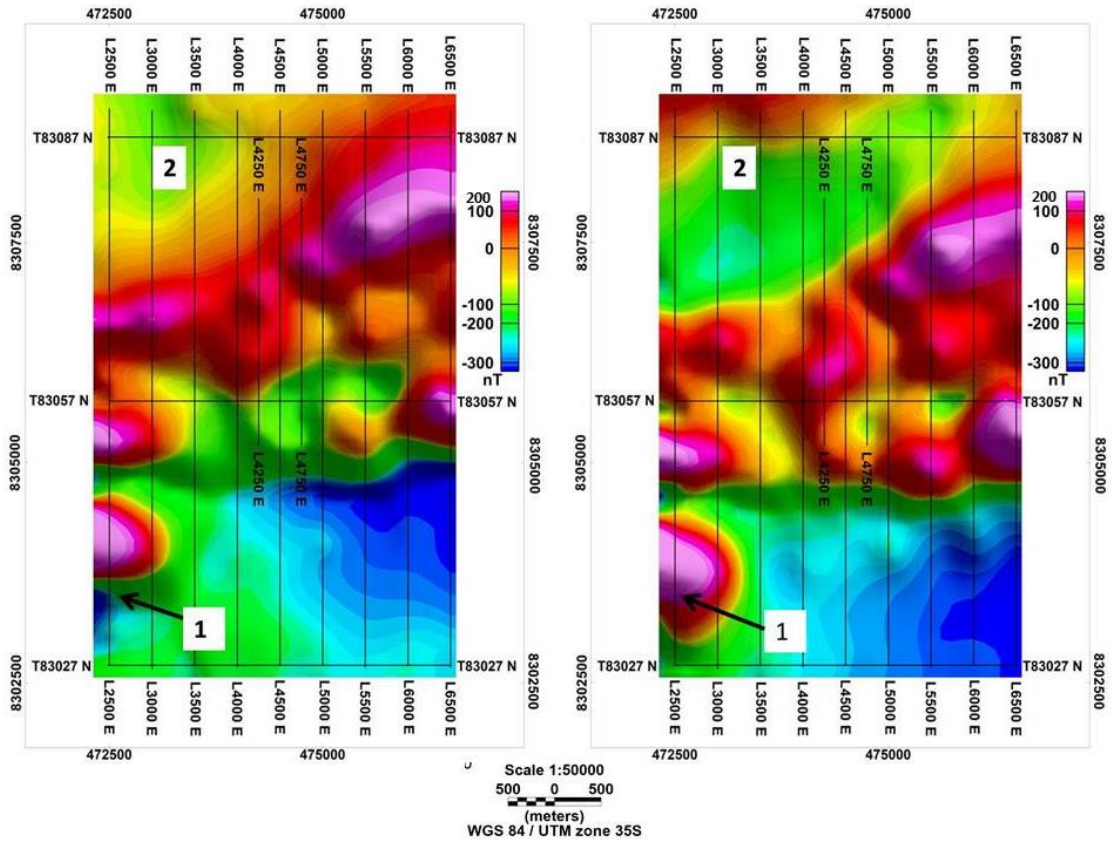

Figure 4.21. IGRF corrected ground magnetic data of the area of study. a) is the Total Magnetic Intensity (TMI) image and b) is the image after the data were Reduced To Pole. The anomalies labelled with 1 show the transformation from asymmetric anomalies to symmetric anomalies while the anomalies associated labelled with 2 shows a change from a narrow anomaly to a wide anomaly after application of RTP operator.

Analytical Signal

For this project analytic signal was used as an edge detection tool, to reveal anomalous texture and highlight discontinuities of the major structures in the study area (Figure 4.22). This was performed using Geosoft Oasis Montaj.

The analytical signal produces a sharper response over body edges and at the same time it is more sensitive to noise because it uses derivatives.

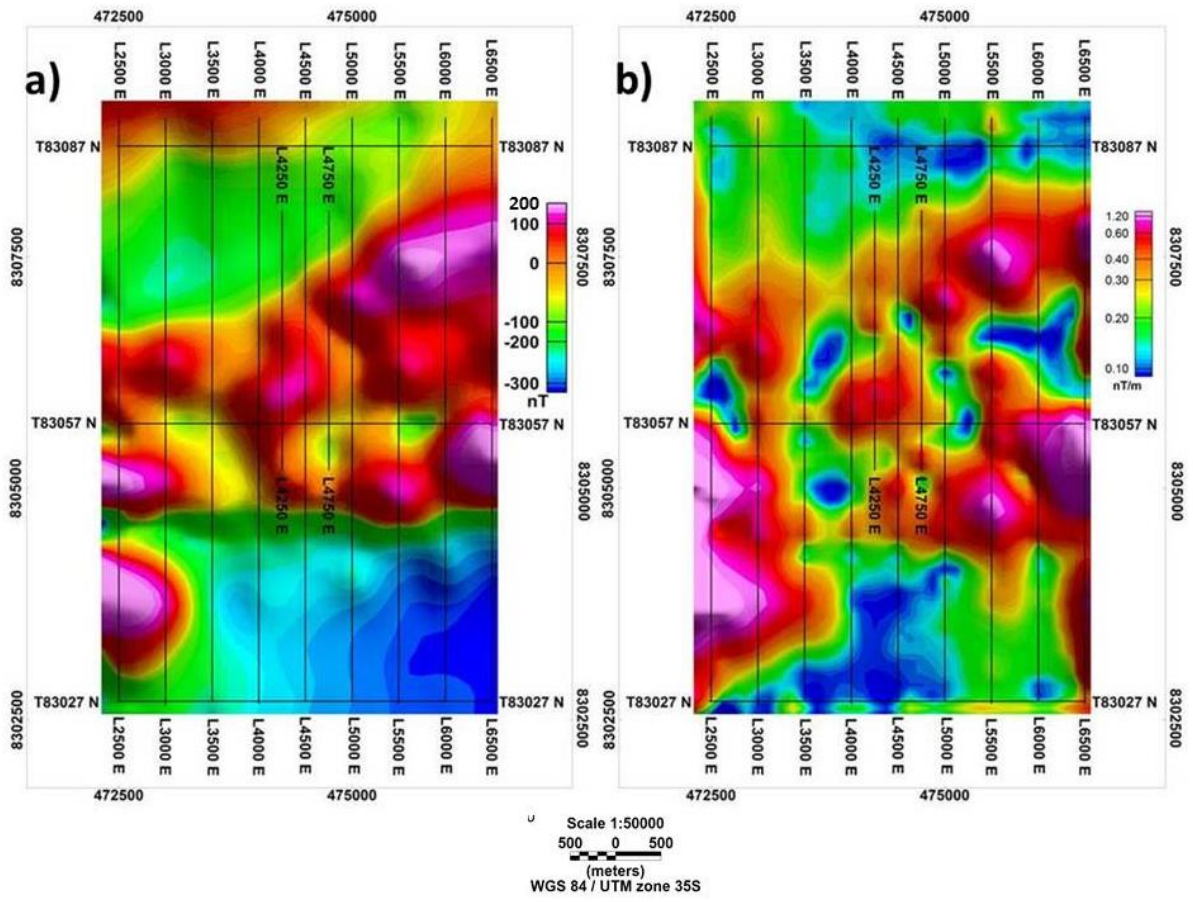

Figure 4.22. IGRF corrected ground magnetic data of the area of study. a) is the Reduced To Pole Total Magnetic Intensity (TMI) image and b) is the image after analytic signal filter was applied to the data.

Interpretations of the analytical signal map shows that there are three different major colour units which are attributed to three different causative basement sources. The analytic signal nicely enhanced the boundaries between these anomalies and also enhanced some small anomalies (blue) that were suppressed inside wide lithological units (Figure 4.22). These small anomalies characterized by low amplitudes can be attributed to discontinuities (foliation fractures) in the granitoids.

Vertical derivative

To enhance anomalies due to shallow sources (high frequences), the vertical derivative of the IGRF corrected TMI data was perfomed using Geosoft Oasis software (Figure 4.23). The first vertical derivative map (Figure 4.23b) shows magnetic anomalies due to shallow sources.

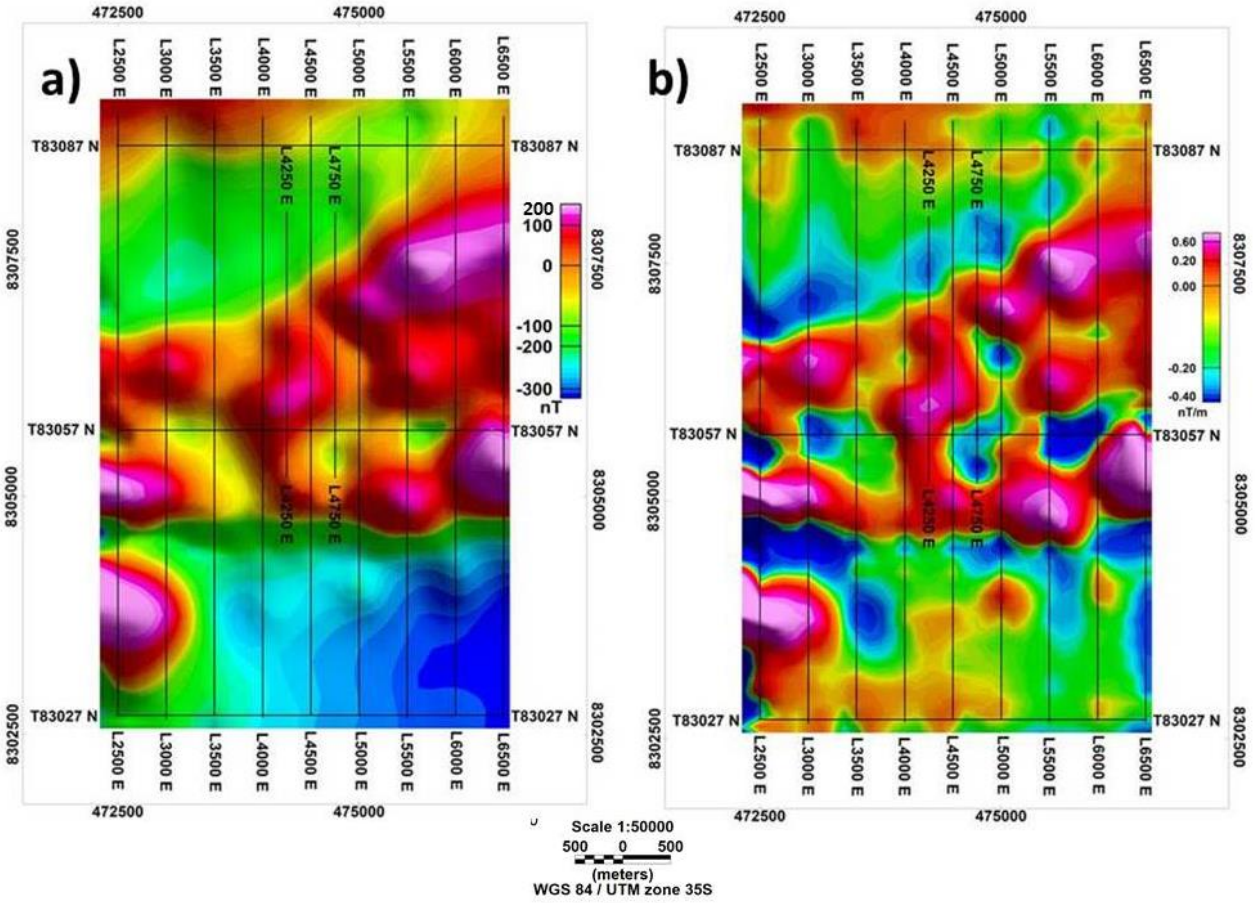

Figure 4.23. Ground magnetic data of the study area. a) is Reduction To Pole (RTP) filtered data. b) First vertical derivative filtered data. First vertical derivative filter (1VD) enhances noise compared to RTP data.

The first vertical derivative shows that the NE striking high magnetic anomaly in the TMI image (Figure 4.23b) is characterised by highest magnetic gradients greater than 0.20 nT/m. It is also observed to have a high frequency high magnetic gradient lineament bounded by very low magnetic gradient lineaments to its north and south. These very low magnetic gradient lineaments are also observed inside the high magnetic anomaly and are characterised by magnetic gradient values that are less than -0.20 nT/m. High magnetic gradient and high frequencies means that the causative bodies are very shallow.

4.6.5 Ground magnetic data interpretation

For better interpretation the RTP and1VD grids were overlain on top of the new geological map that was interpreted from aeromagnetic data, geological map by Abell (1970) and the Google Earth image (Figure 4.24 and 4.25) respectively.

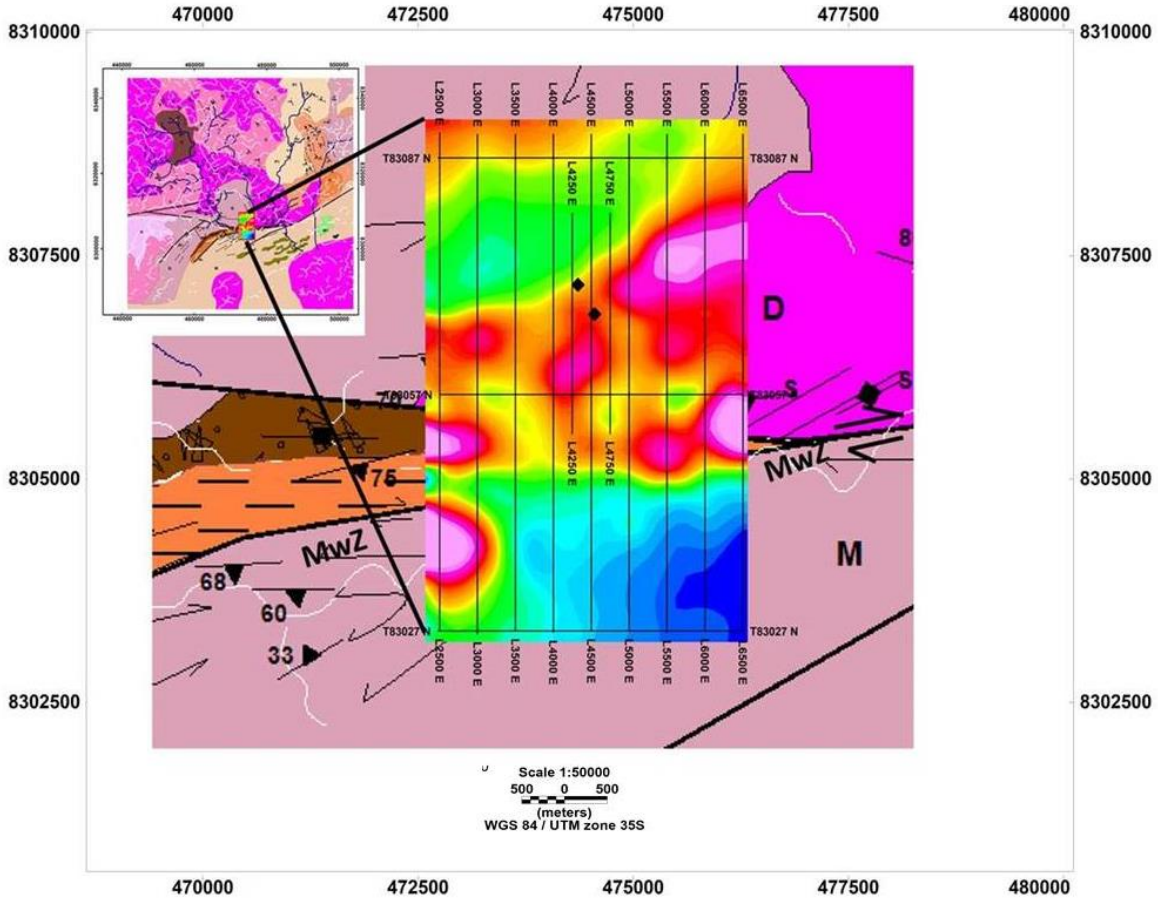

Figure 4.24. Reduce to pole (RTP) Total Magnetic Intensity (TMI) grid overlain on the new geological map of the study area that was interpreted from the aeromagnetic data, the geological map by Abell (1970) and the Google Earth image. The high amplitude anomaly corresponds well with the Hook Batholith rocks and is bounded by "quiet" low amplitude, low-frequency anomalies corresponding to the metasedimentary rocks of the Lufilian Arc and the Zambezi Belt in the north and south respectively. Refer to Figure 3.8 for legend to the geology and Figure 4.9a for legend to the RTP TMI image

The magnetic anomalies' boundaries correspond well with the geological boundaries and hence the high magnetic amplitude can be attributed to the Hook Batholith rocks whilst the low magnetic amplitude can be attributed to the metasedimentary rocks of the Lufilian Arc and Zambezi Belt.

Different results from different enhancement methods were used to map different targets e.g. the first vertical derivative enhanced the shallow features whilst the analytic signal enhanced lithological contacts (Figure 4.25).

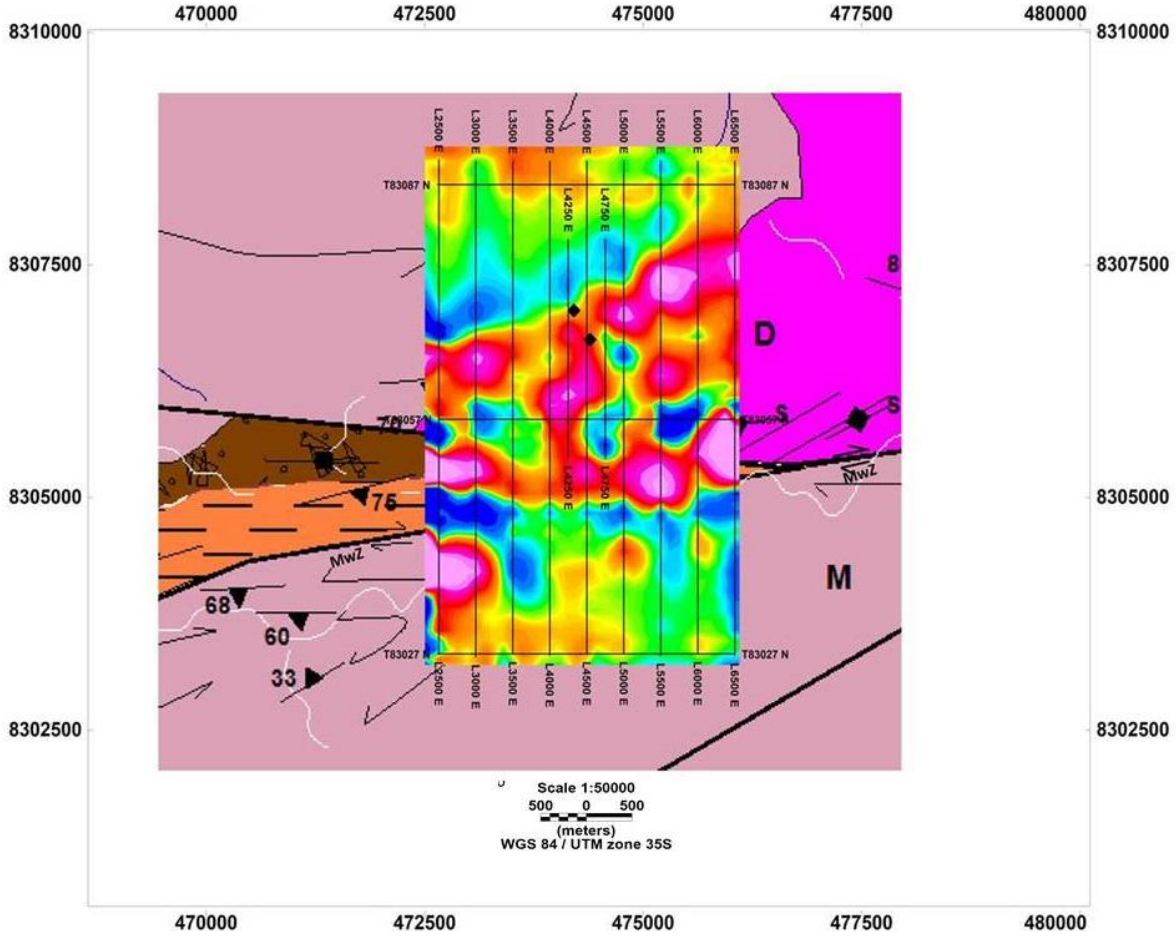

Figure 4.25. Reduce to pole (RTP) first vertical derivative (1-VD) filtered total magnetic intensity (TMI) image of the study area overlain on the new geological map of the study area that was interpreted from the aeromagnetic data, the geological map by Abell (1970) and the Google Earth image. The high amplitude gradient corresponds well with the Hook Batholith rocks and is bounded by "quiet" low gradient, low-frequency anomalies corresponding to the metasedimentary rocks of the Lufilian Arc and the Zambezi Belt in the north and south respectively. Refer to Figure 3.9a for legend to the geology and Figure 4.9b for legend to the first vertical derivative image.

The first vertical derivative enhanced shallow, magnetic low, lineaments that are parallel and inside the high magnetic anomalies (Figure 4.25). These low magnetic anomalies have high frequencies and can be attributed to the aligned micaceous minerals along the foliated fractures as suggested previously. Magnetic low, lineaments are also following the strike of the Mwembeshi Shear Zone faults. Another magnetic low lineament is observed in the north along the boundary between the high magnetic signature and the low magnetic signature (Figure 4.25). In order to determine whether there are any fractures or joints associated with the two hot springs, the 250 m line spaced data set was gridded on its own using minimum curvature gridding with grid cell size of 63 m and desampling factor of 2 (Figure 4.26). The grid cell sizes where chosen according to Reid's criteria using the line spacing of 500 m and 250 m. A first vertical derivative filter was also applied on this small grid and overlain on the above image (Figure 4.26).

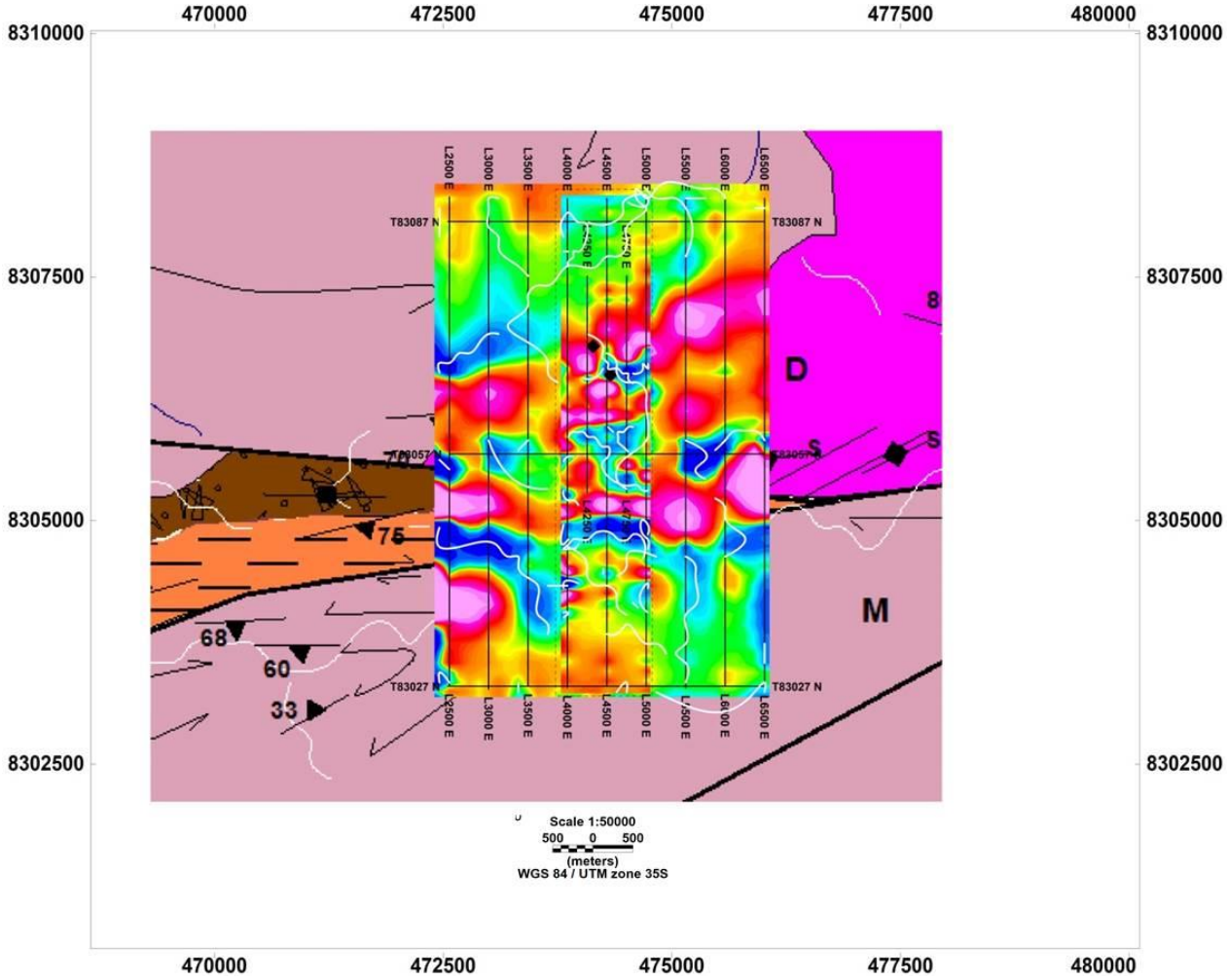

Figure 4.26. Reduce to pole (RTP) first vertical derivative (1-VD) filtered total magnetic intensity (TMI) image of the study area overlain on the new geological map of the study area that was interpreted from the aeromagnetic data, the geological map by Abell (1970) and the Google Earth image. The small grid is the gridded 250 m line spaced data. The high amplitude anomaly corresponds well with the Hook Batholith rocks and is bounded by "quiet" low amplitude, low-frequency anomalies corresponding to the metasedimentary rocks of the Lufilian Arc and the Zambezi Belt in the north and south respectively. The black diamonds represent the hot springs. Refer to Figure 3.9a for legend to the geology and Figure 4.9b for legend to the first vertical derivative image.

The grid for the 250 m line spaced data enhanced more magnetic low, lineaments. It also enhanced a NW magnetic low, lineament on which the two hot springs lie (Figure 4.26). This corresponds well with the suggested fault giving rise to the trend of the hot springs.

The phase symmetry algorithm that was developed by Kovesi (1997) was used to automatically detect, vectorise and effectively map the shallow magnetic negative lineaments that were enhanced by the first vertical derivative filter and the smaller line spacing. A smallest filter wavelength of 500 m, and 4 filter scales were used to detect negative magnetic lineaments orientated in all angles (Figure 4.27). These are attributed to the alignment of the micaceous minerals in the gneissic rocks. The negative lineaments correspond to the foliation trends, which also map the foliation fractures and joints that could have been zones of weakness where rivers and streams follow.

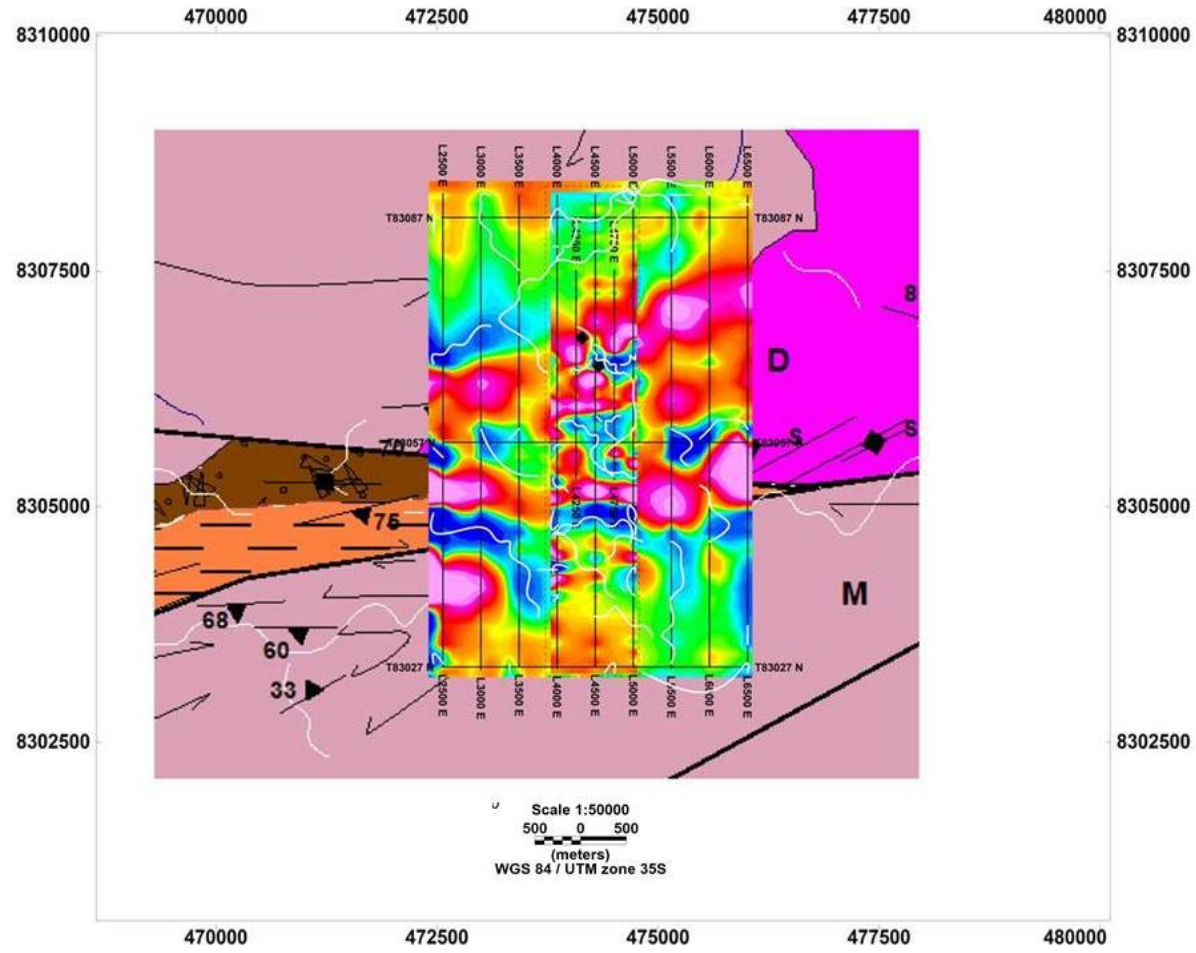

Figure 4.27. Reduce to pole (RTP) first vertical derivative (1-VD) filtered total magnetic intensity (TMI) image of the study area overlain on the new geological map of the study area that was interpreted from the aeromagnetic data, the geological map by Abell (1970) and the Google Earth image. The small grid is the gridded 250 m line spaced data. The white lines represent the negative magnetic lineaments. Refer to previous Figure for legends.

The ground magnetic survey with smaller line spacing enhanced more negative magnetic lineaments which are attributed to shallow foliation fractures (Figure 4.28). These were not mapped by the aeromagnetic survey.

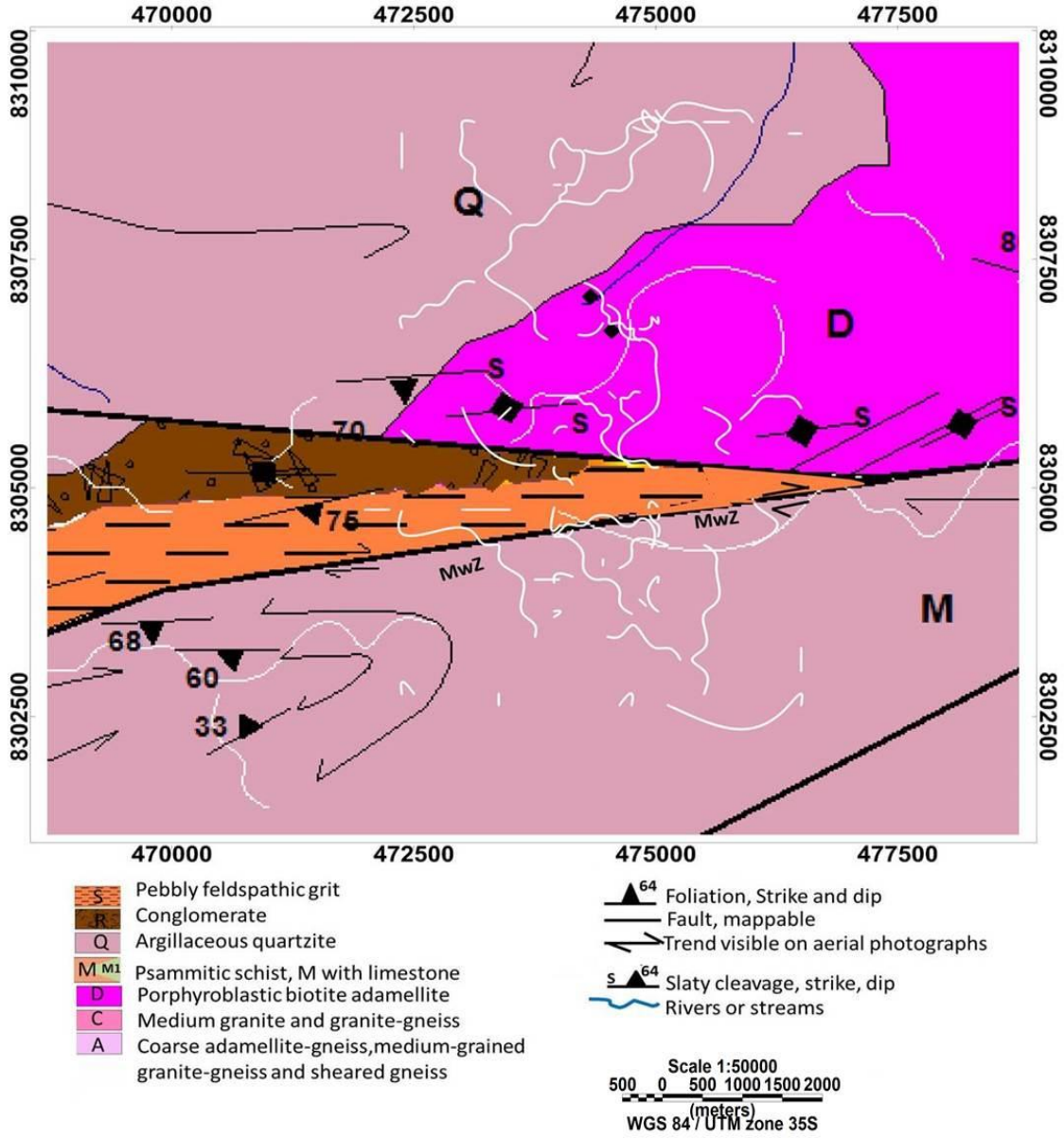

Figure 4.28. Old and new negative magnetic lineaments (white lines) on the new geological map interpreted from aeromagnetic data, Google Earth image and geological map of the area published by Abell (1970). The new negative magnetic lineaments were enhanced by smaller line spacing.

4.6.6 Summary

The current information shows that the area is highly faulted and sheared due to the Mwembeshi Shear Zone. This created a lot of fractures that have almost the same NE trending as the faults of the Mwembeshi Shear Zone (Figure 4.28). Also pre-Katanga and Lufilian aged tectono-thermal events resulted in foliation fractures trending NE, NW and NS. Permeability due to faulting and fracturing plus abundant water as evidenced by rivers in the area and the hot springs make the area conducive for a geothermal energy resource. In the following section, magnetic modelling of the ground magnetic data was carried out to produce a preliminary geological model.

4.7 Magnetic modelling

Forward modelling involves creating a possible geological model and calculating the expected geophysical response from that geological model. The methods of Talwani et al. (1959), and Talwani and Heirtzler (1964) which are based on the algorithms described in Won and Bevis (1987) are used to calculate the potential field response.

4.7.1 Euler deconvolution

For effective interpretation, 3D Euler deconvolution was applied on the Total Magnetic Intensity grid data using standard Geosoft Oasis Montaj's Euler deconvolution. This was done to produce apparent depths to lithology contacts on the grid. Better clustering depths were achieved using a structural index (SI) of 1 and 0, solution window size of 4 and 10% depth tolerance. The depth solutions for structural index 1 were plotted on the colour shaded analytical signal map respectively (Figure 4.29).

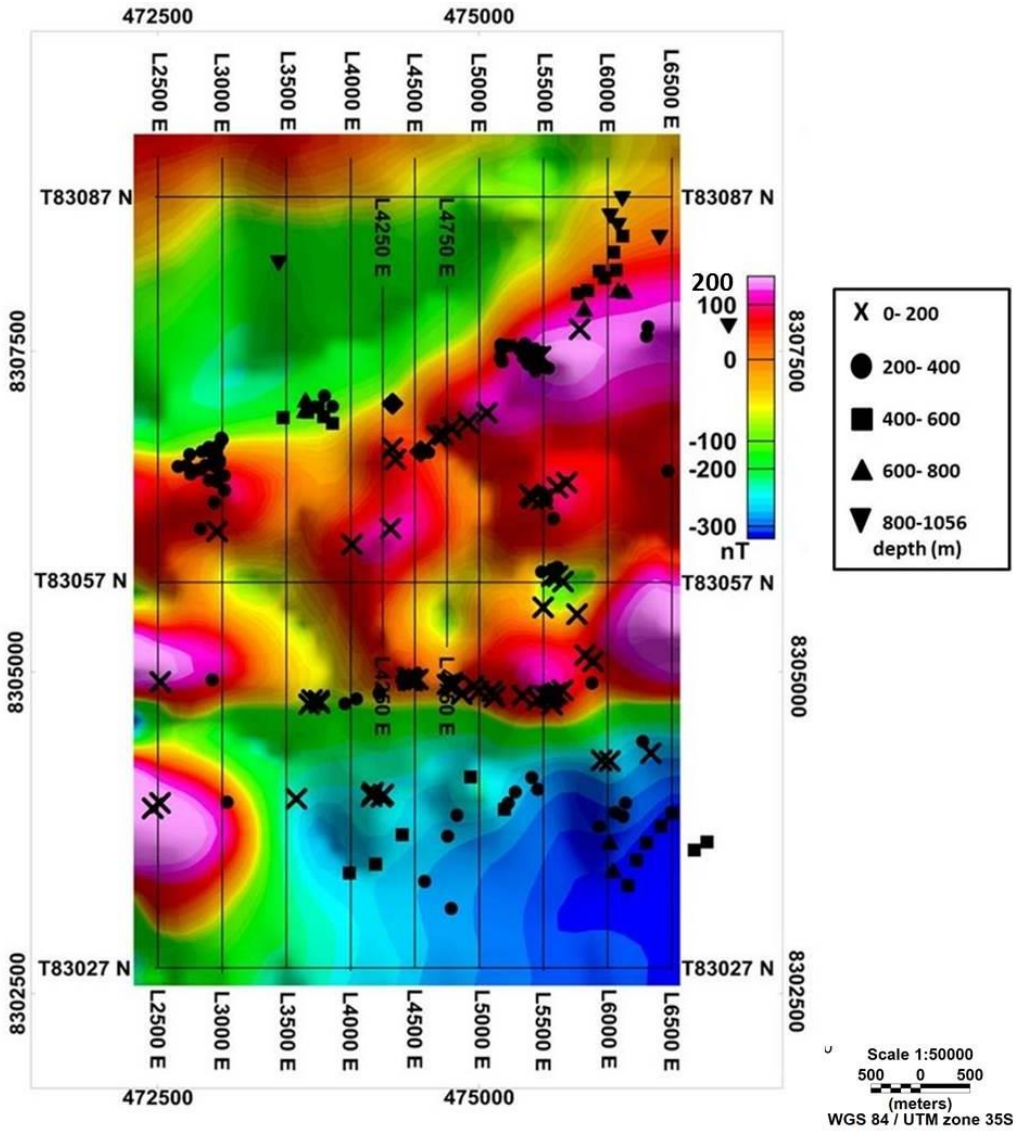

Figure 4.29. 3D Euler's depth solutions (structural index 1) plotted on the colour shaded IGRF RTP total magnetic intensity map.

4.7.2 Construction of the forward models

A combination of physical, spatial and magnetic parameters of the source body influence the amplitude and shape of any magnetic anomaly (Cole et al., 2013). The magnetic intensity, inclination and declination of the inducing field are determined by the location of the source body. When constructing the forward models, the width, depth, dip, magnetic susceptibility and remanent magnetisation of the magnetic source were considered. The remanent magnetism of the source body is defined by its intensity, inclination and declination (Cole et

al., 2013). These physical and magnetic parameters of the source bodies were then used as input parameters or constraints for the forward modelling process.

4.7.3 2D magnetic forward models

2D magnetic forward modelling was performed using total magnetic intensity data for profile L4500 using 2.5D modelling software called Mag2dc (Cooper, 2003) (Figure 4.30).

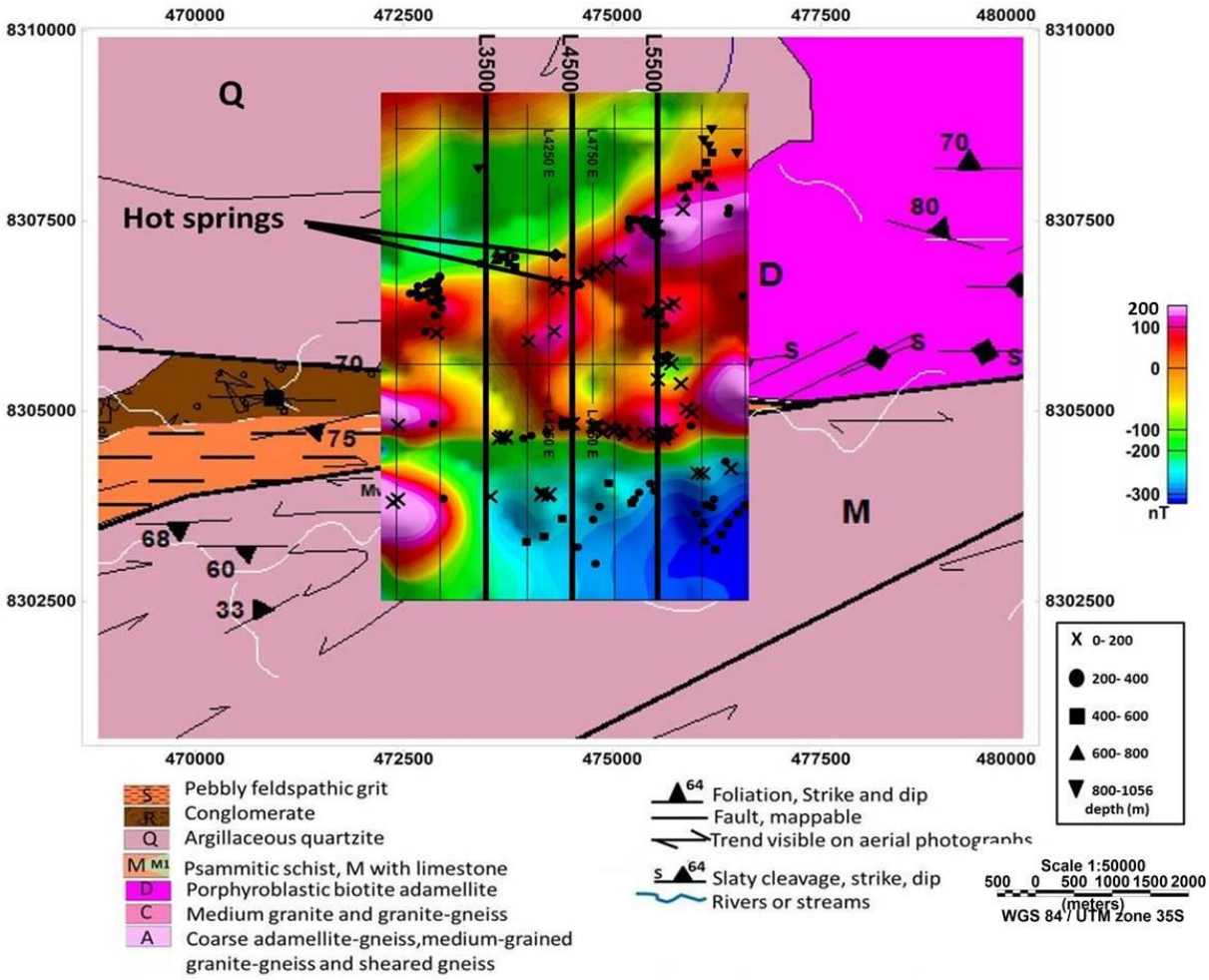

Figure 4.30. Location of the 2D magnetic profiles (black lines) overlain on the Reduced To Pole Total Magnetic Intensity map of the area showing the negative magnetic lineaments inferred using the ground magnetic data (white lines) and the two hot springs. Overlain on the map are the 3D Euler's depth solutions and the IGRF RTP total magnetic intensity image.

Mag2dc enables computation of the anomalous field caused by 2D bodies and structures that are arbitrary in shape by outlining a cross-section of the subsurface with irregular polygons. The program achieves a good fit between the observed and computed anomalies by the use of a trial and error procedure.

The geological bodies and structures were assumed to be two dimensional with the geomagnetic parameters set at declination of 0°, inclination of 0° and magnetic field intensity of 0 nT since the data was extracted from a grid that was reduced to pole and had geomagnetic field removed.

Since potential field modelling is non-unique, the area has very few outcrops, there are no seismic data and borehole data in the vicinity of the magnetic profiles and this allows multiple scenarios (models) producing the same observed magnetic data. The depth and lateral extent of magnetic sources was further constrained by Euler deconvolution. Magnetic susceptibility values measured in the field (Table 4.1) guided by compatible published magnetic susceptibility values were assigned to the lithologies.

4.7.4 Model interpretations

The magnetic profile (L4500) modelled runs from south to north and cuts across all the lithological units and magnetic anomalies encountered in the study area (Figure 4.30) where some of the above geological observations and magnetic susceptibility measurements were made based on outcrop geology. Since we are more concerned with the deeper structures, more effort was put in modelling the wide anomalies. Moving from south to north, the profile passes through the metasedimentary rocks of the Zambezi belt (Figure 4.31). These rocks are in contact with the Katanga sediments at about 1760 m from the start of the profile and are separated by the MwZ fault. The Katanga sediments are in contact with the Hook Batholith granitoids at about 2100 m (Figure 4.31). The granitoids then form a contact with the metasediments of the Lufillian Arc. At their contact the metasediments are altered because of the intrusion causing a weak zone. The magnetic model suggests that the metasediments of the Katanga (schists of the Zambezi belt) dip to the south whilst the Hook Batholith granitoids dip to the north which agrees with Abell (1970). The metasediments of the Lufilian Arc are also dipping to the north. The undulating surface of the Hook batholith granites can be attributed to lots of fracturing which can be observed in Google Earth image and some

fractures were mapped on surface. The metasediments show no or little undulating which can mean less fracturing affected them.

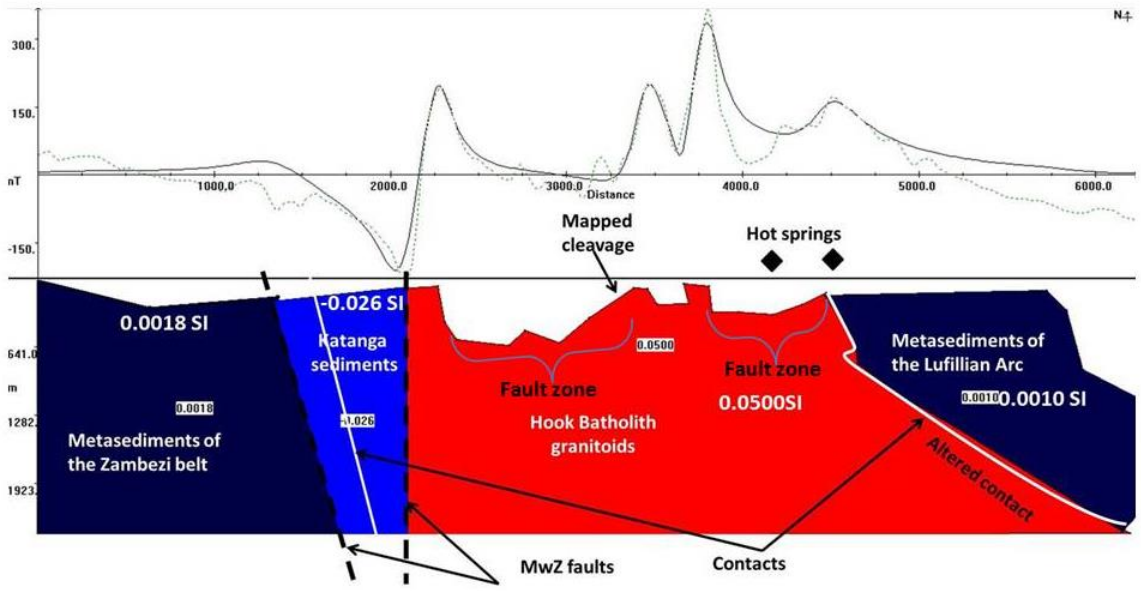

Figure 4.31. 2D magnetic model of profile L4500 with the interpretation of faults and lithological units. The upper panel is the profile's magnetic response with the green dots representing the observed magnetic response and the solid black line the calculated magnetic response from the geological model. The lower panel is a simplified geological interpretation of the 2D magnetic model showing lithologies and magnetic susceptibility values. The location of the profile is shown in Figure 4.16. The Hook Batholith has the highest magnetic susceptibility and the Katanga sediments have the lowest.

A natural source audio-magnetotelluric survey was carried out in order to map the variation of resistivity with depth. Since resistivity is affected by water and porosity we would expect to map any water filled faults or fractured zones. These regions can also be postulated to be hydrothermally demagnetised faulted basement (metasediments) which act as conduits for geothermal fluid flow.

Chapter 5 Natural Source Audio-Magnetotelluric

5.1 Application of resistivity survey

Electrical resistivity tomography is the most useful method in geothermal exploration and delineation of geothermal resources (Hersir and Björnsson, 1991). Resistivity is directly related to salinity, temperature, alteration and permeability (Figure 5.1) and measuring these properties is of great importance to characterise the reservoir (Hersir and Björnsson, 1991). A passive geophysical method called Audio-Magnetotellurics (AMT) was used to measure the resistivity of the subsurface with the aim of mapping the aquifer and the stratigraphy.

The Zonge GDP- 32^{24} (Figure 5.2) multi-receiver system was used for data collection.



Figure 5.1. Zonge GDP- 32^{24} multi-receiver system for acquisition of controlled and natural source geoelectric and EM data.

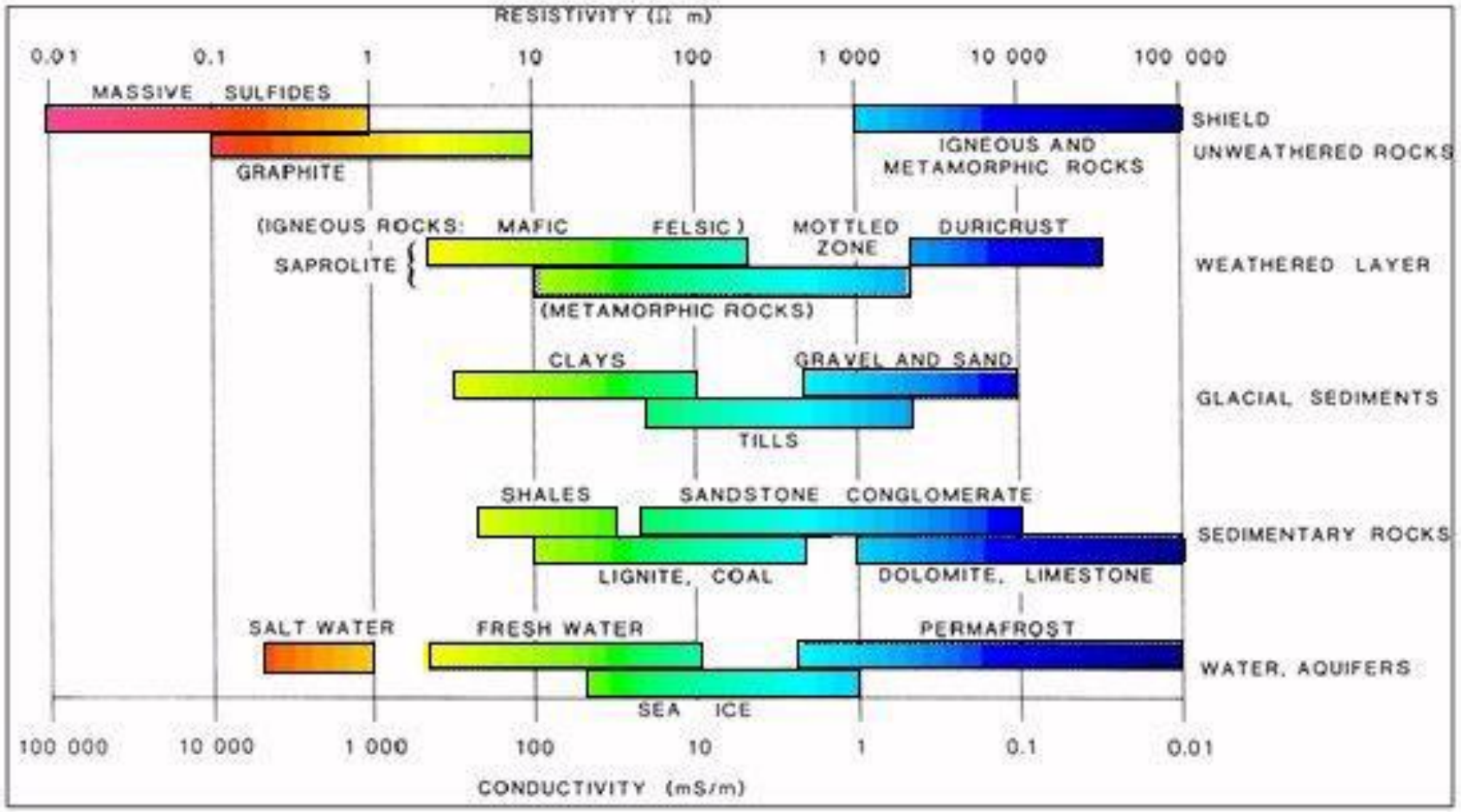

Figure 5.2. Variation of electrical resistivity or conductivity of common Earth materials (Miensopust, 2010).

Tikhonov (1950, reprinted 1986) first propounded the fundamental theory of MT exploration. The method is governed by the fundamental Maxwell's equations and assumptions that describe the relationship between the electrical and magnetic fields.

The principle behind the MT technique is to measure fluctuations in the natural magnetic field of the Earth, H and the induced electric field, E for a wide frequency range ω (H_z). The ratio of the electric field to the magnetic field is used to determine the apparent resistivity of the subsurface. Because of the skin depth effect, low frequencies will penetrate deeper into the Earth than higher frequencies. MT has a broad period range (10^{-3} to 10^{5} s^{-1}) which gives the technique a range of penetration depths, between tens of meters to several hundred kilometres.

For this survey, two bands of the natural EM-field spectrum (0.0001 s^{-1} to 0.1 s^{-1}.) were used, low band (0.333 s^{-1}- 0.00390 s^{-1}) and high band (0.00520 s^{-1}- 0.000122 s^{-1}).

5.2 Magnetotelluric sources

The MT technique uses naturally occurring electromagnetic signals that are created by lightning strikes and interactions between the ionosphere, atmosphere and magnetosphere (Cagniard, 1953; Tikhonov, 1950). The dominant sources for signals in the frequency range 1 Hz to 10 kHz (the audio range) are lightning discharges in the atmosphere whereas frequencies lower than 1 Hz arise from hydromagnetic waves in the magnetosphere. Solar winds periodically batter the magnetosphere and ionosphere causing diurnal variations and magnetic storms in the Earth's magnetic field (Vozoff, 1991). This has direct effects on the ionospheric currents and magnetic field and induces telluric currents in the Earth. The space between the ionosphere and Earth's surface acts as a waveguide for the induced electromagnetic field. The EM field propagates over large distances with slight attenuation (Simpson and Bahr, 2005). The field propagates by bouncing back and forth between the ionosphere and the Earth surface. From a large distance this behaves as a plane wave of variable frequency (10^{-5} Hz up to the audio range). These magnetotelluric fields then penetrate the Earth (a conductor) hence inducing secondary telluric currents.

High frequency signals, greater than 1 Hz are created by lightning strikes and generate electromagnetic fields that also spread over great distances in the waveguide mentioned earlier (Garcia and Jones, 2002). These electromagnetic waves propagate in a direction perpendicular to the direction of the electric and magnetic fields and are attenuated or amplified depending on frequency.

There is a reduction of MT data quality at the transition zone between lightning and solar wind induced signals at frequencies between 0.1 Hz and10 Hz. This low-amplitude region is called the dead-band of MT sounding curves (Simpson and Bahr, 2005).

5.3 Assumptions of the MT Method

Below are different assumptions that have been made in order to simplify the MT data inversion when considering electromagnetic induction in the Earth as described below (e.g., Cagniard, 1953; Vozoff, 1991 and Simpson and Bahr, 2005):

I. Maxwell's general electromagnetic equations are obeyed.
II. The Earth only absorbs or dissipates electromagnetic energy and does not generate it.
III. All fields away from their source can be presumed to be conservative and analytic.
IV. The natural electromagnetic source fields utilized are generated by large-scale ionospheric current systems that are relatively far away from the Earth's surface. Therefore, they can be treated as uniform inducing fields that are incident at right angles on the Earth's plane (plane wave assumption).
V. No free charges are expected to accumulate or to be sustained within a 1D layered Earth. Charges can only accumulate along discontinuities in a 2D or 3D Earth. This phenomenon is known as static shift.
VI. Charge is conserved and the Earth acts as an ohmic conductor, obeying the equation: $\mathbf{J} = \sigma\mathbf{E}$, where j is total electric current density (inAm^{-2}), σ is the conductivity of the sounding medium (in Sm^{-1}), and E is the electric field (in Vm^{-1}).

VII. The time-varying displacement currents are negligible compared to the time-varying conduction currents (quasi-static approximation). Therefore, the induction process is a pure diffusion process.

VIII. Variations of the electrical permittivity and magnetic permeability of rocks are negligible compared with variations in the bulk rock conductivity.

5.4 The fundamental equations of the Magnetotelluric technique

The propagation or dissipation of electromagnetic fields at any given frequency is explained by four partial differential equations called the Maxwell's general electromagnetic equations (Maxwell, 1892).

Assuming uniform inducing fields with a time harmonic of the form $e^{-i\omega t}$ (ω is the angular frequency given by $\omega = 2\pi f$, f representing frequency and t representing time) in a linear, isotropic medium, where displacement currents are negligible and where only variations in bulk rock conductivities are important and applying the constitutive relationships:

$B = \mu H$, $D = \varepsilon E$, $J = \sigma E$

where B is the magnetic field (in nT), μ is the magnetic permeability (in free-space: $\mu = \mu_0 = 1.2566 \times 10^{-6}$ Hm^{-1}), ε is the electric permittivity, J is the electric current density, σ is the electric charge density, H and E are vector magnetic and electric fields respectively.

Therefore, Maxwell's equations can be written as:

1. Faraday's Law: A time varying magnetic field (B) give rise to a proportional electrical field (E) perpendicular to the direction of the inducing magnetic field,

$$\nabla \times E = -\frac{\partial B}{\partial t} = -i\omega B \qquad (5.1)$$

2. Ampere's Law: A magnetic field is induced by a flowing current or time varying electric field that is proportional and perpendicular to the direction of the electric field (conduction plus displacement current),

$$\nabla \times H = \frac{\partial D}{\partial t} + J \text{ ; where } \frac{\partial D}{\partial t} \text{ is Maxwell's displacement current} \qquad (5.2)$$

3. Gauss' Law for electric field: The electric field in a volume has a divergence equal to the enclosed total charge density, q

$$\nabla \cdot D = q_C \quad (5.3)$$

4. Gauss' Law for magnetic field: The magnetic field (B) in a volume has a divergence of zero, meaning that the magnetic field is dipolar in nature, since the magnetic field B is solenoidal.

$$\nabla \cdot B = 0 \quad (5.4)$$

Applying the curl operator to equation 1 and 2 and applying the vector calculus identities (Equation 5.5 and 5.6 below), a diffusion equation for the time varying electric and magnetic fields is derived

$$\nabla \times (\nabla \times A) = \nabla (\nabla \cdot A) - \nabla A^2, \quad (5.5)$$

$$\nabla \times (\Psi A) = \Psi \nabla \times A - A \times \nabla \Psi \quad (5.6)$$

where A and Ψ are vector and scalar electric and magnetic fields respectively.

Applying the curl operator on the electric field

$$\nabla \times (\nabla \times E) = \nabla \times (-i\omega B) \quad (5.7a)$$

$$\nabla \cdot \nabla \cdot E - \nabla^2 E = -i\omega \nabla \times B \quad (5.7b)$$

Simplifies to $\nabla^2 E = i\omega\mu_0 \sigma E - \nabla (E \nabla ln\sigma)$ (5.7c)

Equation 5.7(c) is the diffusion equation for a time varying electric field, E.

Similarly, the diffusion equation of the electric field can also apply to the magnetic field, B.

For a uniform half space, with conductivity σ constant ($\nabla\sigma$=0), equation 5.7c simplifies to:

$$\nabla^2 E = i\omega\mu_0 \sigma E \quad (5.7d)$$

And similarly for a magnetic field

$$\nabla^2 B = i\omega\mu_0\sigma B \qquad (5.7e)$$

Equations (5.7d) and (5.7e) are second order differential equations with solutions valid for an external, uniform, time-varying electromagnetic source field of the form:

$$E = E_1 e^{i\omega t - qz} + E_2 e^{i\omega t + qz} \text{ and } B = B_1 e^{i\omega t - qz} + B_2 e^{i\omega t + qz} \qquad (5.7f)$$

where the first and second terms describe downward and upward travelling waves respectively, t is the time and q is defined by equation 5.7i below. Since the Earth can only absorb or dissipate EM fields and does not generate them (assumption ii) above and it cannot support arbitrary large electric and magnetic fields amplitudes, B_2 and E_2 are equal to zero (Simpson and Bahr, 2005). Applying the solution Equation (5.7f) to the left-hand side of Equation (5.7d) and assuming a vertical incidence such that $\frac{\partial E}{\partial x} = \frac{\partial B}{\partial x} = 0$ yields;

$$\nabla^2 E = \frac{d^2 E}{d^2 z} = q^2 E_1 e^{i\omega t - qz} = q^2 E, \qquad (5.7g)$$

and therefore, Equation (5.7d) becomes

$$q^2 E = i\omega\mu_0\sigma E \Rightarrow q^2 = i\omega\mu_0\sigma \qquad (5.7h)$$

Solving for q yields

$$q = \sqrt{i\omega\mu_0\sigma} = \pm \sqrt{\frac{\omega\mu_0\sigma}{2}} + i\sqrt{\frac{\omega\mu_0\sigma}{2}} \qquad (5.7i)$$

The relation between the EM field components which is the inverse of q is known as the Schmucker-Weidelt transfer function (Weidelt, 1972) and can be expressed as;

$$C = \frac{1}{q} = \frac{E_x}{i\omega B_y} = -\frac{E_y}{i\omega B_x} \qquad (5.7j)$$

The definition for the resistivity ρ in a homogeneous half-space is a result of combining Equation (5.7i) with equation (5.7j) and is given by;

$$\rho = \frac{1}{\sigma} = \quad \frac{1}{|q|2}\omega\mu_0 = |C|^2\omega\mu_0 \qquad (5.7k)$$

Since C has real and imaginary parts, an impedance phase ϕ can be derived and expressed as:

$$\phi = tan^{-1}\left(\frac{\mathrm{ImC}}{\mathrm{ReC}}\right) \qquad (5.7l)$$

The inverse of the real part of q is the frequency-dependent skin depth or penetration depth δ; and is given by:

$$\delta = \frac{1}{\mathrm{Re}(q)} = \sqrt{\frac{2}{\omega\mu_0\sigma}} \quad = \sqrt{\frac{T}{\pi\mu_0\sigma}} \text{ , with period } T=\frac{2\pi}{\omega}$$

The equation states that at a depth δ(T), electromagnetic fields are attenuated to $1/e$ of their amplitude at the surface of the Earth. A typical value for the magnetic permeability μ is the free space value (μ_0 =1.2566 × 10^{-6} Hm^{-1}).

Since the apparent or resistivity (ρ_a) is the reciprocal of the average conductivity, σ of the Earth we can replace σ with ρ_a and the approximate depth of penetration, δ(T) (in metres) can be given by:

$$\delta(T) = 500\sqrt{T\rho_a}$$

If we assume an average resistivity of the Earth's crust and upper mantle of 100 Ωm and a period spectrum for MT measurements of 10^{-3} to 10^{5} s^{-1} we can see that penetration depths between 160 metres and a few hundred kilometres are possible (Simpson and Bahr, 2005). The resistivity and phase which are given by equation (5.7k) and (5.7l) are the most important magnetotelluric parameters and are normally plotted as a function of period T which is inverted for depth (Simpson and Bahr, 2005).

5.5 The Impedance Tensor

In MT, a linear system has two inputs, the horizontal components of the time domain magnetic field [$B_x(t)$] and $B_y(t)$], and two independent outputs, the horizontal components of the time domain electric field [$E_x(t)$] and [$E_y(t)$] (Jones et al., 1989).

When the amplitude of the fields varies with time, and neglecting components of noise, these fields are brought together by convolution to four weighting functions, $z_{xx}(t)$, $z_{xy}(t)$, $z_{yx}(t)$, and $z_{yy}(t)$. These describe how the input [$B_x(t)$] and [$B_y(t)$] is modified to produce the output [$E_x(t)$] and [$E_y(t)$]. Their Fourier transformed equivalent in the frequency domain is the Z-transform or impedance tensor (Jones et al., 1989). A transfer function is a transformation operator used to relate the input signals to the output signals. Berdichevsky (1960, 1964) initially defined the impedance tensor for MT and it is usually described as a 2 x 2 complex transfer functions as shown below:

$$\begin{pmatrix} E_x \\ E_y \end{pmatrix} = \begin{pmatrix} Z_{xx} & Z_{xy} \\ Z_{yx} & Z_{yy} \end{pmatrix} \begin{pmatrix} B_x/\mu_0 \\ B_y/\mu_0 \end{pmatrix} \qquad \text{or } E = \underline{\underline{Z}}B/\mu_0 \qquad (5.8a)$$

where B, E and $\underline{\underline{Z}}$ are in S.I. units (Vm^{-1}, $T = V_s m^{-2}$ and $\Omega = V/A$).

Using the relationship $B = \mu_0 H$ between the magnetic induction B and the magnetic intensity H (in Am^{-1}) in equation (5.8a) results in

$$\begin{pmatrix} E_x \\ E_y \end{pmatrix} = \begin{pmatrix} Z_{xx} & Z_{xy} \\ Z_{yx} & Z_{yy} \end{pmatrix} \begin{pmatrix} H_x \\ H_y \end{pmatrix} \qquad \text{or } E = \underline{\underline{Z}}H. \qquad (5.8b)$$

Each component of the impedance tensor defines two horizontal components of E and B that are perpendicular to each other measured in the field. For instance in the 1D Earth, the component $Z_{xy}=E_x/H_y$ is the impedance given by the electric field in the x-direction and the magnetic field in the y-direction.

The impedance tensor (Z) is a stable property of the subsurface while H and E are generated by non-stationary phenomena outside the Earth (Booker, 2012).

Similar to DC resistivity, one can scale the magnitude-squared of the impedance (Z) to give an apparent resistivity by

$$\rho_{a,xy}(\omega) = \frac{1}{\omega\mu_0}\left|\frac{E_x(\omega)}{H_y(\omega)}\right|^2 = \frac{1}{\omega\mu_0}|Z|^2 \quad (5.8c)$$

which is equal to the true resistivity of the uniform half space where μ_0 =1.2566 × $10^{-6} Hm^{-1.}$

The impedance phase, which is the angle between the impedance vector and the positive real axis on the complex plane is given by ϕ = arg (Z).

The phase relationships in Z can be expressed by a second-rank tensor known as the MT phase tensor

$$\phi = X^{-1}Y = \begin{pmatrix} \phi_{xx} & \phi Z_{xy} \\ \phi_{yx} & \phi Z_{yy} \end{pmatrix} \quad (5.8d)$$

(Caldwell et al., 2004)

The horizontal and vertical components of the magnetic field are related by a complex function called the geomagnetic transfer function (Parkinson, 1959).

$$H_x = \begin{pmatrix} T_x T_y \end{pmatrix}\begin{pmatrix} H_x \\ H_y \end{pmatrix} \quad (5.8e)$$

The geomagnetic transfer function, H_X is also named the tipper vector (a measure of the tipping of the magnetic field out of the horizontal plane). It can be used to represent the presence, or absence of lateral variations of conductivity, that generate vertical magnetic fields (Simpson and Bahr, 2005). Therefore if conductivity distribution varies laterally, the real part of the geomagnetic transfer function will point towards the area of highest conductance (Parkinson, 1962).

5.6 The Impedance tensor for 1D Earth

If the conductivity only varies with depth, the diagonal components ($Z_{xx}$and Z_{yy}) of the impedance tensor in equation 5.8a, which are related to the parallel electric and magnetic fields, will be reduced to zero. The off-diagonal elements (Zxy and Zyx) have the same

amplitude since there is no lateral conductivity change. Simpson and Bahr (2005) suggest that they must have a different sign to preserve the right-hand rule.

Consequently the transfer function for a 1D case can be outlined as:

$$\begin{pmatrix} E_x \\ E_y \end{pmatrix} = \begin{pmatrix} 0 & Z_{xy} \\ -Z_{xy} & 0 \end{pmatrix} \begin{pmatrix} B_x/\mu_0 \\ B_y/\mu_0 \end{pmatrix} \tag{5.9a}$$

Decomposing the transfer function into its components and solving for Z_{yx} yields;

$$Z_{yx} = -\mu_0 \frac{E_y}{B_x} = \mu_0 \frac{E_x}{B_y} = Z_{xy} \tag{5.9b}$$

For the 1D case, this can also be derived from Maxwell's Equations and is equivalent to the Schmucker-Weidelt transfer function (Equation 5.7j). The only difference is in the definition of the transfer function where $Z = i\omega\mu_0/q$ for the impedance tensor and $C = \frac{1}{q}$ for the Schmucker-Weidelt function and the two transfer functions are related by $Z = i\omega\mu_0 C$. Therefore, for a 1D layered Earth apparent resistivity and phase are given by;

$$\rho = \frac{1}{\sigma} = \frac{1}{|q|^2}\omega\mu_0 = \frac{|Z|^2}{\mu_0 w} \tag{5.9c}$$

$$\phi = tan^{-1}\left(\frac{ImC}{ReC}\right) \tag{5.9d}$$

These equations (equation 5.9c and 5.9d) are similar to Equations 5.7k and 5.7l. However, apparent resistivity in their case is defined as the average resistivity of a homogenous half-space.

5.7 The Impedance tensor for 2D Earth

When the geological structures are relatively long compared to their width, then two-dimensional (2-D) approaches can be used. Here conductivity varies with depth and along a single lateral dimension. The electric field is then confined perpendicular or parallel to the strike of the regional conductivity distribution and separates into two independent modes (Wannamaker et al., 2008). Berdichevesky (1960) suggested that a magnetic field parallel to strike induces an electric field perpendicular to strike and vice versa and when one of the

involved fields, either the magnetic or electric field, is parallel to the strike direction, the diagonal impedance components (Z_{xx} and Z_{yy}) are zero and the off-diagonals now differ from each other. As a result the transfer function is given by;

$$\begin{pmatrix} E_x \\ E_y \end{pmatrix} = \begin{pmatrix} 0 & Z_{xy} \\ Z_{yx} & 0 \end{pmatrix} \begin{pmatrix} B_x/\mu_0 \\ B_y/\mu_0 \end{pmatrix} \quad (6.1a)$$

The above equation is for when the x-axis is parallel to the strike direction. Consequently, the impedance tensor's off-diagonal elements represent two polarisation modes, defined as the transverse magnetic (TM) (B- polarisation) and transverse electric (TE) (E polarisation). In terms of the electromagnetic field components B_x, E_y and E_z for the transverse magnetic field and E_x, B_y and B_z for the transverse electric field, we can write (Simpson and Bahr, 2005) as:

$$\left.\begin{aligned} \frac{\partial E_x}{\partial y} &= i\omega B_z \\ \frac{\partial E_x}{\partial z} &= -i\omega B_y \\ \frac{\partial B_z}{\partial y} - \frac{\partial B_y}{\partial z} &= \mu_0 \sigma E_x \end{aligned}\right\} \text{TE-Mode} \qquad \left.\begin{aligned} \frac{\partial B_x}{\partial y} &= \mu_0 \sigma E_z \\ -\frac{\partial B_x}{\partial z} &= \mu_0 \sigma E_y \\ \frac{\partial E_z}{\partial y} - \frac{\partial E_y}{\partial z} &= i\omega B_x \end{aligned}\right\} \text{TM-Mode}$$

Considering a situation when we are profiling across strike, the electric field E_y will be discontinuous across the vertical contact and the current density j_y across the boundary is conserved (obeying Ohm's law). As a result, impedances associated with E_y will be discontinuous and made up of Z_{yx} only, since Z_{yy} is zero in the ideal case. The magnitude of the discontinuity in electric field and in the associated impedance is σ_2/σ_1 (Figure 5.3). Therefore, the apparent resistivity perpendicular to the strike direction will also observe Ohm's law (discontinuous) and will have a magnitude of $(\sigma_2/\sigma_1)^2$. The discontinuous behaviour of ρ_{yx} across the vertical contact (Figure 5.3) results in the B-polarization (TM mode) resolving lateral conductivity variations better than the E-polarization (TE mode) resistivities. Since the geomagnetic transfer function is sensitive to lateral changes in

conductivity and is only associated with the TE mode, the TE mode can also be used to map lateral conductivity contrasts.

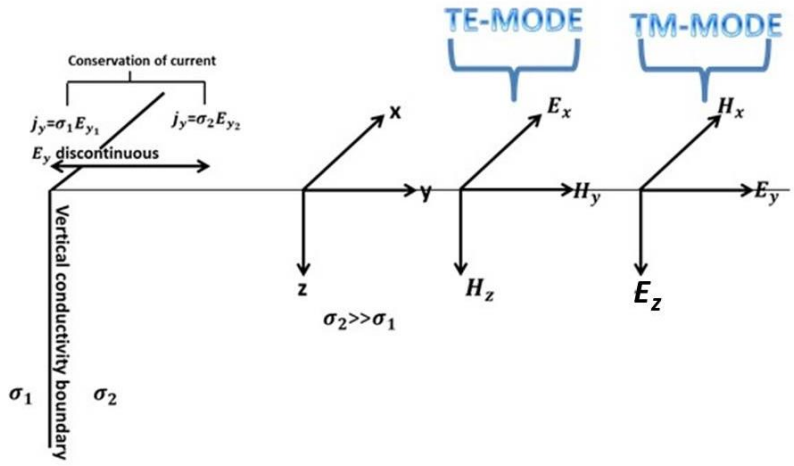

Figure 5.3. 2D model with two quarter-spaces with different conductivities (σ_1 and σ_2) separated by a vertical boundary. The contact extents to infinity and strikes into the x-direction. Across the contact current is conserved which leads to the y-component of the electric field (E_y) being discontinuous. The EM fields can be decoupled into a mode that is incorporating electric fields parallel to strike with induced magnetic fields perpendicular to strike and in the vertical plane (TE-mode), and a second mode, which incorporates magnetic fields parallel to strike and induced electric fields parallel to strike and in the vertical plane (TM-mode); modified from (Simpson and Bahr, 2005).

The assumptions made for the transfer function (equation 6.1a) in the case of a 2D Earth model that induction is of electric fields that are parallel or perpendicular to the electromagnetic strike direction does not hold for most MT recordings in a real Earth situation because the strike direction is usually not known at the time of a field survey (Vozoff, 1991). This results in the diagonal components of the impedance tensor (Z_{xx}, Z_{yy}) not being equal to zero and off diagonal components (associated with TE and TM-mode), will be mixed within the tensor. However, if we assume an ideal distortion-free 2D structure case, it is possible to rotate the impedance tensor around a vertical axis, until the diagonal components reduce to zero and the 2D impedance tensor Z_{2D} is in strike coordinates. Using the Cartesian rotation matrix R with rotation angle θ, the ideal 2D impedance tensor can be calculated as:

$$Z_{2D}=RZ_{obs}R^{T}, \text{ where} \qquad (6.1b)$$

R is the rotation matrix and is given by:

$$R=\begin{pmatrix}\cos\theta & \sin\theta\\ -\sin\theta & \cos\theta\end{pmatrix} \quad (6.1c)$$

and R^T is its transpose and is given by:

$$R^T=\begin{pmatrix}\cos\theta & -\sin\theta\\ \sin\theta & \cos\theta\end{pmatrix} \quad (6.1d)$$

Z_{obs} (in equation 6.1b) is the observed impedance tensor from the measured data. All things considered, the angle of rotation between the strike direction and the survey direction can be derived. Rotating the 2D impedance tensor by increasing the rotation angle will result in the diagonal components being zero. The best rotation angle can be examined by plotting the off-diagonal impedances on a polar diagram. However, this is highly affected by noise and hence a suitable rotation angle cannot be deduced and such techniques can yield incorrect results (Jones and Groom, 1993). Results are also affected by galvanic distortions and as a result distortions should always be accounted for when selecting a strike rotation angle.

5.8 Distortion effects

As discussed earlier, for a one dimensional Earth, the diagonal terms are zero and the off-diagonal terms are equal to each other except for a sign difference and for two dimensional Earth, the diagonal terms are zero whilst the off-diagonal terms are different from each other. When the impedance tensor does not fall under any one of these, then the Earth is three dimensional but with distortion effects. These distortion effects are a result of topography and small-scale conductivity variations near to the surface that cannot be resolved within the conductivity model of the subsurface. Distortion effects can be practically grouped into two groups, namely inductive and galvanic effects. The time-varying magnetic field induces currents, which, if flowing in closed loops, induces a secondary magnetic field that adds to the primary magnetic field and this distortion effect is called the inductive effect (Jones, 1988; Jiracek, 1990). Where there are local conductivity variations in the subsurface, flux through the boundaries of these various conductors by the regional current results in the

accumulation of charge at these boundaries (Price, 1973). These charges create a secondary electric field that distorts the regional (primary) current flow in that area. Where the distorting conductors are small relative to the scale size of the experiment, this effect is known as galvanic distortion.

The galvanic effect can also be produced in a similar manner by 2D topography (galvanic topographic distortion) when the primary electric field is perpendicular to the trend of the topography (Jiracek, 1990). When shallow conductive or resistive bodies are enclosed in bigger bodies, boundary charges accumulate at the surface of the bodies and consequently secondary electric fields are created, which add vectorically to the primary field. This results in channelling or deflection of the current around the inhomogeneities. Consequently when you record MT soundings directly above a surficial resistive body the apparent resistivities recorded are therefore shifted upwards (current deflection) whereas they are shifted downwards over a conductive body (current channelling). This upward or downward shift is not time-dependent (in contrast to induction) and is called static shift. It does not affect the impedance phase of the transfer functions.

Different authors have proposed different distortion correction techniques in order that they can be applied to remove the unwanted galvanic distortion effect from the data (Jiracek, 1990; Groom and Bahr, 1992).

Pellerin and Hohmann (1990) suggested the use of either joint inversion of Transient ElectroMagnetic (TEM) and magnetotelluric (MT) data, allowing vertical shifts in the MT apparent resistivity curves, or by the use of 1D inversion of TEM soundings to correct for static shifts in the MT response. A synthetic MT response is computed for high frequency ($\geq$ 1 Hz) from the estimated 1D structure. Static shift is then corrected by shifting the observed MT curves to match the computed curves. De Groot-Hedlin (1991, 1995) describes the different approaches to accomplish static shift correction.

A common mathematical approach is the decomposition of the data into a non-inductive response, owing to multi-dimensional local heterogeneities and a response owing to an underlying regional 1D or 2D structure (Simpson and Bahr, 2005). The determination of the electromagnetic strike direction involves decomposing the measured impedance tensor Z_{obs} (equation 6.1b) into matrices representing the inductive and non-inductive parts. The complex inductive part (Z_{2D}) is composed of magnitudes and phases, whereas the non-

inductive part (D) is the distortion tensor, which is real and frequency independent as shown below:

$$Z_{2D}=\begin{pmatrix} 0 & Z_{xy} \\ Z_{yx} & 0 \end{pmatrix} \quad \text{and} \quad D=\begin{pmatrix} D_{xx} & D_{xy} \\ D_{yx} & D_{yy} \end{pmatrix} \tag{6.2a}$$

A decomposition technique to determine the regional 2D strike direction (a measure of the anisotropy and galvanic distortion effects from distorted measured data) proposed by Groom and Bailey (1989) is commonly used.

5.9 Groom- Bailey decomposition

Groom and Bailey (1989) introduced a distortion impedance tensor decomposition that is based on a physical model of idealized distortion for a 2D regional conductivity structure. The approach shows that the electric galvanic distortion matrix is more important than the inductive distortion tensor which plays a minor role (or in the case of strong channelling, it plays no role at all). The hypodissertation requires that the distortion tensor must be frequency independent and real. The local effects of the 3-D current channelling are separated from the regional 2D inductive behaviour by the factorization of the distortion matrix D into a scaling or site gain factor, g, and three tensors: shear (S), twist (T), and local anisotropy (A). The impedance tensor in a rotational reference frame therefore yields:

$$Z_{obs}=R_{\theta}[gTSA]Z_{2D}R_{\theta}{}^{T}, \tag{6.2b}$$

where D=gTSA and θ is the regional strike angle.

The equation allows the calculation of the strike angle, θ, and the apparent impedance tensor, twist and shear parameters.

5.10 NSAMT Data Collection and Processing

5.10.1 Methodology

The Zonge GDP- 32^{24} (Figure 5.2) multi-receiver system was used for data collection. A preliminary geoelectric strike direction was estimated at an azimuth of 90˚ by using the

magnetic anomaly signature and orientation of the geologically mapped faults. MT data were acquired along 3 lines, each 4 km long and lines of 1 km line spacing (L3500, L4500 and L5500) cutting across the Mwembeshi Shear Zone and the fractured foliations using the geologist's strike mapping (Figure 5.4). In the south, the lines cut across the contact between the Katanga sediments and the Hook Batholith granitoids and across another contact between the Hook batholith granites and the metasediments of the Lufilian Arc towards the north (Figure 5.4 and Figure 5.5). Data were recorded over two bands of the natural EM-field spectrum i.e. 3- 256 H_z (low band) and 192- 8192 H_z (high band) with sampling rate of 5 minutes per stack and 5 stacks per station.

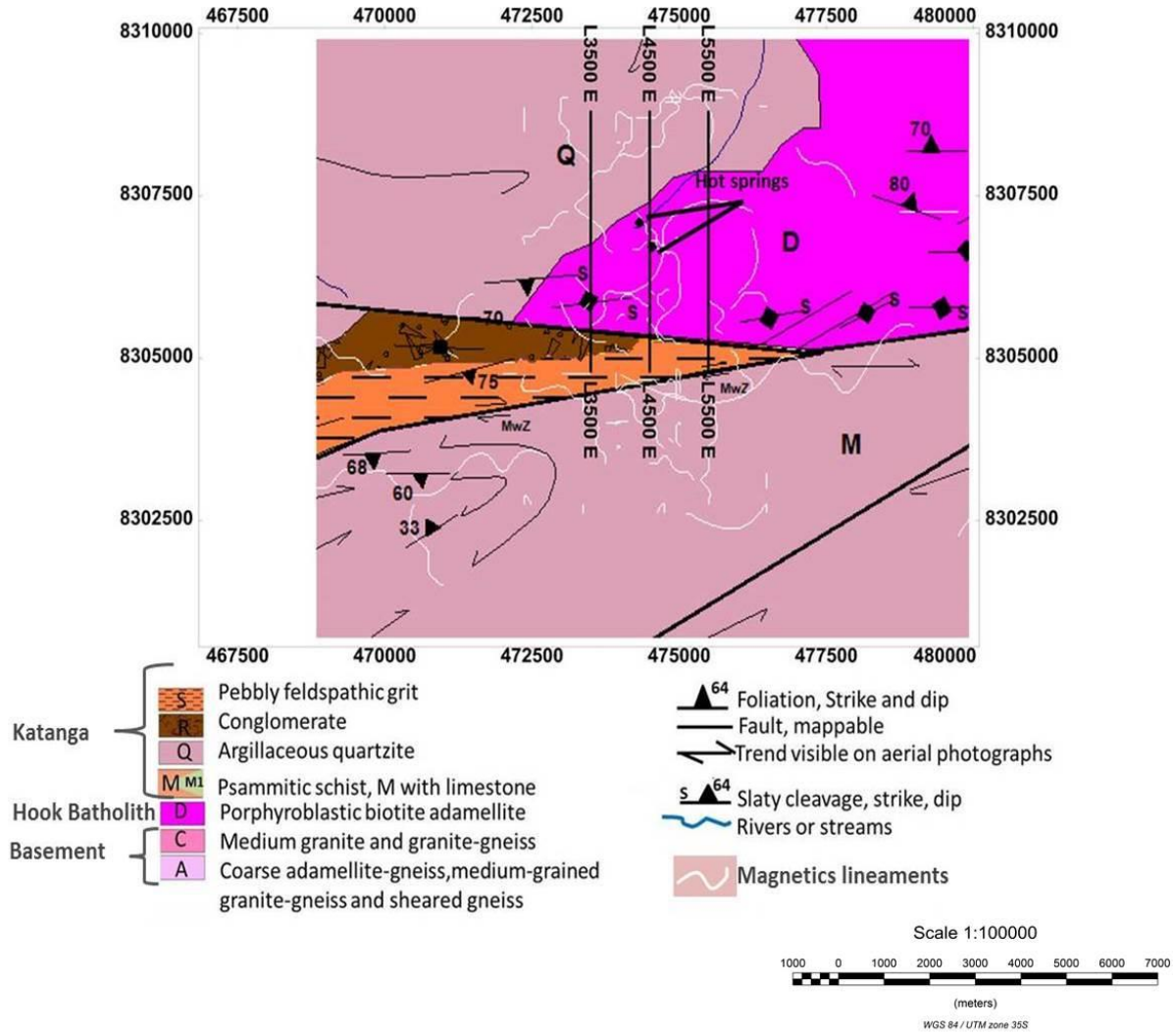

Figure 5.4. Study area showing AMT survey lines (thick black lines) overlain on top of the new geological map as interpreted from magnetic data and the old geological map modified after (Abell, 1970).

On the first vertical derivative magnetic map starting from the south, the lines start just after the boundary between the low magnetic amplitude zone and the high magnetic amplitude

zone (Figure 5.5). This boundary is characterized by an almost E-W negative magnetic gradient lineament (Figure 5.5). All the lines pass through the negative magnetic lineaments along the northern branch of the Mwembeshi Shear Zone in the south. Line 3500 also passes through one NE and one NW negative magnetic lineaments (Figure 5.5). Line 4500 passes through the NW magnetic negative lineament that could be controlling the two hot springs and NE magnetic negative lineaments (Figure 5.5). Line 5500 passes through E-W magnetic negative lineament and along a N-S lineament in the north.

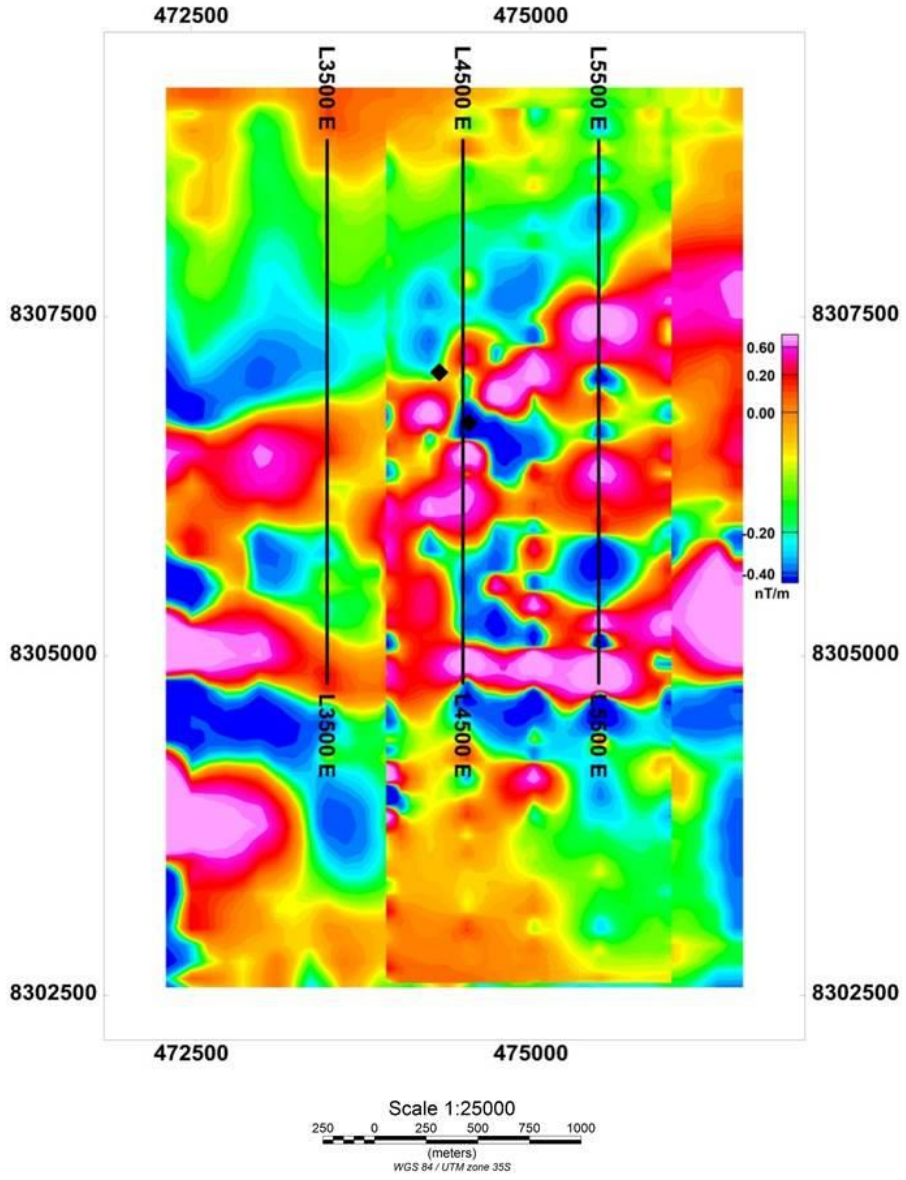

Figure 5.5. Study area showing AMT survey lines (thick black lines) overlain on top of the Reduce to pole (RTP) first vertical derivative (1-VD) total magnetic intensity (TMI) image of the whole area and of the infill lines.

5.10.2 Data quality control

The processing at this stage was undertaken using Zonge's MTFT24 and MTEDIT. MTEdit is a utility program for processing and reviewing magnetotelluric Fourier coefficients data collected by Zonge receivers (Zonge International, 2010). By implementing the algorithm by Egbert (1997) and using the measured magnetic and electric fields as inputs, the program calculates average impedance and apparent resistivity values from unaveraged spectral data. It includes options for both automated processing and interactive quality control editing (de Swart et al.,1965) (Zonge International, 2010).

Figure 5.6 shows each channel on the instrument as a trace recording time-series over time. Green is electric field dipoles, blue is magnetic field antenna and each spike is an event.

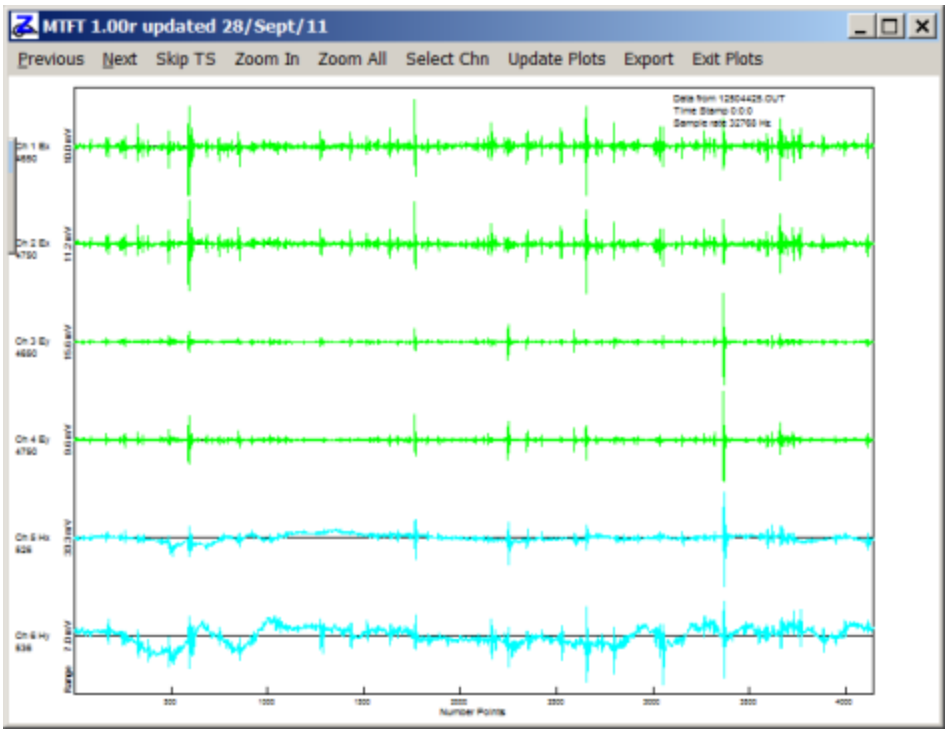

Figure 5.6. Zonge's MTFT24 screen showing each channel on the instrument as a trace recording time-series over time. Green is electric field dipoles, blue is magnetic field antenna and each spike is an event.

5.10.3 Static Corrections

For quality control and to obtain a first order idea of the data, the MT data were loaded into a utility program called ASTATIC, which provides editing and analysis tools (Zonge International, 2013) (Figure 5.7, Appendix A for other original responses). It was used for

reviewing the NSAMT, calculating static corrections and clearing of skip flags on each data point. Figure 5.7 below shows a sounding example demonstrating the range of data quality of the MT records. Apparent resistivities for the TE mode (Zxy, B), TM mode (Zyx, C), Zxx (A), Zyy, (D) and phases (ϕ xy and ϕ yx) are plotted against the period. The quality of the data was determined by examining the size of the error bars and whether the phase lies within a 90° tolerance.

ASTATIC uses a fixed-length-moving-average (FLMA) filter along a line at a selected frequency to estimate static-corrected resistivity shifts (Zonge International, 2013). The FLMA filter estimates static-corrected apparent resistivities at a single reference frequency by calculating a profile of average impedances along the length of the line (Zonge International, 2013). Sounding curves are then shifted so that they intersect the averaged profile. The highest frequency with clean data should be selected as the static-correction reference frequency.

The two plots of apparent resistivity below show the effects of static-correction moving-average filters (Figure 5.7a and 5.7b). Some plots are also shown in the Appendix A.

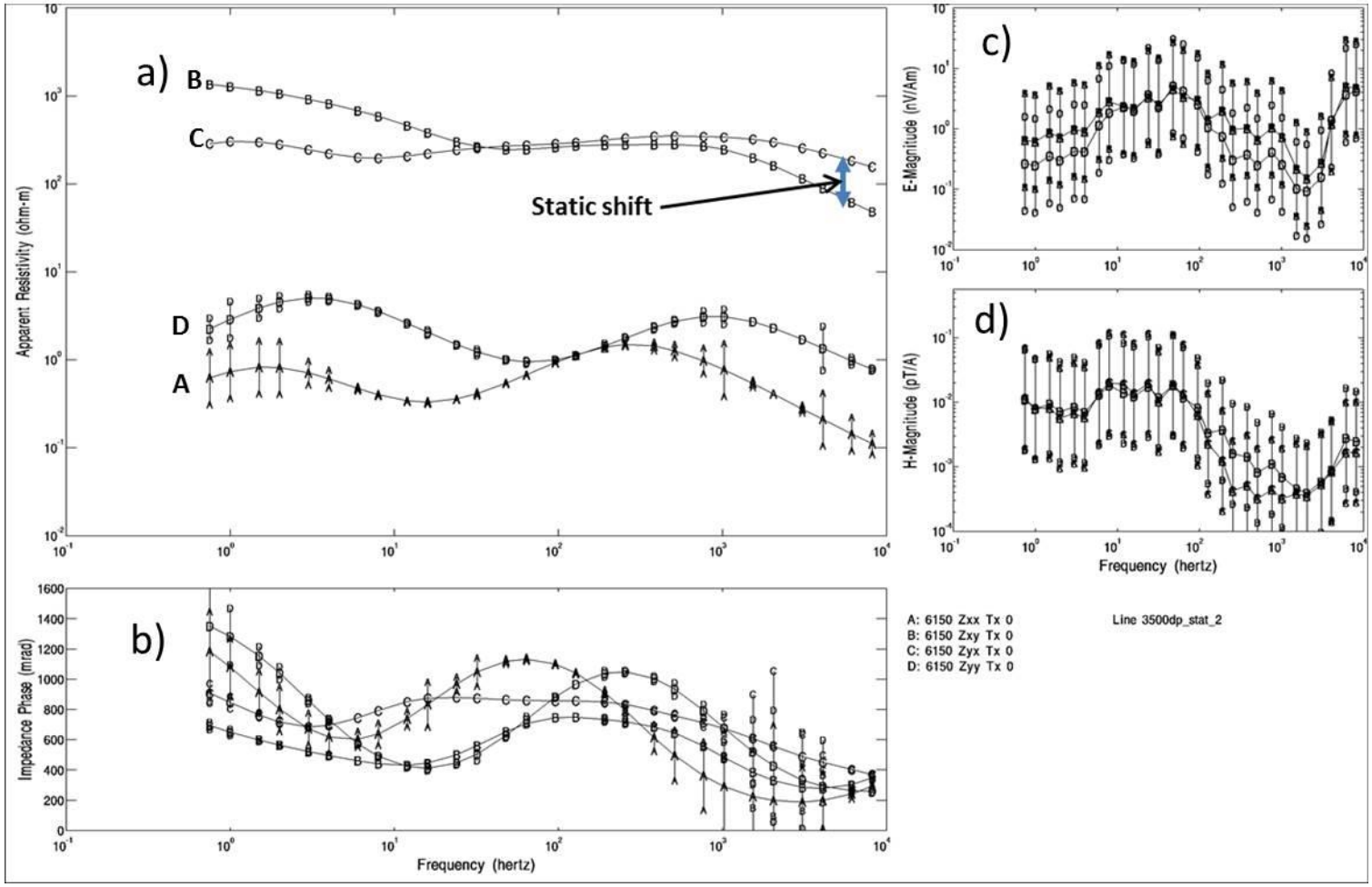

Figure 5.7a. MT soundings for L3500 station 14 showing apparent resistivities for the TE mode, Zxy, the TM mode, Zyx, Zxx mode and Zyy mode represented by B, C, A and D respectively are plotted against the period before static correction on window a. Window b shows phases ϕ xy and ϕ yx also plotted against the period. Windows c and d show the measured electric and magnetic fields respectively plotted against period. Effect of static shift can be observed towards the high frequencies of curves B and C (gap shown by double blue arrow).

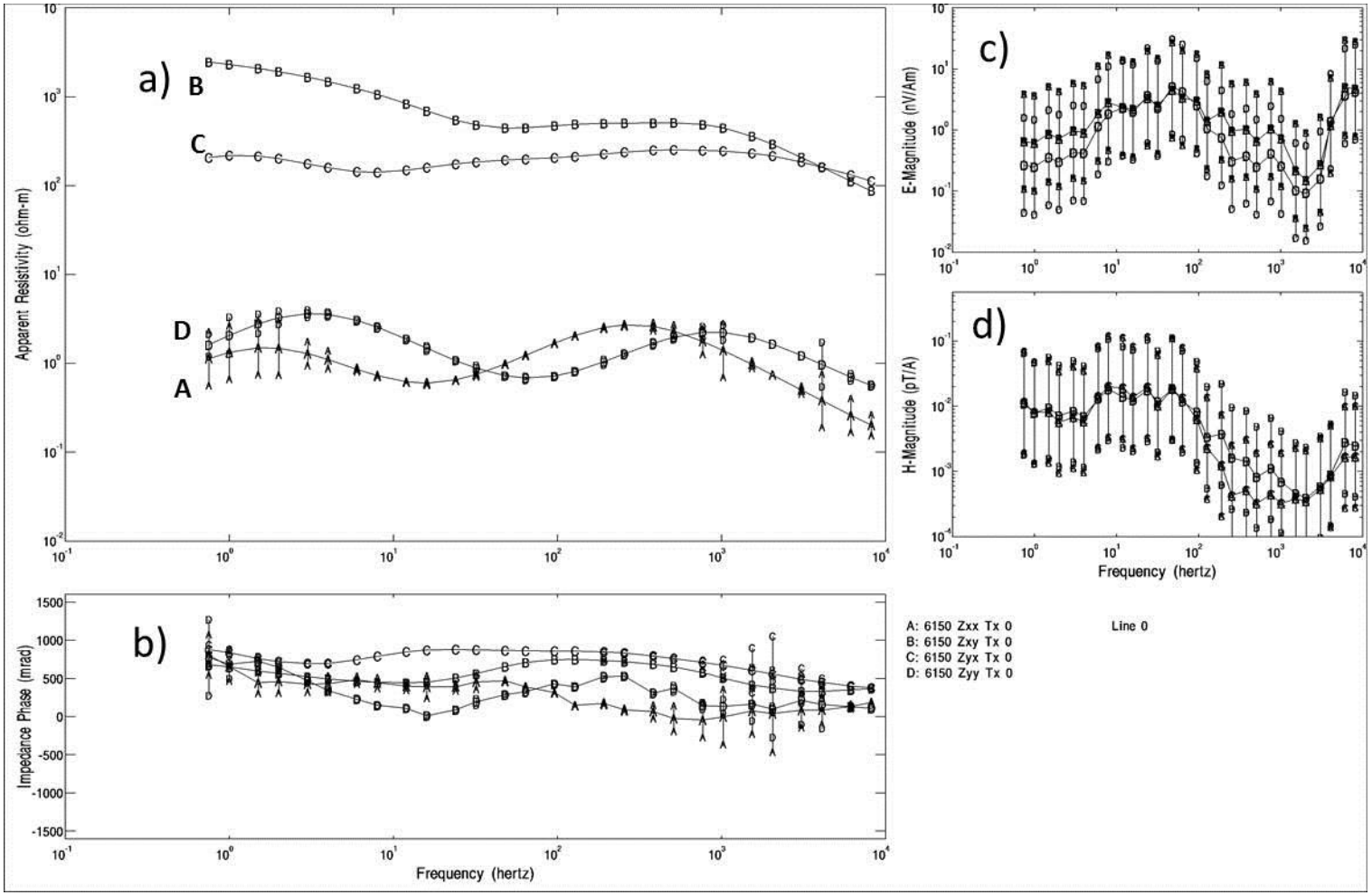

Figure 5.7b. MT soundings for L3500 station 14 showing apparent resistivities for the TE mode, Zxy, the TM mode, Zyx, Zxx mode and Zyy mode represented by B, C, A and D respectively are plotted against the period before static correction on window a. Window b shows phases ϕ xy and ϕ yx also plotted against the period. Windows c and d show the measured electric and magnetic fields respectively plotted against period after static correction. Static correction can be observed by shift of the observed MT curves (B and C) to match the calculated curves.

5.10.4 Strike Analysis and Decomposition

Realistically, MT measurements are most likely not carried out perpendicular or along the direction of geological strike and usually the dimensionality of the problem is fairly unknown. One of the main tasks of the analysis is to deduce the appropriate dimensionality of the data by determining whether the data are 1D or 2D or 3D, to within experimental error and at which periods and for which sites. Hence when dealing with a two dimensional subsurface in the presence of telluric distortion, we need to decompose the measured impedance tensor Z_{obs}. The decomposition approach of Groom and Bailey (1989) computes the regional 2D strike direction and yields a measure of the distortion effects. It achieves this by splitting the measured impedance data into recalculated impedance and distortion matrices (Equation 6.2b). A rotational framework around these matrices tries to recalculate the impedance matrix in such a way that the resulting matrix (Z_{2D}) describes an ideal 2D impedance tensor (along strike case, where the diagonal elements are zero) (equation 6.2a). The angle, θ that is used by the rotation matrices 6.2b is referred to as the strike angle. These calculations have to be done independently on a frequency-by-frequency and site-by-site basis (Groom and Bailey, 1989). A misfit (RMS error) between the observed impedance tensor Z_{obs} and the calculated decomposition factors (right side of equation 6.2b) is statistically analysed hence proving the validity of the galvanic distortion and dimensionality assumption. A less time-consuming approach to determine the most suitable strike direction and electromagnetic distortion parameters for a range of frequencies and stations was proposed by McNeice and Jones (2001), called multi-frequency, multi-site analysis. McNeice and Jones (2001) developed a computer program called STRIKE that is based on the multi-site/multi-frequency approach of the Groom and Bailey decomposition analysis.

Although the data were collected almost perpendicular to the geologic strike, STRIKE code was used to prove that the data are still perpendicular to geoelectric strike or 2 dimensional. Data from each site were then analysed with the STRIKE program over different period (depth) ranges. Table 5.1 shows an example of the output from a calculation with STRIKE for a period range of 1 x 10^{-4} s^{-1} to 1 x 10^{-3} s^{-1} for each station. The best fitting strike angle is determined by the RMS error, which gives the misfit between the observed impedance tensor and the result from the decomposition (left and right side of equation 5.7b). The smaller the error, the better a certain geoelectric strike angle, together with its associated distortion parameters will fit the observed data. The decomposition to strike is not simply a rotation of the coordinate system into the strike direction, but rather a recalculation of the impedance tensors and the removal of distortion effects at the same time. The example in Table 5.1 therefore shows that each station

has different RMS errors (rms) and distortion parameters (shear, twist) for a certain strike angle.

Multifrequency analysis of all of the data from some sites independently yields the following distortion parameters, for period 1 x 10^{-4} $s^{-1}$to 1 X 10^{-3} s^{-1}, as shown in Table 5.1.

Table 5.1. Extract from the output of the program STRIKE that was run for the station 1 of each profile for the period range 1 x 10^{-4} $s^{-1}$to 1 X 10^{-3} s^{-1}. For each single station the output shows the misfit (RMS error, the shear angle e and the twist angle t.

Station	Strike	RMS	Shear	Twist
L3500dp_stat_1	-2.7 (87.3)	0.2	0.0	3.2
L4500dp_stat_1	61 (-29.0)	1.0	4.0	-0.2
L5500dp_stat_1	52.8 (-37.2)	1.2	-0.5	11.6

The first column represents the station number. The first number in the second column denotes the angle of the geological feature in strike direction (TE mode) and the number in brackets the direction perpendicular to strike (TM mode).

The second approach was a single site analysis where each site was assessed independently for all possible azimuths (0 -90˚) with an increment of 5 ° to assess the sensitivity to the 2D strike direction. More results from the program STRIKE for the study area are presented inAppendix B, C and D. This was performed for different frequency bands. The accuracy of the strike analysis beneath each station is calculated by examining the RMS misfit modelled values to the data. The RMS plots also show sensitivity of the data to the geoelectric strike angle. Lower RMS values indicate stations that are compatible with, the geoelectric strike direction of the geology beneath the station.

The calculated RMS errors had values less than three. It can be seen that the majority of the stations accept the whole azimuth range (0 to 90 degrees) at different depths (frequencies). Strike analysis results from station 1, 10, 20, 30 and 40 of each line are attached in this report.

Since the calculated RMS error values show that most of the stations are relatively compatible with the geoelectric strike with an RMS value of less than 1.5, hence we could use Zonge's

SCS2D modelling software which assumes that the data were collected perpendicular to strike (MacInnes and Zonge, 1996).

When using Zonge's SCS2D modelling it is not necessary to decompose the data before 2D modelling because the algorithm assumes that the profiles run across strike at right angles and that the geology is of infinite strike extent (MacInnes and Zonge, 1996). Program SCS2D computations are based on two dimensional models that have uniform properties perpendicular to the section or profile (MacInnes and Zonge, 1996). Thus, prior to data collection, preliminary geoelectric strike direction was estimated at an azimuth of ˜ 90˚ by using the magnetic anomaly signature and orientation of the geologically mapped faults.

5.11 NSAMT Bostick inversion and modelling

5.11.1 Forward Modelling

Forward modelling is the prediction of the geophysical response given a geologic model. A probable geological situation for a sedimentary hosted geothermal energy resource was modelled using SCS2D software for a 2D model. Figure 5.8 show synthetic models for a geological situation comprising of a deep seated fault in a sedimentary basin, a capping rock and basement rock. SCS2D was also used for inversion to calculate apparent resistivity values versus elevation (Figure 5.9) of the modelled geological situation.

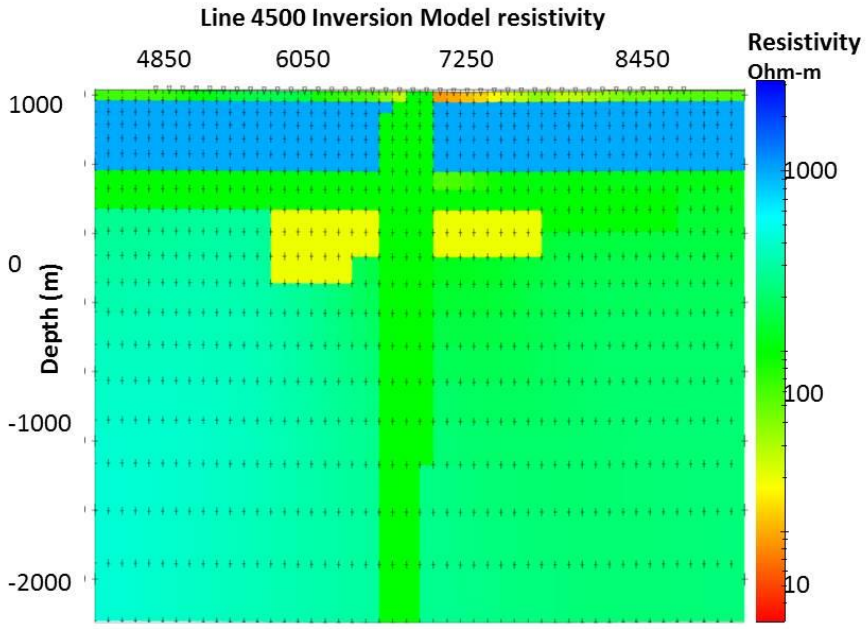

Figure 5.8. Synthetic model for a geothermal energy resource consisting of four layers and a deep seated conductive vertical fault zone. The near surface sedimentary layer was assigned very high resistivity values (1000 Ωm) and low resistivity values (< 100 Ωm) assigned to the layer underlying it. Also introduced was a deep seated conductive vertical discontinuity zone (< 100 Ωm) that outcrops to surface. The portion that makes the basement was assigned high resistivity values (>1000 Ωm).

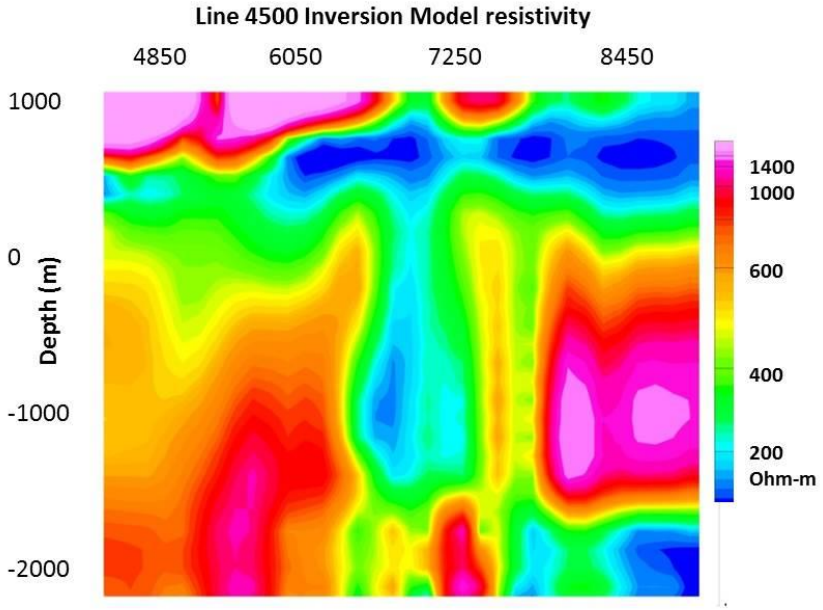

Figure 5.9. Example of a 2D inversion results of a four layer synthetic geothermal energy resource consisting of a deep seated conductive vertical fault. The near surface can be attributed to the sediments, whilst the near surface conductive layer that is conductive can be associated with the mudstones. The vertical conductive zone can be attributed to the deep seated fault. The crystalline basement layer gives rise to the high resistivity bottom layer.

5.11.2 SCS2D Inversion Modelling workflow and parameters used

The resulting processed data (.avg file format), produced by the CSAVGW program, were then inverted to a resistivity versus depth model cross-section using SCS2D, a 2D smooth-model inversion program developed by Zonge International. The program uses the inversion algorithm by Bostick (1977). It is a robust method for converting passive AMT data to resistivity model cross-sections. The Bostick inversion algorithm generates a continuous resistivity distribution versus depth (Bostick, 1977) which was automatically computed for 1D curves and 2D cross sections.

SCS2D inverts observed impedance phase and apparent resistivity data from a line of soundings to determine resistivities in a model cross-section (MacInnes & Zonge, 1996). Smooth modelling decreases non-essential features which can complicate interpretation of the data hence the model should be as smooth as possible (Constable et al., 1987). Either TM-mode data, TE-mode or both were inverted for each edited MT sounding curve.

As smooth-model inversion does not need any initial information about geologic structure, we did not provide preliminary information regarding any known geological structure to our model and observed data were automatically transformed to a resistivity model cross-section providing an image of the subsurface. A background resistivity model computed from a 2D moving average of observed apparent resistivity data was used to generate default starting and background models for this study. SCS2D model sections are always perpendicular to strike. Observed data are automatically transformed to a resistivity model cross-section providing an image of the subsurface (Figure 5.11).

To calculate apparent resistivity and impedance phase for a given model section, SCS2D uses a 2D, finite-element algorithm to calculate far-field passive MT data (MacInnes and Zonge, 1996). SCS2D uses Bostick inversion algorithm to iteratively minimise the difference between observed and calculated data, the difference between background and inversion models, and inversion-model roughness by checking RMS of the inversion model. It also uses an estimate of the maximum far-field, depth-of-investigation to set the default model section depth extent. Data are mapped to the model section using station location and Bostick depths. A RMS model roughness plot is displayed on the lower-left corner of the screen during the RSCS1D and RSCS2D inversion process.

During the inversion, model section-pixel resistivities were adjusted for 8 iterations or until the misfit between the calculated apparent resistivity and impedance phases and the observed data are minimal.

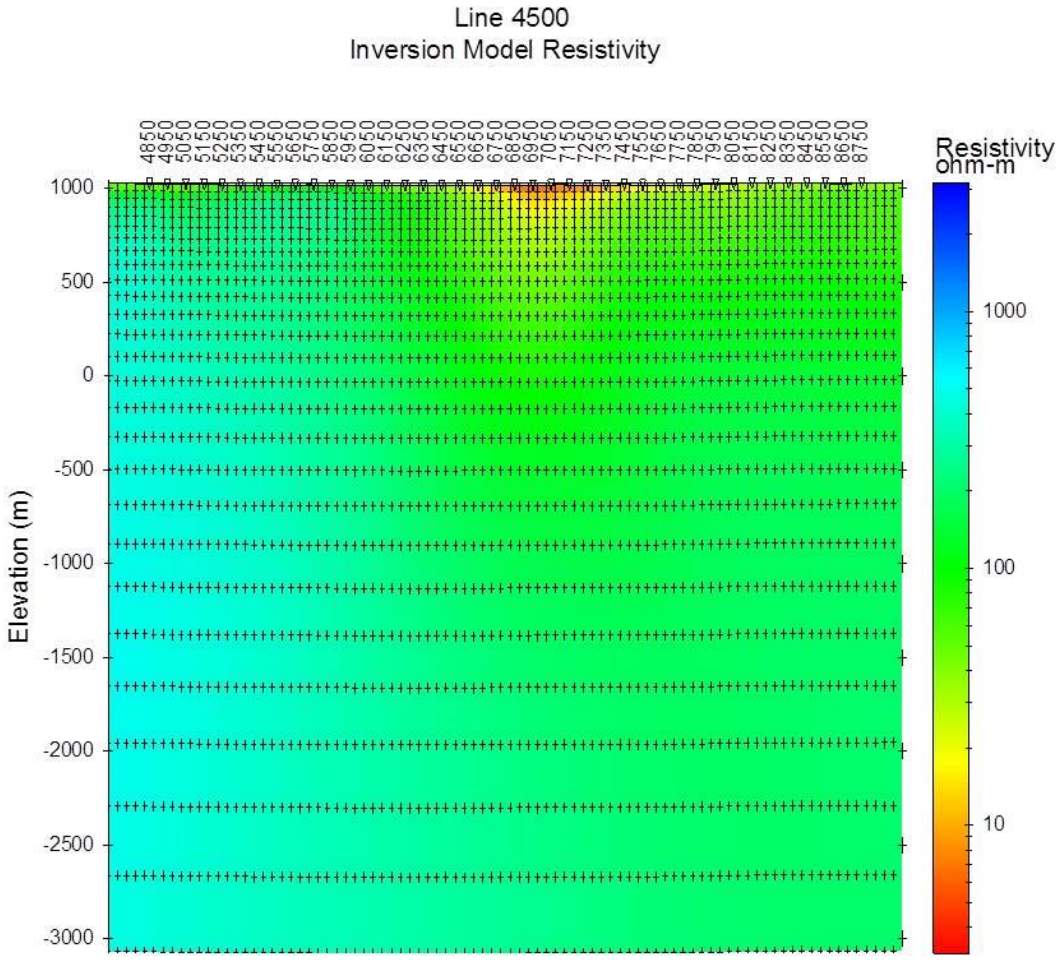

Figure 5.10. Calculated resistivity model section built using L4500 data with the lowest far-field frequency set to 192 Hertz, and a 2D moving-average of data for background resistivity. Calculated resistivity data are mapped to the model section using station location and Bostick depths.

Model sensitivities properties are also saved as percentage values. They provide an estimate to the maximum depth of investigation using the skin depth effect. Areas with hundred percent values are resolved fully by observed data for the depth. Data resolution of model-section depends on the percent sensitivity. One percent or two percent sensitivity roughly contours the maximum depth of investigation. Model structure below the 1% sensitivity contour is primarily controlled by model constraints and not by field data. The maximum depth of investigation is reduced by broad conductive areas, while high resistivity features increase the depth of investigation relative to a uniform half space. Model sensitivities are plotted as contours on all model sections in this study.

5.11.3 Data review after building models

The log/ log plots of observed data [$\log_{10}$ (apparent resistivity) versus $\log_{10}$ (frequency)] plots of individual sounding curves are generated by selecting "Review Data" from the main menu of RSCS2D and are helpful to determine the variation of apparent resistivity with frequency (Figure 5.11). The log/log plots also show uncertainties in the model sensitivities which will guide your interpretations at different depths (length of error bars represent model sensitivity at that depth).

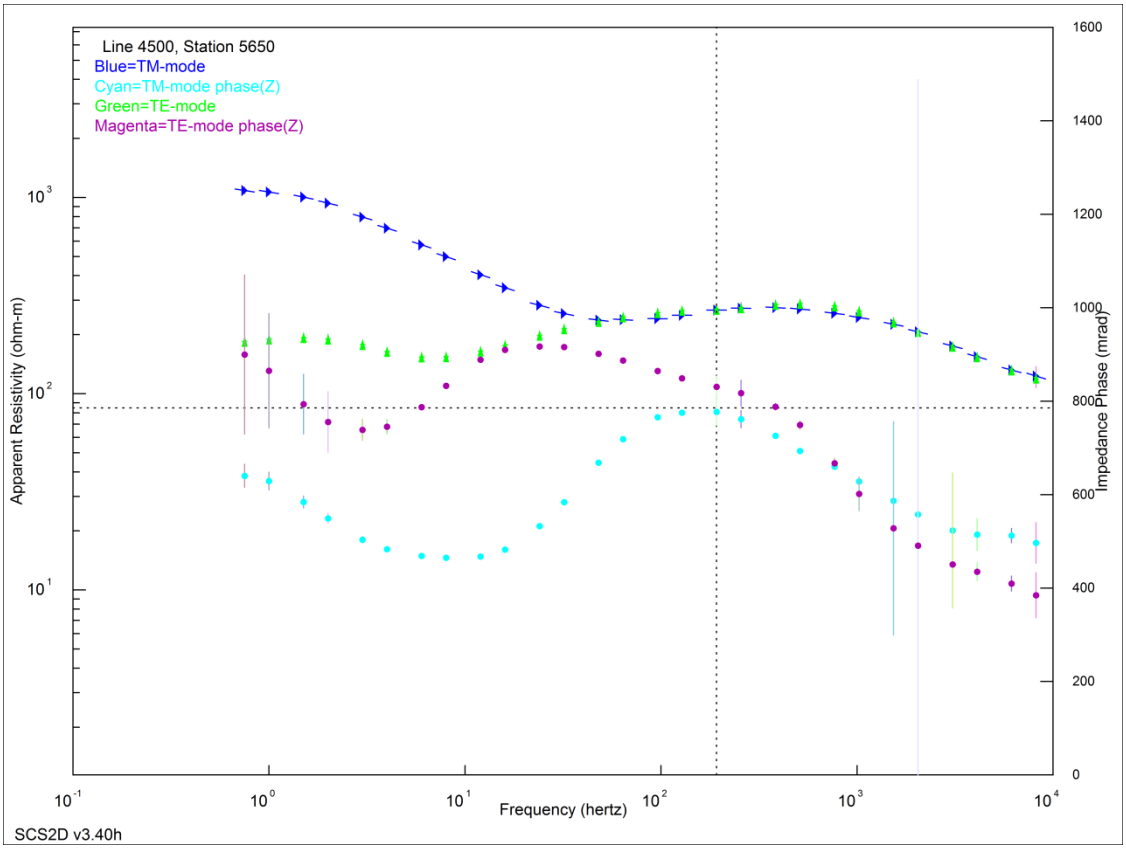

Figure 5.11. Log $_{10}$ (apparent resistivity) and phase versus $\log_{10}$ (frequency) plots of sounding curve at Line 4500, station 5650.

5.11.4 1D Inversion Modelling

The models were inverted by selecting the 1D CS/NS Inversion menu option from SCS2D's main menu. SCS2D uses the Bostick inversion algorithm to invert data for each station by using models with many horizontal layers to approximate smooth resistivity variation with

increasing depth (Figure 5.12). The Bostick inversion algorithm generates a continuous resistivity distribution versus depth (Bostick, 1977) which is automatically computed for 1D curves as shown in Figure 5.13.

For each sounding the edited invariant (combination of TE and Tm modes) mode data were chosen for calculation for an inversion model because it calculates the geometric resistivity mean of Z_{xy} and Z_{yx} and the arithmetic mean of the two phases ϕ_{xy} and ϕ_{yx} (WinGLink, 2005). The smooth-model automatically transforms the observed data to a resistivity model pseudosection providing an image of the subsurface. The results from the SCS2D program for each station of all lines are shown in Appendix E and one is shown below (Figure 5.13), including the best-fit model calculation.

Observed apparent resistivity values are shown by posted triangles with TM-mode and TE-mode data in blue and green respectively. Apparent resistivity error is indicated by short vertical lines although it is not shown in the diagram since the sounding was of good quality. When inversion is complete, calculated apparent resistivities are shown by a solid curve on the right hand side (Figure 5.13).

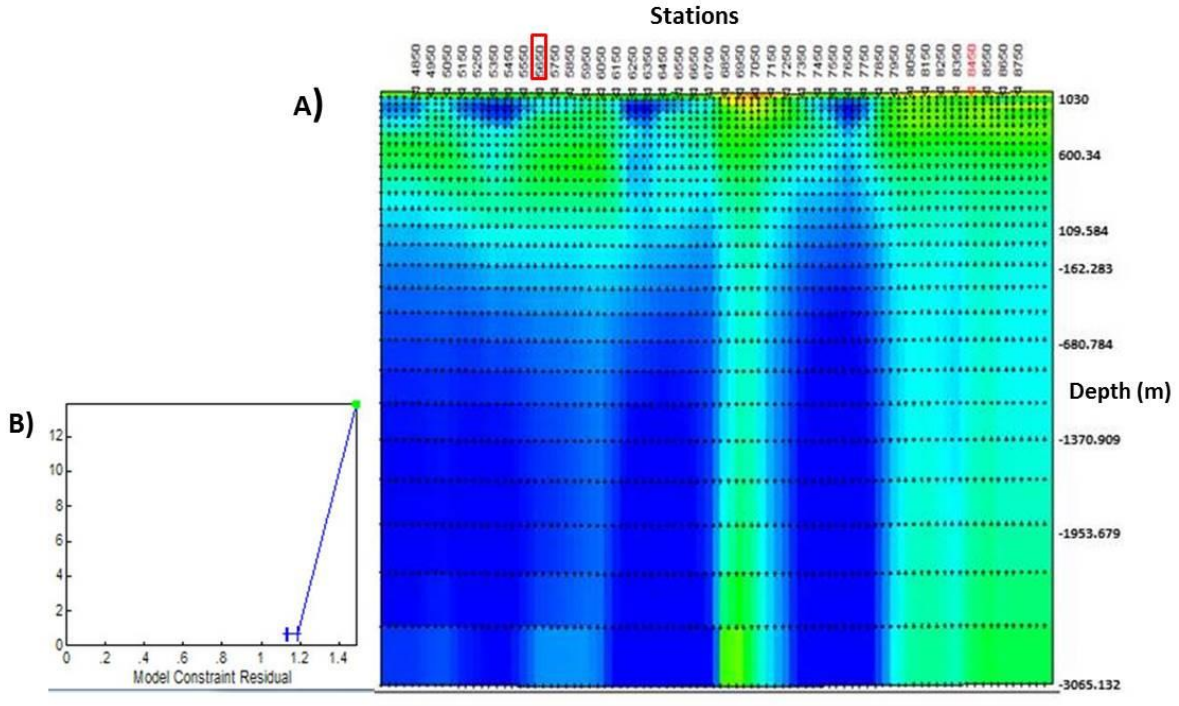

Figure 5.12. A) shows inversion model from averaged data using 1D inversion algorithm by Bostick (1977). This example shows all stations from line 4500 combined together to give a pseudo cross-section. B) shows a plot of data-fit residuals versus model constraint residuals which emphasises trade-off between fitting observed data versus maintaining a smoothly varying mode.

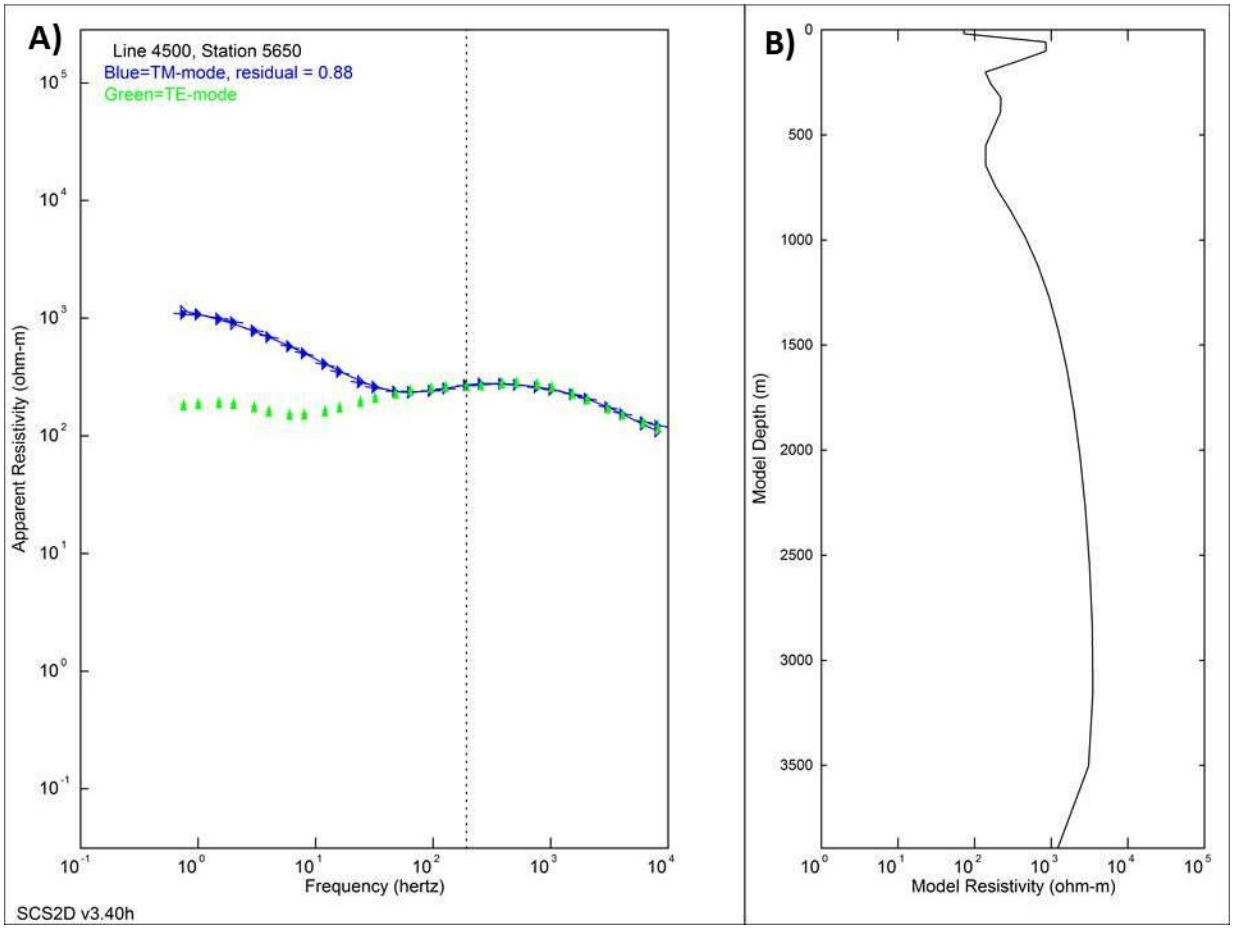

Figure 5.13. 1D Inversion model from averaged data using inversion algorithm of Bostick for line 4500, station 5650 (red box in Figure 5.12). Diagram A) shows observed apparent resistivity values indicated by triangle, with TM-mode data (blue) and TE-mode data (green). Apparent resistivity error is indicated by short vertical lines. The best-fit model of the calculated apparent resistivity is shown by the solid black line in B).

All models show a highly resistive (~10^3 Ωm) top layer that overlies a zone of low resistivity (~10^2 Ωm) between 250 and 750 m depth, which can be interpreted as the sedimentary basin. This conductive zone is underlain by a thick layer of high resistivity (>10^3 Ωm) which extends to depths greater than the mapped depth of 2500 m.

5.11.5 Results of the AMT 1D inversion cross sections

The AMT 1D inversion cross-sections are 1D curves that have been interpolated for resistivity against depth (period) and then contoured images. In these plots, high resistivities are shown in "cool" colours (blue, green) whilst "warm" colours (orange, red) represent low resistivities. Below are detailed discussions of the inversion cross sections. The interpolated pseudosections of the TE, TM and invariant modes are divided into the conductive layers (CL), conductive bodies (CB), resistive layers (RL), resistive bodies (RB) and discontinuities (D).

Profile L3500

This profile (Figures 5.4 and 5.5) is located at easting 473500 and is oriented south to north (from northing 8304750 m to 8308750 m). It is situated in the highly magnetic granitoids of the Hook Batholith. Moving from the south, 0 – 300 m, the profile goes through the pebbly feldspathic grit, 300-650 m, it goes through the conglomerates both of the Katanga group, cuts across the faults of the Mwembeshi Shear Zone at 650 m from the start and from 650 to 2000 m it then goes through the porphyroblastic biotite adamellite rocks of the Hook Batholith. From 2000 to 4000 m the line goes through the argillaceous quartzite rocks of the Lufilian Arc.

The AMT 1D resistivity model (Figure 5.14) shows a thin horizontal resistive layer (RL1) with a depth range of 0 m to 50 m starting from the south of the line, 8304750 m up to northing 8305345 m where its depth range starts increasing towards northing 8306115 m. This layer has inwards dip from this point. The layer has its maximum depth of 200 m. This highly resistive surface layer ends at northing 8306900 m, starts again at northing 8308475 m and continues until the end of the profile. The vertical discontinuity zone (D1) marks the contact between the resistive top layer and another top layer that is very conductive named CL1. D1 starts from northing 8307410 m to 8308000 m and seems to extent beyond the modelled depth of 2500 m. Another less conductive discontinuity (D2) cuts CL1 and extents to surface cutting the highly resistive top layer at about northing 8306405 m. The resistive top layer is characterized by resistivity values greater than 1000 Ωm whilst CL1 is characterized by resistivity values of ~200 Ωm up to 750 Ωm. CL1 is underlying the highly resistive top layer from the beginning of the line until it is truncated by the discontinuity structure. It extents to depths of about 1000 m. Inside the conductive layer are more conductive bodies CB1, CB2 and a very thin conductive layer CL2. These are characterized by resistivity values less than 100 Ωm

Underlying the conductive layer (CL1) are two highly resistive bodies (RB1 and RB2) characterised by resistivity values greater than 1000 Ωm. They both extent to depths beyond the modelled depth of 2500 m. These two resistive bodies are also cross cut by the vertical discontinuity (D).

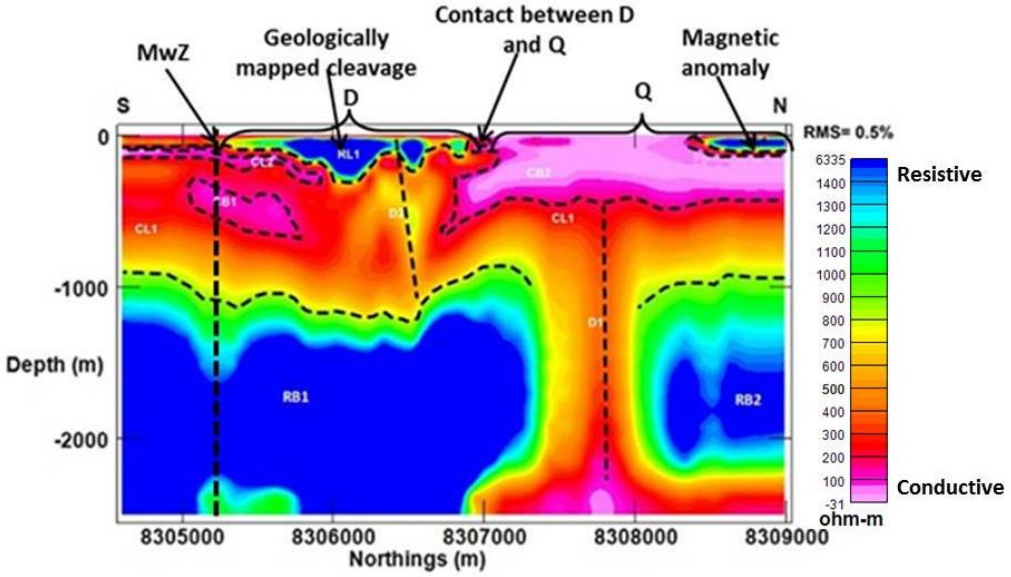

Figure 5.14. MT 1D resistivity cross-section of profile L3500 modelled using the 1D inversion algorithm at depth interval of 0-2500 m. An average of TM and TE modes (INV) was used. The conductive layers (CL), conductive bodies (CB), resistive layers (RL), resistive bodies (RB) and discontinuities (D) are discussed in the text.

Profile L4500

Profile L4500 (Figures 5.4 and 5.5) is located at easting 474500 and is oriented south to north (from northing 8304750 m to 8308750 m). It is situated in the highly magnetic granitoids of the Hook Batholith. Moving from the south, 0 – 560 m, the profile goes through the pebbly feldspathic grit of the Katanga group, cuts across the faults of the Mwembeshi Shear Zone at 560 m from the start and from 560 to 2660 m it then goes through the porphyroblastic biotite adamellite rocks of the Hook Batholith. The profile passes a hot spring at 2020 m from start and the other one at 2370 m from the start but slightly on the western side. From 2660 to 4000 m the line goes through the argillaceous quartzite rocks of the Lufilian Arc.

The resistivity section (Figure 5.15) shows a top undulating resistive horizontal layer (RL1) that starts from 8304750 m up to northing 8307785 m although being interrupted at some points along the profile. RL1 is characterised by resistivity values greater than 1000 Ωm and is in the depth range of about 0 – 225 m. This layer is truncated by a D1 at northing 8305900 and another conductivity discontinuity; D2 starting from northing 8306815 m to 8307275 m. Underlying this top resistive layer is conductive layer (CL1) starting from northing 8304960 and extending beyond the end of the profile. It is characterized by resistivity values of 200 Ωm

up to 800 Ωm. It is within an average depth range of 200 – 1400 m in the southern part of the profile and from northing 8307925 m it extents to depths beyond the modelled depth of 2500 m. More conductive layer and conductive zones characterized by resistivity values less than 100 Ωm are found within the conductive layer (CL1). Another thin conductive layer (CL2) is also undulating and is within a depth range of 100 - 240 m and outcrops at surface at discontinuity zone (D2) located at 8307100 m. It starts from northing 8306810 m and ends at northing 8307310 m. The more conductive layer (CL2) also outcrops to surface and extends beyond the modelled depth from northing 8307785 m up to beyond the mapped length. Two more conductive bodies (CB1 and CB2) are found within the conductive layer (CL1). They are both characterized by very low resistivity values of less than 100 Ωm and are both in the depth range of about 390 m to 1340 m. CB1 is located from northing 8305190 m to 8306270 m whilst CB2 is from northing 8306750 up to 8307180 m. They are both in the vicinity of the two discontinuity zones D1 and D2. D1 and D2 are both discontinuity zones that crosscut the high resistivity bodies that make up the basement and can also be observed in the top layers. These basement high resistivity bodies (RB1 and RB2) are characterised by resistivity values > 900 Ωm and are found in the depth ranges of 1340 m extenting deeper than the modelled depth of 2500 m although it extents to surface towards the beginning of the profile.

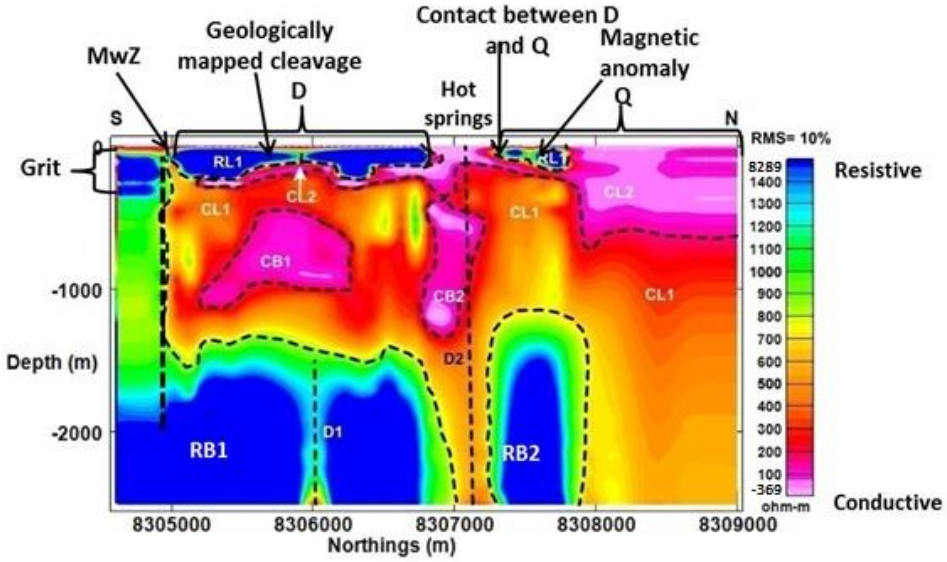

Figure 5.15. MT 1D resistivity cross-section of MT profile L4500 modelled using the 1D inversion algorithm at depth interval of 0-2500 m. An average of TM and TE modes (INV) was used. The conductive layers (CL), conductive bodies (CB), resistive layers (RL), resistive body (RB) and discontinuities (D) are discussed in the text.

Profile L5500

Profile L5500 (Figures 5.4 and 5.5) is located at easting 475500 and oriented south to north (from northing 8304750 m to 8308750 m) and is situated in the highly magnetic granitoids of the Hook Batholith. Moving from the south, 0 – 440 m, the profile goes through the pebbly feldspathic grit of the Katanga group, cuts across the faults of the Mwembeshi Shear Zone at 440 m from the start and from 440 to 2630 m it then goes through the porphyroblastic biotite adamellite rocks of the Hook Batholith. From 2630 to 4000 m the profile goes through the argillaceous quartzite rocks of the Lufilian Arc.

A very resistive thin layer (RL1) can be observed from 8304750 m to about 830480 m (Figure 5.16). It is truncated at northing 8306000 by a conductive discontinuity (D3). RL1 is characterized by resistivity values greater than 1000 Ωm and is found at a depth range from 0 – 30 m. The top resistivity layer is underlain by a conductive layer (CL2) characterized by resistivity values of 200 – 800 Ωm. It occupies depths from about 30 m to about 1800 m. CL2 hosts more conductive bodies (CB1 and CB2) and a resistive body (RB1).

Underlying the conductive layer (CL2) is a high resistivity basement which extents to depths beyond 2500 m and characterized by resistivity values greater than 1000 Ωm to greater than 1400 Ωm. This resistive layer is crosscut by very deep vertical conductive discontinuities (D1, D2, D3 and D4).

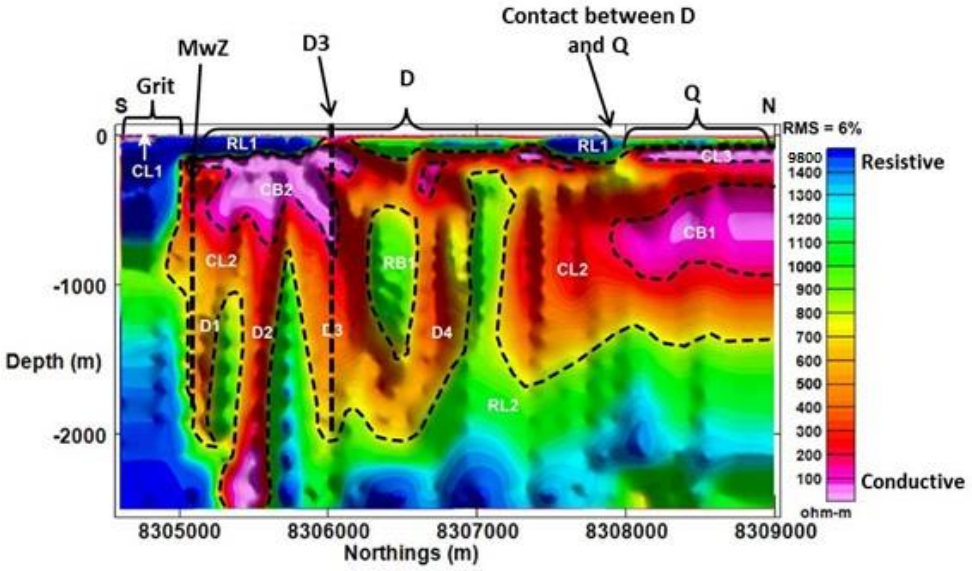

Figure 5.16. MT 1D resistivity cross-section of profile L5500 modelled using the 1D inversion algorithm at depth interval of 0-2500 m. An average of Tm and Te modes (INV) was used. The conductive layers (CL), conductive bodies (CB), resistive layers (RL), resistive bodies (RB) and discontinuities (D) are discussed in the text.

In general, the 1D MT modelling of the profiles (Figures 5.14 to 5.16) may be divided into two generally flat layers, vertical discontinuity zones and basement of the following electrical response:

- A shallow (variable depth from 0-200 m) domain of very high resistivity >1000 Ωm. This high resistivity domain does not always outcrop especially at those areas that are water rich. This high resistivity surface layer can be attributed to the conglomerate and feldspathic grit rocks of the Katanga group.
- A second domain underlying the high resistivity surface layer that is associated with low resistivity <400 Ωm. This layer can be attributed to the argillaceous quartzite and metasedimentary psammitic schists of the Lufillian Arc. This layer has a maximum depth of about 1000 m.
- Very conductive bodies are also found within the above conductive layer associated with resistivity values less than 100 Ωm. These can be attributed to water rich regions and are usually found around discontinuity zones.
- Very conductive discontinuity zones that are deeply seated and are associated with resistivity values less than 400 Ωm. These can possibly be attributed to faults.
- The crystalline granitic basement is generally associated with high resistivity >1000 Ωm with gradual resistivity changes across steeply dipping boundaries (conductive vertical features). The basement starts from at least 1000 m depth.

The 1D models were very helpful in giving a first indication of the resistivity structure of the geothermal energy resource and for providing a rough idea of constraints to use for the 2D inversion.

5.12 2D Inversion Modelling

1D inversion produces resistivity-depth images that are distorted by 2D topography, while 2D inversion images are not. 2D smooth model inversion produces estimated resistivity values that vary smoothly both horizontally along the plane of the section and with depth (MacInnes and Zonge, 1996). This section describes the 2D inversion of the Kwako Hills data. To create a model, 2D inversion was carried out on the data by selecting the "2D CS/NS Inversion" menu option from SCS2D's main menu. Different inversion parameters and constraints were tested in order to derive the most reasonable result. The data were then gridded using Geosoft Oasis

Montaj. The best models were determined with reference to the known geology, ground magnetic interpretations and 1D inversion results.

Due to their different sensitivities to geology, TE and TM modes will produce different resistivity models but their different results complement each other (Unsworth et al., 1999) e.g. Figure 5.17. For this study, three models were created for each profile using TE, TM and INV (a combination of TE and TM modes) modes. Berdichevsky et al. (1998) discovered that while TM mode is more favourable for mapping near surface structure, TE mode will map deeper structures. Also the TE mode is more successful in mapping 3-D resistive structures whilst the TM mode is more successful in mapping 3-D effects caused by conductive structures. A bimodal MT inversion 2D vector mode (invariant) which is a mode with equal weighting on the TM and TE components produces better models that are close to the expected geology. For better results, joint modelling of the TM and TE mode (Invariant mode) may help clarify the modelling results by filling gaps left by one mode by using the other mode.

5.12.1 Results of the 2D MT inversion cross-sections

The results of processing and modelling the data for each profile are shown below with their RMS values (Figures 5.17 to Figure 5.19). The root mean square values are used to compare calculated data and measured data to assess the validity of the model. Like the 1D sections, high resistivities are shown in "cool" colours (green, blue) whilst "warm" colours (red, orange) represent low resistivities. The interpolated psuedosections of the TE, TM and invariant (INV) modes are divided into the conductive layers (CL), conductive bodies (CB), resistive layers (RL), resistive bodies (RB) and discontinuities (D).

Profile L3500

Figure 5.17a shows the 2-D apparent resistivity sections for the TE mode, Figure 5.17b for the TM mode and Figure 5.17c for the INV mode for profile L3500 for a depth range of 0 – 2500 m. Since the invariant mode is a combination of the TM and TE mode it will be used more for the discussion or interpretation of the models. Two horizontal layers and intrusive bodies can be identified in all the three modes by analysing the changes in values of resistivity. A very resistive undulating layer (RL1) is observed along the surface of the cross sections. Since TE mode is more sensitive to resistive structures, RL1 is more prominent in the TE mode than the

TM mode. RL1 is characterised by resistivity values >1000 Ωm. In the TE mode it stretches from northing 8304975 m to the end of the profile whilst in the TM mode its extent is not clearly shown (Figure 5.17a). RL1 actually looks like small circular features in the TM mode results.

It can be observed that RL1 is truncated along the profile by conductive discontinuities namely D1, D2 and D3. Two discontinuities (D2 and D3) are shallow and extent to surface with D2 located at northing 8307500 m and D3 at 8308000 m. D1 is located at northing 830700 m and extents to a depth beyond the mapped depth of 2500 m.

RL1 is underlain by a semi-conductive layer (CL1) that is characterised by resistivity values in the range of 150- 850 Ωm. This layer is observed in both the TE and TM modes. Since the TM mode is more sensitive to conductive features than the TE mode (discussed earlier), TM mode can confidently be used to describe CL1 (Figure 5.17b). This layer forms an almost anticlinal shape with its peak located at about northing 8306730 m and the bottom of the peak at a depth of about 1000 m. Both sides of the peak extent deeper than the modelled depth of 2500 m. Unlike on the TE mode, on the TM mode, CL1 is starting from close to surface which could be because TM mode is not sensitive to resistive features.

Underlying CL1 is a very resistive body characterised by resistivity values >1000 Ωm. It is split into two bodies (RB1 and RB2) by a discontinuity zone (D1). This split of the resistive body is well shown in TM and INV modes.

The INV mode, a result of bimodal inversion or the information from the TE and TM modes complementing each other clearly shows the semi conductive layer (CL1) being sandwiched by the resistive layer and the resistive body (RL1 and RB). It shows RL1 starting from northing 8304975 until the end of the profile and being truncated by conductive discontinuities, D1, D2, D3 and D4. RL1 is within depth range of 0 – 200 m.

RL1 is underlain by a semi conductive layer (CL1) which has an anticlinal shape with its crest located at about northing 8306730 and its bottom at a depth of about 1000 m. Observed inside this layer are very conductive bodies (CB1, CB2, CB3 and CB4) characterised by resistivity values less than 100 Ωm. CB1 has apparent southward dip whilst CB2 has an apparent northward dip.

The basement is made up of a very resistive body (RB1) that also exhibits same anticlinal shape as the layer above it (CL1). This shape is caused by the conductive features that truncate

the layers. RB1 is within depth ranges of about 1000 m to depths beyond the modelled depth of 2500 m.

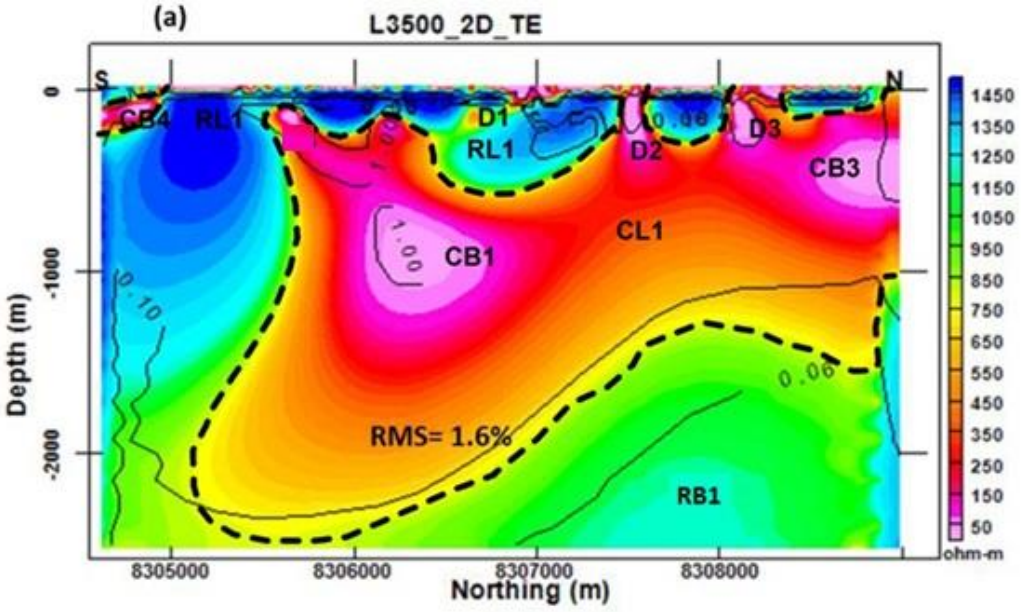

Figure 5.17 a. Two-dimensional MT TE mode modelling results for profile L3500. RMS is the root mean square (observed – calculated data). The maximum depth of investigation is shown by percent sensitivity contours (solid lines). The dashed lines show conductive layers (CL), conductive bodies (CB), resistive layers (RL) and discontinuities (D) that are discussed in the text.

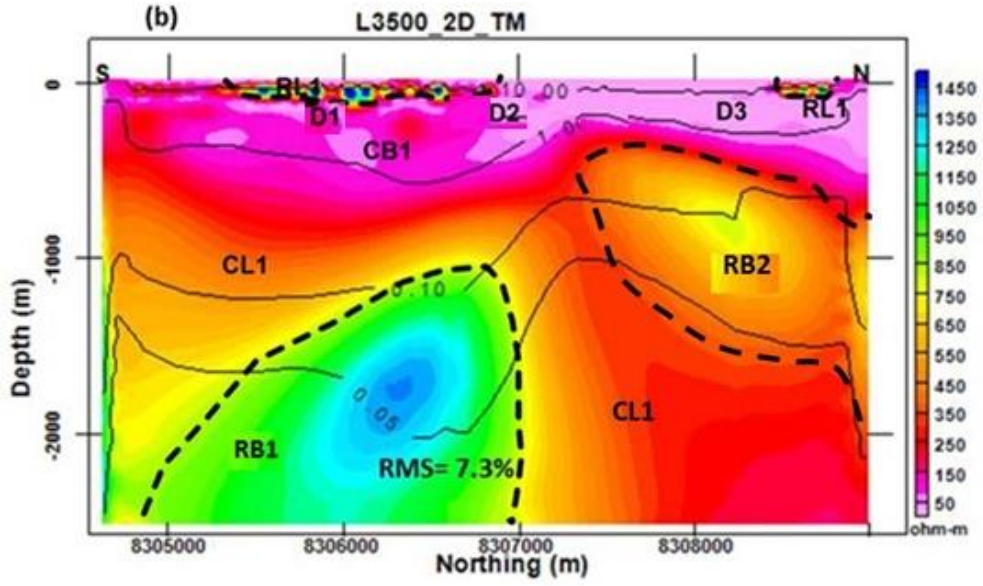

Figure 5.17b. Two-dimensional MT TM mode modelling results for profile L3500. RMS is the root mean square (observed – calculated data). The maximum depth of investigation is shown by percent sensitivity contours (solid lines). The dashed lines delineate conductive layers (CL1), conductive bodies (CB), resistive layers (RL), conductive layers and discontinuities (D) that are discussed in the text.

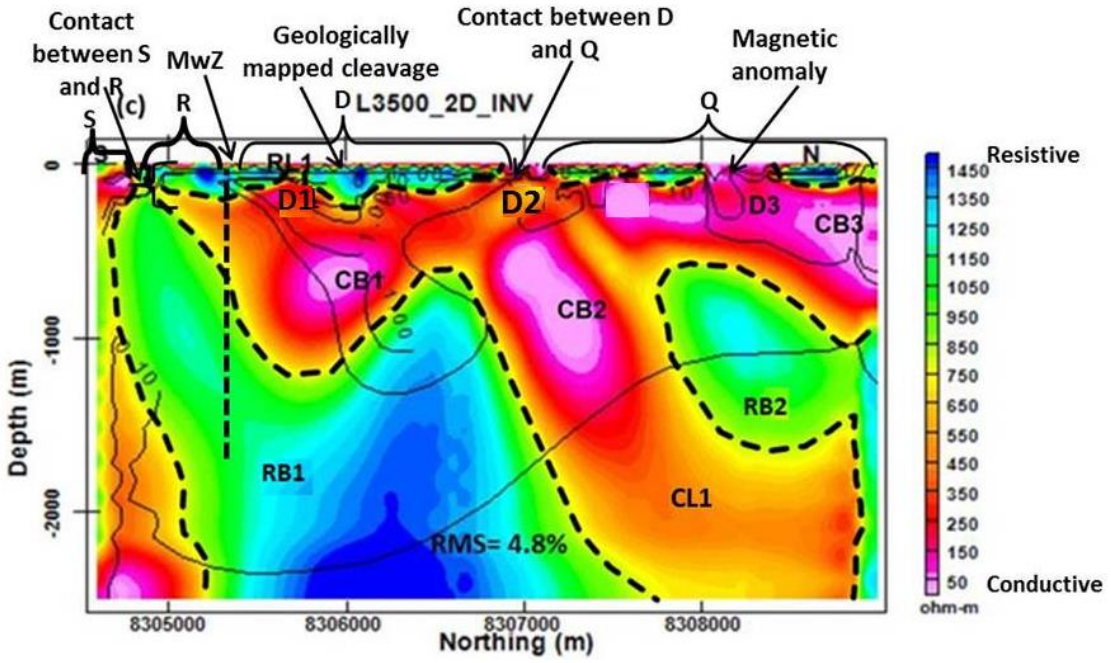

Figure 5.17c. Two-dimensional MT INV mode modelling results for profile L3500. RMS is the root mean square (observed – calculated data). The maximum depth of investigation is shown by percent sensitivity contours (solid lines). The dashed lines delineate conductive layers (CL1), conductive bodies (CB), resistive layers (RL), conductive layers and discontinuities (D) that are discussed in the text.

Profile L4500

The results of the TE mode (Figure 5.18a) shows a very resistive top layer near to the surface (RL1) stretching from the start of the profile up to about northing 8306775 m. This layer is characterised by resistivity values >1000 Ωm and it is interrupted by vertical conductive discontinuities namely D1, D2 and D3. D1 and D3 are found at northing 8306108 m and 8307900 m respectively and are close to the surface whilst D2 is located around northing 8306800 starting from surface and extending to depths beyond than 2500m. RL1 is an undulating layer within depth ranges of about 0 - 180 m. RL1 is not very clear in the TM mode section since TM mode is more sensitive to conductive anomalies (Figure 5.18b).

Underlying this resistive top layer is a semi conductive layer (CL1) characterised by resistivity values in the range of about 150-850 Ωm. This layer is more defined in the TM mode (Figure 5.18b) than in the TE mode (Figure 5.18a). This conductive layer is intruded by a more resistive body (RB) characterised by resistivity values >1000 Ωm. RB1 and RB2 are more defined in the TE mode (Figure 5.18a) and is observed to be within varying depth ranges

extending deeper than 2500 m (Figure 5.18b). In the TE mode, RB is observed to be starting close to surface in the region close to the start of the profile.

The invariant (INV) mode is a result of bimodal inversion that combines the TE and TM modes hence providing a better model (Figure 5.18c). The invariant mode shows the same top resistive layer (RL1), the basement resistive bodies (RB1 and RB2) which were both observed in the TE mode and the sandwiched semi conductive layer (CL1) observed in the TM mode (Figure 5.18c). Also the three discontinuities, D1, D2 and D3 are clearly shown in the INV mode. Discontinuity zone, D2 can be observed to cut across all the three layers from surface to depths greater than 2500. In the INV mode the resistive body is observed to have been split by a discontinuity zone (Figure 5.18c). The semi-conductive layer encompasses a more conductive body (CB1) and a more conductive smaller layer (CL2). These conductive features are more prominent or resolved in the TM mode than in the TE mode where they seem to be one body. The very conductive features are characterised by resistivity values less than 100 Ωm. CB1 is an almost vertical anomaly located along discontinuity zone D2 starting from near the surface to about 1000 m deep. CL2 is another very conductive feature found to the north of the discontinuity zone D2 and dipping to the north. It is in depth ranges of 215 m to 670 m, located from northing 8307460 m and stretches out of the mapped area. Features or layers on different sides of discontinuity zone D2 have different dips which give an anticlinal shape to the stratigraphy with the most resistive body right under the crest and dividing the conductive layer into two layers on either side of the crest or the resistive body (Figure 5.18c).

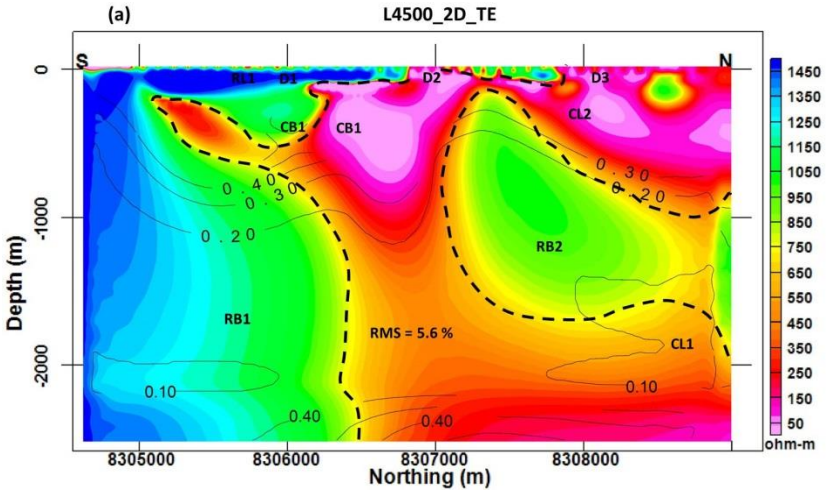

Figure 5.18a. Two-dimensional MT TE mode modelling results for profile L4500. RMS is the root mean square (observed – calculated data). The maximum depth of investigation is shown by percent sensitivity contours (solid lines). The dashed lines show conductive layers (CL), conductive bodies (CB), resistive layers (RL), conductive layers and discontinuities (D) that are discussed in the text.

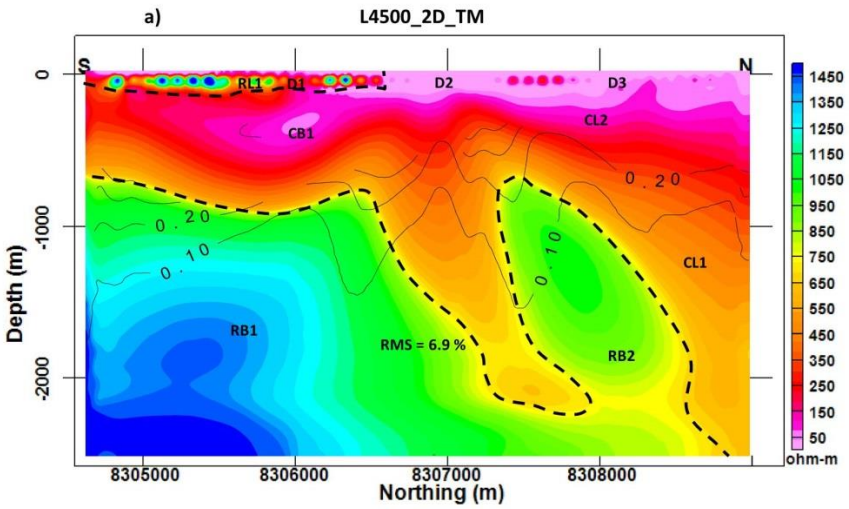

Figure 5.18b. Two-dimensional MT TM mode modelling results for profile L4500. RMS is the root mean square (observed – calculated data). The maximum depth of investigation is shown by percent sensitivity contours (solid lines). The dashed lines show conductive layers (CL), conductive bodies (CB), resistive layers (RL) and discontinuities (D) that are discussed in the text.

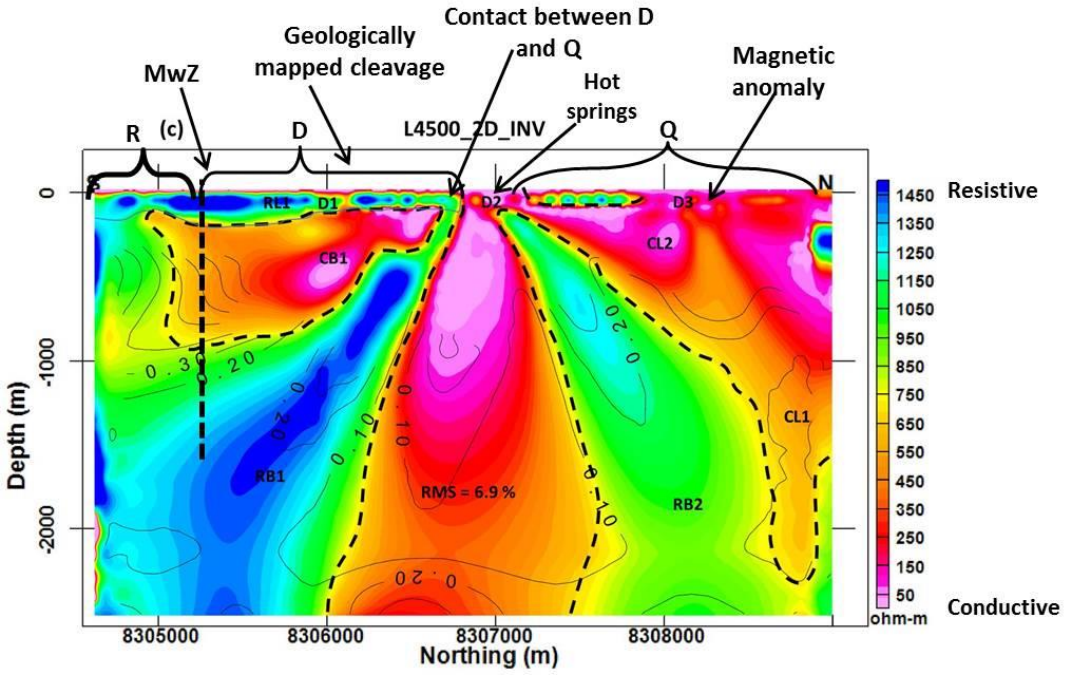

Figure 5.18c. Two-dimensional MT INV mode modelling results for profile L4500. RMS is the root mean square (observed – calculated data). The maximum depth of investigation is shown by percent sensitivity contours (solid lines). The dashed lines show conductive layers (CL), conductive bodies (CB), resistive layers (RL) and discontinuities (D) that are discussed in the text.

Profile L5500

Figures 5.19 a, b and c show the 2-D apparent resistivity sections for the TM, TE and INV modes for the profile L5500 for the depth of 0 – 2500 m.

Figure 5.19a shows the TE mode inversion results of profile L5500. The results clearly show the top resistive layer (RL1) which is not very clear in the TM mode results (Figure 5.19b) although it has the same parameters. Also observed in the TE mode results is a semi conductive layer similar to CL1 in the TM mode results below. It extents to depths of about 2180 m and is characterised by resistivity values in the range of 150 Ωm – 850 Ωm. This conductive layer (CL1) is divided into two bodies with same resistivity values by a resistive body (RB1) with resistivity values >1000 Ωm. RB1 continues to depths deeper than the modelled depth of 2500 m. The results of the TE mode clearly shows the top resistive layer (RL1), it also clearly shows the shallow discontinuities truncating RL1 namely D1, D2 and D3.

The TM mode is more sensitive to conductive features so it was used more to analyse the conductive anomalies along profile L5500 (Figure 5.19b). Figure 5.19b shows that there is a top thin horizontal resistive layer (RL1) starting from northing 8304800 m up to 8307950 m and within depth range of 0- 90 m. It is characterised by resistivity values >1000 Ωm. This thin layer is truncated by shallow discontinuities namely D1 and D2 located at northing 8306000 and 8307100 respectively (Figure 5.19b). Underlying RL1 is a semi conductive layer (CL1) which is outcropping at surface from the start of the profile to about northing 8304780 m and also outcrops from northing 8307950 beyond the end of the mapped length. It is characterised by resistivity values from 150 Ωm -850 Ωm. CL1 is dipping towards the north and is underlain by a very resistive body (RB1) which also dips towards the north (Figure 5.19c). RB1 is crosscut by Mwembeshi discontinuity zone (Figure 5.19c). Found inside the semi conductive layer (CL1) are very conductive bodies CB1, CB2 and CB3 located within depth ranges of 90 – 290 m. CB3 is located at northing 8306700 m (Figure 5.19b).

Figure (5.19c) shows the results of the joint inversion of TE and TM modes called INV mode. The results still show the top resistive layer (RL1) similar to the one observed in the TE mode results. Another conductive body CB1 is located right under the MwZ (Figure 5.19c). CB1 is within depth range of about 50 m – 1180 and like the other conductive bodies it is characterised by resistivity values less than 100 Ωm. The results also show the shallow discontinuities D1, D2, D3 crosscutting the top resistive layer (RL1). Also observed are the very conductive bodies CB1, CB2 and CB3 that are clearly shown in the TM mode results.

Underlying CL1 is a very resistive body (RB1) that is only crosscut by the MwZ fault at 8305260 m . RB1 extents to depths beyond 2500 m.

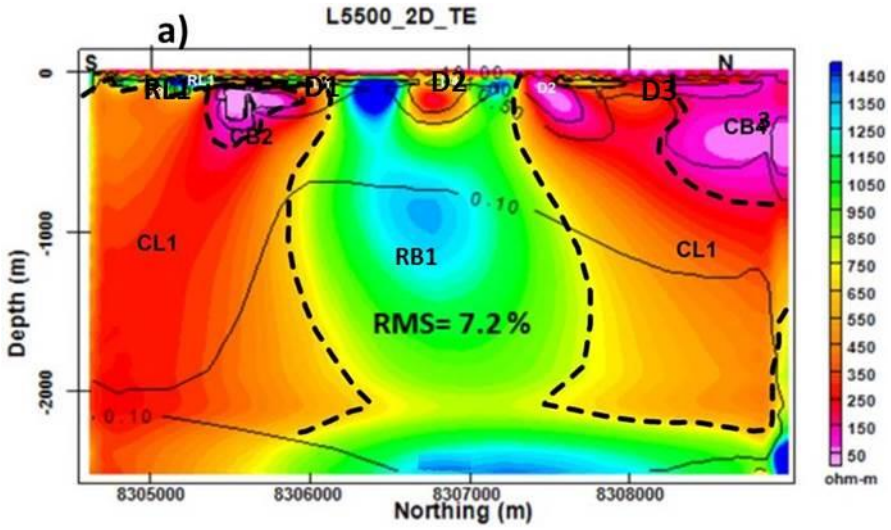

Figure 5.19a. Two-dimensional MT TE mode modelling results for profile L5500. RMS is the root mean square (observed – calculated data). The maximum depth of investigation is shown by percent sensitivity contours (solid lines). The dashed lines show conductive layers (CL), conductive bodies (CB), resistive layers (RL and discontinuities (D) that are discussed in the text.

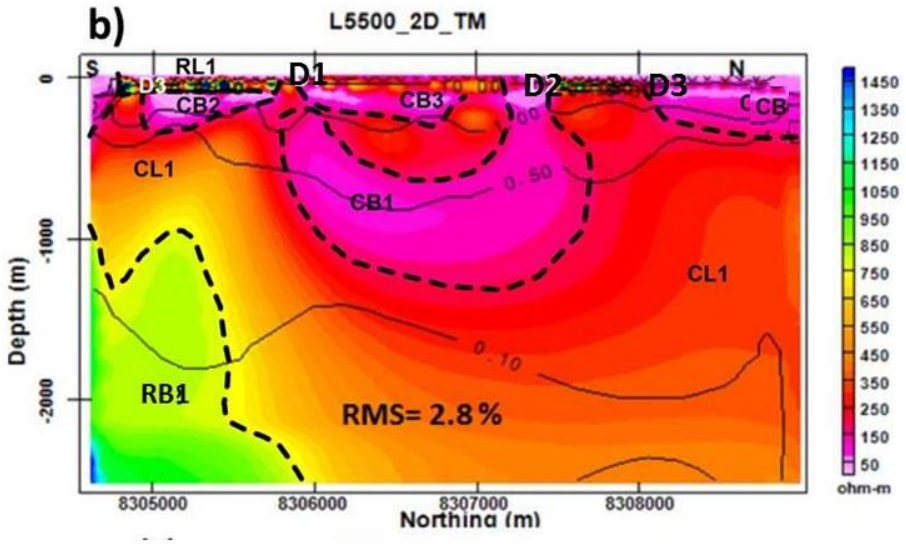

Figure 5.9b. Two-dimensional MT TM mode modelling results for profile L5500. RMS is the root mean square (observed – calculated data). The maximum depth of investigation is shown by percent sensitivity contours (solid lines). The dashed lines show conductive layers (CL), conductive bodies (CB), resistive layers (RL and discontinuities (D) that are discussed in the text.

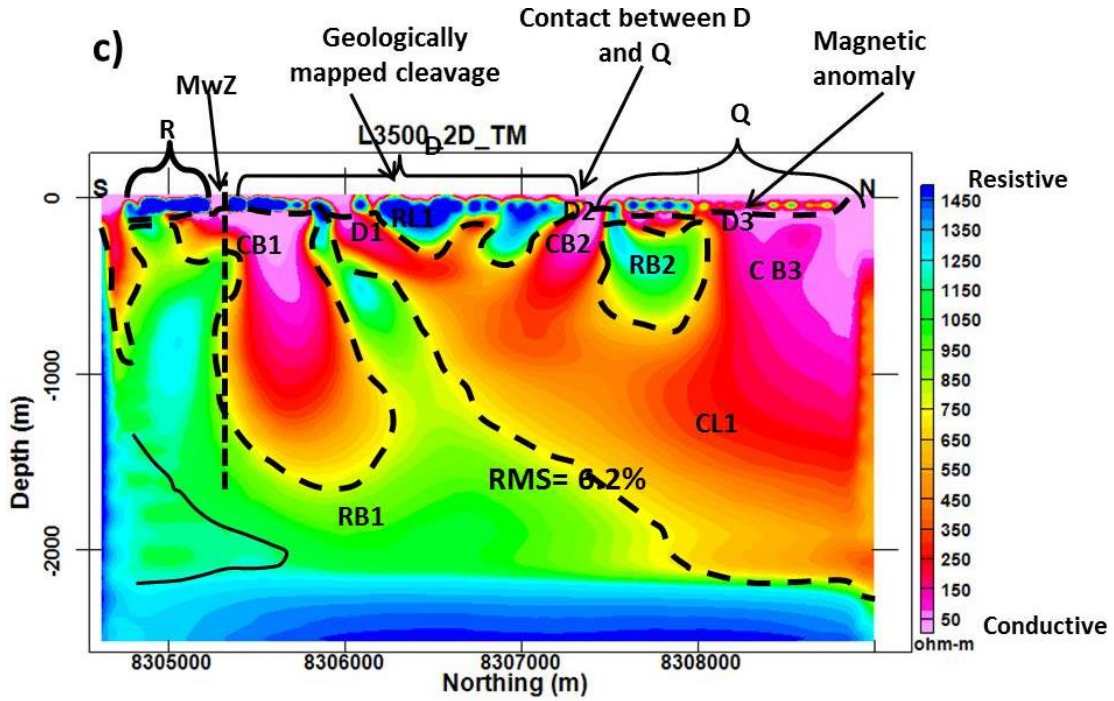

Figure 5.19c. Two-dimensional MT INV mode modelling results for profile L5500. RMS is the root mean square (observed – calculated data). The maximum depth of investigation is shown by percent sensitivity contours (solid lines). The dashed lines show conductive layers (CL), conductive bodies (CB), resistive layers (RL) and discontinuities (D) that are discussed in the text.

5.12.2 Summary

The interpretations of the MT profiles are preliminary and simplified cases based on limited geological studies and potential field data. All the inversion results have a low misfit and show similar resistivity characteristics when compared to the lithology information from the geology and ground magnetic maps. For instance, the high resistivity outcropping layers observed at the beginning of each profile almost exactly coincide with the outcropping conglomerates and feldspathic grit. The resistivity sections inverted from the three MT profiles show a conductive zone with resistivity values in the range of 150 – 850 Ωm that is overlain by a very resistive layer (>1000 Ωm). This can be clearly observed in TE and INV modes sections. Higher conductive bodies can be observed inside the conductive layer and they are clearer in the TM modes sections. They are characterised by resistivity values less than 50 Ωm. Very conductive vertical discontinuity zones that are deeply seated can be observed to be crosscutting the layers. Sometime these discontinuity zones reach the surface and in some areas extenting to depths beyond 2500 m**.**

The highly conductive layers coincide with the areas in the vicinity of the water rich regions and hot springs observed on surface. The outcropping vertical conductive anomalies that extent to surface also coincide with the faults, hot springs locations, fractures mapped by the magnetic

method and by geological mapping. At depth and in the absence of metallic conductors and graphite, these conductive anomalies can be attributed to the electrolytes in the pores or fractures of fractured rocks. The semi conductive layers also coincide well with the metasedimentary rocks of the Lufilian Arc. The difference in the exact position of the conductive layers between the profiles might be explained by the different positions and directions of the lines with respect to each other.

The 1D MT resistivity sections were produced from stitching together a series of 1-D models based on assumptions of a flat Earth with layered geology under the individual measuring sites with the vertical scale being depth. This resulted in the 1D resistivity-depth images that show good layering but poorly map the dip of the geological structures. The 1D MT resistivity sections clearly show the vertical structures compared to dipping ones. The 1D sections near surface resistivity contacts agree quite well with the contacts geologically mapped on surface and with ground magnetics method. 1-D inversion is shown to be more sensitive when mapping near surface features than 2-D inversion. Also 2D MT inversion model sections show 2D shaped structures whilst stitched 1D MT inversion model sections do not. The results show that TE and TM modes are affected differently according to the position of the 2D or 3D structures causing distortions. These distortions are avoided by combined 2D inversion of the TE and TM modes called invariant (INV) mode. For a better understanding and interpretation of the geology, the natural source audio magnetotelluric, geological mapping, magnetic susceptibility and magnetic data were integrated in the following section.

Chapter 6 Data integration and discussion

This section discusses the integration of the natural source audio magnetotelluric, geological mapping, magnetic susceptibility and magnetic data in characterising the geothermal resource at Kwako Hills prospect in the Mumbwa area in Zambia. The 1D and 2D MT resistivity models that were produced provide an indication of vertical discontinuities, the number and thickness of conductive and resistivity layers or bodies with depth. Results from magnetic susceptibility measurements taken from rock samples together with geological mapping information and close to surface results from the resistivity sections will aid with a preliminary geological map of the surface. On the other hand the results from ground magnetic provide information of the resultant magnetism of the study area starting from surface to basement rock. Integrating it with documented stratigraphic succession of the area and resistivity sections, we can come up with a preliminary geological model of the subsurface. For the purpose of near surface interpretation only AMT inversion results up to a depth of 1000 m were used. The resistivity sections from AMT data were overlain on-top of the geological map, Reduced To Pole TMI and first vertical derivative filtered data and geological maps of the study area that have faults and structures mapped from geological mapping, ground magnetic and aeromagnetic data (discussed earlier).

6.1 Profile L3500

Looking at the resistivity section overlain on the Reduced To Pole TMI image and moving south to north, the geological contacts between the Hook Batholith rocks and the Lufilian Arc rocks coincide very well with the magnetic contact between the high and low magnetic anomalies (Figure 6.1a). They also coincide with magnetic low, lineaments shown on the first vertical derivative filtered Reduced To Pole TMI image (Figure 6.1b). Moving from south to north, the profile starts on the Mwembeshi Shear Zone which is overlain by sedimentary rocks consisting of conglomerate and grit (Figure 6.1c). This sedimentary layer coincides with the high resistivity layer (RL1) on the AMT section and stretches from the start of the profile up to the end except at some zones where it is truncated by conductive discontinuities. After the sedimentary rocks of the MwZ, RL1 can be attributed to the outcropping porphyroblastic biotite adamellite rocks of the Hook Batholith and lastly the psammitic schists of the Lufilian Arc as shown on the geological map (Figure 6.1c).

Low resistivity discontinuity zones D1, D2, D3 and D4 that are characterised by very low resistivity values starting from surface and continuing with depth (Figure 6.1c). All the discontinuity zones coincide with low magnetic gradient anomalies hence can be attributed to sediments overlaying the foliated zones (Figure 6.1b). The resistivity section shows that there is a vertical conductive feature at the beginning of the profile that starts from the surface and extents to depths beyond than 1000 m. This feature coincides with the fault that was geologically mapped as the Mwembeshi Shear Zone fault. The high magnetic anomalies on the Reduced To Pole TMI image can be attributed to the high magnetic susceptibility measured on an outcropping porphyroblastic biotite adamellite sample along the profile. Since the magnetic method is ambiguous, the measured magnetic field intensity (high or low) is not due to the outcropping rocks only but a resultant of all the rocks below the measuring point. RL1 is not continuous all the way from the start to the end of the profile but is truncated at several discontinuity zones namely D1, D2, D3 and D4. The discontinuity zones D2 and D3 coincide with the contacts between the MwZ, Hook Batholith and Lufilian Arc outcropping rocks and D4 was mapped with ground magnetics (Figure 6.1c). The top conductive layer observed in resistivity section that starts from about northing 8307000 to the end of the profile coincides very well with the location of the alluvium field valley. These low resistivity values can be attributed to the water rich soil due to the water from the hot springs. Also observed on the AMT section is two high resistivity bodies RB1 and RB2. Their locations coincide with high magnetic anomalies with RB2 being deep seated whilst RB1 is in contact with RL1 (Figure 6.1a).

RB1 and RB2 should also be contributing to the high magnetic anomalies that are attributed to basement rocks. The first vertical derivative filter enhanced shallow high magnetic anomalies associated with outcropping RL1 and RB1 (Figure 6.1b). It also enhances shallow low magnetic anomalies coinciding with discontinuity zones D1, D2 and D4 mapped as fractured zones or geological contacts. Using the documented stratigraphy of the area, the resistive layer (RL1), the semi conductive middle layer (CL1) and the resistive bottom layer (RL2) can be attributed to the granites of the Hook Batholith, fractured, water filled metasediments in the Kundelungu series of the Lufilian Arc and granites and the basement granite-gneiss respectively. The images show that the fractured zone D2 is a deep seated fault extenting to depths beyond 1000 m in the resistivity section. The highly conductive bodies with resistivity values <100 Ωm can be attributed to regions filled with water. This is supported by the existence of the two hot springs in the area.

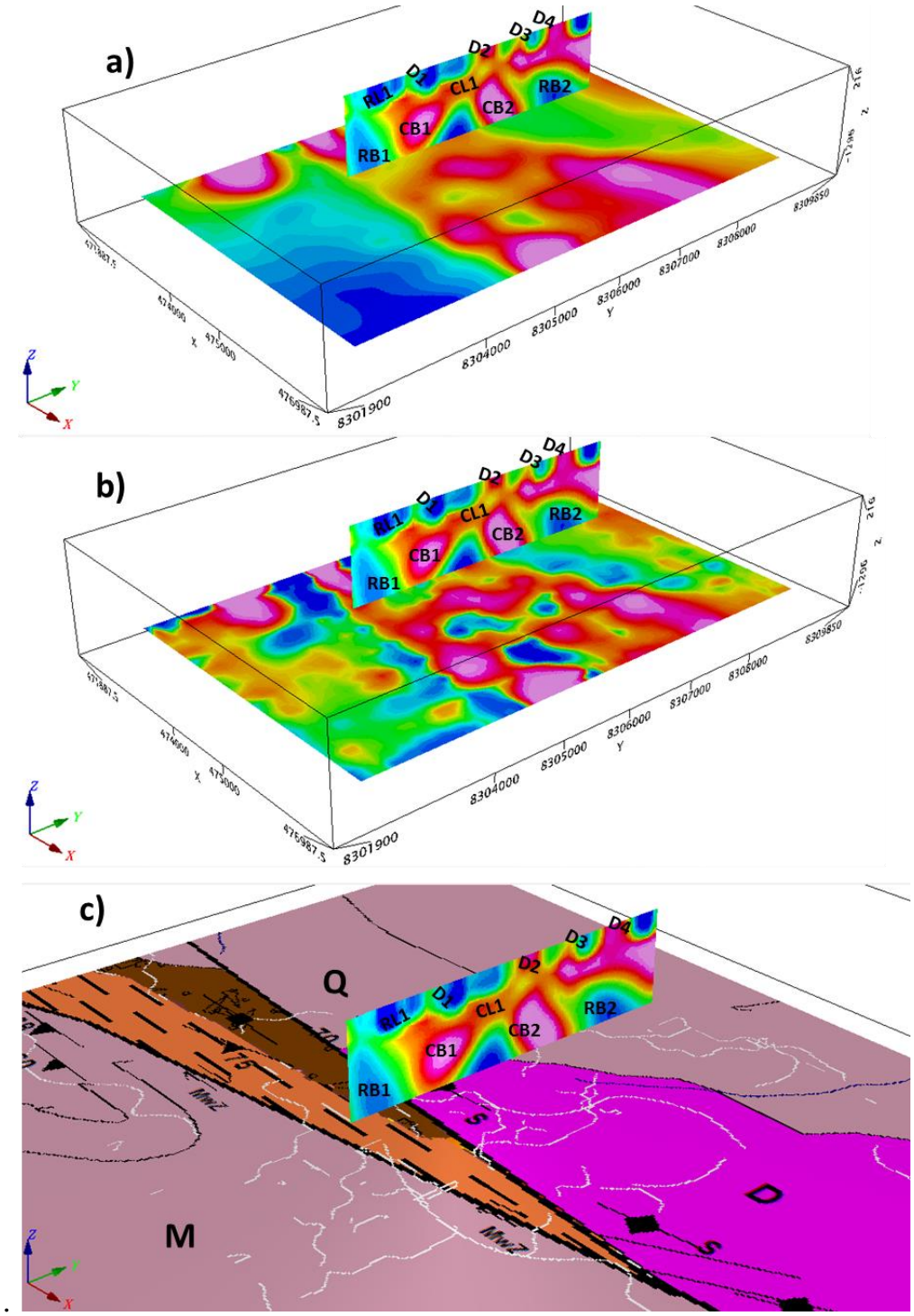

Figure 6.1. AMT section for profile L3500 overlain on the a) RTP TMI, b) first vertical derivative images and c) geological map with conductive layers, conductive bodies, resistive layers and discontinuities zones labelled as CL, CB, RL and D respectively. M, D and Q represent the psammitic schists, porphyroblastic biotite adamellite and argillaceous quartzite respectively as labelled on the geological map. The white lines represent the magnetic low lineaments mapped using the magnetic data.

6.2 Profile L4500

The resistivity section for profile L4500 was also overlain on the Reduced To Pole total magnetic intensity image, the first vertical derivative of the Reduced To Pole magnetic intensity image and on the geological map (Figure 6.2). Moving south to north, the geological contacts between the Hook Batholith rocks and the Lufilian Arc rocks also coincide very well with the magnetic contact between the high and low magnetic anomalies (Figure 6.2a). They also coincide with magnetic low, lineaments shown on the first vertical derivative filtered Reduced To Pole TMI image (Figure 6.2b). The profile also starts on the Mwembeshi Shear Zone which is overlain by sedimentary rocks consisting of conglomerate and grit (Figure 6.2c). As on profile L3500, the high resistivity layer (RL1) on the AMT section for profile L4500 can also be attributed to the sedimentary rocks which stretch from the start of the profile up to the end except at some zones where it is truncated by conductive discontinuities that are characterised by lower resistivities. After the sedimentary rocks of the MwZ, RL1 can be attributed to the outcropping porphyroblastic biotite adamellite rocks of the Hook Batholith and lastly the psammitic schists of the Lufilian Arc as shown on the geological map (Figure 6.2c). Low resistivity discontinuity zones D1, and D3 are shallow and were enhanced by the first vertical derivative filter (Figure 6.1b) unlike D2 which can be observed on the total magnetic intensity image and extents to depths beyond 1000 m on the resistivity section. All the discontinuity zones coincide with low magnetic gradient anomalies hence can be attributed to sediments overlaying the fractured zones. The northern part of profile L4500 passes through multiple fractured zones or magnetic low, lineaments (Figure 6.2c) which result in that region being characterised by a low resistivity. The resistivity section shows that there is a vertical conductive feature at the beginning of the profile that starts from the surface and extents to depths beyond than 1000 m. This feature coincides with the fault that was geologically mapped as the Mwembeshi Shear Zone fault. The high magnetic anomalies on the Reduced To Pole Total Magnetic Intensity image can be attributed to the high magnetic susceptibility measured on an outcropping porphyroblastic biotite adamellite sample along the profile. The discontinuity zones D2 and D3 coincide with the contacts between the MwZ, Hook Batholith and Lufilian Arc outcropping rocks (Figure 6.2c). The conductive zone around D3 can be attributed to the fractured rocks in the fault zone. This top conductive layer observed in resistivity section towards the end of the profile coincides very well with the location of the alluvium field valley. These low resistivity values can be attributed to the dissolved salts in the water rich soil due to the water from the hot springs that was observed in the area. Underlying the top resistivity layer (RL1) is a conductive layer (CL1). This layer can be attributed to moisture or dissolved salts in the fractured meta-sediments that were fractured during the

intrusion of the Hook Batholith. Also observed on the AMT section underlying CL1 are two high resistivity bodies RB1 and RB2. Their locations coincide with high magnetic anomalies with RB2 being deep seated whilst RB1 is in contact with RL1 (Figure 6.1a). RB1 and RB2 should also be contributing to the high magnetic anomalies that are attributed to basement rocks. The first vertical derivative filter enhanced shallow high magnetic anomalies associated with outcropping RL1 and RB1 (Figure 6.2b). It also enhanced shallow low magnetic anomalies coinciding with discontinuity zones D1 and D2 mapped as fractured zones or geological contacts. Using the documented stratigraphy of the area, the resistive layer (RL1), the semi conductive middle layer (CL1) and the resistive bottom layer (RL2) can be attributed to the granites of the Hook Batholith, fractured, dissolved salts or moisture in fractured Kundelungu meta-sediments of the Lufilian Arc and granites and the basement granite-gneiss respectively. The images show that the fractured zone D2 is a deep seated fault extending to depths beyond 1000 m in the resistivity section. The highly conductive bodies with resistivity values <100 Ωm can be attributed to fractured zones with dissolved salts or moisture. This is supported by existences of two hot springs in the area. The NW to SE trend of the fractured zones also coincides with the trend of the two hot springs in the area.

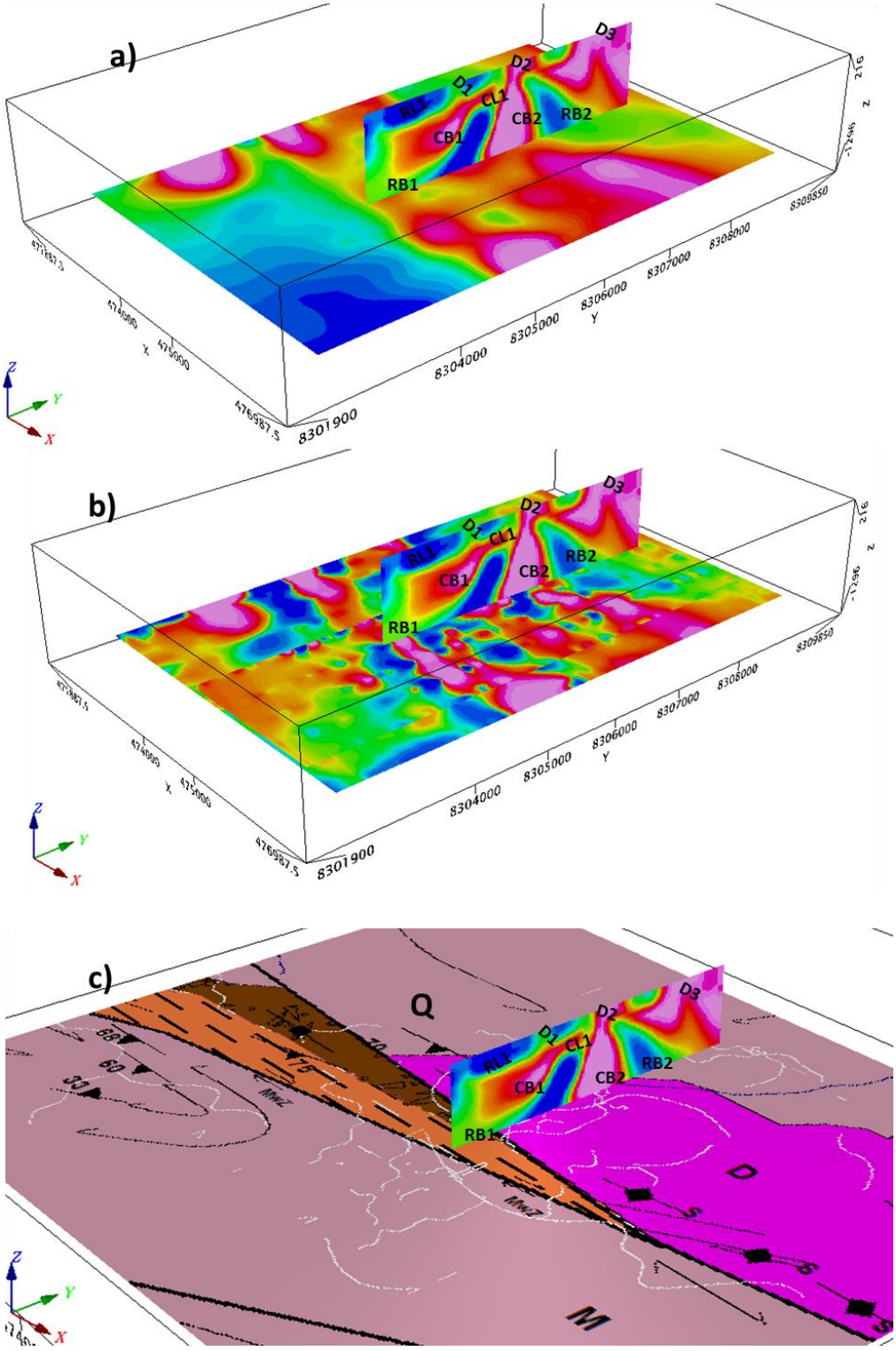

Figure 6.2. AMT section for profile L4500 overlain on the a) RTP TMI, b) first vertical derivative images and c) geological map with conductive layers, conductive bodies, resistive layers and discontinuities zones labelled as CL, CB, RL and D respectively. M, D and Q represent the psammitic schists, porphyroblastic biotite adamellite and argillaceous quartzite respectively as labelled on the geological map. The white lines represent the magnetic low, lineaments mapped using the magnetic data.

6.3 Profile L5500

The resistivity section for profile L5500 was also overlain on the Reduced To Pole total magnetic intensity image, the first vertical derivative of the Reduced To Pole magnetic intensity image and on the geological map (Figure 6.3). Moving south to north, the geological contacts between the Hook Batholith rocks and the Lufilian Arc and Zambezi Belt rocks in the north and in the south respectively also coincide very well with the magnetic contacts between the high and low magnetic anomalies (Figure 6.3a). They also coincide with magnetic low, lineaments shown on the first vertical derivative filtered Reduced To Pole TMI image (Figure 6.3b). Like profile L3500 and L4500, profile L5500 also starts on the Mwembeshi Shear Zone which is overlain by sedimentary rocks comprising of conglomerate and grit (Figure 6.3c). Like on profile L3500 and L4500, the high resistivity layer (RL1) on the AMT section for profile L5500 can also be attributed to the sedimentary rocks and sediments which stretch from the start of the profile up to the end except at some zones where it is truncated by conductive discontinuities and that are characterised by lower resistivities. After the sedimentary rocks of the MwZ, RL1 can be attributed to the outcropping porphyroblastic biotite adamellite rocks of the Hook Batholith and lastly the psammitic schists of the Lufilian Arc as shown on the geological map (Figure 6.3c). Low resistivity discontinuity zones D1 and D3 are shallow and were enhanced by the first vertical derivative filter (Figure 6.3b) whilst D2 can be observed on the total magnetic intensity image and extends to depths beyond 1000 m on the resistivity section. All the discontinuity zones coincide with low magnetic gradient anomalies hence can be attributed to sediments overlaying the fractured zones. The northern part of profile L5500 passes through multiple fractured zones or magnetic low, lineaments (Figure 6.3c) which result in that region being characterised by a low resistivity zone. The resistivity section shows that there is a vertical conductive feature at the beginning of the profile that starts from the surface and extents to depths beyond 1000 m. This feature coincides with the fault that was geologically mapped as the Mwembeshi Shear Zone fault. The high magnetic anomalies on the Reduced To Pole total magnetic intensity image can be attributed to the high magnetic susceptibility measured on an outcropping porphyroblastic biotite adamellite sample along the profile. The outcropping layer might not be the only rocks causing the high magnetic anomaly but contributing to the measured magnetic field. Profile L5500 cuts across two oppositely dipping and conductive discontinuity zones namely D1 and D2. D1 dipping to the north whilst D2 dipping to the south forming a graben in between them. The two shallow seated discontinuity zones coincide with the two easterly striking magnetic lineaments that were enhanced by the first vertical derivative filter (Figure 6.3b). The discontinuity zones D2 and D3 coincide with the contacts between the MwZ, Hook Batholith and Lufilian Arc outcropping

rocks. The conductive zone around D3 can possibly be attributed to the water rich or high moisture fractured zone. This top conductive layer observed in resistivity section towards the end of the profile coincides very well with the location of the alluvium field valley. These low resistivity values can possibly be attributed to the water rich soil due to the water from the hot springs. Underlying the top resistivity layer (RL1) is a conductive layer (CL1). Also observed on the AMT section underlying CL1 are two high resistivity bodies RB1 and RB2 and their locations coincide with high magnetic anomalies. A deep seated vertical discontinuity cuts between the resistive body RB1 and constitutes a very conductive body (CB1). Both RB1and RB2 underlie RL1 towards the south of the profile (Figure 6.3a). RB1 and RB2 should also be contributing to the high magnetic anomalies that are attributed to basement rocks. The first vertical derivative filter enhanced shallow high magnetic anomalies associated with outcropping RL1 and RB1 (Figure 6.3b). It also enhances shallow low magnetic anomalies coinciding with discontinuity zones D1, D2 and D3 mapped as fractured zones or geological contacts. Using the documented stratigraphy of the area, the resistive layer (RL1), the semi conductive middle layer (CL1) and the resistive bottom layer (RL2) can be attributed to the granites of the Hook Batholith, fractured, water filled metasediments in the Kundelungu series of the Lufilian Arc and granites and the basement granite-gneiss respectively. The images show that the fractured zone D2 could be a deep seated fault extending to depths beyond 1000 m in the resistivity section. The highly conductive bodies with resistivity values <100 Ωm can be attributed to regions with higher moisture content.

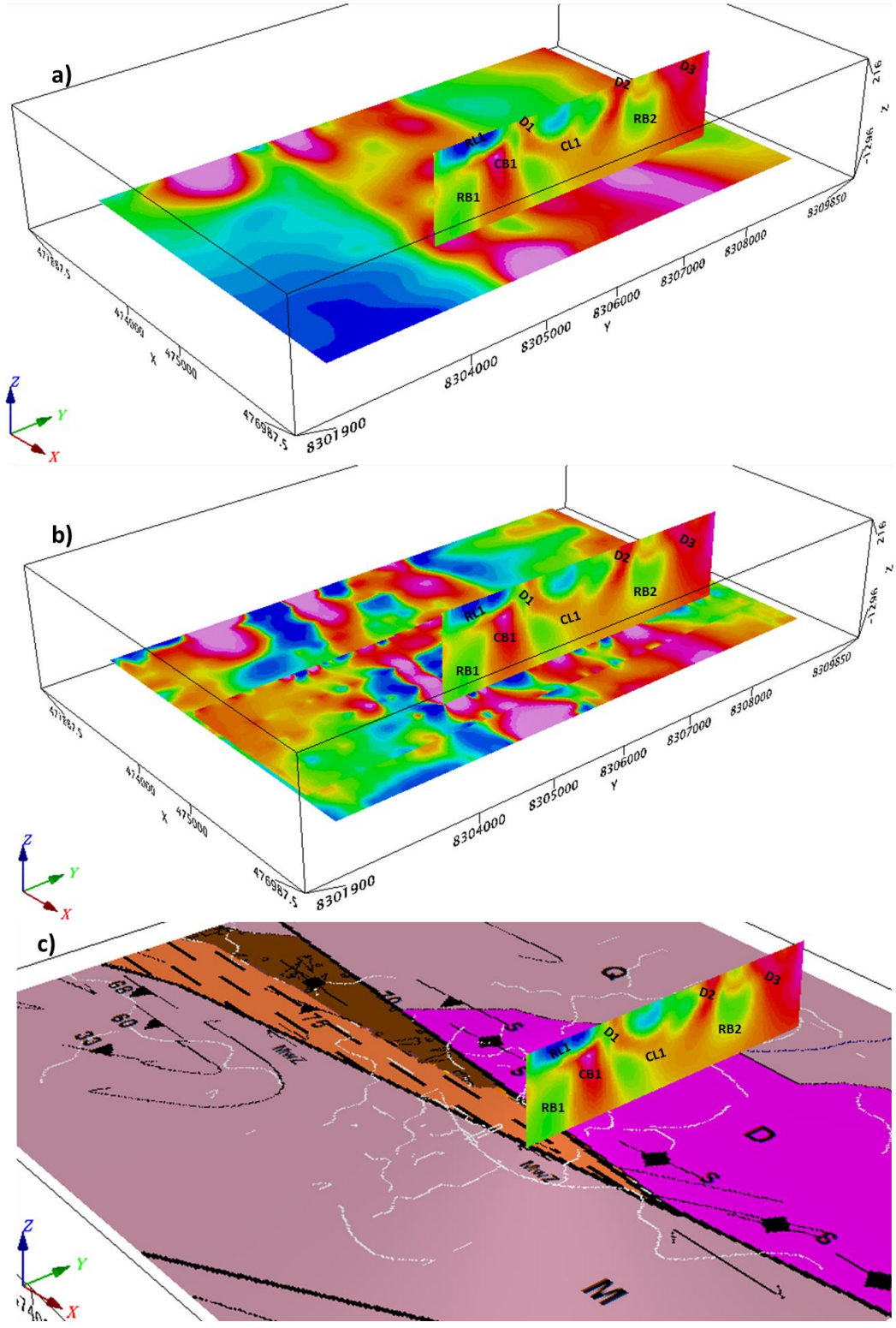

Figure 6.3. AMT section for profile L5500 overlain on the a) RTP TMI, b) first vertical derivative images and c) geological map with conductive layers, conductive bodies, resistive layers and discontinuities zones labelled as CL, CB, RL and D respectively. M, D and Q represent the psammitic schists, porphyroblastic biotite adamellite and argillaceous quartzite respectively as labelled on the geological map. The white lines represent the magnetic low, lineaments mapped using the magnetic data.

All the lines also pass through a shallow NW-SE fault dipping to the south named, D1. It is cut by profile L3500, L4500 and L5500 at northing 8305795 m, 8306020 m and 8307430 m respectively. The zones along this fault that were passed by profile L3500 and L4500 are less conductive (green) close to surface but more conductive (red) at the zones passed by profile L5500. On profile L3500, the fault stretches beyond the mapped depth. The 3D voxi shows that the fault is overlain by sediments and does not outcrop to surface (Figure 6.5). Another long NW-SE fault passes through the middle of grid dipping to the north (D2). It is cut by profile L3500, L4500 and L5500 at northing 8307868 m, 8306990 m and 8305850 m respectively. It outcrops to surface whilst extending to beyond the mapped 2500 m depth on all the sections and is characterized by high conductivity (red). This is the fault that can be associated to the hot springs found in the area which confirms the fluid pathways used by the hydrothermal fluids. At the northern end of all the sections, a NE-SW west long fault dipping to the north was mapped D3. This fault follows the contact between the Hook Batholith granites and the metasediments of the Lufilian Arc. This contact can be observed on the resistivity 3D voxi as a long conductive lineament (red) (Figure 6.5). The broad conductive zone towards the northern section of the area (D3) can be attributed to a lot of conjugate small faults close to the contact. Unfortunately the 3D nature of the voxi or sections overlain on geological map or ground magnetics map, interpretations of has to be done using 3D software.

6.4 Summary

The surveyed area can be divided into three zones that are separated by the Mwembeshi Shear Zone faults in the south. The area south of the Mwembeshi Shear Zone is covered by a layer of sedimentary rocks which is characterised by low magnetic anomaly and high resistivity (RL1). This layer is underlain by the low magnetic susceptibility metasediments of the Zambezi Belt which together with the top sedimentary layer give rise to a moderate magnetic anomaly. These metasediments make up the basement rocks south of the Mwembeshi fault and are characterised by high resistivities (RB1). Underlying RL1 is a semi-conductive layer (CL1) that has very conductive bodies. This layer can be attributed to fractured metasediments that are water filled.

To the north of the Mwembeshi fault is the Lufilian Arc metasediments that were intruded by the Hook Batholith granites. The high magnetic anomaly in the middle of the surveyed area can be attributed to the Hook Batholith granites that are characterised by a high magnetic susceptibility. The high resistivity bodies in the middle of the profiles can also be attributed to the Hook Batholith granites. In the south, these granites are dipping to the south and in the north they dip northwards. There is a deep vertical discontinuity zone (D2) that truncates the Hook Batholith in the middle and continues to surface. This zone is characterised by low resistivity and can be attributed to a deep seated fault zone filled with water. To the north the Hook Batholith rocks are in contact with the Lufilian Arc metasediments. This is a major contact zone characterised by a very magnetic low, lineament and low resistivity zone that strikes almost east west and dips southwards. The low magnetic anomaly in the north of the Mwembeshi fault can be attributed to the Lufilian Arc metasediments.

There are also shallow fault zones (discontinuity zones) that truncate the top highly resistive sedimentary layer namely D1 and D2. These zones are characterised by very low magnetic anomalies which were enhanced by the first vertical derivative filter of the TMI data.

There was good correlation between the high magnetic anomalies and the high resistive anomalies which can be attributed to the Hook Batholith granites (Figure 6.4). Also the low magnetic anomalies correlate well with the low conductivity anomalies which can be attributed to the contacts, fractured or fault zones (Figure 6.4). Integration of geophysical interpretations also concurs with surface observations e.g. hot springs; faults and ground magnetic results which also mapped some faults (Figure 6.4). The subsurface investigations reveal the presence of these fluids in vertical (funnel shaped) structures that extent to depth. The positions of these structures on NSAMT models coincide with the faults mapped by magnetic data and the positions of hot springs observed during field mapping. Two main fault trends associated with the Mwembeshi Shear Zone intersect to produce conduits for geothermal waters to reach the surface. Fluid up-flow zones occur at the intersections of these faults in the vicinity of the hot springs. The subsurface investigations also reveal the presence of a three layered Earth consisting of the Hook Batholith, alluvium, metasedimetary rocks and the basement. Another possible reason for the low-resistivity sedimentary rocks could be fracturing, since the area is located on the fractured tectonically active Mwembeshi Shear Zone.

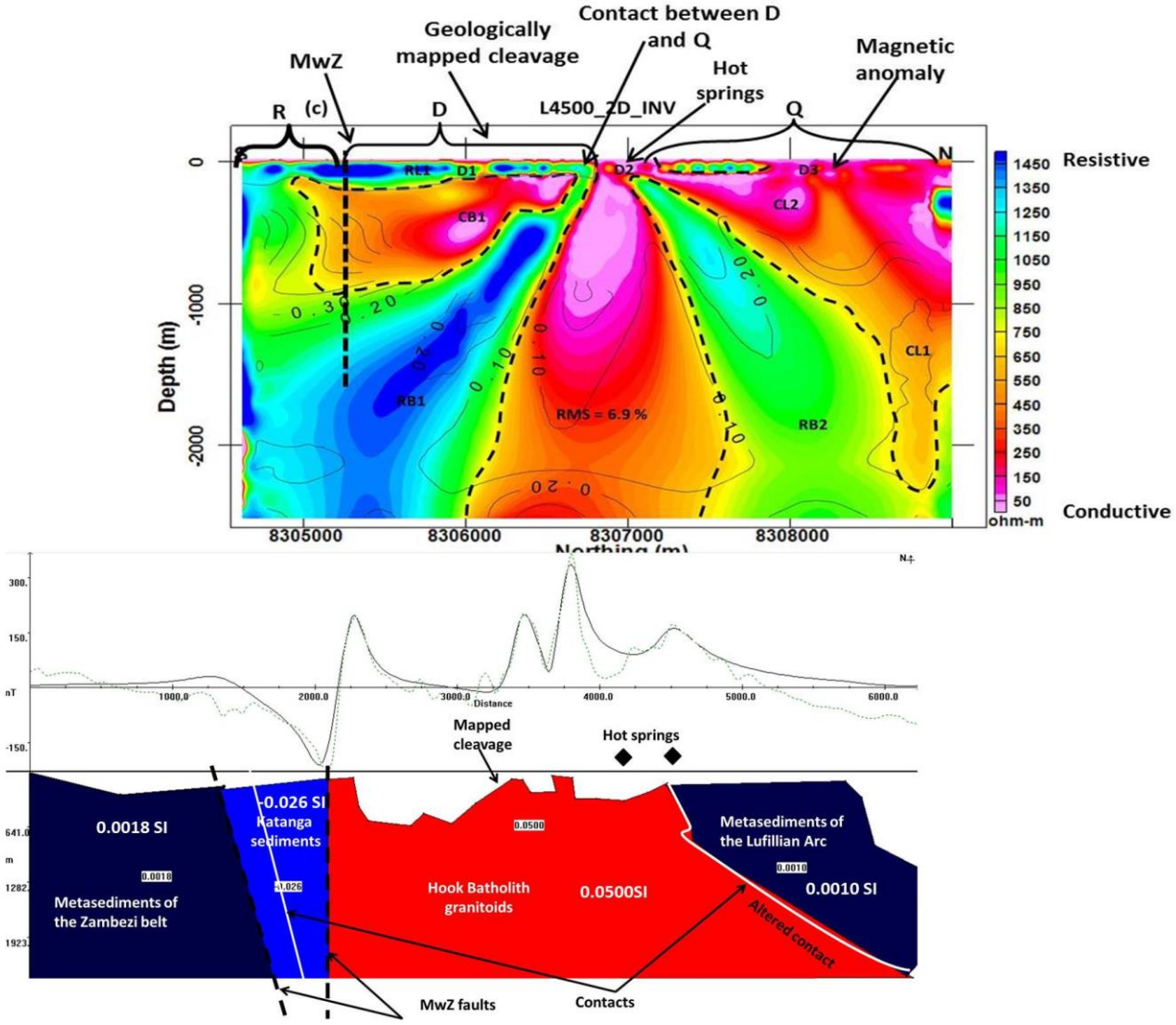

Figure 6.4. Correlation between the 2D MT invariant mode resistivity section (top) and the 2D magnetic model showing the contacts, faults and different rocks.

Since there were some slight differences between the MT modes inversion sections because of the 3D nature of the structures in the area, it was necessary to view the resistivity data in 3D. The three MT invariant sections were stitched together to form a 3D voxi (Figure 6.5). A cell size of 90 and a blanking distance of 16 cell sizes were used so as to cover all spaces between the lines. The 3D voxi was overlain on top of the geological map. A good correlation can be observed between the resistivity contact and the contact between the Hook Batholith and the metasediments of the Lufillian Arc. The northeast –southwest conductivity zone following the contact can be attributed to the fractured or altered zone due to the Hook batholith intrusion. This zone seems to be extending with depth and its high conductivity can be associated with water. It is on this zone where the hot springs lie. Another lateral high conductivity zone can be

observed inside the Hook Batholith which can be attributed to water filled fractures in the granites. This can be treated as the water table. It can be conclude that we have two types of aquifers, 1) the one that is vertical and follows the contact and 2) the lateral aquifer in between the granites (Figure 6.5).

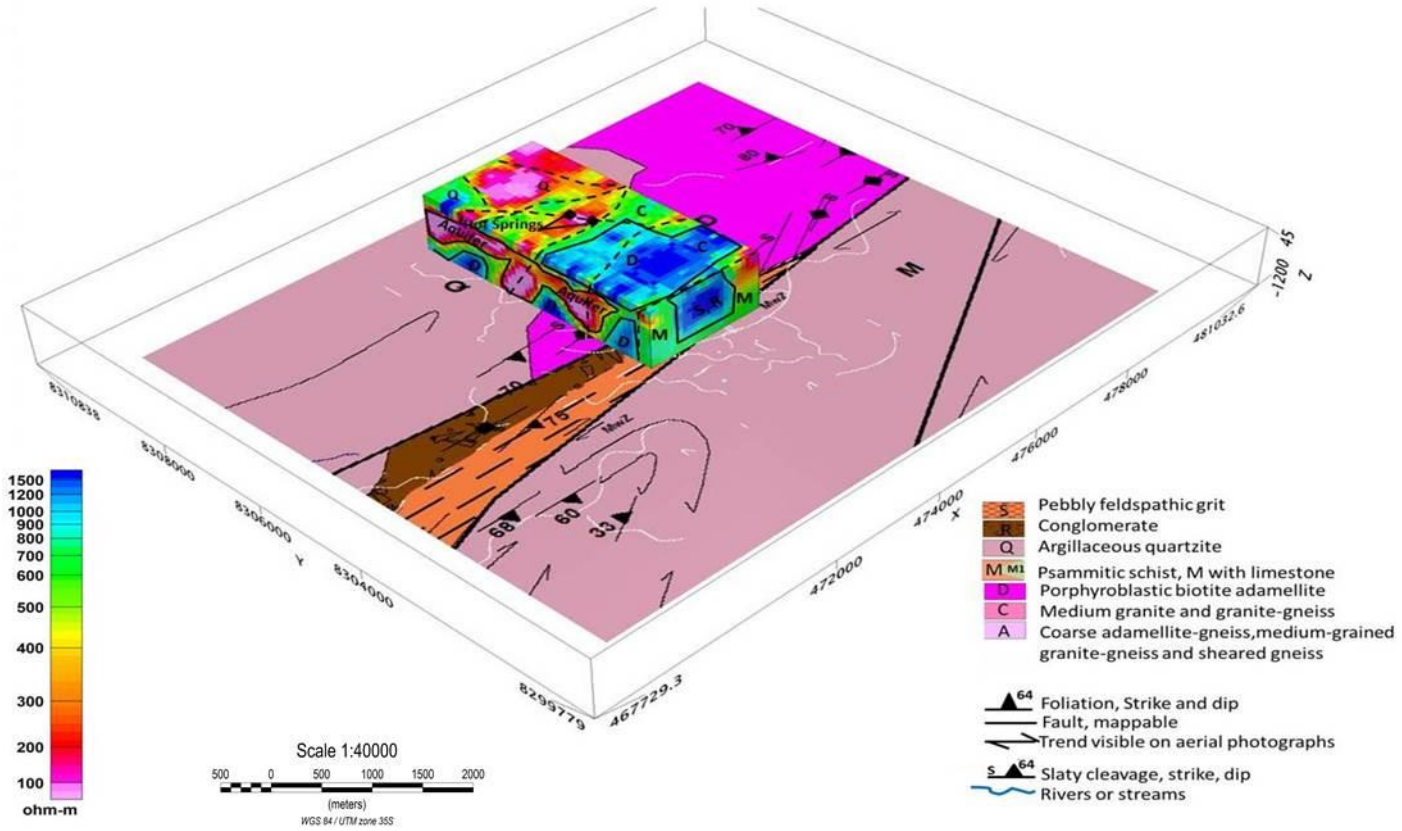

Figure 6.5. Correlation between the magnetic and resistivity contrasts of the crust at 1000 m depth with geologically mapped lithologies. On the geological map, the white lines represent the magnetic low, lineaments. The lateral conductive anomaly represents the aquifer at about 150 m depth. Vertical conductive anomalies represent steeply dipping fractures associated with either shearing or faulting. On surface their strike was mapped by either magnetic method or geological mapping and is represented by dashed or solid lines.

The integration of geophysical methods (ground magnetic and AMT) and geology were used to characterise the geothermal resource by investigating the subsurface tectonic lineaments, thermal structures and lithology. Geophysical data (NSAMT and magnetic) interpretations delineated the subsurface geometry of the conjugate faults associated with the Mwembeshi Shear Zone and the north-northwest fault that control the hot springs. From the integration of the ground magnetic, geological mapping and NSAMT data a number of structures (known and unknown) were confirmed. The N-NW trending Mwembeshi Shear Zone fault (F) that was traversed by the profiles along the southern end was confirmed by NSAMT as a conductivity lineament (red) and by magnetic method as a magnetic low, lineament (blue). The low resistivity can be attributed to fractured zone filled with water. It is cut by profile L3500, L4500 and L5500 at northing 8305530, 8305420 and 8305330 respectively. The resistivity sections show that the Mwembeshi Shear Zone fault is deep seated and extends beyond the mapped depths. Its continuity can be traced on the 3D voxi as a conductive (low resistivity) lineament. The fault is also cut by smaller NW-SE faults that are shallower. Near surface sedimentary rocks (conglomerate and grit) of the upper Katanga occupy the southern side of the MT grid. They are in contact with outcropping porphyroblastic biotite adamellite rocks of the Hook Batholith with the MwZ fault marking the contact. Further to the north, the Hook Batholith is in contact with the Katangan argillaceous quartzite of the Lufillian Arc. Underlying this top surface sedimentary rocks are the metasedimentary rocks of the Lufillian Arc or Zambezi Belt. The basement is made up of granitic gneiss and the Hook Batholith granites that were crosscut by deep seated faults associated with the MwZ.

Chapter 7 Conclusions and future work

7.1 Conclusions

Geophysical methods (magnetic and AMT) were used to preliminary characterise a potential geothermal resource by mapping the distribution at depth and on surface of the Hook Batholith, basement granites, Lufillian Arc or Zambezi Belt metasedimetary rocks, the Upper Katanga sedimentary rock, the associated faults and fractured zones. Integration of these geophysical methods and geological mapping enabled robust interpretation of main features but drilling will aid in confirming the interpretations.

The high resistivity in the south is attributed to the sedimentary rocks of the Katanga unit (quartzite and conglomerate) bound by the two Mwembeshi Shear Zone fault which starts from surface up to 600 m depth.

A new structural geological map was developed on the basis of aeromagnetic and ground magnetic data being constrained by field observations, magnetic susceptibility measurements, Google Earth images and published maps.

The use of high pass filtered images clearly delineated the extent of the Hook Batholith, Katangan sediments and structures. It also suggested that the Mwembeshi Shear Zone controls structural trends in its vicinity.

Further northwards from the Mwembeshi Shear Zone faults, the high resistivity is attributed to unfractured basement rocks which were not affected by the intrusions. Generally the older basement has a high resistivity but in this case it is relatively lower than that of the younger batholith intrusions. Resistivity sections demonstrate that it is within the older basement where we find hydrothermal fluid pathways which arose due to fracturing during intrusion of the Hook Batholith. This also reduced the resistivity close to these fluid pathways.

The impermeable basement rocks directly underlie the permeable layer of metasediments whilst the shales or mudstones of the upper Kundelungu series act as a cap rock which prevents the upward movement of the hot fluid.

The geothermal fluids circulate along deeply seated significant faults and steeply dipping fractures being heated by the increasing temperatures at depth due to the geothermal gradient of the area.

The manifestations of hot springs in the area are largely supported by the presence of the mapped Mwembeshi Shear Zone faults, associated fractures and the new faults and fractures mapped in this study.

The geological set up of the study area is conducive for a geothermal energy reservoir with the aquifer found at about 150 m depth.

7.2 Proposed future work

Based on the results obtained, it would be more advantageous if an exploratory borehole is to be drilled in the area to aid interpretation and modelling of the data. Since the methods used are non-unique, drilling would aid in coming up with a more constrained model.

Also more physical properties like conductivity and magnetic susceptibility are needed to be measured on the core samples with depth. Heat flow values and geothermal gradients should also be investigated by using temperature logging. This will help to decide whether the resource could be developed for low or high enthalpy commercial geothermal power production if it is hot enough or for direct or indirect uses if it is not. The temperatures derived from the geothermometers and the geothermal gradients will give us an idea on whether the resource is in the range for low or high enthalpy commercial geothermal power production and if the source is likely to be at a realistic depth within the basin.

More closely spaced AMT lines should be acquired especially between profiles L3500 and L4500. This will help in mapping the extent of the intrusion with depth. Also a high resolution AMT survey will produce a better 3D image of the subsurface. The higher resolution resistivity mapping can be done to resolve the different sedimentary layers and to differentiate them from the basement rocks.

All this data will improve our understanding of the resource and another final magnetic and AMT model is recommended when more constraining data have been acquired.

Appendix A

The plots of apparent resistivity below show the effects of static-correction moving average filters for several stations. First image is data before static correction and next image is static corrected data (next page)

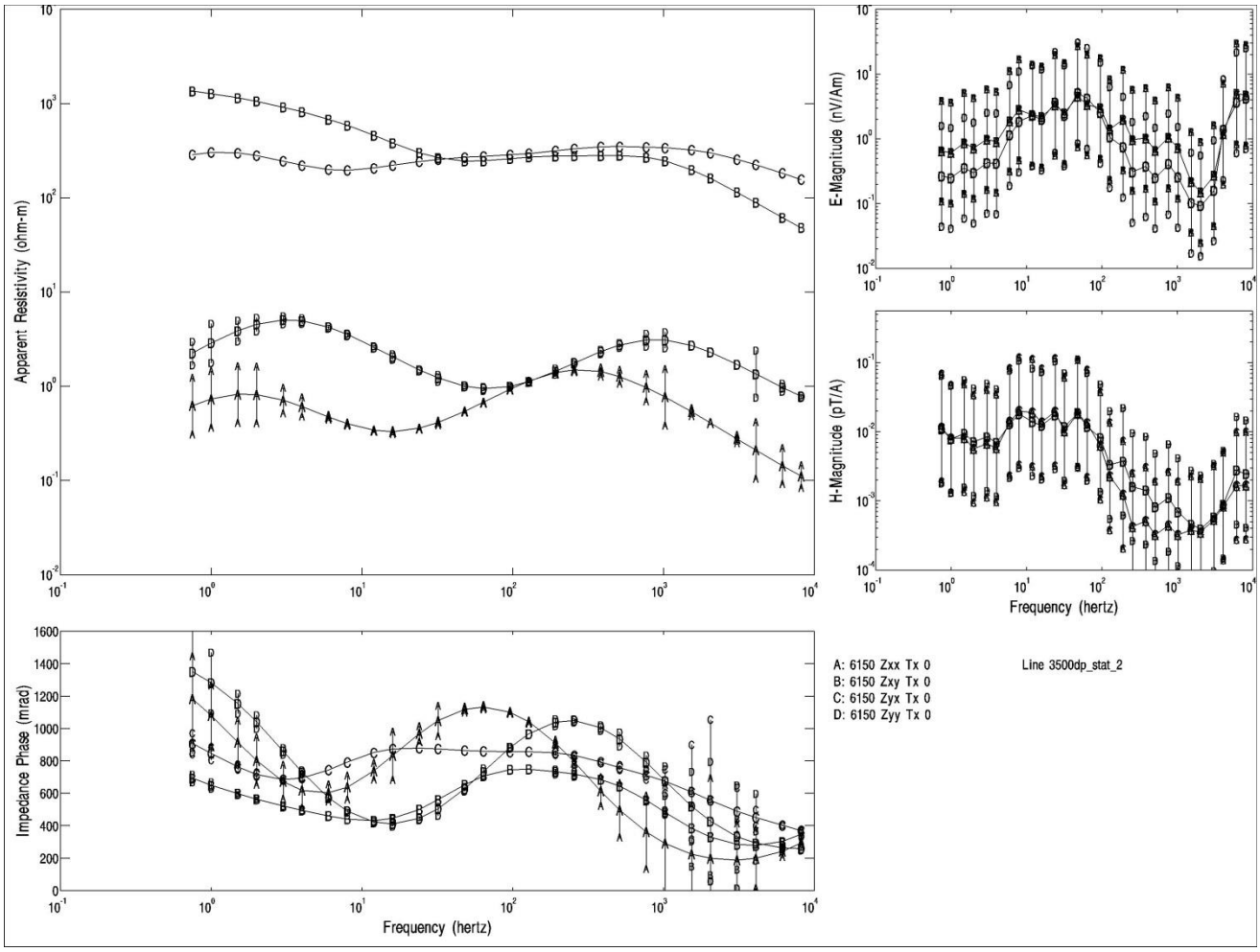

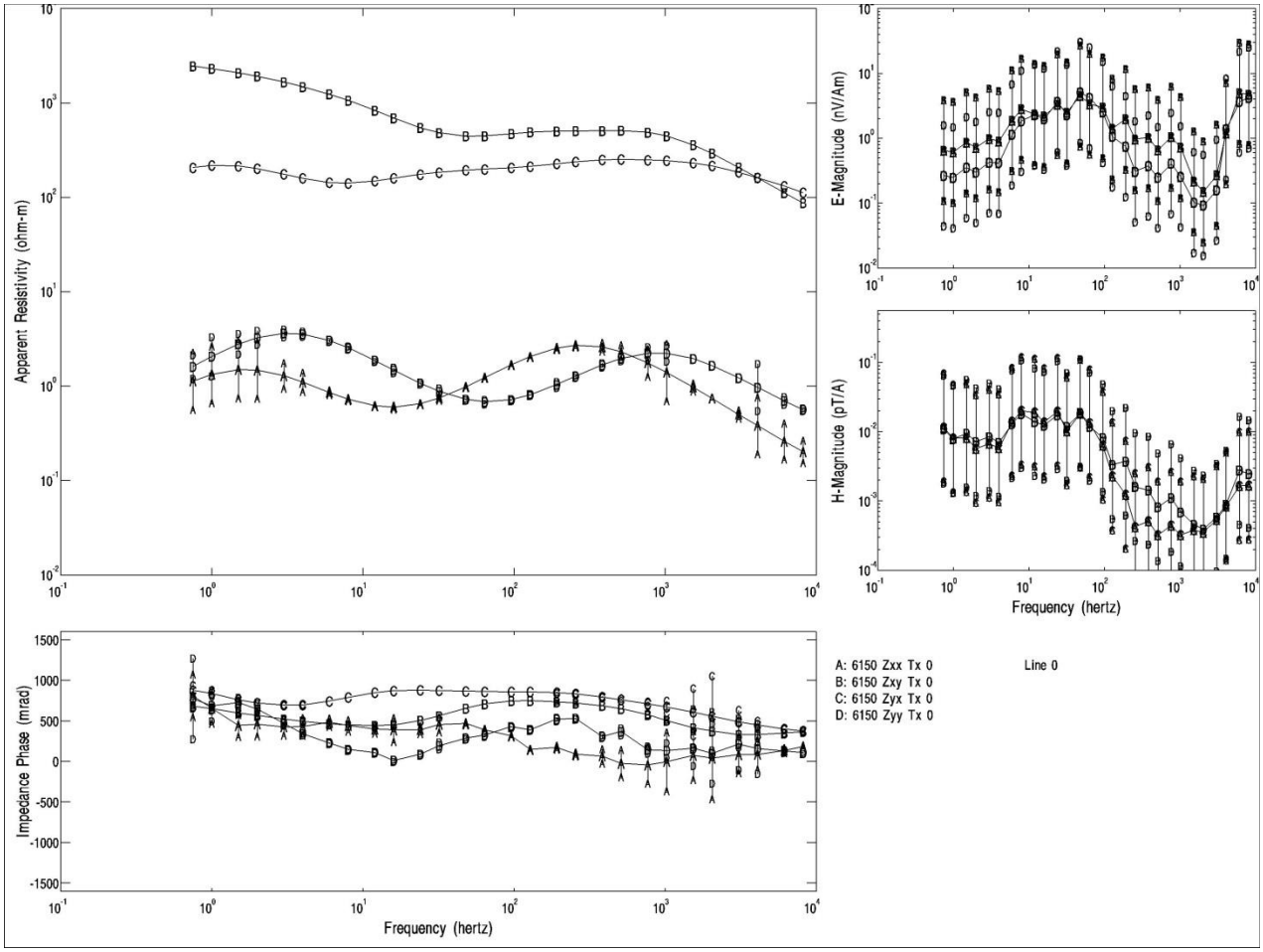
Apparent Resistivity (ohm-m)
E-Magnitude (nV/Am)
H-Magnitude (pT/A)
Frequency (hertz)
Impedance Phase (mrad)
Frequency (hertz)
A: 6150 Zxx Tx 0
B: 6150 Zxy Tx 0
C: 6150 Zyx Tx 0
D: 6150 Zyy Tx 0
Line 0

Appendix B

Example of the results of the single site strike analysis for profile L3500. Each station was divided into 4 depth ranges. For each depth range a strike sensitivity analysis was carried out for each station independently for all possible azimuths (0 - 90˚) with an increment of 5°.

Station	**Strike (˚)**	**Frequency Band (Hz)**			
		10000 -1000	**1000-100**	**100-10**	**10-1**
L3500_dp_stat_1	0	0.3	0.3	0.2	0.0
L3500_dp_stat_1	5	0.3	0.2	0.4	0.4
L3500_dp_stat_1	10	0.5	0.2	0.8	0.6
L3500_dp_stat_1	15	0.6	0.3	1.2	0.8
L3500_dp_stat_1	20	0.7	0.3	1.6	1.0
L3500_dp_stat_1	25	0.7	0.4	1.8	1.2
L3500_dp_stat_1	30	0.8	0.5	2.1	1.3
L3500_dp_stat_1	35	0.8	0.5	2.3	1.4
L3500_dp_stat_1	40	0.9	0.6	2.4	1.4
L3500_dp_stat_1	45	0.8	0.6	2.4	1.5
L3500_dp_stat_1	50	0.8	0.6	2.4	1.5
L3500_dp_stat_1	55	0.8	0.6	2.2	1.4
L3500_dp_stat_1	60	0.7	0.6	2.1	1.3
L3500_dp_stat_1	65	0.6	0.6	1.8	1.2

L3500_dp_stat_1	70	0.5	0.5	1.5	1.1
L3500_dp_stat_1	75	0.4	0.5	1.2	0.9
L3500_dp_stat_1	80	0.3	0.4	0.8	0.7
L3500_dp_stat_1	85	0.3	0.3	0.4	0.5
L3500_dp_stat_1	90	0.3	0.3	0.2	0.3
L3500_dp_stat_20	0	0.2	0.2	0.5	0.4
L3500_dp_stat_20	5	0.3	0.2	0.8	0.5
L3500_dp_stat_20	10	0.6	0.2	1.0	0.7
L3500_dp_stat_20	15	0.8	0.3	1.3	0.8
L3500_dp_stat_20	20	1.0	0.3	1.5	0.9
L3500_dp_stat_20	25	1.2	0.3	1.6	0.9
L3500_dp_stat_20	30	1.3	0.3	1.8	1.0
L3500_dp_stat_20	35	1.4	0.3	1.8	1.0
L3500_dp_stat_20	40	1.4	0.3	1.8	1.0
L3500_dp_stat_20	45	1.4	0.3	1.8	0.9
L3500_dp_stat_20	50	1.4	0.3	1.7	0.8
L3500_dp_stat_20	55	1.4	0.3	1.6	0.8
L3500_dp_stat_20	60	1.3	0.3	1.4	0.6

Appendix C

Continuation of Appendix B above.

Station	Strike (˚)	Frequency Band (Hz)			
		10000 -1000	1000-100	100-10	10-1
L3500_dp_stat_30	0	0.7	0.3	0.2	0.7
L3500_dp_stat_30	5	0.9	0.4	0.2	0.6
L3500_dp_stat_30	10	1.3	0.5	0.2	0.6
L3500_dp_stat_30	15	1.7	0.5	0.2	0.6
L3500_dp_stat_30	20	2.1	0.6	0.3	0.6
L3500_dp_stat_30	25	2.4	0.7	0.3	0.6
L3500_dp_stat_30	30	2.6	0.7	0.4	0.6
L3500_dp_stat_30	35	2.8	0.7	0.4	0.6
L3500_dp_stat_30	40	2.8	0.7	0.4	0.6
L3500_dp_stat_30	45	2.8	0.7	0.5	0.6
L3500_dp_stat_30	50	2.8	0.7	0.5	0.6
L3500_dp_stat_30	55	2.6	0.7	0.5	0.6
L3500_dp_stat_30	60	2.4	0.7	0.5	0.7
L3500_dp_stat_30	65	2.1	0.6	0.5	0.7
L3500_dp_stat_30	70	1.7	0.5	0.5	0.7
L3500_dp_stat_30	75	1.3	0.4	0.4	0.7

L3500_dp_stat_30	80	0.9	0.3	0.3	0.7
L3500_dp_stat_30	85	0.7	0.3	0.2	0.7
L3500_dp_stat_30	90	0.7	0.3	0.2	0.7
L3500_dp_stat_40	0	0.1	0.4	0.8	0.3
L3500_dp_stat_40	5	0.1	0.4	0.7	0.3
L3500_dp_stat_40	10	0.2	0.5	0.2	0.3
L3500_dp_stat_40	15	0.3	0.6	0.2	0.4
L3500_dp_stat_40	20	0.4	0.7	1.2	0.5
L3500_dp_stat_40	25	0.4	0.7	1.5	0.6
L3500_dp_stat_40	30	0.5	0.8	1.8	0.7
L3500_dp_stat_40	35	0.5	0.8	2.1	0.8
L3500_dp_stat_40	40	0.6	0.8	2.2	0.8
L3500_dp_stat_40	45	0.6	0.9	2.4	0.8
L3500_dp_stat_40	50	0.6	0.8	2.4	0.8
L3500_dp_stat_40	55	0.6	0.8	2.4	0.8
L3500_dp_stat_40	60	0.5	0.8	2.4	0.8
L3500_dp_stat_40	65	0.5	0.7	2.2	0.7
L3500_dp_stat_40	70	0.4	0.6	2	0.6
L3500_dp_stat_40	75	0.3	0.5	1.7	0.6

Appendix D

Example of the results of the single site strike analysis for profile L4500. Each station was divided into 4 depth ranges. For each depth range a strike sensitivity analysis was carried out for each station independently for all possible azimuths (0 -90˚) with an increment of 5 degrees

Station	**Strike (˚)**	**Frequency Band (Hz)**			
		10000 -1000	**1000-100**	**100-10**	**10-1**
L4500_dp_stat_1	0	1.2	0.1	0.3	0.3
L4500_dp_stat_1	5	1.3	0.3	0.2	0.2
L4500_dp_stat_1	10	1.4	0.5	0.5	0.4
L4500_dp_stat_1	15	1.4	0.8	0.8	0.7
L4500_dp_stat_1	20	1.4	1.1	1.1	1
L4500_dp_stat_1	25	1.4	1.3	1.4	1.2
L4500_dp_stat_1	30	1.3	1.4	1.6	1.4
L4500_dp_stat_1	35	1.3	1.5	1.7	1.6
L4500_dp_stat_1	40	1.2	1.5	1.8	1.7
L4500_dp_stat_1	45	1.1	1.6	1.8	1.7
L4500_dp_stat_1	50	1.1	1.5	1.8	1.8
L4500_dp_stat_1	55	1	1.5	1.8	1.7
L4500_dp_stat_1	60	1	1.4	1.7	1.6
L4500_dp_stat_1	65	0.9	1.3	1.6	1.5
L4500_dp_stat_1	70	0.9	1.1	1.4	1.3
L4500_dp_stat_1	75	1	0.9	1.2	1.1
L4500_dp_stat_1	80	1	0.7	0.9	0.8
L4500_dp_stat_1	85	1.1	0.4	0.6	0.5
L4500_dp_stat_1	90	1.2	0.1	0.3	0.3
L4500_dp_stat_10	0	0.5	0.1	0.2	0.4
L4500_dp_stat_10	5	0.5	0.1	0.6	0.6
L4500_dp_stat_10	10	0.5	0.2	0.9	0.7
L4500_dp_stat_10	15	0.6	0.3	1.2	0.9
L4500_dp_stat_10	20	0.6	0.4	1.5	1
L4500_dp_stat_10	30	0.6	0.5	1.9	1.1
L4500_dp_stat_10	40	0.5	0.6	2.1	1.1
L4500_dp_stat_10	45	0.5	0.6	2.1	1.1
L4500_dp_stat_10	50	0.5	0.6	2.1	1.1
L4500_dp_stat_10	55	0.5	0.6	1.9	1
L4500_dp_stat_10	60	0.5	0.6	1.8	0.9

Appendix E

Apparent resistivity depth sounding model including the best-fit model calculation. Observed apparent resistivity values are shown by posted triangles with TM-mode and TE-mode data in blue and green respectively.

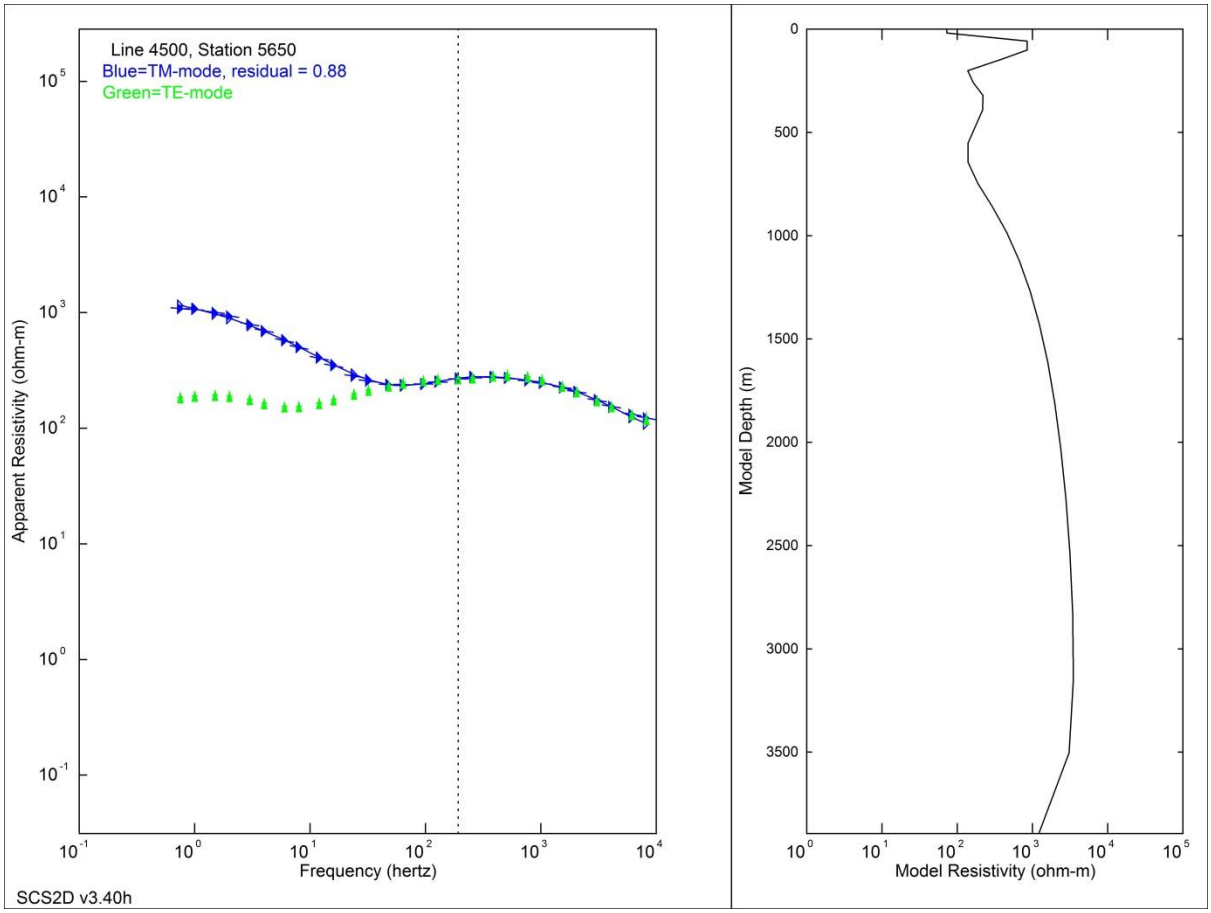

References

Abell, S. (1970). The geology of the Nansenga River area. Explanation of degree sheet 1526 N.E. quarter. Lusaka: Geological Survey of Zambia.

Ármannsson, H., and Fridriksson, T. (2009). Application of Geochemical methods in geothermal exploration. Short Course on Surface Exploration for Geothermal Resources organised by UNU-GTP and LaGeo, (pp. 1-2). Ahuachapan and Santa Tecla.

Atekwana, E. A., Hogan, J. P., Kampunzu, A. B., and Modisi, M. P. (2004). Early structural evolution of the nascent Okavango rift zone, NW Botswana. Proceedings of the East African Rift system: Geodynamics, Resources, and Environment conference, (pp. 12-16). Addis Ababa.

Baranov, V. (1957). A new method for interpretation of aeromagnetic maps: pseudo-gravimetric anomalies. 22, 359-383.

Barnwell, C. J. (1973). Geophysical methods in geothermal exploration. In: Proceedings UN. Symposium on the development and utilisation of geothermal resources. Geothermics, Spec. Issue 1, 32-56.

Berdichevsky, M. N. (1960). Priciples of magnetotelluric profiling theory. Applied Geophysics, 28:70–91.

Berdichevsky, M. N. (1964). Linear relationships in the magnetotelluric field. Applied Geophysics, 38: 99–108.

Berdichevsky, M.N., Dmitriev, V.I., and Pozdnjakova, E.E. (1998). On two-dimensional interpretation of magnetotelluric soundings. Geophysical Journal International, 133, 585 – 606.

Blakely, R. J. (1995). Potential theory in gravity and magnetic application. Cambridge: Cambridge University Press.

Blakely, R. J., Brocher, T. M., and Wells, R. E. (2005). Subduction-zone magnetic anomalies and implications for hydrated forearc mantle. 33, 445-448.

Booker, J. (2012). The magnetotelluric phase tensor: a critical review. 21st Electromagnetic Induction Workshop. Darwin, N.T., Australia.

Bostick, F. X. (1977). A simple almost exact method of MT-analysis. In Workshop on Electrical Methods in Geothermal Exploration. U.S. Geological Survey Contract No. 14080001–8–359.

Briggs, I.C., 1974. Machine contouring usingminimum curvature. Geophysics 39: 39-48.

Caldwell, T. G, Bibby H. M, Caldwell. C (2004) The magnetotelluric phase tensor. Geophysics Journal International, 158:457–469

Cagniard, L. (1953). Basic theory of the magneto-telluric method of geophysical prospecting. Geophysics, 18, 605-635.

Cole, J., Finn, C. A., and Webb, S. J. (2013). Overview of the magnetic signature of the Palaeoproterozoic Rustenburg Layered Suite, Bushveld Complex, South Africa. Precabrian Research, 236, 193-213.

Constable, S. C., Parker, R. L., and Constable, C. G. (1987). Occam's inversion: a practical algorithm for generating smooth models from electromagnetic sounding data. Geophysics, 52, 289-300.

Cooper, G. R. J. (2004). Euler deconvolution applied to potential field gradients. Exploration Geophysics 35, 165-170.

Cooper, G. R. J., and Cowan, D. R. (2005). Differential reduction to the pole. 31, 989-999.

Cooper, G. R., and Cowan, D. R. (2004). Filtering using variable order vertical derivatives. Computers and Geosciences. 30, 455-459.

Cordell, L., and Grauch, V. (1985). Mapping basement magnetisation zones from aeromagnetic data in the San Juan basin, New Mexico. In: Hinze, W.J. (Ed.), The utility of regional gravity and magnetic anomaly maps. Society of Exploration Geophysicists, 181-198.

Coward, M.P., Daly, M.C., 1984. Crustal lineaments and shear zones in Africa: their relationship to plate movements. Precambrian Res. 24, 27–45.

Daly, M.C., 1986. Crustal shear zones and thrust belts: their geometry and continuity in Central Africa. Philos. Trans. R. Soc. Lond. A317, 111–128.

de Groot-Hedlin, C. (1991). Short Note: Removal of static shift in two dimensions by regularized inversion. Geophysics, 56 (12), 2 102 – 2 106.

de Groot-Hedlin, C. (1995). Inversion for regional 2-D resistivity structure in the presence of galvanic scatters. Geophysical Journal International, 122, 877 – 888.

de Swart, A. M., Gerrard, P., and Simpson, J. (1965). Major zones of transcurrent dislocation and superposition of orogenic belts in part of Central Africa. Bull. Geol. Soc. Am., 76, 89-102.

Dirks, P. H., Kröner, A., Jelsma, H. A., Sithole, T. A., and Vinyu, M. I. (1999). Structural relations and Pb-Pb zircon ages for the Makuti gneisses: evidence for a crustal-scale pan-African shear zone in the Zambezi belt, northwest Zimbabwe. J. Afr. Earth Sci, 28, 427-442.

Doell, R. and Cox, A., 1967. Magnetization of Rocks. In: SEG Mining Geophysics Volume Editorial Committee (Editors), Mining Geophysics, Volume 2: Theory. Society of Exploration Geophysicists, Tusla, 446-453.

Duffield, W. A., and Sass, J. H. (2003). Geothermal Energy- Clean power from the Earth's heat. p. 1.

Egbert. (1997). Robust multiple-station magnetotelluric data processing. Geophysics Journal International, 130, 475-496.

El Dawi, M. G., Tianyou, L., Hui, S., and Dapeng, L. (2004). Depth estimation of 2-D magnetic anomalous sources by using Euler deconvolution method. American Journal of Applied Sciences 1 (3), 209-214.

Fitzgerald, D., Yassi, N. and Dart, P., 1997. A case study on geophysical gridding techniques: INTERPID perspective. Exploration geophysics 28: 204-208.

FitzGerald, D., Reid, A.B. and McInerney, P. (2004). New discrimination techniques for Euler deconvolution. Computers and Geosciences, 30, 461 - 469.

Garcia, X., and Jones, A. G. (2002). Atmospheric sources for audio-magnetotelluric (AMT) sounding. Geophysics, 67(2), 448-458.

Glassley, W. E. (2010). Geothermal Energy: Renewable Energy and the Environment. Florida: Taylor and Francis Group.

http://www.cangea.ca/images/uploads/120202_Canada_Geothermal Project Overview.pdf, a

Grant, F. S., (1985). Aeromagnetics, geology and ore environments: In: Magnetite inigneous, sedimentary and metamorphic rocks: An overview: Geoexploration, 23, 303-333.

Groom, R.W., and Bahr, K. (1992). Corrections for near surface effects: Decomposition of the magnetotelluric impedance tensor and scaling corrections for regional resistivities: A tutorial. Surveys of Geophysics, 13 (4-5), 341 – 379.

Groom, R. W., and Bailey, R. C. (1989). Decomposition of Magnetotelluric impedance tensors in the presence of local three dimensional galvanic distortion. Journal of Geophysical Research, 94(B2), 1913-1925.

Hanson, R. E., Wardlaw, M. S., Wilson, T. J., and Mwale, G. (1993). U–Pb zircon ages from the Hook granite massif and Mwembeshi dislocation: constraints on pan-African deformation, plutonism, and transcurrent shearing in central Zambia. Precambrian Res., 63, 189-209.

Hersir, G. P., and Björnsson, A. (1991). Geophysical exploration for geothermal resources, Principles and application. Reykjavik, Iceland: UNU Geothermal Training Programme, Report 15, 94 pp.

Irving, E. (1964). Paleomagnetism and its application to geological and geophysical problems. New York: John Wiley and Sons, Inc., United States of America.

Isaacs, K. N. (1968). Interpretation report of an airborne geophysical survey in the Republic of Zambia for the Geological Survey of Zambia. Unpublished Report, Canadian Aero Services Ltd.

Jiracek, G. R. (1990). Near-surface and topographic distortions in electromagnetic induction. Surveys in Geophysics, 11, 163-203.

John, T and Schenk, V., (2003). Partial eclogitisation of gabbroic rocks in a late Precambrian subduction zone (Zambia): prograde metamorphism triggered by fluid infiltration. Contrib. Mineral. Petrol. 146, 174–191.

John, T and Schenk, V., Haase, K., Scherer, E and Tembo, F., (2003). Evidence for Neoproterozoic Ocean in south-central Africa from mid-oceanic-ridge-type geochemical signatures and pressure–temperature estimates of eclogites. Geology 31, 243–246.

John, T., Schenk, V., Mezger, K and Tembo, F., (2004a). Timing and PT evolution of white schist metamorphism in the Lufilian Arc-Zambezi Belt orogen (Zambia): implications for the assembly of Gondwana. J. Geol. 112, 71–90.

John, T., Scherer, E.E., Haase, K and Schenk, V., (2004b). Trace element fractionation during fluid-induced eclogitization in a subducting slab: trace element and Lu–Hf–Sm–Nd isotope systematics. Earth Planet. Sci. Lett. 227, 441–456.

Johnson, S. P., and Oliver, G. J. (2004). Tectonothermal history of the Kaourera Arc, northern Zimbabwe: implications for the tectonic evolution of the Irumide and Zambezi belts of south central Africa. Precambrian Res, 130, 71-97.

Johnson, S. P., De Waele, B., Evans, D., Banda, W., Tembo, F., Milton, J. A., et al. (2007). Geochronology of the Zambezi supracrustal sequence, southern Zambia: a record of Neoproterozoic divergent processes along the southern margin of the Congo Craton. J. Geol, 115, 355-374.

Jones, A. G., and Groom, R. W. (1993). Strike angle determination from the magnetotelluric tensor in the presence of noise and local distortion: rotate at your peril! Geophysics Journal Int. 113, 524-534.

Jones, A. G., Chave, A. D., Egbert, G., Auld, D., and Bahr, K. (1989). A comparison of techniques for magnetotelluric response function estimation. Journal of Geophysical Research, 94, 14 201-1 4 203.

Jones. A. G. (1988). Static shift of magnetotelluric data and its removal in a sedimentary basin environment. Geophysics, Vol. 53, No 7, 967-978.

Kalahari GeoEnergy. (2013). Work cmpleted by Kalahari GeoEnergy Ltd (March 2011-May 2014). http://www.kalaharigeoenergy.com/exploration.html. Accessed 10/07/2015.

Kampunzu, A.B., Milesi, J.P., Descamps, Y. (2003). Africa within Rodinia supercontinent: Evidence from the Kibaran orogenic system. The Geological Society of America. Retrieved 21/07/2015.

Katongo, C., Koeberl, C., Reimold, W. U., and Mubu, S. (2002). Remote sensing, field studies, petrography, and geochemistry of rocks in central Zambia: no evidence of a

meteorite impact in the area of the Lukanga Swamp. Journal of African Earth Sciences, 35, 365-384.

Katongo, C., Koller, F., Kloetzli, U., Koeberl, C., Tembo, F., and De Waele, B. (2004). Petrography, geochemistry, and geochronology of granitoid rocks in the Neoproterozoic-Paleozoic Lufilian–Zambezi belt, Zambia: implications for tectonic setting and regional correlation. J. Afr. Earth Sci., 40, 219-244.

KenGen. (2014). Geoscientific investigations of the Kapisya and Chinyunyu geothermal fields, Zambia. www.kengen.co.ke/index.php?page=businessandsubpage=cgeothermal. Accessed 12/05/2014.

Key R.M., Liyungu A.K., Njamu F.M., Somwe V., Banda J., Mosley P.N., and Armstrong R. A. (2001). The western arm of the Lufilian Arc in NW Zambia and its potential for copper mineralization. Journal of African Earth Sciences, 33, 503 - 528.

Kombe, C., and Sinyiza, A. (2008). Geothermal exploration in Zambia – status report and discussion. SHORT COURSE III ON EXPLORATION FOR GEOTHERMAL RESOURCES (p. 6). Naivasha, Kenya: United Nations University Geothermal Training, KenGen.

Kovesi, P. (1997). Symmetry and asymmetry from local phase, AI'97, Tenth Australian Joint Conference on Artificial Intelligence. 2 - 4 December 1997.

Kroner, A., and Stern, R. J. (2004). Pan-African orogeny. Enycyclopedia of Geology, vol. 1, 1-12.

Legg, C. A. (1974). A reconnaissance survey of the hot and mineralised springs of Zambia. Lusaka: Republic of Zambia Ministry of Mines and Industry. Geological survey, Zambia, Lusaka.

Luyendyk, A. P. (1997). Processing of airborne magnetic data. AGSO Journal of Geology and Geophysics, 17, 31-38.

MacInnes, S., and Zonge, K. (1996). Two-dimensional Inversion of resistivity and IP data with topography. 102 Annual Northwest Mining Association Convention. Spokane, Washington.

MacNitt, J. R. (1970). The geologic environment of geothermal fields as a guide to exploration. Geothermics, Spec. Issue 2, V2 (1), 2-31.

Mantlik, F., and Karous, M. (2013). Use of gravimetry in detailed geophysical prospection of potential geothermal energy exploitation sites: Case studies in the Czech Republic. Geophysics, 78, No. 5, B305-B315.

Maxwell, J. R. (1892). A Treatise on Electricity and Magnetism (3rd ed., Vol. 2). Oxford,: Clarendon Press.

McNeice, G.W. and Jones, A.G. (2001). Multiscale, multifrequency tensor decomposition of magnetotelluric data. Geophysics, 66, 158 - 173.

Merill, R. T., McEthinny, M. W. and McFadden, P.L. (1996). The magnetic field of the Earth: paleomagnetism, the core and the deep mantle. Academic Press, San Diego, 531.

Miensopust, M. P. (2010). Multidimensional magnetotelluric: A case study and a 3D approach to simultaneously invert for resistivity structure and distortion parameters. Galway, Ireland: Unpublished Ph.D. Dissertation, National University of Ireland.

Musonda, G., and Sikazwe, M. (2005). Geothermal Exploration and Development in Zambia. Proceedings World Geothermal Congress . Antalya, Kenya: UNU-KenGen.

Naydenov, K. V., Lehman, J., Saalmann, K., Milani, L., Kinnaird, J. A., Charlesworth, G., et al. (2014). New constraints on the Pan-African Orogeny in Central Zambia: A structural and geochronological study of the Hook Batholith and the Mwembeshi Zone. Tectonophysics, 637, 80-105.

Naydenov, K. V., Lehmann, J., Saalmann, K., Milani, L., Poterai, J., Kinnaird, J. A. (2015). The geology of the Matala Dome: an important piece of the Pan-African puzzle in Central Zambia. (DOI 10.1007/s00531-015-1222-y).

Nyambe, I., and Phiri, C. (2010). Database of mineral resources of Zambia. International Workshop on UNFC-2009. Theory and Practice. Warsaw.

Omenda, P. A. (2010, October-November 29- 19). The geology and geothermal activity of the East African Rift. Papers presented at "Short course V on Exploration for Geothermal Resources" organised by UNU-GTP, KenGen and GDC at Lake Bogoria and Naivasha, Kenya.

Parkinson, W. D. (1959). Directions of rapid geomagnetic fluctuations. Geophysical Journal of the Royal Astronomical Society, 2(1), 1-14.

Parkinson, W. D. (1962). The influence of continents and oceans on geomagnetic variations. Geophysical Journal of the Royal Astronomical Society, 6, 441-449.

Pellerin, L. and Hohmann, G.W. (1990). Transient electromagnetic inversion: a remedy for magnetotelluric static shifts. Geophysics, 55 (9), 1 242 – 1 250.

Price, A. T. (1973). The theory of geomagnetic induction. 181, 227-233. Physics of the Earth and Planetary Interiors, 7, 181, 227-233.

Reeves, C. (2005). Aeromagnetic Survey: Principles, Practice and Interpretation, Geosoft, Inc.

Reid, A.B., Allsop, J.M., Granser, H., Millett, A.J. and Somerton, I.W. 1990. Magnetic interpretation in three dimensions using Euler deconvolution, Geophysics, 55, 80 - 91.

Roest, W. R., Verhoef, J., and Pilkington, M. (1992). Magnetic interpretation using 3-D analytic signal. 57, 116-659.

Saviaro, K. (1980). Preliminary analysis of airborne magnetic surveys in Zambia. Occasional Paper of the Geological Survey of Zambia, 98, p. 8.

Simpson, F., and Bahr, K. (2005). Practical magnetotelluric. United Kingdom: Cambridge University Press, London, 270pp.

Singhal, B. B and Gupta, R. P. (2010). Applied Hydrogeology of Fractured Rocks. Springer Dordrecht Heidelberg London New York, p. 408

Talwani, M and Heirtzler, J. R. (1964). Computation of magnetic anomalies caused by two dimensional bodies of arbitrary shape. In: Parks, G. A. (Ed.), Computers in the mineral industries, Part 1. Stanford University Publication, Geological Sciences, 9 (1), 464 - 480.

Talwani, M., Worzel, J. L. and Landisman, M. (1959). Rapid gravity computations for two dimensional bodies with application to the Mendocino submarine fracture zone. Journal of Geophysical Research, 64 (1), 49 - 59.

Teklemariam, M. (2008). Overview of geothermal resource utilisation and potential in East African Rift System. Short Course on Geothermal Project Managenment and Development. Imperial Botanical Beach hotel, Entebbe, Uganda: UNU-GTP, KenGen.

Telford, W. M., Geldart, L. P., and Sheriff, R. E. (1990). Applied Geophysics, Second Edition. Cambridge University Press.

Thompson, D. T. (1982). EULDPH – A new technique for making computer – assisted depth estimates from magnetic data. 47, 31-37.

Tikhonov, A. N. (1950). The determination of the electrical properties of deep layers of the Earth's crust. Dokl. Acad. Nauk, SSR:73, 295-297.

Vozoff, K. (1991). The magnetotelluric method. In: Electromagnetic methods in applied geophysics, edited by M. N. Nabighian. Society of Exploration Geophysics, 2B, 641-711.

Vrána, S., Prasad, R., Fediukova, E., 1975. Metamorphic kyanite eclogites in the Lufilian Arc of Zambia. Contrib. Mineral. Petrol. 51, 39–160.

Wannamaker, P. E., Hasterok, D. P., Johnston, J. M., Stodt, J. A., Hall, D. B., Sodergren, T. L., et al. (2008). Lithospheric dismemberment and magmatic processes of the Great Basin-Colorado Plateau transition, Utah implied from magnetotelluric. Geochemistry Geophysics Geosystems, 9 (5), 1-38. 9(Q05019, doi:10.1029/ 2007GC001886).

Weidelt, P. (1972). The inverse problem of geomagnetic induction. 38, 257-289.

Wendorff, M. (2011). Tectonosedimentary expressions of the evolution of the Fungurume foreland basin in the Lufilian Arc, Neoproterozoic-Lower Palaezoic, Central Africa. The Formation and Evolution of Africa: A synopsis of 3.8 Ga of Earth History. Geological Society. 72.

WinGLink, M. (2005). WinGlink user's guide. Milan, Italy: Geosystems SRL.

Won, I. J. and Bevis, M. (1987). Computing the gravitational and magnetic anomalies due to a polygon: Algorithms and Fortran subroutines. Geophysics, 52, 232 - 238.

Zonge International. (2010). MTEdit Documentation. http://www.zonge.com. Accessed 10/07/2015.

Zonge International. (2013). ASTATIC v3.70 Documentation. http://www.zonge.com. Accessed 20/08/2015.